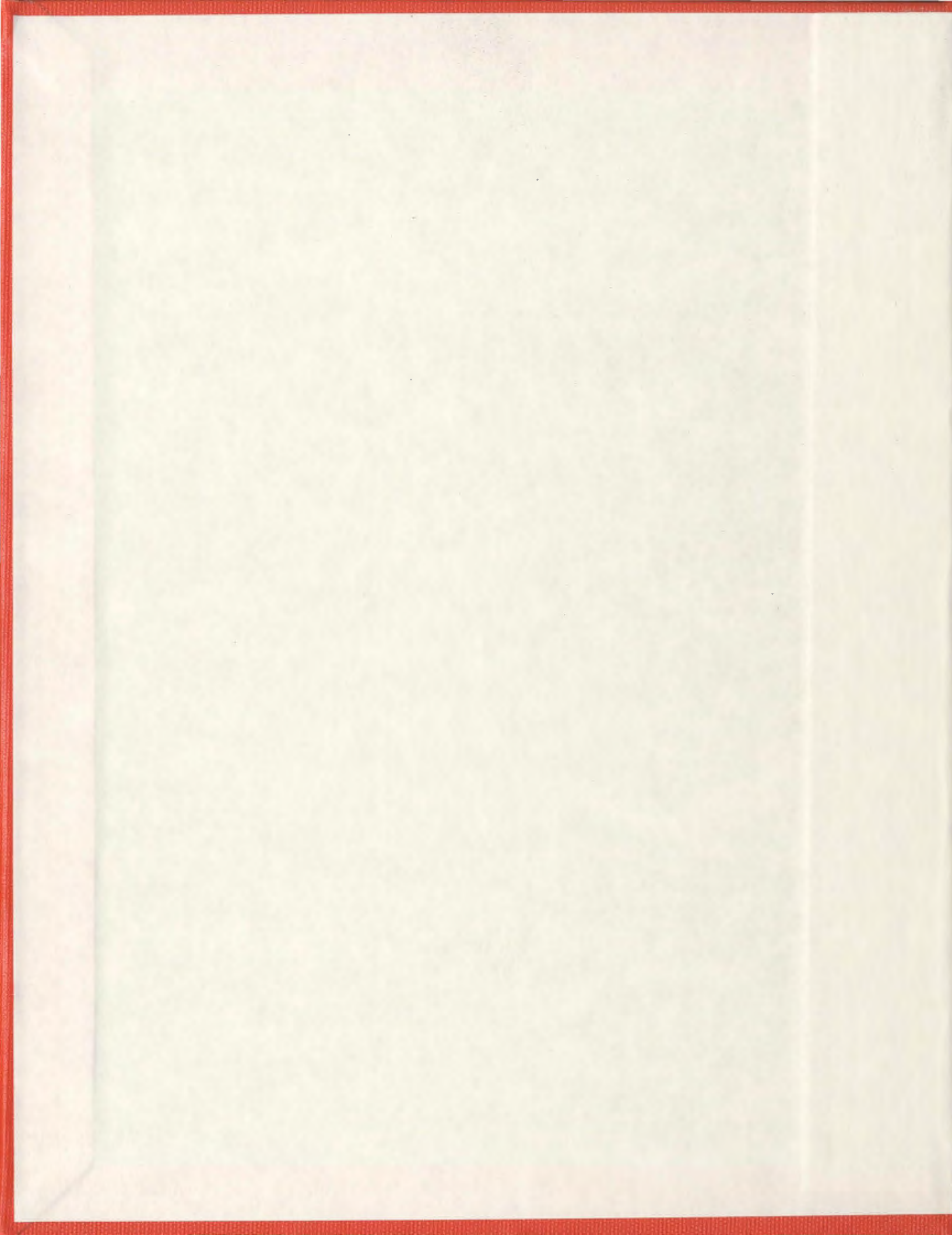


ADAPTING PRESSURE FILMS TO MEASURE PRESSURE
PATTERNS IN ICE-STEEL INTERACTION EXPERIMENTS

CHRISTOPHER ALAN ULAN-KVITBERG



**Adapting Pressure Films to Measure Pressure Patterns in Ice-Steel
Interaction Experiments**

by

Christopher Alan Ulan-Kvitberg, B. Sc.

A thesis submitted to the
School of Graduate Studies
in partial fulfillment of the requirements
for the degree of

Master of Engineering

Faculty of Engineering and Applied Science
Memorial University of Newfoundland

December 2012

St. John's

Newfoundland

Abstract

Exploration and recovery of arctic resources involves potential risks to ships and structures from ice loading. This thesis investigates the suitability of using chemical pressure-sensing films for ice-structure interaction experiments. A method of adapting the pressure films for use in laboratory-scale ice crushing experiments is first developed. Using the films, a series of uniaxial crushing tests under a range of factors are performed to develop 2D and 3D pressure maps, pressure-area curves and load histories. The results are analyzed to determine the spatial changes to ice under load and the connection between *process* and *spatial* pressure-area curves is investigated. Pressure-area equations are developed to compare the results to past research. The suitability of pressure-films for ice tests is analyzed and improvements for future experiments are suggested.

Acknowledgements

Firstly I would like to thank Dr. Claude Daley, Dr. Bruce Colbourne and all of my colleagues in the STePSS project for giving me the opportunity to participate in a groundbreaking research project and for the always thought-provoking discussions.

To my research partner Hyunwook Kim for all of his hard work in solving the many challenges we faced while designing and running these experiments and the insightful discussions on analysis.

To our technician Craig Mitchell the hard work at all odd times of the day and for going the extra step to ensure the success of our experiments, and to the staff at Memorial's Technical Services for their expert advice and craftsmanship.

To Dr. Scott Tiffin and Chris Hill for giving me my start in the ice field and for suggesting Memorial for my Master's Degree.

To my family for putting up with the years of separation.

Lastly, and most importantly, to my wife Ramona for accepting the rigours of living with a graduate student and all that it entails with good humour, grace and always with love.

Table of Contents

List of Figures	v
List of Tables.....	xiv
Nomenclature	xv
Author's Note.....	1
1. Introduction	2
1.1 Objectives of Study	3
1.2 Scope of Study.....	3
1.3. Thesis Outline.....	3
2. Literature Review	5
3. Experimental Motivation.....	25
4. Experimental Design	29
5. Pressure Films	40
6. Imaging Analysis.....	55
6.1: Creating Pressure-Area and Load History Curves from MTS Data	66
7. Results and Analysis.....	68
7.1: Primary Analysis of Data and Spatial Maps and Curves.....	68
7.1.1: Treatment Combination (1)	71
7.1.2: Treatment Combination bc	82
7.1.3: Treatment Combination bd.....	90
7.1.4: Treatment Combination cd	97
7.1.5: Treatment Combination ad	103
7.1.6: Treatment Combination ac	110
7.1.7: Treatment Combination abcd	117
7.1.8: Treatment Combination ab	125
7.2: Data Tables	133
7.3 Curve Fitting.....	140
8. Conclusions and Recommendations.....	145
References	148
Appendix A	150
Appendix B.....	230

List of Figures

Figure 1 - Ramping Sawtoothed Ice Loads (taken from Daley [5])	6
Figure 2 - Conceptual Hierarchy of Ice Failure (taken from Daley et al. [3])	8
Figure 3 - Results of Hobson's Choice Ice Island Tests (taken from Frederking et al. [7])	10
Figure 4 - X- Shaped Zone of High Pressure (taken from Gagnon [8])	12
Figure 5 - Instrumented Sub-Panel Layout, Louis St. Laurent (taken from Frederking [9])	13
Figure 6 - Instrumented Sub-Panel Layout for Oden (taken from Frederking [9])	14
Figure 7 - Pressure Curves, Louis St. Laurent (taken from Frederking et al. [9])	15
Figure 8 - Proposed <i>Spatial</i> and <i>Process</i> Pressure-Area Link (taken from Daley [10])	17
Figure 9 - Pressure and Load Plots, Terry Fox Impact Trials (taken from Ritch et al. [11])	19
Figure 10 - Progression of Pressures, Terry Fox Trials (taken from Ritch et al. [11])	20
Figure 11 - SGA and IP Panel Data Comparison (taken from Ritch et al. [11])	21
Figure 12 - Calibration Pressure Patterns (taken from Liggins et al. [12])	23
Figure 13 - Sample Pressure-Film Calibration Curve (taken from Liggins et al. [12])	24
Figure 14 - Shaped Ice Frozen into Ice Holders	25
Figure 15 - Confined and Unconfined Ice Conditions	26
Figure 16 - Ice Cone, 100 mm/s Impact. Unconfined (L) and Confined (R)	27
Figure 17 - Load Histories for Ice Cone (L) and Steel Cone (R), 100mm/s	27
Figure 18 - Constrained Ice Cone, 10 mm/s Impact Speed	28
Figure 19 - Demonstrating the Pressure Film	29
Figure 20 - Effect of Cone Angle on Contact Area	30
Figure 21 - MTS Machine Used to Crush Ice	31
Figure 22 - Cold Room at Memorial University of Newfoundland	32
Figure 23 - Ice-Growing Container	33
Figure 24 - Ice Chip Filtering	34

Figure 25 - Insulated Ice-Growth Containers in Freezer	35
Figure 26 - Shaping Ice Samples in Cones	35
Figure 27 - Treatment Combination Factors	37
Figure 28 - Ice Sample in MTS Machine, Ready for Crushing Against Steel Plate	39
Figure 29 - Nominal Contact Area from Penetration Depth	40
Figure 30 - Activated vs. Active Area (image taken from Kim [1])	42
Figure 31 - Accumulation of Pressure in the Pressure Films	43
Figure 32 - Pressure Film Ranges	44
Figure 33 - Impact Pattern from 2" Steel Rod	45
Figure 34 - Hertzian Contact Effects in Pressure Pattern	46
Figure 35 - Machined Calibration Tip	46
Figure 36 - Steel Contact Tip, Polycarbonate Plate and Steel Pressure Plate	47
Figure 37 - Close-Up of Calibration Tip and Polycarbonate Plate	48
Figure 38 - Pressure Patterns Determined from Calibration Tests	49
Figure 39 - Medium Range Calibration Curve	50
Figure 40 - Uninterrupted and Stepped Test Force Histories	52
Figure 41 - Method of Stepped Crushing for 30° Cone	54
Figure 42 - Unclean and Clean Pressure Films	56
Figure 43 - Step-By-Step Film Alignment	57
Figure 44 - Sample RGBColour Chart (table adapted from [21])	58
Figure 45 - Chart for 32-Bit Grey Scale (table adapted from [21])	59
Figure 46 - Multiple Pressure Readings due to Film Layering	60
Figure 47 - Selecting the Peak Pressure from Layered Films	61
Figure 48 - Expanding Square Sub Areas	62
Figure 49 - Merging Background and Pressure Pattern Arrays	63
Figure 50 - Finding Max Subarea A_T	64

Figure 51 - Examples of Sub Areas from A_1 to A_{100}	65
Figure 52 - Schematic of Creating <i>Spatial</i> PA Curve from Pressure Pattern	66
Figure 53 - Flowchart of Data Analysis	71
Figure 54 - Force-Displacement Curves, Treatment Combination (1)	72
Figure 55 - Pressure Films for F1T2 (l-r: Step a, b and c, t-b: L, M and H)	74
Figure 56 - 2D <i>Spatial</i> Pressure Maps, F1T2	75
Figure 57 - 3D <i>Spatial</i> Pressure Maps, F1T2	76
Figure 58 - <i>Spatial</i> and <i>Process</i> Pressure-Area Curves, F1T2	77
Figure 59 - <i>Process</i> Pressure-Area Curves, Treatment Combination (1)	78
Figure 60 - Force-Displacement Curve, Treatment Combination bc	82
Figure 61 - Progression of Pressure Patterns, F28T1 (l-r: Step a, b, c, t-b: L, M, H)	84
Figure 62 - "Missing" Spaces in Pressure Pattern	85
Figure 63 - Nominal and Actual Contact Areas, Low Range Film, F28T1	85
Figure 64 - 2D <i>Spatial</i> Pressure Maps, F28T1	86
Figure 65 - 3D <i>Spatial</i> Pressure Maps, F28T1	87
Figure 66 - Pressure-Area Curves, Treatment Combination bc	88
Figure 67 - <i>Process</i> Pressure-Area Plot, F28T1	89
Figure 68 - Force-Displacement Curve, Treatment Combination bd	91
Figure 69 - Pressure Films for F13T1 (l-r: Step a, b, c and d, t-b: L, M and H)	92
Figure 70 - 2D <i>Spatial</i> Pressure Maps, F13T1	94
Figure 71 - 3D <i>Spatial</i> Pressure Maps, F13T1	95
Figure 72 - <i>Spatial</i> and <i>Process</i> Pressure-Area Curves, F13T1	96
Figure 73 - <i>Process</i> Pressure-Area Curve Showing Effects of Confinement, F13T1	97
Figure 74 - Force-Displacement History, Treatment Combination cd	98
Figure 75 - Progression of Pressure Patterns, F13T2 (l-r: Step a, b, c, d t-b: L, M, H)	99
Figure 76 - 2D <i>Spatial</i> Pressure Maps, F13T2	100

Figure 77 - 3D <i>Spatial</i> Pressure Maps, F13T2	101
Figure 78 - <i>Spatial</i> and <i>Process</i> Pressure-Area Curves, F13T2	102
Figure 79 - <i>Process</i> Pressure-Area Curve, F13T2	103
Figure 80 - Force Displacement Histories, Treatment Combination <i>ad</i>	104
Figure 81 - Pressure Films for F13T3 (l-r: Step a, b, c and d; t-b: L and M)	105
Figure 82 - 2D <i>Spatial</i> Pressure Maps, F13T3	106
Figure 83 - 3D <i>Spatial</i> Pressure Maps, F13T3	107
Figure 84 - <i>Spatial</i> and <i>Process</i> Pressure-Area Curves, F13T3	107
Figure 85 - <i>Process</i> Pressure-Area Curves, Treatment Combination <i>ad</i>	108
Figure 86 - <i>Process</i> Pressure-Are Curves, Treatment Combination <i>ad</i>	109
Figure 87 - Force-Displacement History, Treatment Combination <i>ac</i>	111
Figure 88 - Progression of Pressure Patterns, F16T1, (l-r: Step a, b, c, d; t-b: L, M, H)	112
Figure 89 - 2D <i>Spatial</i> Maps, F16T1	113
Figure 90 - 3D <i>Spatial</i> Pressure Maps, F16T1	114
Figure 91 - <i>Spatial</i> and <i>Process</i> Pressure-Area Curves for F16T1	115
Figure 92 - <i>Process</i> Pressure-Area Curves, Treatment Combination <i>ac</i>	116
Figure 93 - Load History, Treatment Combination <i>abcd</i>	118
Figure 94 - Progression of Pressure Patterns, F20T1 (l-r: Step a, b, c, d; t-b: L, M, H)	119
Figure 95 - 2D <i>Spatial</i> Pressure Maps, F20T1	120
Figure 96 - 3D <i>Spatial</i> Pressure Maps, F20T1, Treatment Combo <i>abcd</i>	121
Figure 97 - Distinctive High Pressure Zone, F20T1d	122
Figure 98 - <i>Spatial</i> and <i>Process</i> Pressure-Area Curves, F20T1	122
Figure 99 - <i>Process</i> Pressure-Area Curves, Treatment Combo <i>abcd</i>	123
Figure 100 - Force-Displacement Curves, Treatment Combo <i>ab</i>	125
Figure 101 - Force-Displacement for F20T2a and F20T2b	126
Figure 102 - Progression of Pressure Patterns, F20T2 (l-4: Step a, b, c; t-b: L, M, H)	127

Figure 103 - 2D <i>Spatial</i> Pressure Maps, F20T2	129
Figure 104 - 3D <i>Spatial</i> Pressure Maps, F20T2	129
Figure 105 - <i>Spatial</i> and <i>Process</i> Pressure-Area Curves, F20T2	130
Figure 106 - <i>Process</i> Pressure-Area Curves, Treatment Combo <i>ab</i>	131
Figure 107 - Curve Fitting F1T2b	141
Figure 108 - Curve Fitting 'Envelope', F1T2	143
Figure 109 - F1T2a Low (1cm x 1cm Grid Spacing)	150
Figure 110 - F1T2a Medium (1cm x 1cm Grid Spacing)	151
Figure 111 - F1T2a High (1cm x 1cm Grid Spacing)	152
Figure 112 - F1T2b Low (1cm x 1cm Grid Spacing)	153
Figure 113 - F1T2b Medium (1cm x 1cm Grid Spacing)	154
Figure 114 - F1T2b High (1cm x 1cm Grid Spacing)	155
Figure 115 - F1T2c Low (1cm x 1cm Grid Spacing)	156
Figure 116 - F1T2c Medium (1cm x 1cm Grid Spacing)	157
Figure 117 - F1T2c High (1cm x 1cm Grid Spacing)	158
Figure 118 - F13T1a Low (1cm x 1cm Grid Spacing)	159
Figure 119 - F13T1a Medium (1cm x 1cm Grid Spacing)	160
Figure 120 - F13T1a High (1cm x 1cm Grid Spacing)	161
Figure 121 - F13T1b Low (1cm x 1cm Grid Spacing)	162
Figure 122 - F13T1b Medium (1cm x 1cm Grid Spacing)	163
Figure 123 - F13T1b High (1cm x 1cm Grid Spacing)	164
Figure 124 - F13T1c Low (1cm x 1cm Grid Spacing)	165
Figure 125 - F13T1c Medium (1cm x 1cm Grid Spacing)	166
Figure 126 - F13T1d Low (1cm x 1cm Grid Spacing)	167
Figure 127 - F13T1d Medium (1cm x 1cm Grid Spacing)	168
Figure 128 - F13T2a Low (1cm x 1cm Grid Spacing)	169

Figure 129 - F13T2a Medium (1cm x 1cm Grid Spacing)	170
Figure 130 - F13T2a High (1cm x 1cm Grid Spacing)	171
Figure 131 - F13T2b Low (1cm x 1cm Grid Spacing)	172
Figure 132 - F13T2b Medium (1cm x 1cm Grid Spacing)	173
Figure 133 - F13T2b High (1cm x 1cm Grid Spacing)	174
Figure 134 - F13T2c Low (1cm x 1cm Grid Spacing)	175
Figure 135 - F13T2c Medium (1cm x 1cm Grid Spacing)	176
Figure 136 - F13T2c High (1cm x 1cm Grid Spacing)	177
Figure 137 - F13T2d Low (1cm x 1cm Grid Spacing)	178
Figure 138 - F13T2d Medium (1cm x 1cm Grid Spacing)	179
Figure 139 - F13T2d High (1cm x 1cm Grid Spacing)	180
Figure 140 - F13T3a Low (1cm x 1cm Grid Spacing)	181
Figure 141 - F13T3a Medium (1cm x 1cm Grid Spacing)	182
Figure 142 - F13T3a High (1cm x 1cm Grid Spacing)	183
Figure 143 - F13T3b Low (1cm x 1cm Grid Spacing)	184
Figure 144 - F13T3b Medium (1cm x 1cm Grid Spacing)	185
Figure 145 - F13T3b High (1cm x 1cm Grid Spacing)	186
Figure 146 - F13T3c Low (1cm x 1cm Grid Spacing)	187
Figure 147 - F13T3c Medium (1cm x 1cm Grid Spacing)	188
Figure 148 - F13T3d Low (1cm x 1cm Grid Spacing)	189
Figure 149 - F13T3d Medium (1cm x 1cm Grid Spacing)	190
Figure 150 - F16T1a Low (1cm x 1cm Grid Spacing)	191
Figure 151 - F16T1a Medium (1cm x 1cm Grid Spacing)	192
Figure 152 - F16T1a High (1cm x 1cm Grid Spacing)	193
Figure 153 - F16T1b Low (1cm x 1cm Grid Spacing)	194
Figure 154 - F16T1b Medium (1cm x 1cm Grid Spacing)	195

Figure 155 - F16T1b High (1cm x 1cm Grid Spacing)	196
Figure 156 - F16T1c Low (1cm x 1cm Grid Spacing)	197
Figure 157 - F16T1c Medium (1cm x 1cm Grid Spacing)	198
Figure 158 - F16T1c High (1cm x 1cm Grid Spacing)	199
Figure 159 - F20T1a Low (1cm x 1cm Grid Spacing)	200
Figure 160 - F20T1a Medium (1cm x 1cm Grid Spacing)	201
Figure 161 - F20T1a High (1cm x 1cm Grid Spacing)	202
Figure 162 - F20T1b Low (1cm x 1cm Grid Spacing)	203
Figure 163 - F20T1b Medium (1cm x 1cm Grid Spacing)	204
Figure 164 - F20T1b High (1cm x 1cm Grid Spacing)	205
Figure 165 - F20T1c Low (1cm x 1cm Grid Spacing)	206
Figure 166 - F20T1c Medium (1cm x 1cm Grid Spacing)	207
Figure 167 - F20T1c High (1cm x 1cm Grid Spacing)	208
Figure 168 - F20T1d Low (1cm x 1cm Grid Spacing)	209
Figure 169 - F20T1d Medium (1cm x 1cm Grid Spacing)	210
Figure 170 - F20T1d High (1cm x 1cm Grid Spacing)	211
Figure 171 - F20T2a Low (1cm x 1cm Grid Spacing)	212
Figure 172 - F20T2a Medium (1cm x 1cm Grid Spacing)	213
Figure 173 - F20T2a High (1cm x 1cm Grid Spacing)	214
Figure 174 - F20T2b Low (1cm x 1cm Grid Spacing)	215
Figure 175 - F20T2b Medium (1cm x 1cm Grid Spacing)	216
Figure 176 - F20T2b High (1cm x 1cm Grid Spacing)	217
Figure 177 - F20T2c Low (1cm x 1cm Grid Spacing)	218
Figure 178 - F20T2c Medium (1cm x 1cm Grid Spacing)	219
Figure 179 - F20T2c High (1cm x 1cm Grid Spacing)	220
Figure 180 - F281a Low (1cm x 1cm Grid Spacing)	221

Figure 181 - F28T1a Medium (1cm x 1cm Grid Spacing)	222
Figure 182 - F28T1a High (1cm x 1cm Grid Spacing)	223
Figure 183 - F28T1b Low (1cm x 1cm Grid Spacing)	224
Figure 184 - F28T1b Medium (1cm x 1cm Grid Spacing)	225
Figure 185 - F28T1b High (1cm x 1cm Grid Spacing)	226
Figure 186 - F28T1c Low (1cm x 1cm Grid Spacing)	227
Figure 187 - F28T1c Medium (1cm x 1cm Grid Spacing)	228
Figure 188 - F28T1c High (1cm x 1cm Grid Spacing)	229
Figure 189 - F1T2a	230
Figure 190 - F1T2b	231
Figure 191 - F1T2c	232
Figure 192 - F13T1a	233
Figure 193 - F13T1b	234
Figure 194 - F13T1c	235
Figure 195 - F13T1d	236
Figure 196 - F13T2a	237
Figure 197 - F13T2b	238
Figure 198 - F13T2c	239
Figure 199 - F13T2d	240
Figure 200 - F13T3a	241
Figure 201 - F13T3b	242
Figure 202 - F13T3c	243
Figure 203 - F13T3d	244
Figure 204 - F16T1a	245
Figure 205 - F16T1b	246
Figure 206 - F16T1c	247

Figure 207 - F20T1a	248
Figure 208 - F20T1b	249
Figure 209 - F20T1c	250
Figure 210 - F20T1d	251
Figure 211 - F20T2a	252
Figure 212 - F20T2b	253
Figure 213 - F20T2c	254
Figure 214 - F28T1a	255
Figure 215 - F28T1b	256
Figure 216 - F28T1c	257

List of Tables

Table 1:	Experimental Factors and Levels	36
Table 2:	Blocking Scheme for ½ Fraction Experiment	38
Table 3:	Data for Calculating Medium Range Calibration Curve	50
Table 4:	Ice Crushing Step and Corresponding Penetration Depth	52
Table 5:	Sample from MTS Machine Data File	67
Table 6:	Experimental Test Schedule and Factor Combinations.....	68
Table 7:	Actual vs. Nominal Contact Area, FIT2	75
Table 8:	Rigorous and Non-Rigorous Methods of Finding Total Pressure on Film.....	81
Table 9:	Comparison of Nominal Contact Area to Actual Contact Area	134
Table 10:	Percentage of Total Area Occupied by High Pressure Zones.....	135
Table 11:	Correlation between SPA Curve End Pressures and PPA Pressures	137
Table 12:	Comparison of Predicted and Measured Maximum Load	138
Table 13:	Curve Fitting Parameters, $P = PoA^c$, Spatial Curves	142
Table 14:	Curve Fitting Parameters, $P = PoA^c$, Process Curves.....	143

Nomenclature

Units:

MPa: Megapascals

Symbols:

A: Contact Area

F: Force

P: Pressure

A_n : Square Sub-Area

L_n : Length of Square Sub-Area Side

n: Number of Sub-Area

y: Penetration Depth

θ : Cone Angle

P_o : Curve-Fitting Parameter

c: Curve-Fitting Parameter

Author's Note

The experiments for this study were performed jointly with Hyunwook Kim, also of the Sustainable Technology for Polar Ships and Structures research group at Memorial University of Newfoundland. The research diverged into different methods of image and data analysis. I highly encourage those who are interested to read the excellent work by Kim et al. [1].

1. Introduction

Developing resources in the arctic involves considerable challenges. At sea, ice is an ever-present risk to ships and offshore structures. The potential rewards for offshore resource development in the arctic are, however, high with an estimated 90 billion barrels of oil and 1670 trillion cubic feet of natural gas [2]. In order to safely exploit these resources, the mechanics of ice loads on ships and structures must be well understood.

Ice is a challenging material to design for. Unlike steel or concrete, exhaustive experiments have not been performed on ice to the point where one can be completely confident in understanding fully its behaviour. Ice is a solid material close to its melting point and as a result its behaviour under load is complex. Collisions with ice will result in an interrelated sequence of brittle fracturing, extrusion, pressure melting, recrystallization and ductile deformation. Ice type, age and temperature as well as load rate will all affect these processes to some degree. Repeated ice crushing tests will result in similar, but not exactly the same, measurements of force and pressure.

There have been many field and laboratory tests on ice over the years, the results of which have allowed engineers to create design codes for arctic ships and structures. These design codes use a number of parameters including interaction geometries and pressure-area relationships to determine design equations. However, the design methods may be further refined through detailed analysis of the mechanics of ice under load.

A particular challenge is measuring ice pressures across contact faces during ice collisions. A promising tool for examining changing ice pressures is the pressure-sensing chemical film. These films have the potential to allow fine-resolution recordings of ice under load but a method of adapting them for use with ice must first be determined.

1.1 *Objectives of Study*

Two concepts of significant interest to engineering design for ice loads are contact geometry and pressure-area relationships. Current design codes assume simplified geometries and pressure-area relationships which is, in part, due to a lack of high resolution pressure sensing instrumentation.

The objective of this study is to adapt high resolution pressure-sensing chemical films for use in small-scale laboratory ice experiments. The films can then be used to measure changes in spatial pressure patterns across ice contact faces under a range of test conditions.

1.2 *Scope of Study*

This study will determine a method of adapting chemical pressure films for use in laboratory-scale ice crushing tests and will then look at the results of repeated uniaxial crushing tests under a variety of test conditions using the films.

1.3 *Thesis Outline*

This thesis is divided into eight chapters. Chapter 2 reviews past research done in ice mechanics and highlights the movement towards studying pressure-area effects. A selection of experiments and field tests are discussed. The concepts of pressure-area effects are introduced and the possible connection between *process* and *spatial* effects is introduced. Pressure sensing methods are investigated, and the pressure sensing chemical

film is introduced. Chapter 3 describes the research and motivation which led to the experimental design of this study. Chapter 4 details the experimental design, describes certain aspects of the experimental apparatus and explains specific choices made for the experimental procedure. Chapter 5 goes in depth into the chemical films, explains how they work, what the benefits of them are and what potential challenges exist in their use, as well as solutions to these challenges. Chapter 6 details the analysis process used to interpret the chemical pressure patterns post-test and explains how the colour patterns were converted into pressure maps and *spatial* pressure-area curves. Chapter 7 presents the results and analysis of the experiments. Chapter 8 summarizes the thesis, presents conclusions and provides recommendations for future experiments using the chemical films. Appendix A and Appendix B provide enlarged copies of all pressure film patterns and 3D pressure maps.

2. Literature Review

The study of the physics of ice failure under load and the governing mechanisms of failure that occur is a complex topic. Ice can fail on a range of scales, ice can bend or it can deform, and failure can be affected by factors such as grain size and orientation, ice temperature and deformation rate, among many others [3]. There have been many experiments performed, both at laboratory and field scale, that have increased understanding of ice behavior. A selection of the experiments leading to the study of ice pressure-area effects are reviewed in this section.

An important early experiment on ice failure mechanisms was performed by Kheisin et al. in 1975 [4] by dropping a steel ball onto an ice sheet and examining the damaged layer of ice in the contact zone once ice impact had occurred. The authors assumed the resulting crushed layer of ice to be a viscous layer of thickness proportional to the pressure on the contact surface. The tests ignored dynamic changes in the contact face over the course of the collision, but the authors were able to develop from the tests one of the first working models of ice pressure.

Daley [5] proposed a model of ice load based upon observations of experiments performed by Joensuu and Riska [6]. Joensuu and Riska's experiments involved crushing a wedge-shaped ice block against either a clear plate window through which a videocamera was placed, or against a metal plate affixed with piezoelectric film pressure sensors. From their tests, load histories were found to follow a ramping sequence of load

spikes in a sawtoothed pattern, where load spikes increased to a maximum followed by a sharp load drop and a re-ramping of load shown in Figure 1.

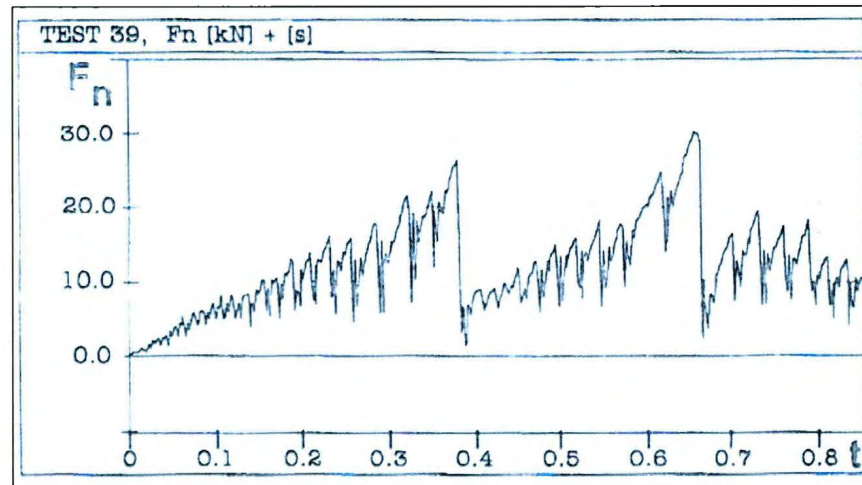


Figure 1 - Ramping Sawtoothed Ice Loads (taken from Daley [5])

Based upon observations of the load histories and the video footage, Daley proposed a model where loads in the ice-structure contact surface cause through-body surface failures to form and run to free edges of the ice, thereby resulting in the formation of flakes which break away from the contact face. Each flake causes a change in the contact surface geometry, and thus a change in loads and pressures. As the contact proceeds, loads are again built and the contact surface grows until internal loads again result in flake formation and a change in contact geometry and loads. This model explained both the sequential ramping of loads in the load history, the seeming line of constant contact seen by Joensuu and Riska, and the seeming randomness in ice load histories. The chaotic behaviour, as determined by the model, is not true randomness but is rather caused by differences in flake sizes. The formation of each flake is, however, entirely deterministic.

Daley et al. [3] then proposed a conceptual model for ice failure as a series of discrete failures, based on the ice load model. In their approach, the authors proposed to treat ice failure as a series of discrete limiting events as opposed to one limiting event. Generally speaking, the proposed model is a nested hierarchy of discrete failure events. At each level of the hierarchy a continuum process, such as elastic deformation of the ice, occurs until a limiting event (e.g. spall formation) disrupts this process. A new continuum process begins at each level following the disruption of the previous continuum process. Limit events on lower levels of the hierarchy stop and start discrete events at higher levels.

In order to provide a specific example of their model, the authors examined simplified local failure of a piece of ice under compression. Several mechanisms of ice pulverization were examined for inclusion in the model including (1) microcracking, where a field of microcracks in the ice caused by applied load leads to explosive crack growth and near instant pulverization; (2) macrocracks and explosion of flakes, where macrocracking leads to formation and subsequent pulverization of flakes from the contact surface; (3) macrocracks and comminution, where flakes are extruded rather than immediately pulverized, but are restricted and broken up in the extruding stream; (4) rapid macrocrack formation, where the ice enters such a stress state that a macrocrack forms but does not cause a flake, leading to the immediate formation of another macrocrack, continuing with rapid formation of macrocracks until the ice is sufficiently broken up as to relieve the stress state. The authors note that the exact failure mechanism which will occur is likely dependent upon such factors as impact velocity whereby at

slow speeds microcracking dominates the failure mode, while at high speeds macrocracking and flaking dominates.

Assuming these failure mechanisms, the authors illustrated the nested hierarchy of ice failure that would result, as demonstrated in Figure 2.

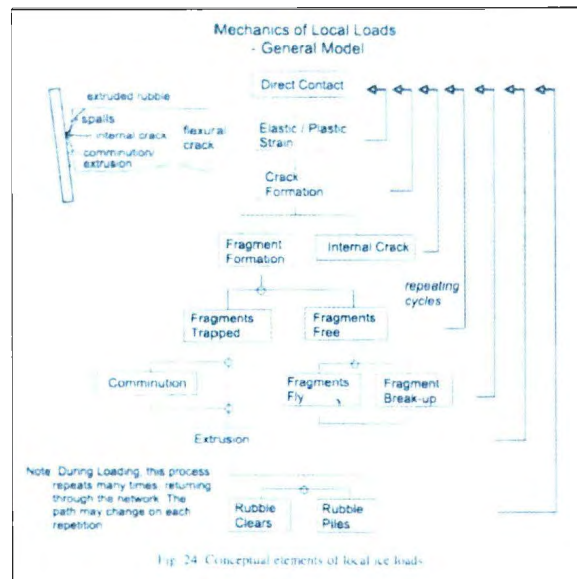


Figure 2 - Conceptual Hierarchy of Ice Failure (taken from Daley et al. [3])

First, there is contact between ice and impact surface leading to elastic and plastic strain, leading to crack formation (whether internal microcracking or flake formation). If a flake is formed, the flake is either trapped or freed from the contact surface. If freed, the flake is either completely extruded or broken up and then extruded. If trapped the flake is either crushed or extruded relatively intact. The final discrete process is where the extruded ice is either completely cleared or piled up outside of the contact zone as rubble. At each discrete process described above, disruption of the process leads to a reset of higher processes and a return to lower processes. For example, fragment formation leads to a

return to direct contact and a rebuilding of strain in the contact surface, leading to new crack formation.

The model suggested by Daley et al. offers a means of breaking down the complex and seemingly random mechanisms of ice failure under load into a set of discrete processes, each of which can readily be understood, but all of which connect together into a hierarchy of failure processes.

The study of ice in the field is an essential part of understanding ice loads. In 1989, a landmark series of medium scale (up to 1 m²) indentation tests were performed on Hobson's Choice Ice Island as part of a joint industry project between the National Research Council, Memorial University of Newfoundland, the Canadian Coast Guard and Sandwell Swan Wooster. Hobson's Choice Ice Island was a 5 km x 8 km and 40 m thick piece of ice comprised mostly of glacial ice, but also containing a large area of thick multi-year ice. A number of research papers resulted from the tests, including a report by Frederking et al. [7].

The tests involved digging a large trench in the ice island and installing large hydraulically actuated rams to drive shaped indenters into the ice. Three types of indenters were used: a rigid spherical indenter, a circular flat compliant indenter, and a rigid flat rectangular indenter. The impact surfaces were specifically prepared for each indenter – for the spherical indenter, the ice test faces were made flat. For both of the flat indenters, the ice test faces were shaped into truncated wedges with shallow angles to allow for the initial contact to induce fracture and for the nominal contact area to greatly increase over the course of a test.

A series of tests were run at speeds ranging from 0.3 mm/s up to 110 mm/s, resulting in maximum loads between 1.8 MN (for a circular, flexible indenter at 19 mm/s) and 4.4 MN (for a rigid, rectangular indenter at 10 mm/s). Pressures were determined as average pressures across the contact area and ranged from 6.3 MPa (for the spherical, rigid indenter at 110 mm/s) to 21.9 MPa (for the rigid, rectangular indenter at 10 mm/s). The tests revealed different failure modes. The test results are shown in Figure 3.

Test No.	Indentor	Ice Face	Rate	Max. Load	Load Time	Pen.	Final Area	Avg. Pres.
			mm/s	MN	s	mm	m ²	MPa
1	spherical	flat	~0.3	3.4	99	35	0.31	10.9
2	spherical	flat	~2.5	3.8	9.8	60	0.54	7.0
3	spherical	flat	~110	2.0	0.22	17	0.32	6.3
4.1	spherical	flat	~4	3.3	4.6			
4.2	spherical	flat	~15	3.5	0.48	19	0.22	16.0
5	spherical	flat	~90	3.6	0.69	22	0.20	18.0
6	flexible	120	19	1.8	1.9	30	0.27	6.7
7	flexible	270 1:3	68	4.5	0.4	25	0.37	12.2
8	rigid	200 1:5	~80	3.8	0.56	31	0.27	14.0
9	rigid	400 1:5	~10	4.4	0.4	1	0.20	21.9
10	rigid	200 1:5	~20	2.8	0.65	12	0.18	15.6

Figure 3 - Results of Hobson's Choice Ice Island Tests (taken from Frederking et al. [7])

Slow impact speeds resulted in creep deformation and large flaking from extended cracking in the surface. High speed impacts resulted in smaller flaking localized to the contact area and the area immediately surrounding, with observable ice extrusion.

Differentiation of pressure across the contact area was determined with pressure cells near the center of contact detecting average pressures 3x higher than the average pressures across the entire contact area. Load oscillations in a sawtoothed pattern were

detected in each test. It was also observed that the ice at the contact surface was largely intact near the center of contact, while everywhere the ice was crushed into a fine-grained material. Near the center, even pulverized ice was found to be very solid while at the edges of contact the pulverized ice was very soft, strongly indicating pressure variations across the contact surface.

During the Hobson's Choice ice island tests, a video camera was placed within each ice indenter with a clear window in the impact face to allow viewing. Gagnon [8] analyzed the video recordings of the indentations, specifically the tests with truncated pyramidal ice surfaces. The author observed that initial contact created a layer of finely crushed ice on the contact surface, but that even early into contact regions of uncrushed ice began to form in the center of contact, forming irregular patterns. These central uncrushed zones were of higher pressure and maintained constant contact with the indenter, while the surrounding ice was constantly crushed and pushed away. These constant-contact zones grew in size throughout the course of the interactions. The author determined conceptually that the shape of the zone was determined by spalling chunks of ice: in the pyramidal tests, spalls were extruded from the flat faces of the pyramid resulting in an X shaped high pressure zone in the contact face. This pattern was clearly seen in the ice island tests as shown in Figure 4.

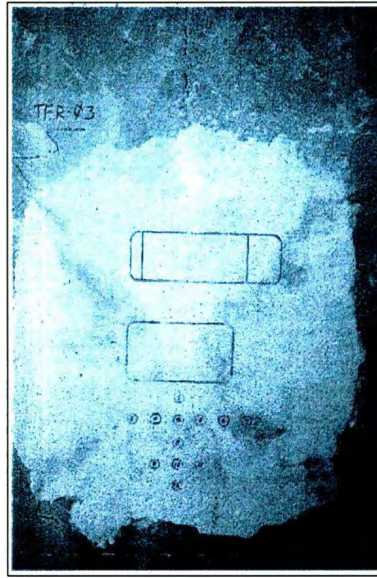


Figure 4 - X- Shaped Zone of High Pressure (taken from Gagnon [8])

By comparing displacement of the indenter, pressure, load and the video recordings, the author determined that loads and pressures build with little damage and reduced displacement until a spalling event occurs, at which point ice is fractured from the contact surface and extruded resulting in a sharp drop in load at which point loads increase again as crushing continues. This pattern gives load history curves during ice collisions of ramping sawtoothed patterns, seen repeatedly in ice research. Extrusion of spalls was seen to occur only at the load drops rather than being a continuous process and forward movement of the indenter during load increases was determined to be due to elastic compression in the ice. Horizontal thin sections cut from the crushed ice showed the high pressure zones (HPZs) to be largely intact and undamaged, surrounded by crushed ice at the peripheries of the contact area. Gagnon determined that these HPZs reached pressures in the 40 to 60 MPa range and supported the majority of the load during the crushing events. The spalling events, according to Gagnon, lead to significant

increases in pressure in the contact zone as the load is immediately transferred to a smaller area.

In order to better understand the formation and distribution of pressures across the contact zone during ice interactions, Frederking [9] proposed the separation of pressure-area curves into what he called *spatial distribution* and *process* pressure-area curves. *Process* curves illustrate how average pressures change as a function of nominal contact area over the course of a collision. *Spatial distribution* curves illustrate the changing average pressures on sub areas within the total contact area at a specific instant in time. The author analyzed data from sea trials aboard the CCGS Louis S. St. Laurent and Oden icebreakers and plotted both *process* and *spatial* curves. The Louis S. St. Laurent was instrumented over an area 7.2 m long by 3 m high covering six frames of the ship, shown in Figure 5.

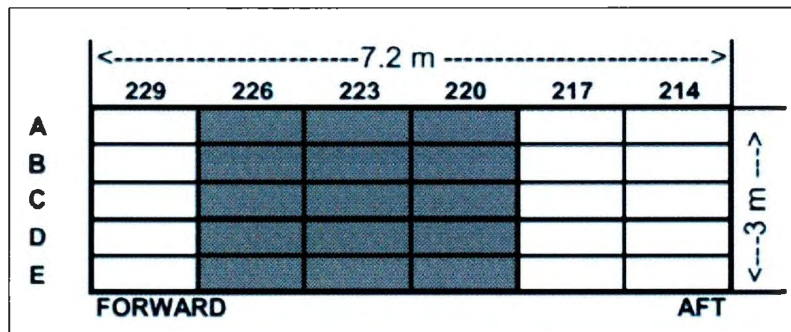


Figure 5 - Instrumented Sub-Panel Layout, Louis St. Laurent (taken from Frederking [9])

The forward frame and rear two frames were fitted with strain gauges at only the top and bottom of the frame, while the interior two frames were fitted with six evenly spaced strain gauges, thus splitting these frames into four equally sized sub panels. Loads on the

exterior frames were extrapolated from the interior frames, thus resulting in 30 sub panels from which average pressure measurements could be deduced.

For the Oden, an area 8.2 m wide by 3 m high covering 10 frames was used. Within that area, 8 frames were instrumented with strain gauges: 5 frames surrounding a central pair of un-instrumented frames and then a further 3 frames shown in Figure 6.

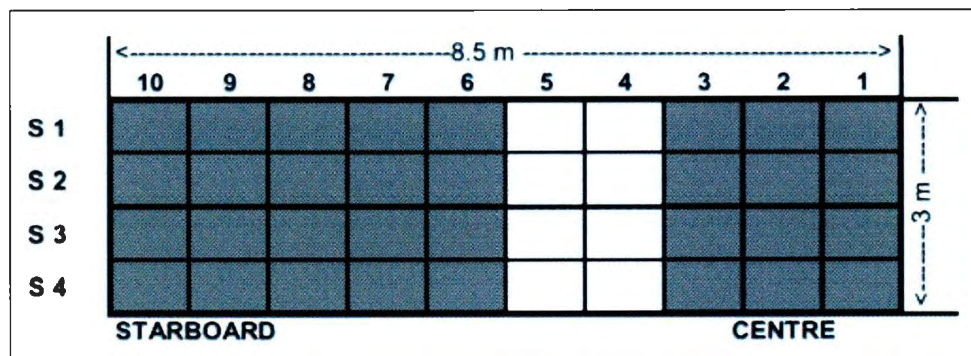


Figure 6 - Instrumented Sub-Panel Layout for Oden (taken from Frederking [9])

For each instrumented frame, 5 strain gauges were used. Loads on the un-instrumented frames were determined by linear interpolation, resulting in a total of 40 sub panels available to measure average pressures.

From the test data for select ice impacts, the author plotted force-time histories, showing the effects of loading and unloading rate due to impact velocities, and *process* pressure-area curves. Figure 7 showing the average pressure curves from 3 specific sub areas from the Louis St. Laurent showed clearly the spatial movement of pressures both in time and space between sub panels, highlighting spatial changes over the course of a collision.

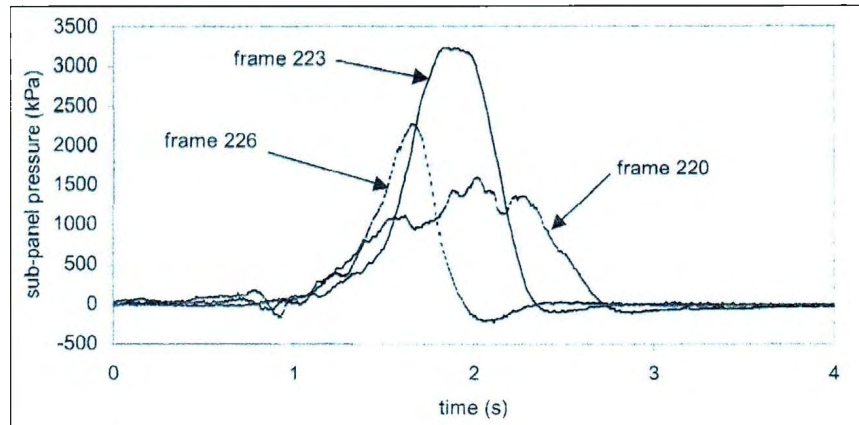


Figure 7 - Pressure Curves, Louis St. Laurent (taken from Frederking et al. [9])

The author plotted *spatial* pressure-area curves by selecting groups of adjacent sub panels at a specific instant in time and expanding the sub-area by adding adjacent panels. For the Louis St. Laurent, an expanding series of sub-areas of 0.72 m², 2.88 m², 4.32 m², 6.48 m² and 8.64 m² were examined to find the extreme average and maximum average pressures. The plot showed an exponentially decreasing curve, and the author determined a best-fit line of the form

[1]

with p being pressure in MPa and A being contact area in m². A similar analysis was performed for data from the Oden and a best-fit line was determined to be

$$p = 3.46A^{-0.51} \quad [2]$$

Importantly, the author makes note that there is no unique method of selecting sub areas when creating *spatial* pressure-area curves. Different methods may have different benefits to the analyst, and each will result in a different *spatial* curve. The end point of a

spatial curve, however, will be the same regardless of the sub area selection method, so long as the analyst expands to the total contact area. This terminal point of the *spatial* curve will be the average pressure across the total contact area, and this in turn is a point on the *process* pressure-area curve.

Daley [10] first reported the link between *process* and *spatial* pressure-area curves. Daley re-analyzed pressure data recorded during ice trials aboard the Polar Sea. In 1984, the USCGC Polar Sea icebreaker was fitted with an array of strain gauges within the hull and over the course of several years was used to impact ice and collect pressure readings. Through previous tests and computer models Daley discovered that in contradiction to the assumptions of many researchers and, more importantly of current code requirements such as CSA 1992 and API 1995, local pressures within the contact area may be important to consider and may be directly correlated with force and inversely correlated with area. Local pressures may be very high over small areas and may even increase as total load increases. He also determined that the *process* pressures may not necessarily decline with increasing area, as is often assumed.

The author assumed in his paper that *process* and *spatial* curves are indeed linked for the same process by the terminal point on each *spatial* curve. The significance of this, according to the author, is that if *process* (average) pressures can indeed rise over the course of an ice collision, then the associated *spatial* curves will also rise, meaning that the average pressures contained in small areas across the contact surface will rise. This is significant because the pressures on small areas within the contact zone can be orders of magnitude greater than the *process* pressures across the entire contact area.

Analyzing the data from the Polar Sea trials, the author saw evidence of the link between *process* and *spatial* curves and also saw that *process* curves do not necessarily decline for an entire ice impact event as shown in Figure 8.

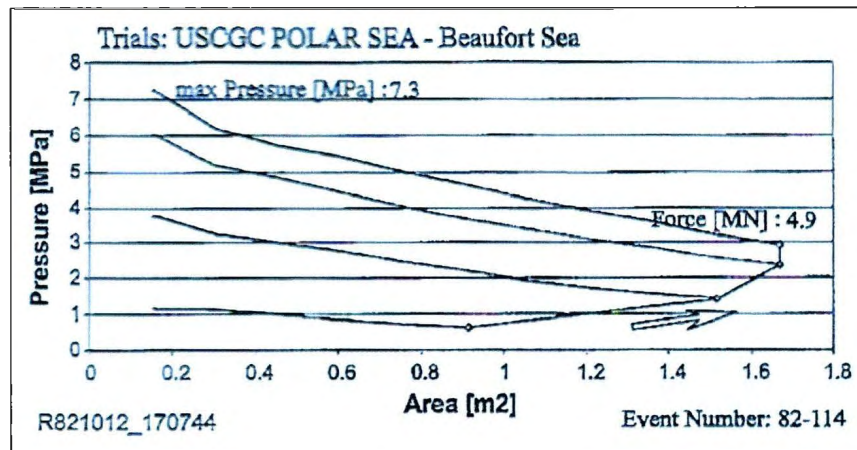


Figure 8 - Proposed *Spatial* and *Process* Pressure-Area Link (taken from Daley [10])

According to the author the link between *spatial* and *process* pressure-area curves is not accounted for by the engineering design codes and is also often overlooked by researchers. In order to determine the significance of this link and its impact on design codes the *spatial* and *process* pressure effects of ice-structure interactions must be rigorously studied and the exact nature of the link understood.

Measuring ice pressures during ice interactions requires the use of novel pressure sensing methods. There have been several studies involving the use of different pressure sensing equipment. In 2001 a series of field tests were performed aboard the CCGS Terry Fox off of North East Newfoundland. The results were reported by Ritch et al. [11]. In these tests the Terry Fox was outfitted, in a section of its bow, with 120 strain gauges in

order to measure 60 locations. The instrumented area was 5.4 m² split into 34 sub-panels based on the ship's geometry. The smallest of these sub-panels were 0.08 m². Before installing the strain gauges, a Finite Element model was created to develop an "influence matrix" to convert strain into force and pressure. During installation, the panels were calibrated with known forces in order to validate the FE model.

The total test plan involved 178 impacts against 19 different bergy bits. Bergy bits are relatively small masses of glacial ice and the test masses ranged from 30 ton to 22 000 ton. The impact speeds ranged from 0.2 m/s to 6.5 m/s. Tests were performed at an ice surface temperature of approximately 0 °C and a core temperature of approximately -15 °C. Data was collected at a rate of 500 Hz.

The authors used several methods to analyze pressure effects from the test data. Sub areas on the test area were referred to as "cells", which are subdivided areas from the FE model. *Spatial* pressure-area curves were created by choosing the "cell" with the highest pressure at a given point in time, plotting that pressure, then choosing the next highest pressure on a contiguous "cell" and plotting that pressure, continuing through all contiguous "cells". Pressures below 0.25 MPa were assumed to be 0 and non-contiguous "cell" data was discounted.

The authors also plotted pressures on each cell as a function of time, thus showing comparative pressure evolution on a cell by cell basis. Comparative plots were made of maximum pressure on a single cell, maximum total force, total contact area at maximum force and average pressure on the total loaded area, shown in Figure 9.

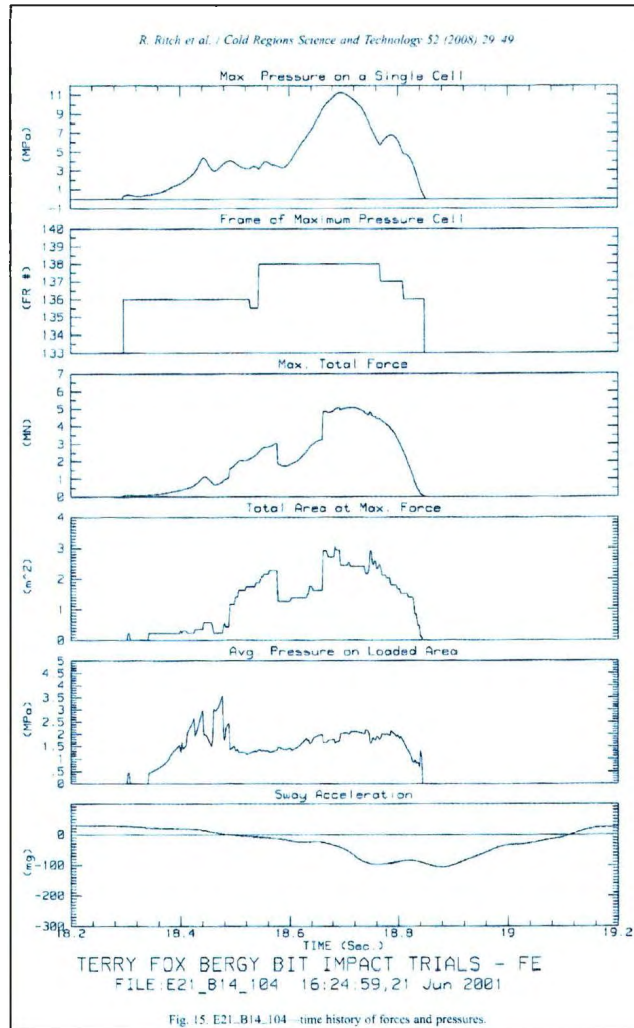


Figure 9 - Pressure and Load Plots, Terry Fox Impact Trials (taken from Ritch et al. [11])

From these plots, a sense of how the load moved across the contact surface was determined as well as the size of the load and contact area, and the peak pressures within the contact area. A peak cell pressure of 11.3 MPa was found on a contact area of 0.12 m², while a maximum total force was measured to be 5.0 MN.

3D plots, shown in Figure 10, were made of the pressure patterns over the course of a collision event, showing a definite "peakiness" to the patterns and very irregular geometries.

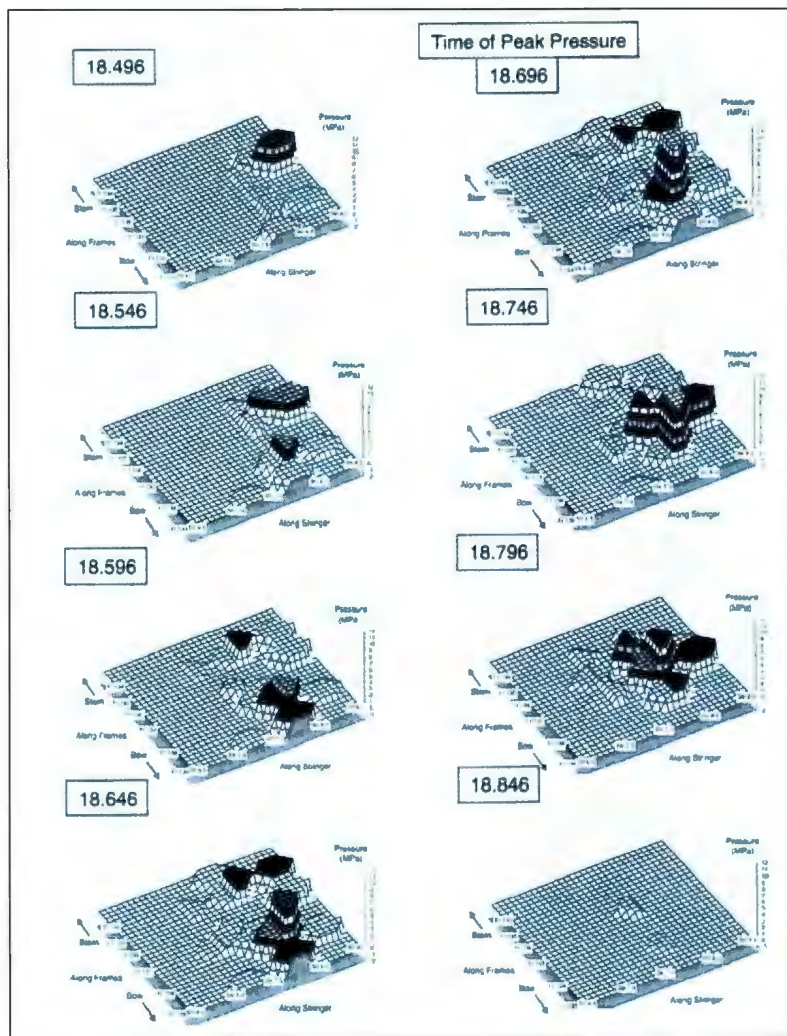


Figure 10 - Progression of Pressures, Terry Fox Trials (taken from Ritch et al. [11])

The authors also created *spatial* pressure-area curves at the time of peak single cell pressure for the four impact events which showed the largest small area pressures. They then plotted an enveloping curve for the four *spatial* curves of the form $P = C_p A^{D_p}$, the same form as used by other researchers as discussed. The authors determined C_p to be 3.5 and D_p to be -0.56. These numbers are similar to those reported by Frederking et al. [9] for the Oden. Spatial curves were plotted for the moments of time with the 10 highest

pressures on a single "cell" area and a total loading area greater than 1 m². Comparison with the total load on the contact area indicated that a higher peak pressure on a single cell led to overall higher pressure across the contact area and therefore a higher load. This is suggestive of the *spatial* and *process* link suggested by Daley.

Lastly, the authors compared the results from their strain gauge panel ("SGA") to the results from another pressure panel used on the Terry Fox during the same trials. This panel ("IP") was built by the Institute for Ocean Technology and was installed at a different point in the hull, thus preventing direct comparison between events. Comparisons of pressure recordings were made by plotting the average pressure across the total contact at the time of maximum load for each event, as well as plotting the average pressures in sub areas over 5 MPa (High Pressure Zones or "hard zones"). The comparison is shown in Figure 11.

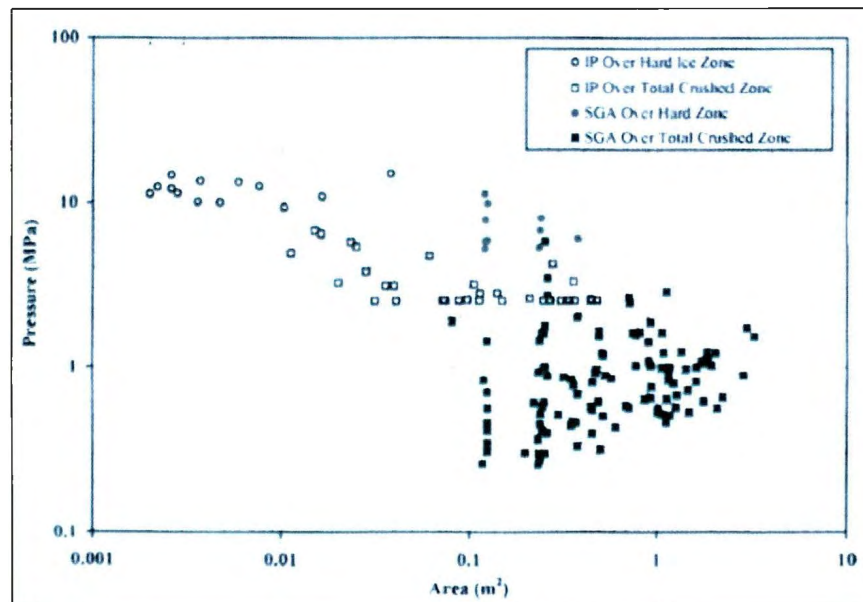


Figure 11 - SGA and IP Panel Data Comparison (taken from Ritch et al. [11])

The comparisons revealed resolution issues with the strain gauge panel since the highest sub pressures measured were lower than the highest pressures measured by the IOT panel, and at larger areas. In addition, the strain gauge panel was found to overestimate the contact area, resulting in generally lower average pressures than the IOT panel. The IOT panel indicated constant to slightly increasing pressures with increasing area on hard zones for areas up to 0.1 m^2 and generally decreasing average pressures across total contact area with increasing area.

High resolution chemical pressure-sensing films offer a potentially attractive means of measuring pressure during ice interactions. Liggins et al. [12] analyzed the use of Fujifilm Prescale pressure-sensitive films for measuring pressures and contact patterns for prosthetic joints. In order to make the use of the pressure films more practical and to ensure the validity of test results outside of the given data sheet ranges provided by Fujifilm, the authors developed a means of calibrating and digitizing the pressure films. The pressure films come in specific valid pressure ranges. Medium range, for example, is valid between 10 MPa and 50 MPa. In order to create calibration patterns, an apparatus was built with a steel base plate, a steel calibration punch, ball bearings and a load cell. All of this was mounted on an MTS test machine. The test film was placed on the base plate and the punch was placed on top of the film. The ball bearing was placed onto the end of the punch in order to reduce eccentric loading and increase the uniformity of the pressure pattern. Loads were then applied to the pressure films at chosen levels across the range of the given data sheets. Pressure patterns were screened for acceptable levels of

uniformity. Truly uniform patterns were difficult to achieve even with the ball bearing apparatus, as seen in Figure 12, therefore mean pressure value across the pressure pattern was used.

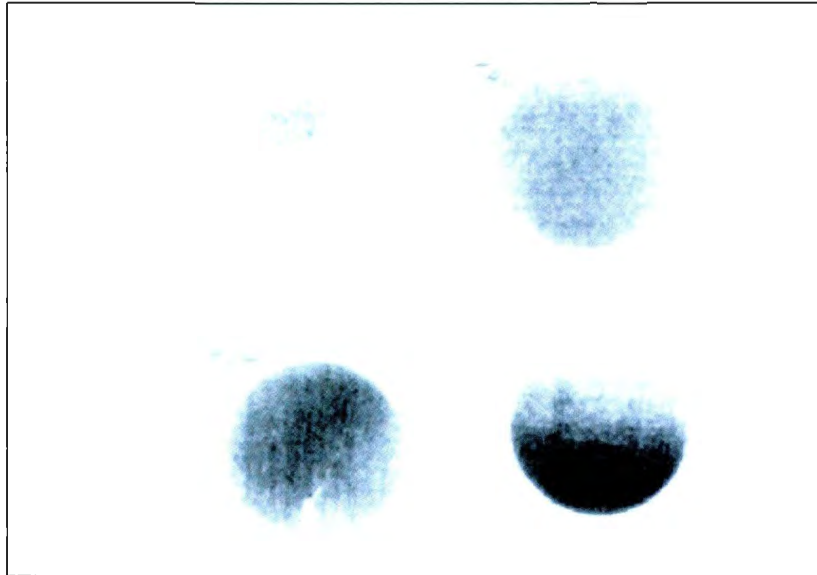


Figure 12 - Calibration Pressure Patterns (taken from Liggins et al. [12])

In order to digitize the chemical pressure patterns, a CCD camera was used to record the pressure patterns. The patterns were filtered by first calculating the mean pixel value of sets of four pixels and then resetting the set of pixels to that value. Once the pixels were all filtered, the mean value of the largest square area within the contact pattern was then determined. This was used as the pixel value for the calibration. After determining the pixel value for each applied load, the pressure on the contact area was determined and pixel-pressure calibration curves were created. An example curve is shown in Figure 13.

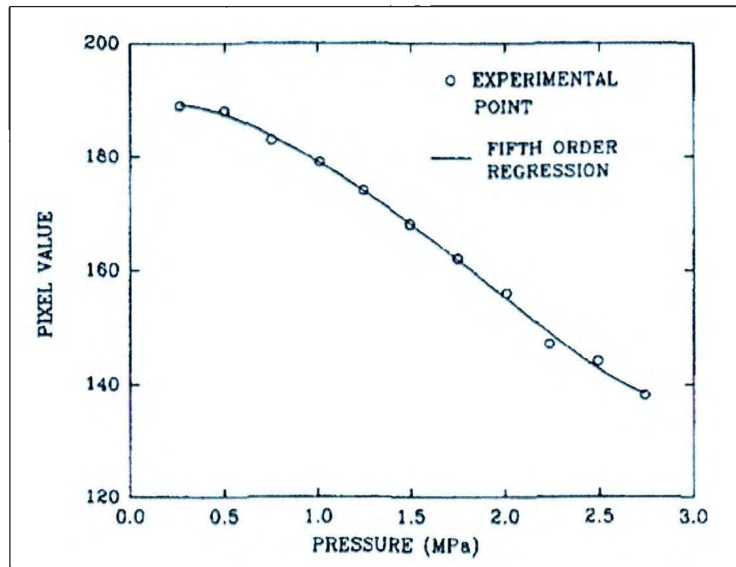


Figure 13 - Sample Pressure-Film Calibration Curve (taken from Liggins et al. [12])

In order to create coloured pressure maps Liggins et al. created software in order to convert the pixel patterns into colour patterns. The authors did not solve the problem of plotting a complete pressure map for a pressure pattern expanding into multiple pressure ranges. A solution will need to be found for this since ice pressures will likely not stay within a single Fujifilm pressure range.

3. Experimental Motivation

One method for studying forces and pressures during ice collisions is the uniaxial ice crushing test. In order to study the effects of ice geometry and the presence of water during these tests, Ulan-Kvitberg et al. [13] and Kim et al [14] performed a series of comparative uniaxial crushing tests. The authors [13] tested the effects of ice geometry and level of ice confinement on load histories and *process* pressure-area curves by shaping clear blocks of ice into 10 cm diameter and 22° cones and wedges. The shaped ice was then frozen into steel ice holders. An example is show in Figure 14.



Figure 14 - Shaped Ice Frozen into Ice Holders

The ice was shaped in one of two conditions: a confined condition, where the shaped portion of the ice lay flush with the ice holder, and an unconfined condition where the shaped portion was extended beyond the ice holder. This is demonstrated in Figure 15.

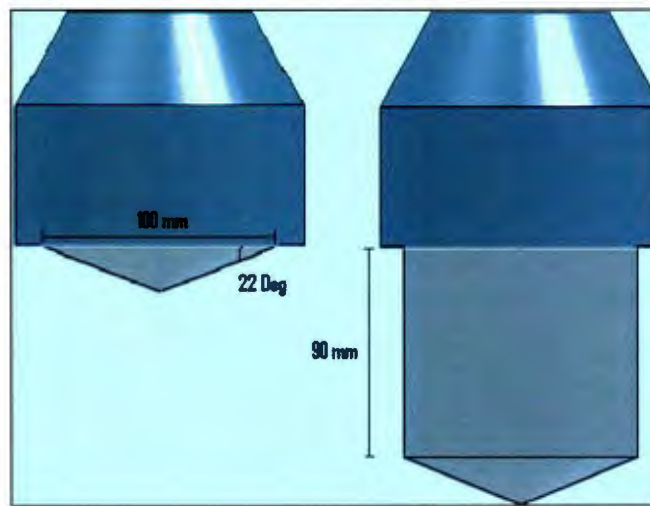


Figure 15 - Confined and Unconfined Ice Conditions

The ice samples were then crushed against a steel plate at a speed of 100 mm/s. The tests were then repeated by crushing steel indenters, shaped into the same geometries as the ice, into blocks of ice. The purpose of the tests was to determine the effect of geometry on ice loads. The unconfined condition in these tests was the ice blocks held in position at only certain points along their edge, while the confined condition was the ice completely frozen into aluminum boxes. The comparative tests revealed that the level of constraint caused significant changes to the *process* pressure-area curves, causing the curves to decrease exponentially for part of the collision before rising past a certain point as shown in Figure 16. Geometry, while not affecting the total loads, did affect the force histories as seen in Figure 17.

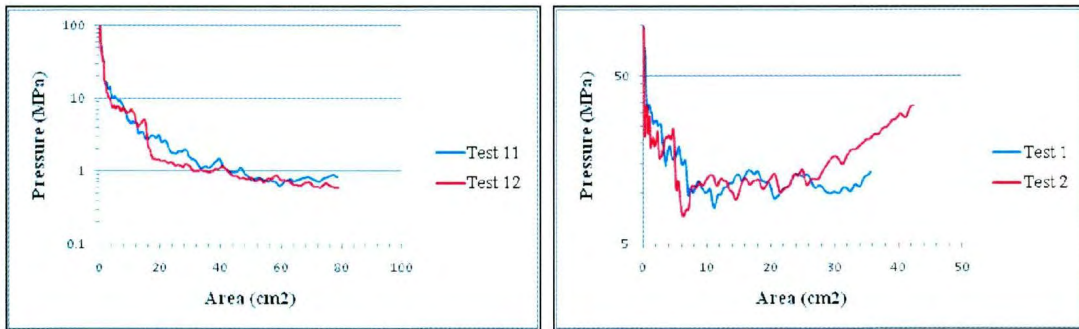


Figure 16 - Ice Cone, 100 mm/s Impact, Unconfined (L) and Confined (R)

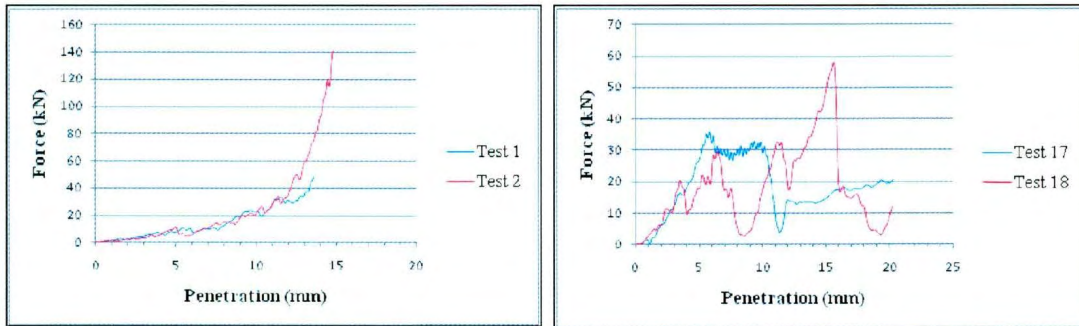


Figure 17 - Load Histories for Ice Cone (L) and Steel Cone (R), 100mm/s

The very high load spike at the end of Test 2 was due to contact between the steel holder and steel plate. The load histories are very different for the steel cone indenter than the ice cone indenters. The *process* pressure rise past a certain crushing depth may be important and overlooked as suggested by Daley [10].

The effect of impact speed was examined by repeating the constrained tests at speeds of 10 mm/s. The resulting curves showed similar behaviour but with a greater increase in force and pressure oscillations in a sawtoothed ramping pattern as shown in Figure 18.

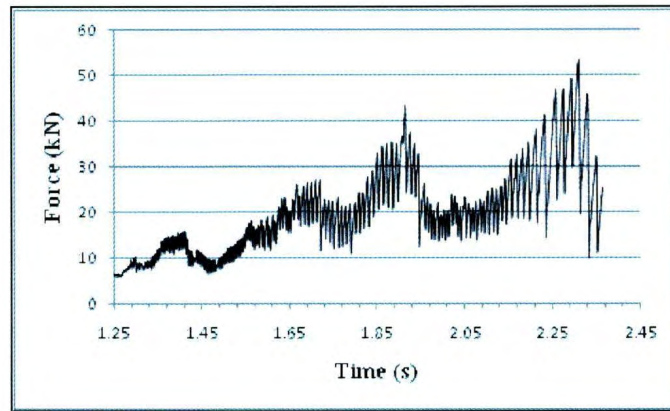


Figure 18 - Constrained Ice Cone, 10 mm/s Impact Speed

The results of the tests suggest that geometry and impact speed, as well as confinement, are important factors to consider in predicting loads during ice impacts. There are other potentially interesting factors, such as grain size and temperature, which may affect ice loads. Therefore, a series of ice crushing tests performed under a range of potentially significant factors would be of value to furthering the understanding of ice crushing physics.

It is this question of factor significance which formed the primary motivation for the design used in this study. However, in order to gain a deeper understanding of the mechanisms occurring during ice crushing, a method is needed to determine not only the average pressures across the contact area, but also the spatial variations in pressure. As discussed, the *spatial* pressure-area curves are very important and appear to be linked to the *process* pressure-area curves. The pressure sensing chemical films developed by Fujifilm and tested by Liggins et al. [12] may provide a means of recording spatial changes in pressures at a very fine resolution, if they can be adapted for use with ice.

4. Experimental Design

The purpose of this study is to adapt chemical pressure films in order to record spatial pressure changes in ice under a range of test factors. An example of the chemical film is shown in Figure 19. Proceeding clockwise from top left, the two sheets containing the chemical reactants are shown. In the next frame, the sheets are laid on top of each other. In the next frame, the sheets are laid on top of each other. Next, a load is imposed on the film, and lastly a pressure pattern is recorded.

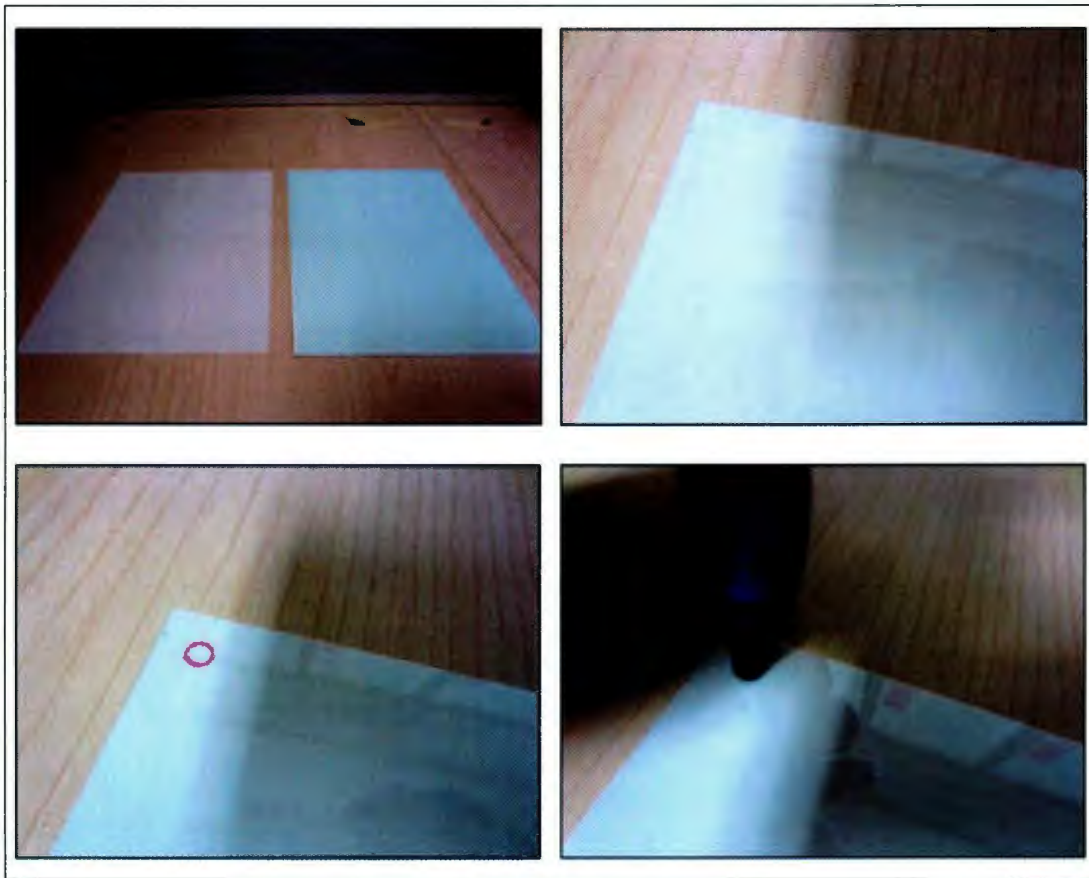


Figure 19 - Demonstrating the Pressure Film

Before determining a way to adapt the pressure films for use with ice, a test design must be determined. In this study, it was decided to continue with the uniaxial crushing tests between ice samples and a 0.5" steel plate. The ice samples were grown in the lab and shaped into cones of two different angles. Crushing cones of different angles, at the same speed, allows for the effect of geometry on contact area growth to be determined, since the steeper the cone angle the less ice will be in contact with the plate at a specific time in the collision event. This is shown in Figure 20.

The crushing tests were performed using an MTS mechanical testing system fitted with a Model 810.24 Load Unit, Model 661.23-01 Force Transducer and a Model 244.41s Linear Hydraulic Actuator, shown in Figure 21.

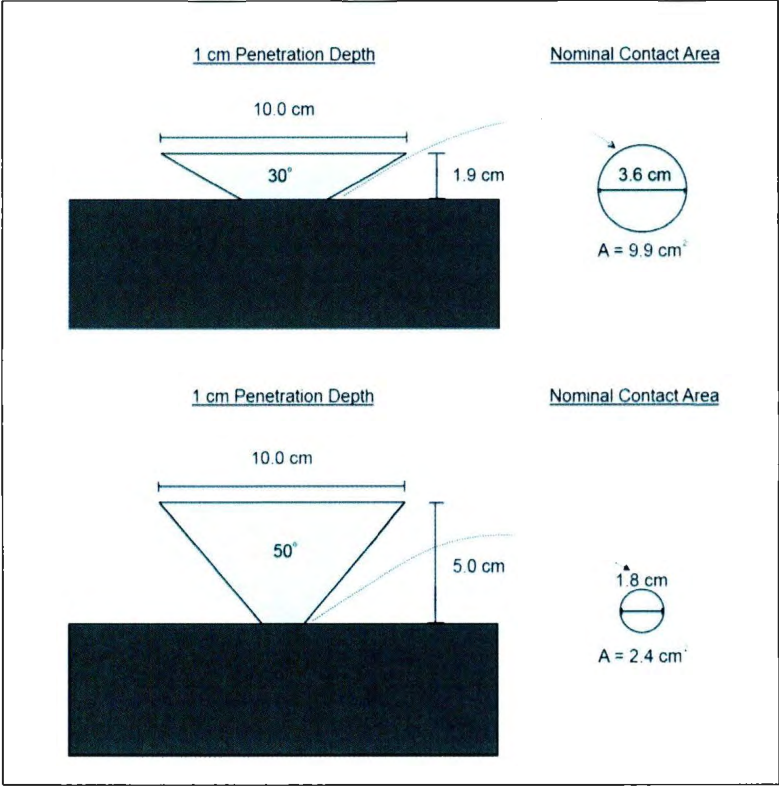


Figure 20 - Effect of Cone Angle on Contact Area

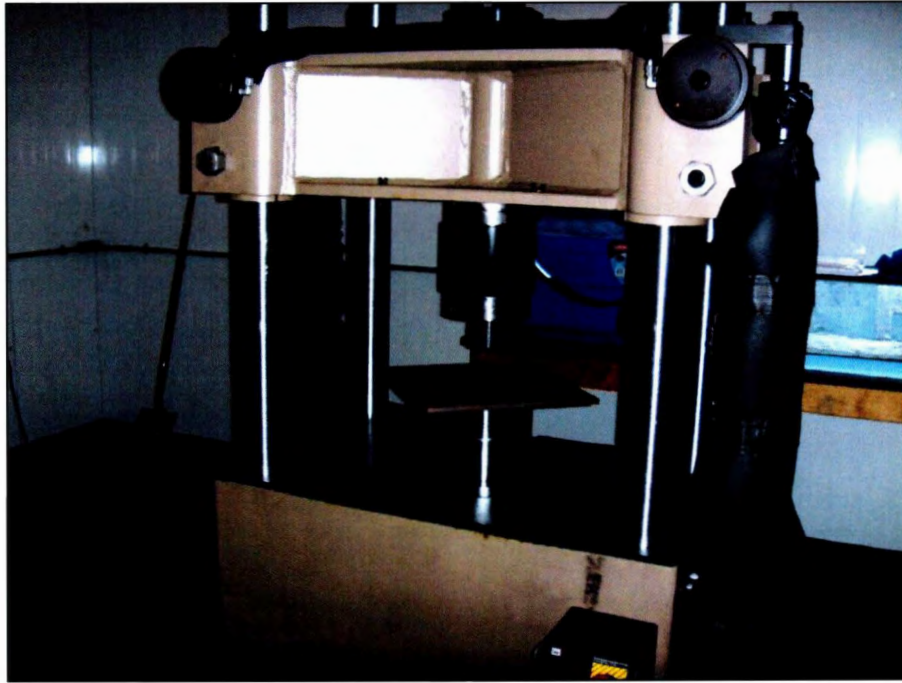


Figure 21 - MTS Machine Used to Crush Ice

The MTS machine can reach up to 100 mm/s. The top section is moved into position using manual controls while the bottom ram is set at a starting position using computer controls. A final ram displacement and speed is entered into the computer controls and the test is run. The design of the MTS machine allows plates and holders affixed with 2'' threaded rods to screw into the top and bottom of the apparatus. The MTS machine is housed within the Cold Room contained within the laboratories of the Memorial University of Newfoundland's Department of Engineering. The Cold Room can sustain temperatures down to approximately -40C and has room for experimental apparatus, tools, workstations and ice storage. For these experiments a band-saw, ice chipper, ice

shaver, and the MTS Machine were employed in ice-shaping and crushing. The Cold Room is shown in Figure 22.



Figure 22 - Cold Room at Memorial University of Newfoundland

Ice was grown in containers, shown in Figure 23, using a method adapted from Bruneau et al. [15]. In order to simulate multi-year ice, the containers were first seeded with grains made from ice cubes run through an ice-chipper. The ice chips were filtered to a desired size range, shown in Figure 24, and poured into the container in a layering method. In this method, a layer of ice chips was poured into the container, water was added and the mix was stirred to allow air to escape. More chips were added, followed by more water, and so on until the container was full.



Figure 23 - Ice-Growing Container

In order to remove impurities that collect along the ice grain boundaries, the water added was first distilled and then deaerated. The filled ice containers were then insulated along the top and sides, but not the bottoms, to ensure a preferential growth from bottom up and thus reduce the amount of cracks and air bubbles trapped between the grain boundaries. The containers were placed in deep freezers to freeze for a minimum of 48 hours as shown in Figure 25.



Figure 24 - Ice Chip Filtering

Once the samples were frozen, they were shaped into cones. In order to shape the cones, a specially designed ice-shaver in the cold room was used. This device features a rotating 'Potter's wheel' and a manually lowered planar blade. Using this apparatus, the ice cylinders were shaped into cones of a specific cone angle as shown in Figure 26.



Figure 25 - Insulated Ice-Growth Containers in Freezer



Figure 26 - Shaping Ice Samples in Cones

The experimental test schedule was designed according to the Design of Experiments methodology. Design of Experiments (DoE) determines the statistical significance of a range of test factors. If significance is low, the factors can be rejected. A set of parametric equations can then be determined for a set of response variables of interest. An introduction to the methods of DoE can be found in Oehlert [16] In order for the statistical significance to be determined, a specific test schedule must be adhered to involving proper randomization of the combinations of test factors. Initial test planning for this study used the DoE method and so the test schedule was designed accordingly.

The test schedule was designed as a two-level, four-factor, half-fraction experiment split into two blocks. This means that four factors were considered, each at two different possible values, and the experiments were to be optimally performed in two runs (blocks). Grain size, impact speed, and temperature were all determined to be factors that will potentially affect ice strength and therefore affect measured loads and pressures. The effect of cone angle was the fourth factor. The factors and their levels are shown below in Table 1.

Table 1: Experimental Factors and Levels

	Factor	Low	High
A	Temperature (°C)	-15	-5
B	Grain Size (mm)	1-5	6-10
C	Impact Speed (mm/s)	1	100
D	Cone Angle (°)	30	50

Experiments were run by factor or “treatment” combinations. For a given treatment combination if the factor letter is written in lower case the experiment is run with that factor at its “High” level. If the factor letter is not listed, the experiment is run with that factor at the “Low” level. This is illustrated in Figure 27.

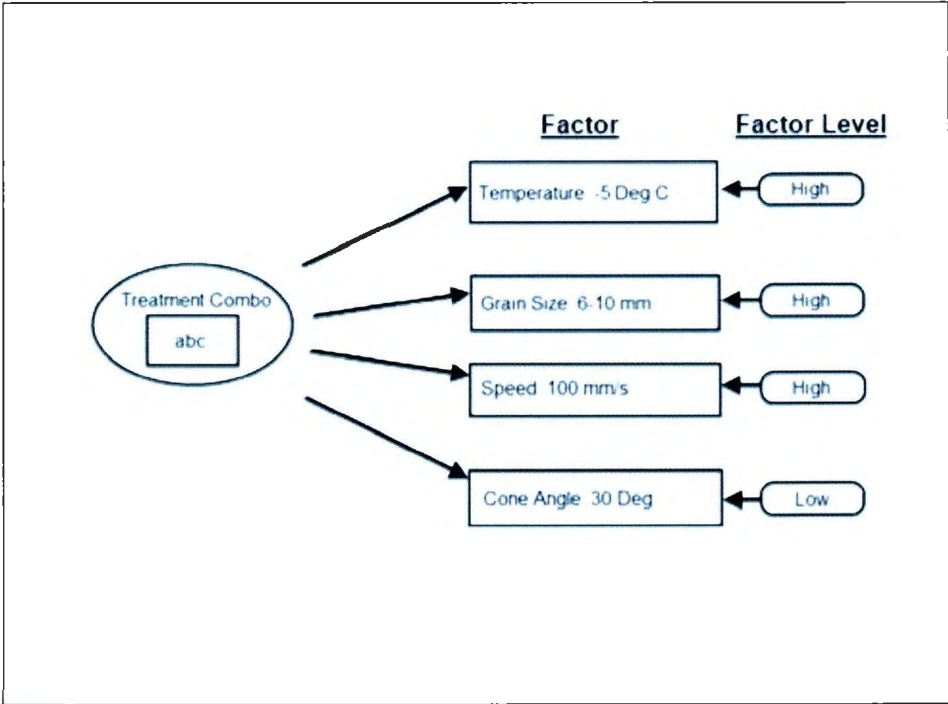


Figure 27 - Treatment Combination Factors

Running a half-fraction experiment meant only half of the test runs needed to be analyzed, which was necessary given a limited supply of pressure films. It was also decided to run one replication of the tests. Replication in a DoE experiment improves the statistical interpretation of the results.

Upon physically testing the experimental apparatus it was determined to be impractical to change the temperature in the cold room before each test due to the time

length required to warm-up or cool-down the room. It was therefore decided to use a DoE technique called “blocking” in order to run all of the treatment combinations at low temperature first, and then all of the combinations at high temperature. The blocking scheme is shown below in Table 2.

Table 2: Blocking Scheme for ½ Fraction Experiment

Low Temp		High Temp	
bc	bc	ad	ad
-1	-1	ac	ac
bd	bd	abcd	abcd
cd	cd	ab	ab

Ultimately, using DoE to analyze the results was rejected because of issues with properly growing the ice. Sporadically the ice holders leaked, or the ice cracked internally. These samples were not used and had to be re-grown. There were also problems with the hydraulic systems of the MTS Machine requiring repairs and maintenance. However, the test schedule developed using the DoE method was kept and adhered to as closely as possible and the use of the DoE term “treatment combination” was kept in the analysis. The final test schedule is shown in Table 6 on page 68.

The ice samples were placed into position on the bottom ram of the MTS machine as shown in Figure 28. The ram was brought up to the position of zero displacement. The upper plate was then brought down until a 1cm space remained between the tip of the ice cone and the plate. This was measured using a 1cm thick aluminum rod to ensure exact spacing, thereby ensuring the exact point of contact could be determined from the data.

The desired crushing distance and impact speed were input into the controls and the ice was allowed to impact the steel plate.

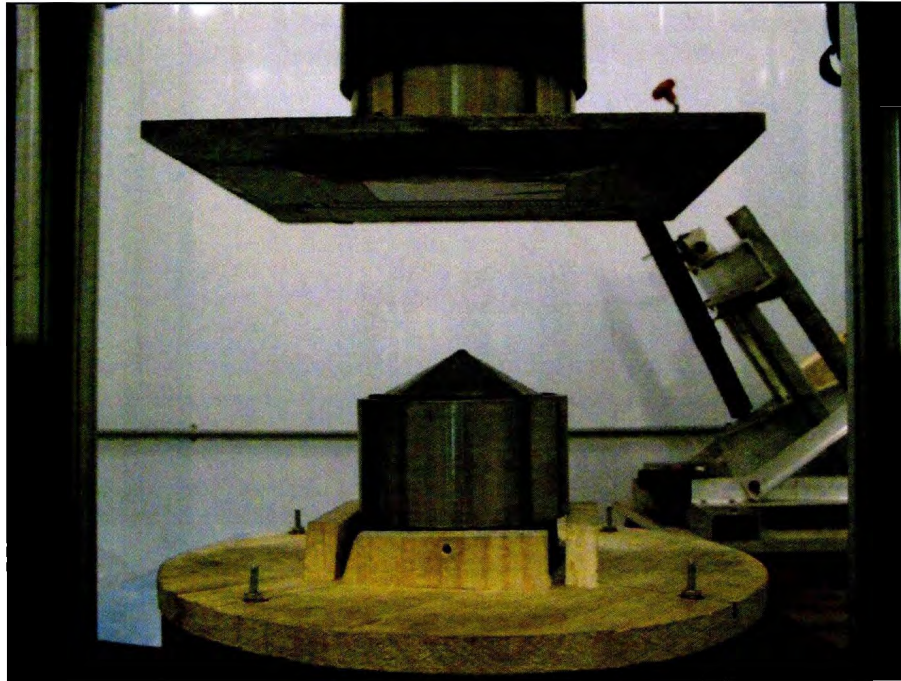


Figure 28 - Ice Sample in MTS Machine, Ready for Crushing Against Steel Plate

5. Pressure Films

The uniaxial crushing tests result in force, displacement and time recordings. From the data, force-time and force-displacement curves can be directly created. *Process* pressure-area curves are then created, as described by Daley [10], by determining the nominal contact area as a function of crushing depth. The method is illustrated in Figure 29.

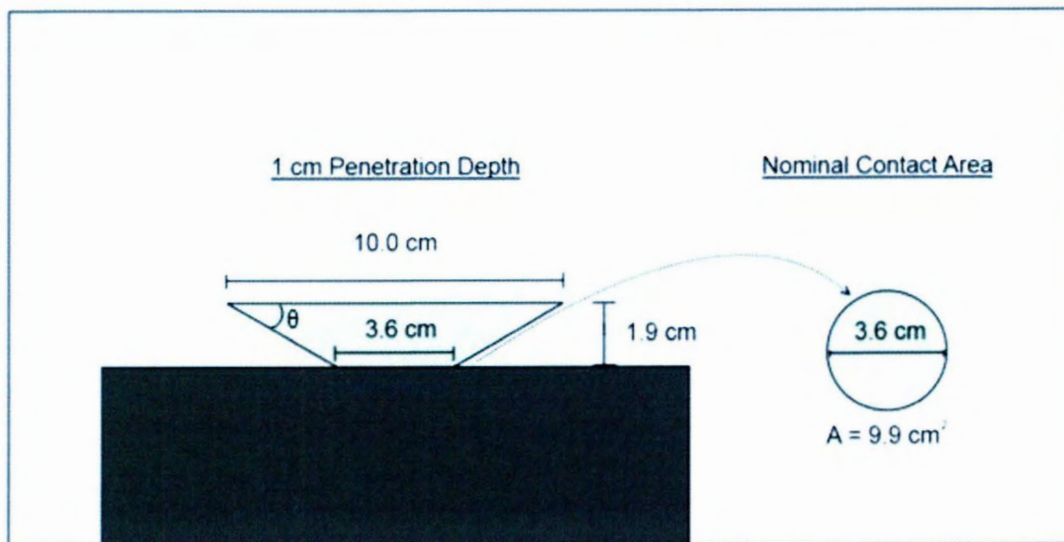


Figure 29 - Nominal Contact Area from Penetration Depth

The formula for calculating nominal contact area from penetration depth and cone angle is:

$$A = \pi y^2 / \tan^2(\theta) \quad [3]$$

where A is the nominal contact area, y is the ice penetration depth, and θ is the ice cone angle. Average pressure is determined for each data recording by dividing the force measurement by the nominal contact area. Plotting the *process* pressures and corresponding nominal contact areas results in a *process* pressure-area curve for that experiment.

In this study, the nominal *process* pressure-area curves for crushing events are to be compared to spatially changing pressures across the contact area during ice collisions. Chemical pressure films, as discussed, are a potentially useful tool for recording these changes at high resolution, but they must be adapted for ice.

Prescale[®] film by Fujifilm contains chemicals that react under specific loads to record pressure pattern and produce colour density based on pressure level. These films are paper, can be affixed to any surface and can easily be trimmed to any desired shape. The recommended test conditions for the film are 20 to 35°C, however they can be used at temperatures as low as -20°C [17]. They can record pressures changes after a minimum of 1 ms of contact and a minimum contact area of 0.1mm². This contact area limit is to ensure an even chemical reaction, however within this contact area the films have a resolution of 5 to 15 microns [18]. The film records pressures as colour densities caused by broken chemical micro-capsules in the film. There are a range of micro-capsules sizes: small micro-capsules break at high pressures and large micro-capsules break at low pressures. The number of broken micro-capsules determines the colour density.

There is one significant drawback to the pressure films which presents its own unique challenge for use in ice impact tests. The pressure films record an accumulated pressure, not an instantaneous pressure. This means that at a given instant in time what is

being shown on the film is not the pressure at that instant in time, but rather the accumulation of all pressures recorded during the period of impact on the film. Kim [1] described this as activated vs. active pressure, which is shown elegantly in Figure 30. In Step 1-1 of the figure, at the initial stage of an impact on the film, the true, active and activated areas are all the same. In Step 1-2, the True contact changes (perhaps ice has fractured away from the contact area); the active area on the film represents the True contact area. However, the True contact area from Step 1-1 is still recorded on the film and thus the activated area is different from the active area. By Step 1-3 the disparity has become even greater.

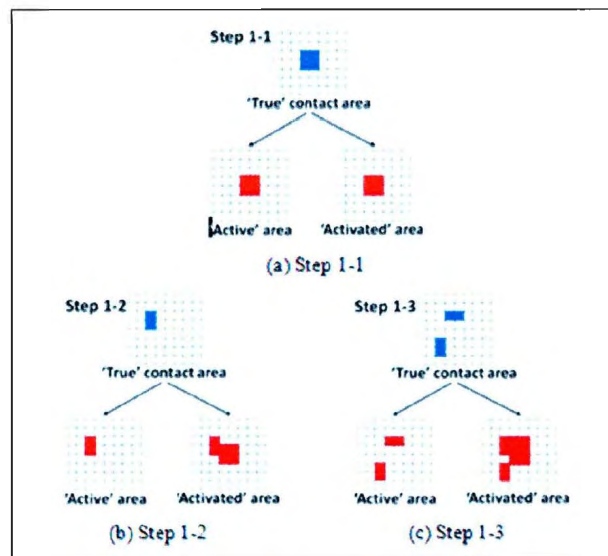


Figure 30 - Activated vs. Active Area (image taken from Kim [1])

A further illustration of the effect is shown by conceptually dragging a circular contact face across a surface in Figure 31. The actual pressure pattern at specific instants in time and the recorded pressure pattern on the film are both shown.

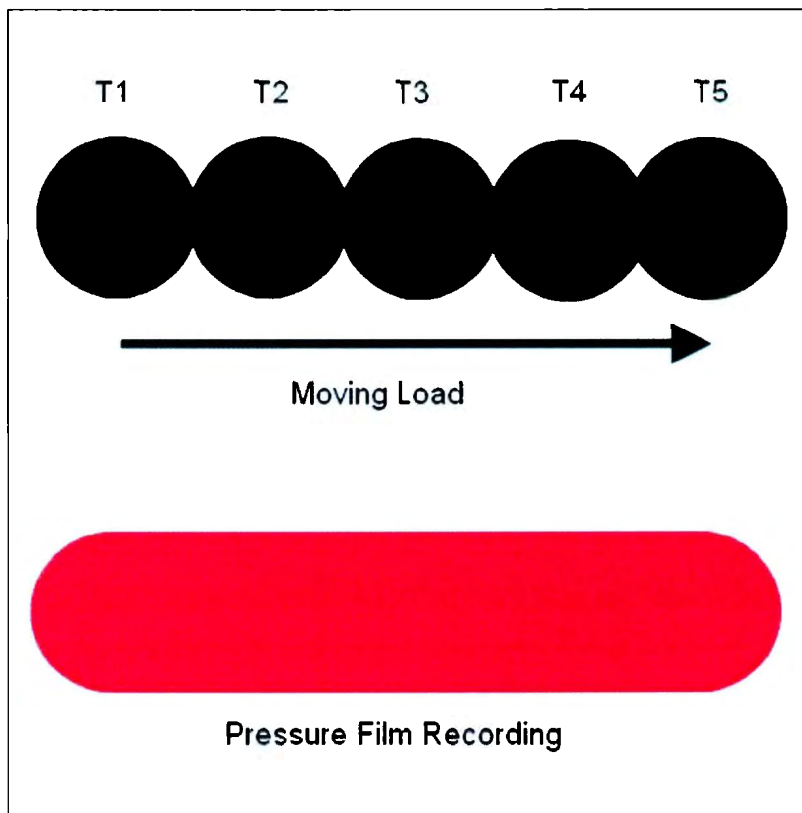


Figure 31 - Accumulation of Pressure in the Pressure Films

Typical uses of the pressure film include situations where the pressures do not greatly change spatially over time and this accumulation is not an issue. However, ice contact area changes rapidly in a collision and this will have to be accounted for.

The pressure films are split into distinct operating ranges. In this study only the Low (2.5 to 10 MPa), Med (10 to 50 MPa), and High (50 to 130 MPa) pressure films were used. This was determined through pre-test analysis of pressure film suitability. The pressure ranges are shown in Figure 32.

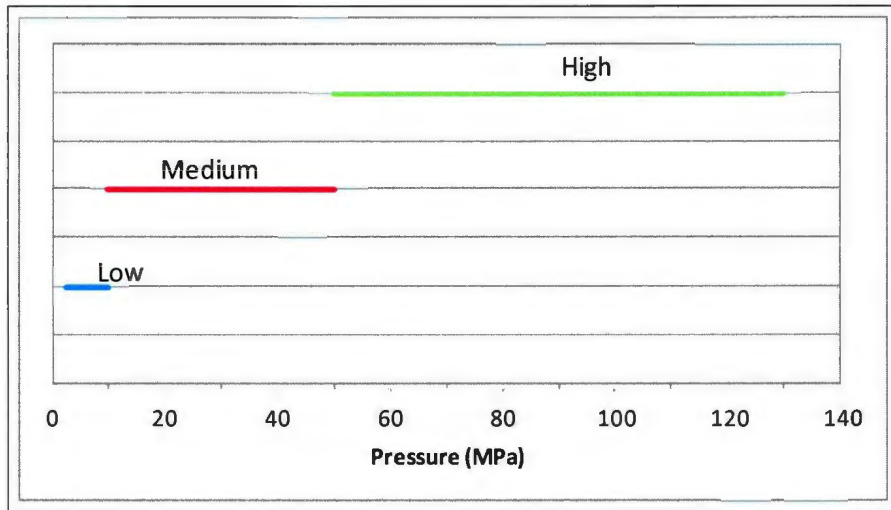


Figure 32 - Pressure Film Ranges

Each pressure range comes with a specific data sheet which gives a calibration curve for converting colour density to pressure. However, these curves are for the 0°C to 35°C operating temperature range, which is above the -15 to -5°C range of these experiments. Incidentally, it is unclear why Fujifilm lists the recommended temperature range as 20°C to 30°C, yet lists data plots for 0-30°C. In order to ensure proper pressure conversions post test it became necessary to perform in-house calibrations of the pressure films under the operating conditions of the experiments. Calibration under the actual test conditions improves confidence in the accuracy of the information derived from the pressure films. A calibration method was used similar to that performed by Liggins et al [12].

To calibrate the films a uniform pattern is created at a determined pressure. Once a range of pressures have been imprinted, each pressure pattern is scanned and analyzed and a pressure-density curve is created. Liggins et al. outlined an analysis method. For this study, a method of image analysis was determined and will be explained in Chapter 6. Each pressure film range will have its own pressure-density curve. To create the

uniform pattern, a 2'' diameter steel rod was affixed to the MTS machine and pressed against a sheet of pressure film. An example of a test pattern using the rod as the impact surface is shown in Figure 33.

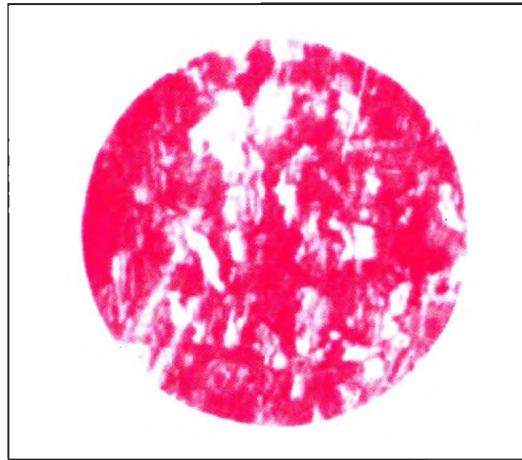


Figure 33 - Impact Pattern from 2'' Steel Rod

The contact pattern is clearly non-uniform since grains within the metal and contact discontinuities are picked up by the pressure film. Highly polishing the contact surface of the rod improved the pattern, but Hertzian Contact effects became apparent at higher pressures as shown in Figure 34. A pressure pattern also appeared in the center of the pattern. The origin of this pattern is not entirely clear. Hertzian contact explains the ring of pressure around the pattern, but not this center effect.



Figure 34 - Hertzian Contact Effects in Pressure Pattern

In order to reduce the effects Hertzian contact and the central patterning, a contact surface smaller than the driving surface was tested. A shaped tip for the steel rod was machined with a highly polished cylindrical contact surface with a diameter of 1.5". This attachment is shown in Figure 35.



Figure 35 - Machined Calibration Tip

In order to prevent pressure patterns from rough patches still present on the polished contact surface and to reduce the effects of Hertzian contact further, a plate of polycarbonate plastic was placed between the pressure film and the steel plate beneath. This plastic plate deformed enough to smooth out any pattern variations but still transmitted loads with minimal loss. The final calibration set-up is shown below in Figure 36 and Figure 37.

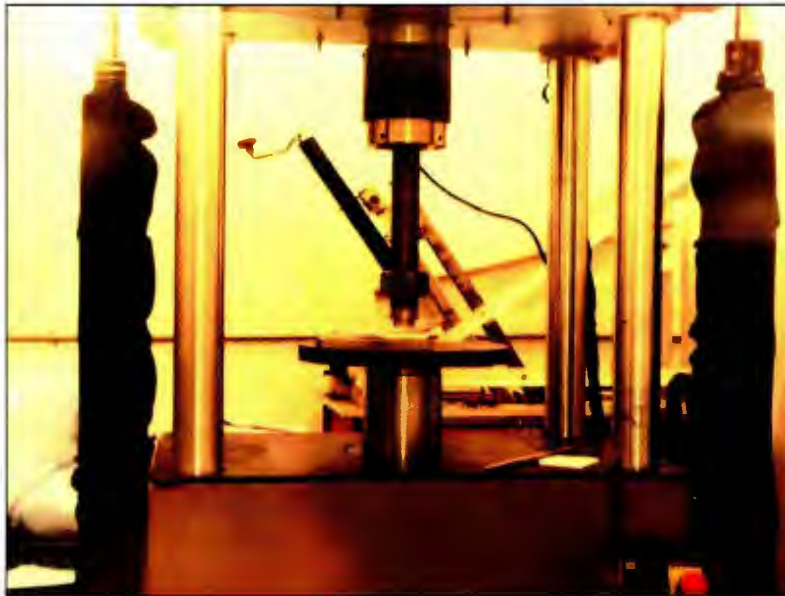


Figure 36 - Steel Contact Tip, Polycarbonate Plate and Steel Pressure Plate

Calibration tests were performed at a temperature of -10°C at a contact speed of 1 mm/s . Before the tests were run, the pressure range of the film being calibrated was converted to a force range based on the equation:

[4]

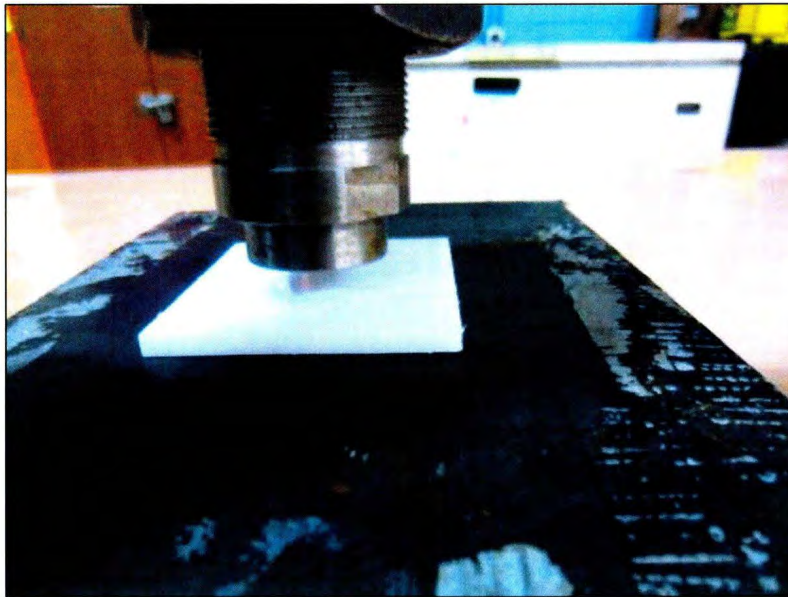


Figure 37 - Close-Up of Calibration Tip and Polycarbonate Plate

A range of forces were picked lying at even spaces within the force range of the film. The steel rod was incrementally brought into contact with pressure film until the desired force was reached. The actual force measured by the force sensor on the MTS machine was recorded and used in creating the calibration curves. After the desired force was reached, the pressure film was removed and a fresh film was affixed to a fresh piece of polycarbonate plastic and brought to the next load level. This was continued until a range of pressure patterns were created, each with known contact area and a measured force. The actual pressure of each pattern was calculated using equation [4]. Examples of the pressure patterns created using this method are shown in Figure 38.

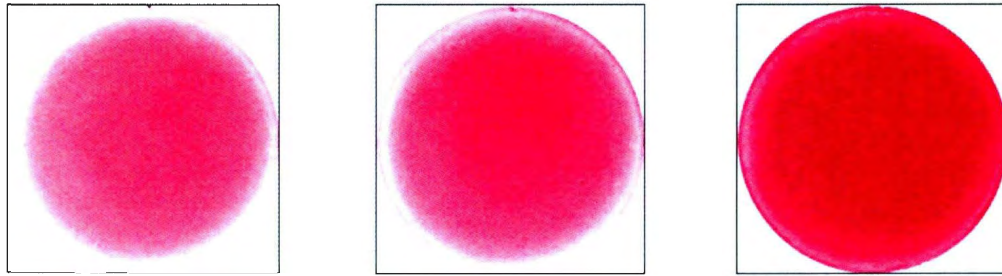


Figure 38 - Pressure Patterns Determined from Calibration Tests

Under the improved calibration apparatus, the pressure patterns were much improved, although still not completely uniform. This highlights the challenges of calibrating the pressure films, as experienced by Liggins et al [12].

The pressure patterns were analyzed using the method described in Chapter 6 to determine colour density for each pressure pattern. Since the contact was often not completely uniform, it was decided that the average density would be used for the calibration curves which introduced a level of potential error in the test results but follows a similar method as Liggins et al [12].

Once all of the pressures and corresponding pixel values for a pressure film range were found and plotted the calibration curve was interpolated. The data set for the medium film range is shown in Table 3 and the resulting calibration curve is shown in Figure 39.

Table 3: Data for Calculating Medium Range Calibration Curve

<u>Pixel</u>	<u>Pressure (MPa)</u>
56.78	16.37
28.92	8.27
51.75	15.98
72.56	22.81
87.64	29.73
103.09	33.09
118.22	39.75
133.85	45.36

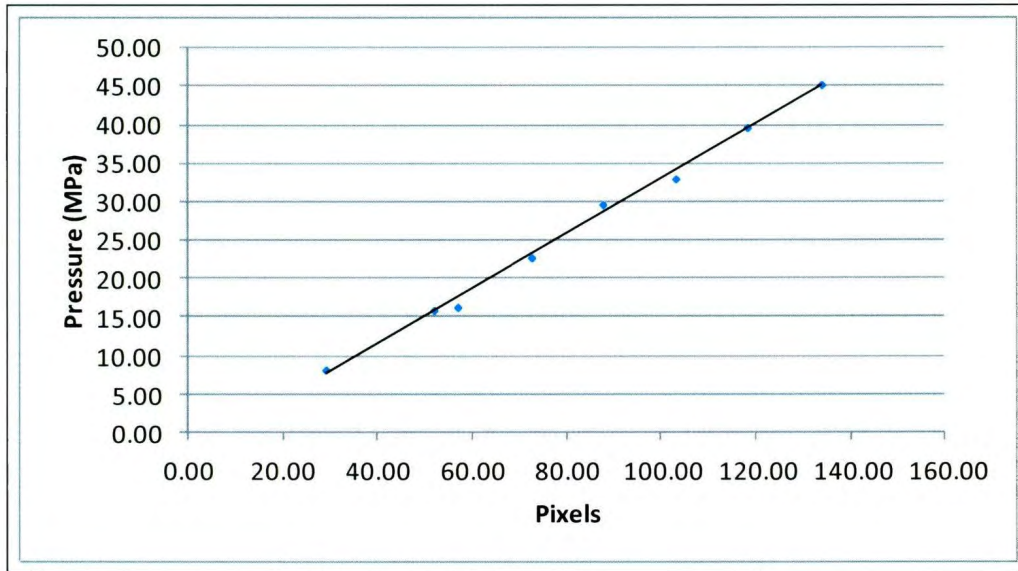


Figure 39 - Medium Range Calibration Curve

The resulting calibration curves for each pressure range were determined to be:

Low: $Pressure = 0.0913(Pixel) - 1.5314$ [5]

Medium: $Pressure = 0.3572(Pixel) - 2.7273$ [6]

High: $Pressure = 1.1021(Pixel) + 43.708$ [7]

These curves were used to convert pressure film scans to actual pressure numbers after each test.

As discussed previously, a challenge in using pressure film was the issue of pressure accumulation. Once a pressure pattern was made it could not be unmade and would therefore persist throughout the entirety of the crushing event. A way to decrease the amount of accumulated data is to reduce the recording time. In other words, it is not reasonable to record an entire crushing event on one film. It was determined that the solution was to crush in incremental steps, replacing the film after each step. This of course also meant that a non-interrupted crushing event could not be measured. However, ice impacts in the arctic are not necessarily uninterrupted events, and so there is validity in analyzing this situation. Comparative tests between stepped and full crushing tests indicate that force histories are not markedly different between an uninterrupted test and a stepped test, as shown in Figure 40.

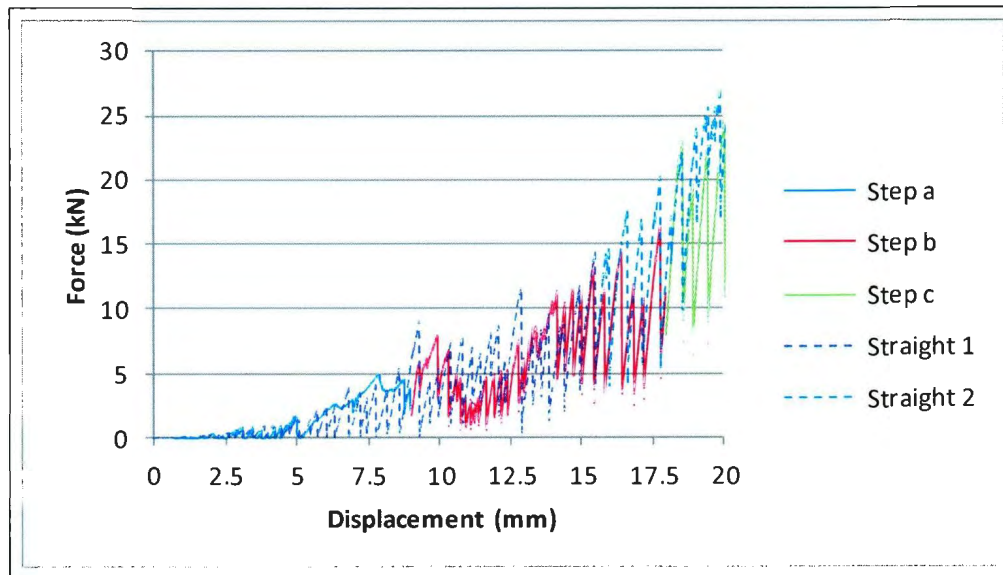


Figure 40 - Uninterrupted and Stepped Test Force Histories

The amount of steps during the crushing test were limited both by the crushable distance (the height of the cone), and the amount of pressure film available. It was therefore decided to run 3 steps for the 30° cones and 4 steps for the 50° cones. For the 30° cones, the impact lengths are then 9mm, 18mm and 27mm. For the 50° cones, the impact lengths are 15mm, 30mm, 45mm and 55mm. The step designations and corresponding penetration depths are listed in Table 4. After each crushing step, the sample was returned to the zero position, the film was replaced with fresh film, and the sample was crushed to the next distance. This is schematically shown in Figure 41.

Table 4: Ice Crushing Step and Corresponding Penetration Depth

30 Deg Cone		50 Deg Cone	
Step	Penetration	Step	Penetration
Step a	9 mm	Step a	15 mm
Step b	18 mm	Step b	30 mm
Step c	27 mm	Step c	45 mm
		Step d	55 mm

The data was acquired at a rate of 2048.0 Hz, or one data acquisition every 0.000488 s.

The pressure films record only over a specific range of pressures. Ice pressures during a collision, however, will reach values across multiple ranges. In order to detect the full range of pressures, the films were layered on top of each other before being attached to the impact plate. Tests were performed to ensure that layering did not greatly affect the resulting pressure patterns.

The next necessary step is determining methods for converting the pressure patterns into useable pressure values. This was required to create the calibration curves, will be necessary in using the films to create *spatial* pressure-area curves and pressure maps, and will now be explained.

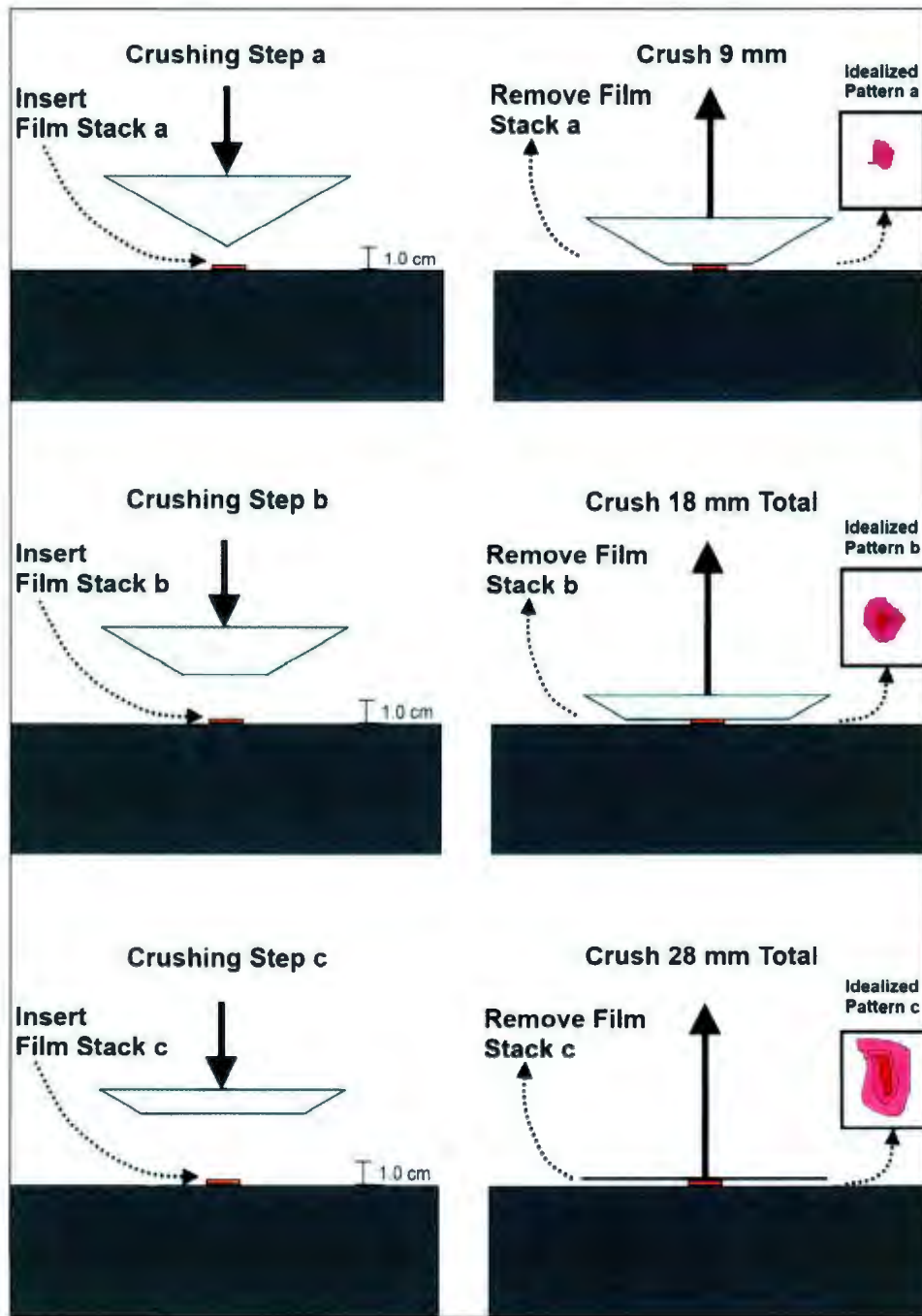


Figure 41 - Method of Stepped Crushing for 30° Cone

6. Imaging Analysis

Once impact tests were completed, the pressure films had to be properly analyzed in order to develop *spatial* pressure-area curves and pressure maps. The first step in this process was to scan the films. This was done using an F2180 series scanner by HP, with scans performed at 1200 dpi. This decision was made in an attempt to find the optimum balance between retaining the maximum amount of data from the micrometer scale pressure films while keeping the files at a manageable size. The scans resulted in images that were (6244 x 7676) pixels at a resolution of 472.44 pixel/cm. These image files were too large to be handled for plotting purposes. However, for image cleaning purposes, the higher resolution allowed for more accurate distinction between noise-data and actual impact information and thus the scans were all made at the higher resolution, processed, and then reduced. The scans themselves were saved as compression-less Tagged Image Files, or .tiff, since this format involves no compression of the file and therefore no loss of data.

Once the films were scanned, they needed to be cleaned. The pressure films are sensitive enough to pick up pressure patterns from such spurious sources as dust and fingerprints, especially the low range films. While every effort was made to prevent contact with the areas of the film containing the impact pattern, noise-data was often recorded in the surrounding regions. This noise-data was easy to detect post measurement and therefore easy to clean. An example of an “unclean” and a “clean” image is shown below in Figure 42.

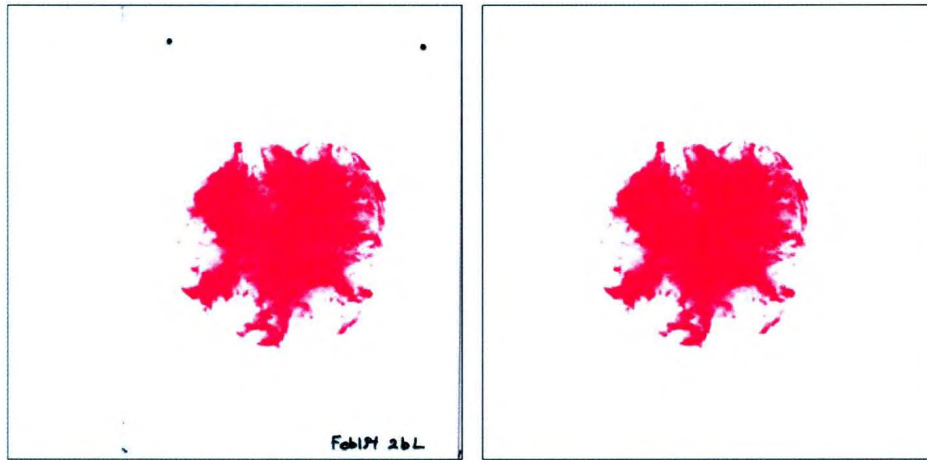


Figure 42 - Unclean and Clean Pressure Films

The cleaning process was done using the Paint.Net program [19], which is a freeware program similar to Microsoft Paint but offers a greater array of image-manipulation features. The entire film outside of the contact area was painted to a uniform white, providing a constant background pixel pattern.

At this point, a drawback to the testing method was discovered. The pressure films were not secured properly together during the tests. This was not an issue during the impacts themselves, as the films did not move. However, placing them into the test apparatus often caused a slight shift in the films before the tests. As a result, once the tests were completed and the films were removed they could not simply be scanned in the same alignment on the scanner. Since this issue was not detected until after the tests were completed, manual alignment post-test was necessary. Manual alignment was facilitated by each film containing a number of distinct pressure features carried through each level of film which could be used for alignment. For each test, using Paint.Net the Low range film was first centered. The orientation of the Low film determines the orientation of the

pattern. The Medium range film was then layered on top and aligned to the Low range film. Lastly the High range film was layered on top of the Medium range film and aligned to it. The alignment process is shown in Figure 43.

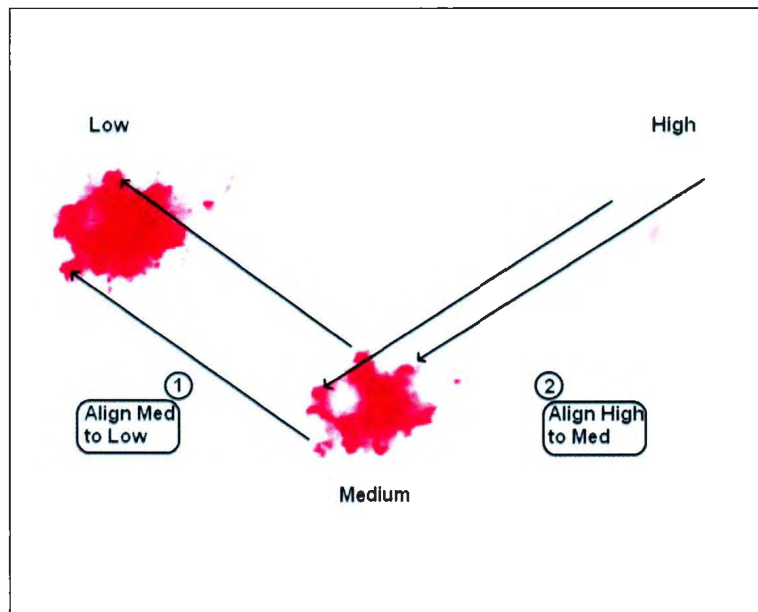


Figure 43 - Step-By-Step Film Alignment

Finally, the films were reduced in size to (500 x 500) pixels. This size was determined by testing to be the largest size not to result in out-of-memory errors or computer crashes during the analysis and plotting stages. At this size the resulting resolution is 37.8 pixels/cm.

The next step in the analysis was to determine the pixel numbers defining colour of the image. Each film was opened in ImageJ [20] and then converted to grey-scale. This was done to reduce the numbers required to describe each pixel from 3 to 1. ImageJ describes colour using a model known as the “RGB Colour Model” where R stands for

Red, G for Green and B for Blue. This is an additive model where every colour is achieved by mixing levels of R, G and B as integer values from between 0 and 255. For example, Red is given by (255,0,0), Green by (0,255,0) and Blue by (0,0,255). Black is given by (0,0,0) and white by (255,255,255). A sample colour chart is given below in Figure 44.

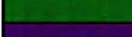
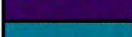
Color	HTML/CSS Name	(R,G,B) Code
	Black	(0,0,0)
	White	(255,255,255)
	Red	(255,0,0)
	Lime	(0,255,0)
	Blue	(0,0,255)
	Yellow	(255,255,0)
	Cyan / Aqua	(0,255,255)
	Magenta / Fuchsia	(255,0,255)
	Silver	(192,192,192)
	Gray	(128,128,128)
	Maroon	(128,0,0)
	Olive	(128,128,0)
	Green	(0,128,0)
	Purple	(128,0,128)
	Teal	(0,128,128)
	Navy	(0,0,128)

Figure 44 - Sample RGBColour Chart (table adapted from [21])

Since the pressure films record colour only within the Red spectrum the image can be converted to Grey Scale without loss of data. The benefit of converting to Grey Scale is that only a single pixel value from 0 to 255 is required to describe the data. A colour chart for 32-Bit Grey Scale, the scale used for the analysis, is shown below in Figure 45.

Color	HTML/CSS Name	Code
	black	0
	dim gray / d im grey	105
	gray / g rey	128
	dark gray / d ark grey	169
	silver	192
	light gray / l ight grey	211
	gainsboro	220
	white smoke	245
	white	255

Figure 45 - Chart for 32-Bit Grey Scale (table adapted from [21])

Once the image was converted to grey-scale, a text file of xyz values, with x and y describing the plane of the film and z representing the pixel level, was created using ImageJ.

In order to efficiently manipulate the xyz text files to complete the image analysis computer scripts were written using the Matlab computer language. Creating Matlab scripts and functions to manipulate the data allowed full automation which greatly improved efficiency of data analysis. Experimental partner Hyunwook Kim performed imaging analysis using spreadsheets and graphing software in lieu of coding and his results can be read in [1]. The first stage of the computer-code analysis was to create reference text files containing the file name for each pressure film, and the maximum pixel range containing the impact pattern. This was used to determine an endpoint for determining the *spatial* pressure-area curves. Many of the pressure patterns were far smaller than the 500x500 pixel maximum size, and therefore it was unnecessary to expand the analysis to the full extent along x and y. Next, each z value in the xyz text file was converted to pressure (MPa) using the appropriate regression equation determined from the pressure film calibration tests.

Each data array of x, y and pressure for each film range was then combined into one and sorted first along x and then along y. This was done to ensure that same coordinates from each pressure film would appear beside each other in the file. Because the pressure films were layered, a point within the contact area would record a value on the Low range film, the Medium range film and the High range film. It is therefore necessary to determine which pressure value is retained and which are removed. The need for pressure selection is shown in Figure 46. Each pressure range will record up to its ceiling. If the actual pressure is above this ceiling, the next film will record the pressure, and so on. Thus, while all films may be recording pressure readings, only the film upon whose pressure range the actual readings lies gives the true pressure.

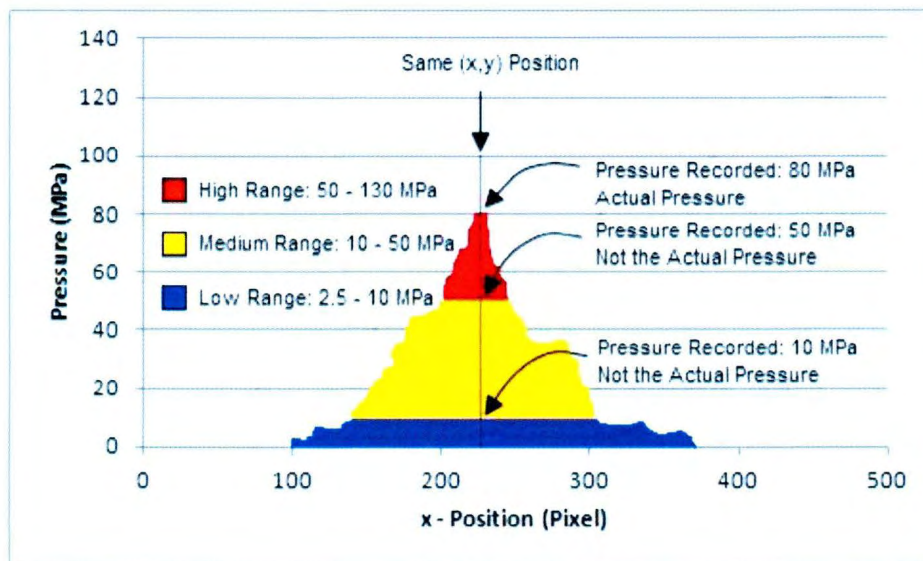


Figure 46 - Multiple Pressure Readings due to Film Layering

The films will also record colour densities outside of their pressure range. This could be due to errors in the calibration method. The calibration curve is an interpolation, and thus

errors may exist. However, for this study the curves were trusted and any pressures detected outside of a film's range needed to be properly altered. Pressures detected higher than the ceiling were changed to the ceiling value. Pressures detected below the specified range could not be properly dealt with, as it was unknown what the true value might be. These pressures were converted to 0 MPa, which may potentially be a source of error in the analysis. This error is likely small since the actual pressures would be less than 2.5 MPa for the Low film, or were picked up by the film range beneath if they were on the Medium or High range films.

Once the pressure values in the data array were cropped, the proper pressure was selected. At each pixel point in the array the highest pressure value detected out of the three films was kept, and the other readings eliminated. For example, if the point [270, 260] had a value of 10 MPa on the Low film, 50 MPa on the medium film, and 57 MPa on the High film, then the 10 MPa and the 50 MPa were rejected, while the 57 MPa was kept. This is shown schematically in Figure 47.

Film	Ceiling	Measured	Ceiling Reached?	Action
Low	10 MPa	10 MPa	Yes	Reject
Medium	50 MPa	50 MPa	Yes	Reject
High	130 MPa	57 MPa	No	Accept

Figure 47 - Selecting the Peak Pressure from Layered Films

The result of the comparison and selection algorithms is an array containing only the peak pressures at each coordinate point.

To create the *spatial* pressure-area curve, it was decided that increasing square sub-areas, centered on the impact pattern, would be used. These sub-areas would expand

until just beyond the furthest extent of the pressure pattern based on the pre-determined end points. The choice of expanding in squares is arbitrary. Square area can be used to model, for example, ice pressures growing on a square panel of a ship hull. Expanding in circles, for example, could also have been used. The concept of expanding square sub areas is illustrated in Figure 48.

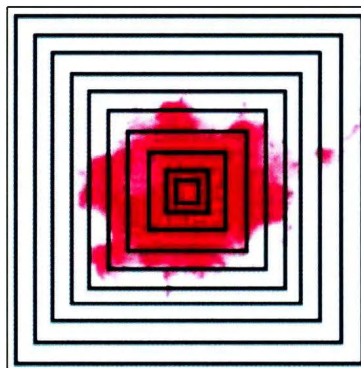


Figure 48 - Expanding Square Sub Areas

Before analyzing the sub-areas, a problem of missing background data needed to be solved. The ImageJ software, while determining the xyz values, eliminates from the text file the background pixel pattern. Since all of the area surrounding the impact pattern was painted a uniform white, all data outside of the impact pattern was removed in the text files. This is problematic since the expanding sub-areas extend to include regions outside of the impact pattern, which results in-out-of-bounds errors during the computer analysis. A background array containing 0 MPa at each coordinate point was created with dimensions equal to the maximum sub-area. The array containing the xyP values was then compared to the background array and any (x,y) point in the background array that

was also located in the impact pattern array was replaced with the proper pressure value.

This is illustrated in Figure 49.

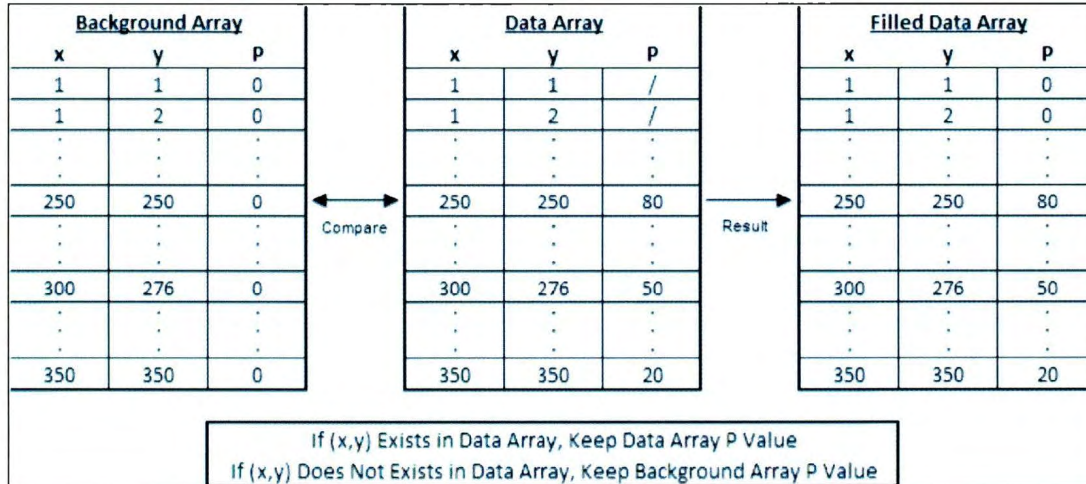


Figure 49 - Merging Background and Pressure Pattern Arrays

The result is a properly filled array containing both the impact pattern and the background. From this filled array, the pressure maps were created using Matlab 2D and 3D plotting commands.

The last step involved calculating the average pressure within each sub-area in order to plot the *spatial* pressure-area curves. To do this, the minimum square area A_T encompassing each impact pattern was found using a specific algorithm. Since each impact pattern was saved as a (500 x 500) pixel image, the algorithm first determined the farthest non-zero pixel from the center point (250,250). A square area with side length 2 times the distance was then centered on (250,250). This area is the area A_T with side length L . The process is shown in Figure 50.

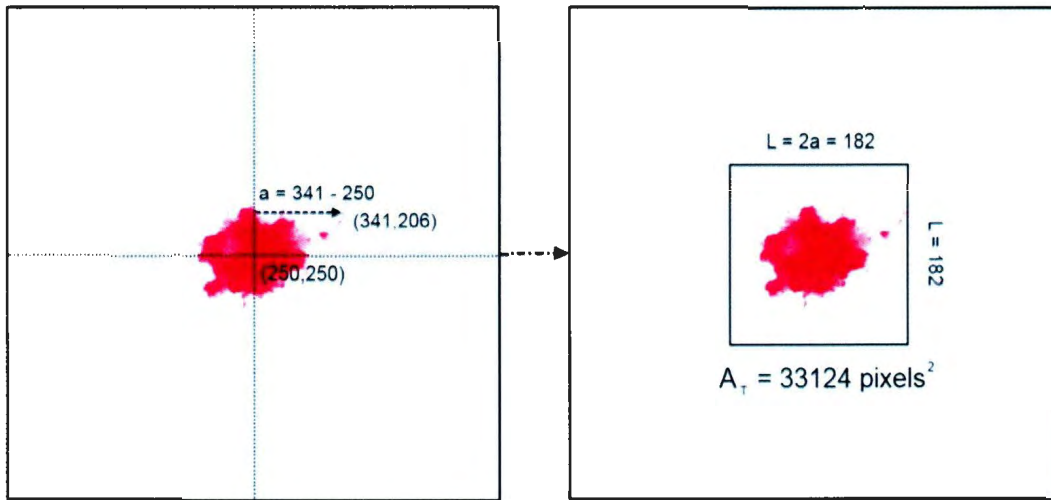


Figure 50 - Finding Max Subarea A_T

Next, A_T was divided by the number, n , of sub-area steps desired. For this analysis 100 sub-area steps were used. Any number of sub-areas could be used but a higher number will result in a more refined *spatial* pressure-area curve, albeit with diminishing returns. From the example of Figure 50, let A_n be the area of a specific sub-area within A_T and L_n be the side length of a sub-area:

$$A_n = n(33124 \text{ pixels}^2)/100 = n(331.24 \text{ pixels}^2) \quad [8]$$

therefore

$$A_1 = 331.24 \text{ pixels}^2$$

$$L_1 = \sqrt{(331.24 \text{ pixels}^2)} = 18.2 \text{ pixels}$$

and

$$A_2 = 2(331.24 \text{ pixels}^2) = 662.48 \text{ pixels}^2$$

$$L_2 = \sqrt{(662.48 \text{ pixels}^2)} \sim 25.7 \text{ pixels}$$

and so on up to A_{100} . All of these equations were implemented using algorithms in the scripts using the xyP text files, but the concept of the expanding sub-areas is shown in Figure 51 where several of the sub-areas are plotted.

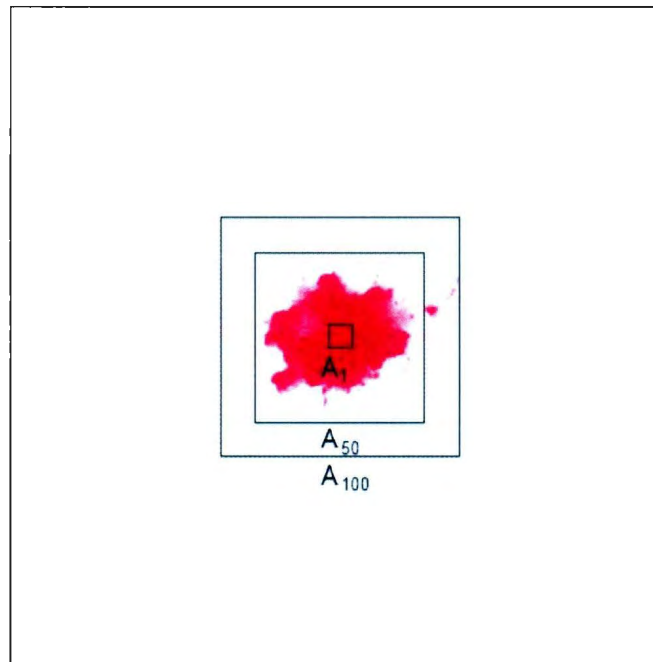


Figure 51 - Examples of Sub Areas from A_1 to A_{100}

Once the corresponding areas A_n of each sub-area were found, pressure values at each pixel within A_n were averaged in order to find the average pressure, P_n , in each sub area. The final output of the scripts was an $(n \times 2)$ array containing A_n and P_n , for each pressure pattern from which the *spatial* pressure-area curve could be plotted for each time step. The entire process of creating a *spatial* pressure-area curve from a pressure pattern is shown schematically in Figure 52.

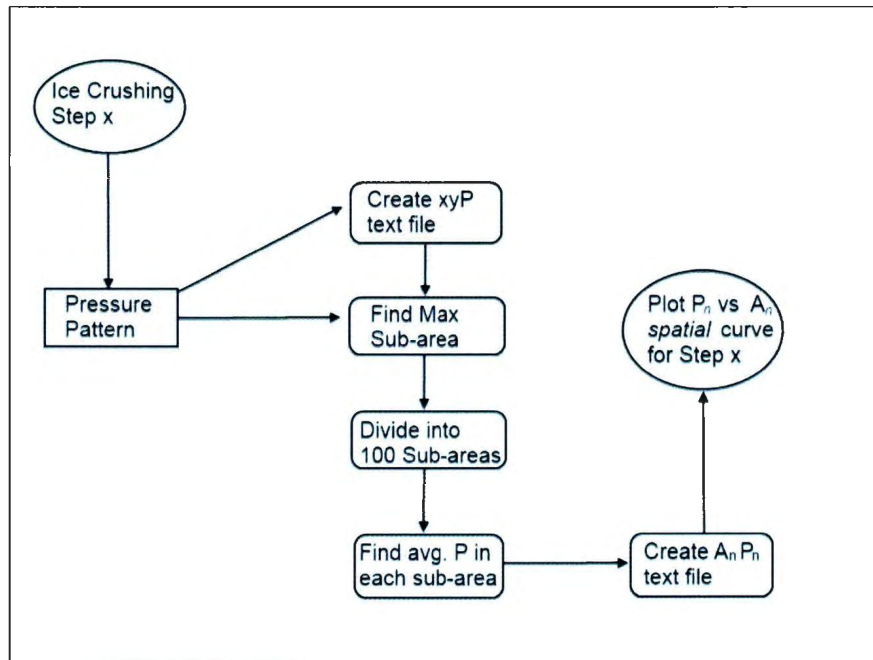


Figure 52 - Schematic of Creating *Spatial* PA Curve from Pressure Pattern

6.1: Creating Pressure-Area and Load History Curves from MTS Data

Process pressure-area and force-displacement curves were plotted using data recorded by the MTS machine load cells. A sample MTS data file is shown in Table 5. The data requires manipulation to properly combine each crushing step.

Table 5: Sample from MTS Machine Data File

MTS793 BTW ENU 1 0 . / : 1 0 0 A							
Data	Header:	Time:	1.021484	Sec	02/01/2012	12:22:56	PM
Data	Acquisition:	Timed					
Station	Name:	500	kN.cfg				
Test	File	Name:	craig.tst				
Ch	1	Displacement	Ch	1	Force	1	Time
mm	kN	Sec					
0.000258	0.15279867	0.017089844					
0.000436	0.15301995	0.017578125					
0.000529	0.15248109	0.018066406					
0.000522	0.15091445	0.018554688					
0.00047	0.14928658	0.019042969					
0.000441	0.14920872	0.01953125					
0.000412	0.15104659	0.020019531					
0.000314	0.15328734	0.020507813					
0.000152	0.15392275	0.020996094					
5.82E-05	0.1524944	0.021484375					
9.53E-05	0.15062042	0.021972656					
0.000126	0.14979574	0.022460938					
5.65E-05	0.15029158	0.022949219					

In order to plot the entire history of the impact, the initial 10 mm worth of data needed to be removed, since this data was recorded across the initial ice-to-plate gap. The remaining displacement and time values then needed to be zeroed. Each crushing step was recorded in its own data file. In order to put the force data for each crushing test together into one data file for plotting purposes, the time values for later steps needed to be re-initialized based upon the last time reading of the preceding step. This was a simple procedure since data was recorded every 0.000488s, therefore a simple algorithm was needed to adjust the time. The MTS machine also recorded force as a negative value so the decision was made to multiply each value by -1 in order to plot positive forces.

7. Results and Analysis

7.1: Primary Analysis of Data and Spatial Maps and Curves

In order to analyze the results of the different tests and their repetitions, it is beneficial to consider each treatment combination separately. The treatment combinations and their corresponding factors and test numbers for all tests are shown again in Table 6.

Table 6: Experimental Test Schedule and Factor Combinations

Test Number	Treatment Combo	Grain Diameter (mm)	Temperature (°C)	Impact Speed (mm/s)	Cone Angle (°)
FIT2	(1)	1-5	-15	1	30
FIT3	(1) Rep	6-10	-15	1	30
F9T1	bc (Rep)	6-10	-15	100	30
F9T2	bd (Rep)	6-10	-15	1	50
F9T3	cd (Rep)	1-5	-15	100	50
F13T1	bd	6-10	-15	1	50
F13T2	cd	1-5	-15	100	50
F13T3	ad	1-5	-5	1	50
F16T1	ac	1-5	-5	100	30
F16T2	ad (Rep)	1-5	-5	1	50
F16T3	ac (Rep)	1-5	-5	100	30
F20T1	abcd	6-10	-5	100	50
F20T2	ab	6-10	-5	1	30
F20T3	ab (Rep)	6-10	-5	1	30
F24T1	bc	6-10	-15	100	30
F24T2	abcd (Rep)	6-10	-5	100	50
F28T1	bc (Rep 2)	6-10	-15	100	30

In the table, “Rep” indicates that the test was a replication and therefore there was no pressure film used. Due to the limited supply of pressure film, it was not possible to run the repeated runs using the pressure films. It was decided to run the first replication using pressure films in order to create *spatial* pressure-area curves and pressure maps, as well

as gather force data from the MTS Machine. The second replications, those marked as “Rep”, were then run without the film with only the force data gathered. This allowed the creation of force-displacement curves and *process* pressure-area curves for both replications, allowing comparison between repeated experiments. *Spatial* pressure-area curves could not be compared upon repetition. The test numbering scheme is an internal indication of the test giving the date the test was performed and the specific test number. For plots indicating specific crushing steps, a letter of a, b, c or d indicates the test step. For example, F1T2a indicates the test was performed on February 1st, it was the 2nd test performed on that day, and it is the first step of crushing for that test. Readers are encouraged to refer to Table 6 during the discussion of test results.

In this analysis, for each Treatment Combination the force-displacement history will be created and discussed. This will give a sense of the fracturing history of the crushing event. The pressure film patterns will then be shown and discussed and the 2D and 3D spatial pressure maps will be analyzed. From the pressure patterns and the MTS machine data, the *spatial* and *process* pressure-area curves will be created and analyzed.

There are several important questions that will be considered throughout the course of the data evaluation. Firstly, it must be determined how closely the terminus points of each *spatial* PA curve meets the *process* PA curve at the same contact area, as per the analysis of the Polar Sea by Daley [10]. Secondly, the actual contact area will be found and compared to the nominal contact area at each crushing step. Nominal contact area is used to calculate the *process* pressure-area curves and is used in engineering ice-design codes, therefore the validity of assuming simple geometry should be analyzed. The appearance of high pressure zones in the contact face are of interest since these are

the regions which are not considered in the design codes and which have the potential to cause damage to a structure, therefore the percentage of the total contact area which is at a high pressure will be determined. In order to determine a sense of the validity of the pressure films, the pressure film-predicted total load on the contact area will be found and compared to the total load measured by the MTS machine. Ideally these should be the same, but the history-accumulating feature of the pressure films will prevent this. The degree to which the pressure films are off must be determined. Lastly, curves will be fitted to the *spatial* and *process* pressure-area curves to determine which equations best describe the trend and what range of parameters appear to fit the data. Sanderson [21] and others have predicted an equation of the form $P=P_0A^{-c}$, as has been discussed. The degree to which the tests fit this equation is analyzed. The methods for determining the answers to these questions will be shown in detail while analyzing the first Treatment Combination. For all subsequent Treatment Combinations, these values will be stated under the assumption that the methods for determining them were the same. The results will be tabulated together in Section 6.3 and discussed in detail there. A flow chart for the data analysis pathway is shown in Figure 53.

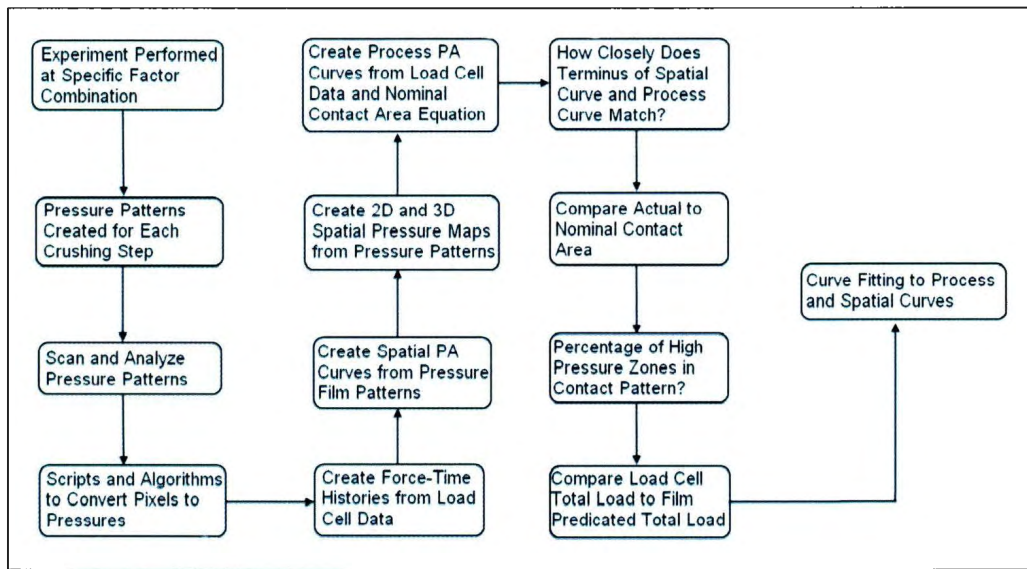


Figure 53 - Flowchart of Data Analysis

7.1.1: Treatment Combination (1)

The first combination to be considered will be (1) or -15°C, 1-5 mm ice grain size, 1 mm/s impact speed and 30° cone angle. The first stage in analyzing the test results is to study the force-displacement curves, created directly from the load cell data from the MTS machine. These are shown in Figure 54.

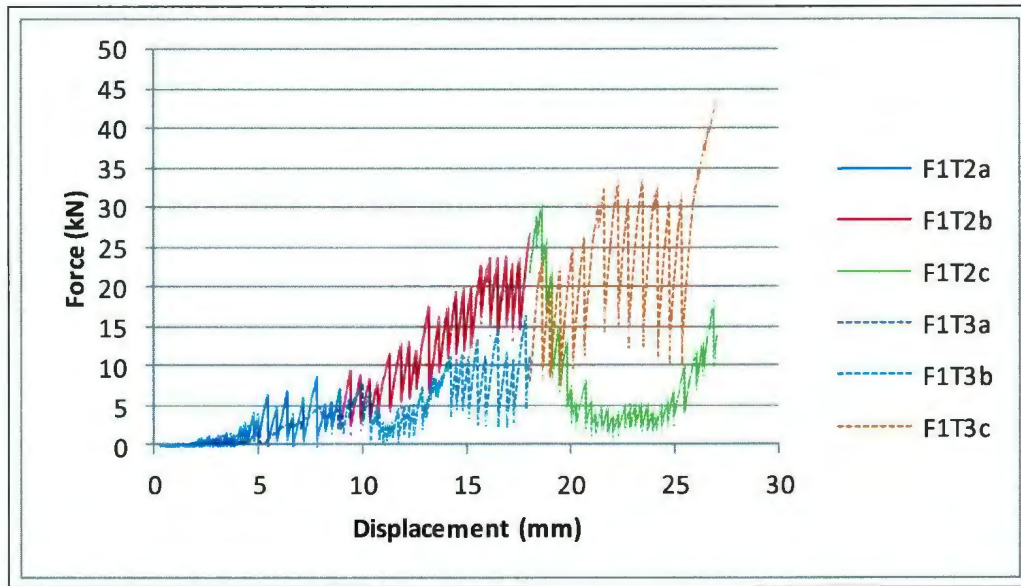


Figure 54 - Force-Displacement Curves, Treatment Combination (1)

Both test curves follow a saw-toothed ramping pattern seen in most ice crushing tests where small drops in force are caused by small scale cracks and spalls, while force builds until a larger spall occurs causing a larger force drop to occur. F1T2 did not appear to undergo any large failure events during the first two steps of the collision as the force appears to increase steadily to a crushing depth of approximately 18 mm. Force drops during this stage of crushing appeared to be consistently on the order of 10 kN. However, at approximately 18 mm crushing depth a large load drop occurred reducing the force from approximately 30 kN down to approximately 2 kN. This was likely due to a relatively large spall breaking free from the contact surface and being extruded, leading to the large force drop. Immediately force begins to again rise although the force drops are closer to 5 kN. By comparison, the load history for F1T3 shows a significant load drop at approximately 10 mm crushing depth but no further large scale load drops in the

remaining history. The small scale load oscillations, however, increase consistently from less than 1 kN through 5 kN to 10 kN and then, at the end of the test, up to 20 kN. Clearly the load was building and had the crushing been allowed to continue, if there had been more ice to crush, an eventual spall would likely have formed leading to a large force drop.

Next the pressure-area curves were created and analyzed. The pressure films for FIT2 are shown in Figure 55. FIT3 contained no pressure film. What is immediately clear from the pressures films is that the patterns are not simple geometric forms. Using the ImageJ computer software, the actual contact areas can be found and compared to the nominal contact areas. The comparison between nominal and actual contact area is shown in Table 7. Actual and Nominal contact areas for each test are gathered in Table 9 in Section 6.2. Clearly the approximation of contact area as a simple geometry is off at all stages of the crushing. Once the pressure films were scanned 2D and 3D spatial pressure maps were created using the methods described in Chapter 6. The 2D maps are shown in Figure 56.

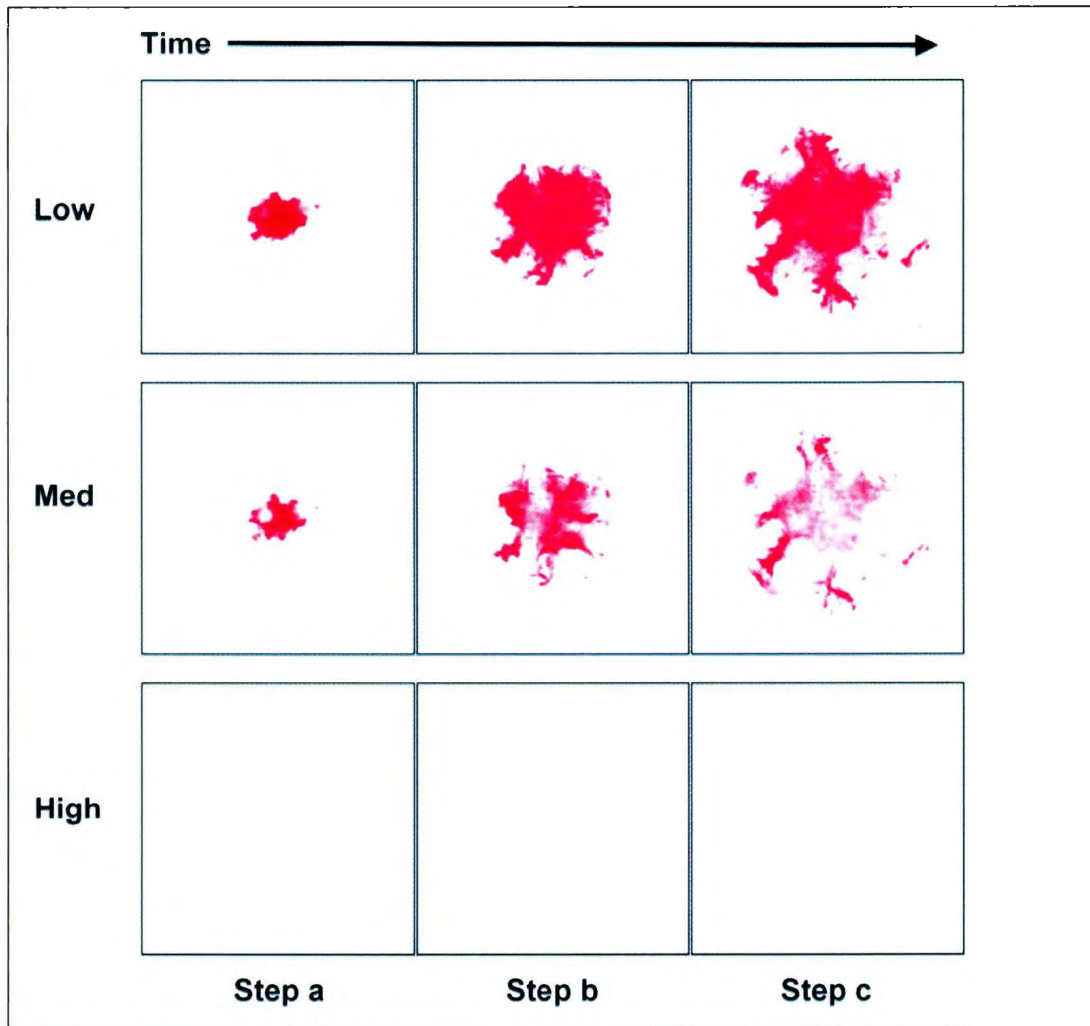


Figure 55 - Pressure Films for F1T2 (l-r: Step a, b and c, t-b: L, M and H)

Table 7: Actual vs. Nominal Contact Area, F1T2

Actual area (mm ²)	Nominal area (mm ²)	% Difference
459.9991	765.93	66.5
2094.507	3059.5	46.1
2906.253	6879.4	136.7

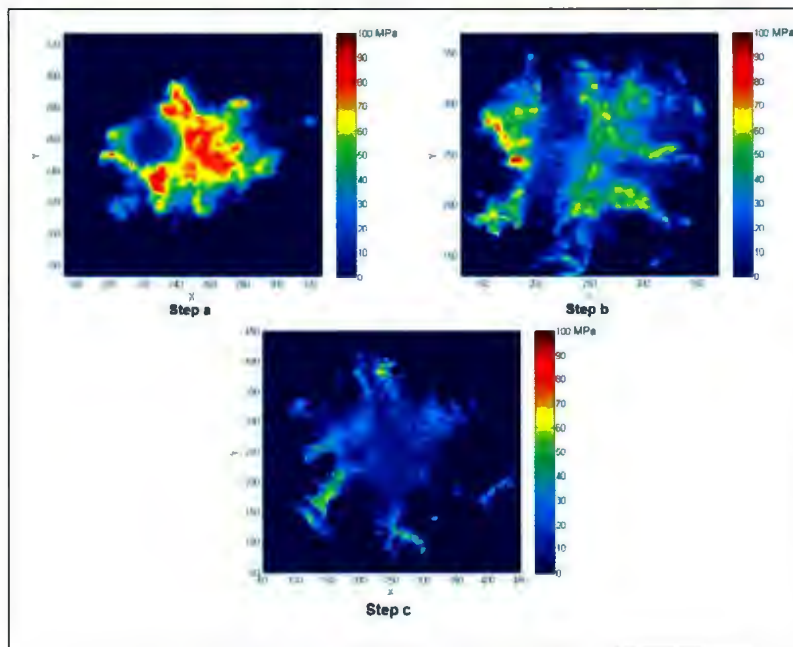


Figure 56 - 2D Spatial Pressure Maps, F1T2

The progression of patterns is shown in 3D in Figure 57.

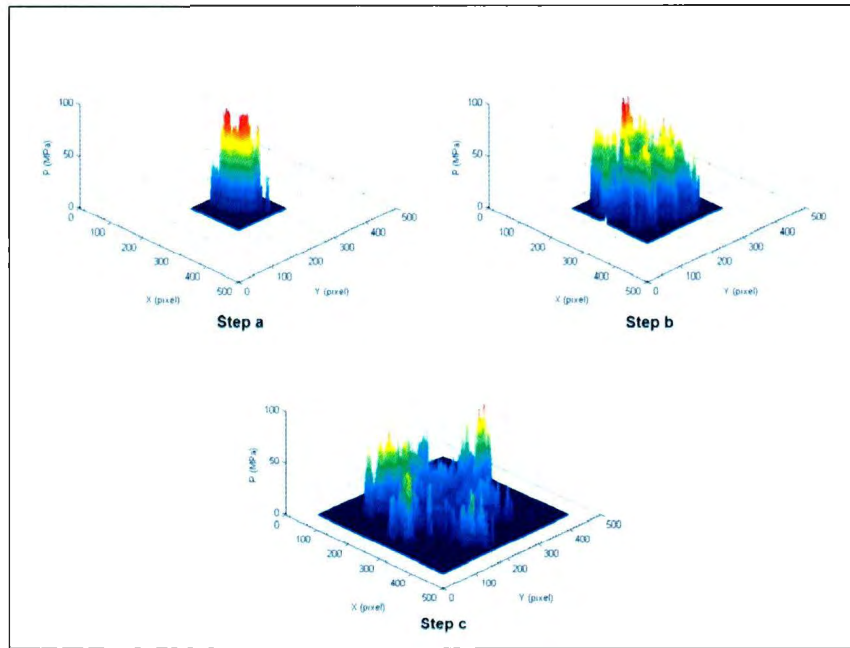


Figure 57 - 3D Spatial Pressure Maps, FIT2

Different orientations of the 3D pressure maps for each test are catalogued in Appendix A for those interested. From these contour plots, the causes of the pressure drops become clearer. The initial contact up to crushing distance of 9mm was a small area with high pressures, up to 80 MPa and even above 90 MPa, in an area of 459.8 mm². As the impact progressed from 9 mm to 18 mm crushing distance and the contact area increased, the regions of high pressure reduced and moved to the edges of the contact area forming branching patterns of the “hard zones” described by Gagnon [8]. However, the number of regions of high pressure, above 50 MPa, decreased greatly and thus the average pressure dropped, as will be seen in the *process* pressure-area curve. The last stage of the impact from 18mm to 27mm crushing distance continued the pattern of pressures zones moving towards the extreme edges of the branching hard zones, with the zones of highest pressure reducing in size.

From the pressure films, the *spatial* pressure area curves were created, whilst the nominal *process* pressure-area curves were created from the MTS machine data. Firstly, the *spatial*- and *process*- pressure-area curves for F1T2 are shown in Figure 58.

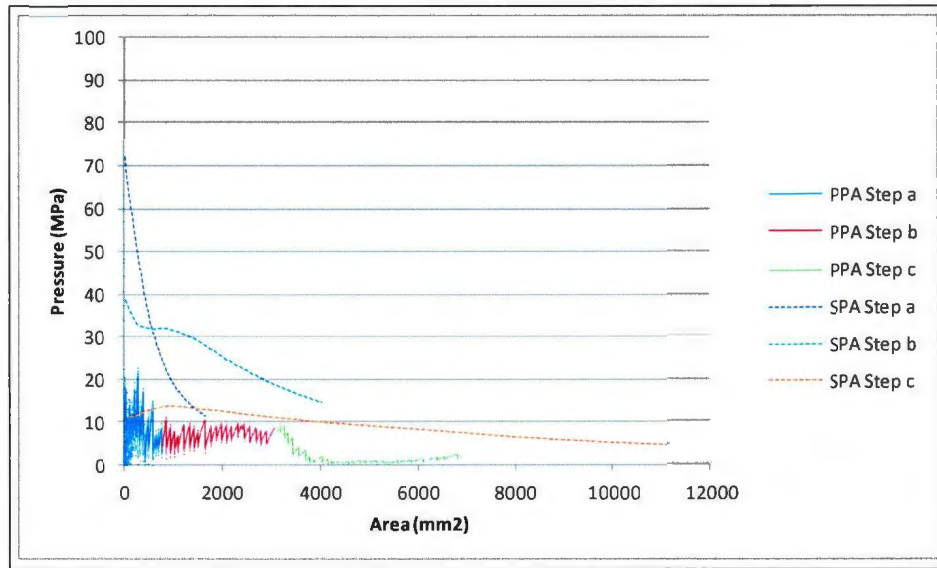


Figure 58 - Spatial and Process Pressure-Area Curves, F1T2

For the *spatial* PA curves, each subsequent step of the crushing event begins with an average pressure roughly 30 MPa below the previous starting average pressure. Pressure drops were roughly exponential, while *step b* showed a pressure drop followed by a plateau and then a resumption of pressure drop. This was likely due to the vertical band of lower pressure clearly seen in Figure 56 beyond which points of higher pressure reappeared. Examining the connection between the *spatial* and *process* PA curves, it is clear that the *spatial* curve for *step a* nearly touches the *process* curve while *step b* and *step c* do not. *Step b* terminates at a pressure almost 15MPa greater than the *process* pressure at approximately 4000 mm² while *step c* stretches far beyond the nominal

contact area. This however is expected since the nominal contact area and the *spatial* PA curve sub-areas do not have the same geometries. The nominal contact area is a circle while the sub-areas are squares, and so the largest sub-area will contain more area than the largest nominal contact area. Areas outside of the pressure pattern are averaged in as 0 MPa as previously discussed. The *process* PA curves of both repetitions of Treatment Combination (1) are compared in Figure 59.

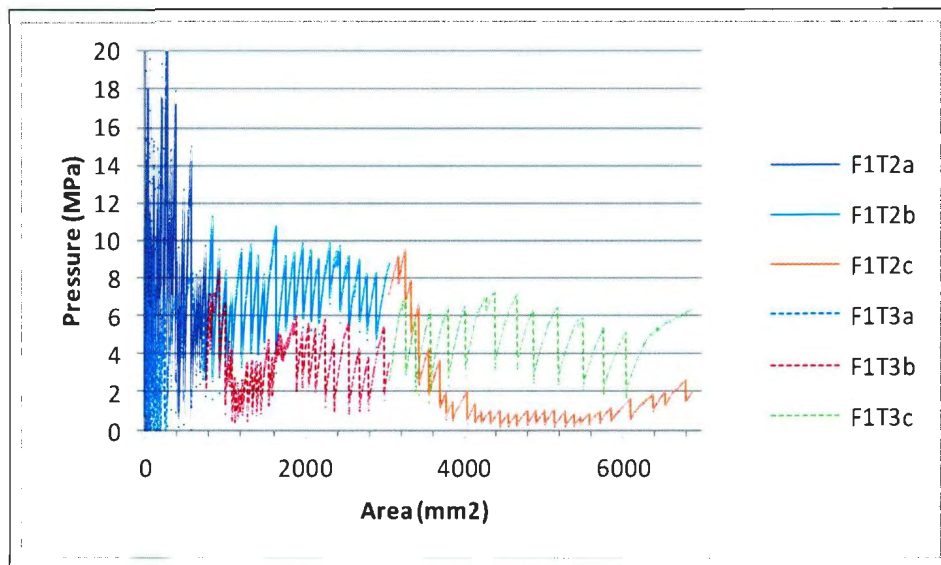


Figure 59 - Process Pressure-Area Curves, Treatment Combination (1)

The PA curves for each test follow a similar pattern until approximately 3200 mm² nominal contact area however they are displaced from each other by approximately 5 MPa on average. This displacement occurs at approximately 1000mm² contact area at which point the pressure of F1T3 drops sharply. F1T3 then follows a fairly constant path, whereas F1T2 shows a significant pressure drop from approximately 9 MPa to approximately 2 MPa at 3200 mm². After this drop, the pressure oscillations of F1T2 are smaller, on the order of ± 0.5 MPa. The reasons for these pressure drops are due to ice

cracking and being removed from the contact area and the resulting changes in actual contact area and *spatial* pressure distribution across the contact surface. At 10.3 s into the crushing event there was a load drop in FIT3 likely caused by a spalling event, which lead to the pressure drop. 19 s into FIT2 there was the substantial load drop seen in Figure 54 which resulted in the process pressure area drop at 3200 mm² nominal contact area. The exact spatial reasons for this change in load and pressure are not entirely clear from the spatial pressure maps. It is clear that the regions of high pressure changed both in individual size and in location (see Figure 56). The large load drop in FIT2 occurred during the third crushing step, *step c*. Comparing the pressure films and *spatial* pressure maps of *step b* and *step c* the total contact area did not greatly increase while the amount of high pressure zones, zones above 50 MPa, were greatly reduced and limited to the peripheries of the contact area.

The total area of high pressure zones (HPZs) for each step were 30.0 % for *step a*, 8.4 % for *step b* and 2.5 % for *step c*. The percentages of HPZs for each test are listed in Table 10. During each step of FIT2 there was a substantial pressure drop in the *process* pressure-area curve. Between each step, there was a substantial drop in the total area of high pressure zones. The drops were due to spalling of ice during the collision event as clearly established by other researchers. The exact spalling events were not, however, captured by the pressure films due to too large of a time gap between successive pressure recordings and the fact that the pressure films retain pressure histories, not spot patterns at a specific time.

Lastly, as discussed in previous sections the pressure films record a pressure history rather than an instantaneous pressure pattern. The negative effects of extra

activated area can be limited by reducing the time between successive pressure measurements, however the extra data cannot be completely removed or accounted for. Therefore, determining how much in error the pressure films are is of value. The error will be determined between the MTS-measured force (the total ice load on the system), F_T , and the total load predicted by pressure film, F_p . F_T is simply measured from the load sensor on the MTS machine at the last data recording of a given crushing step. F_p can be calculated in two ways. The less rigorous method involves taking the average pressure within the largest sub-area square and multiplying it by the actual area of the sub-area to get force:

$$F_p = P_T A_T \quad [9]$$

where P_T is the average pressure within the maximum sub-area and A_T is the area of the maximum sub-area. This method will, however, include data outside of the crushing pattern since, as discussed previously, the square sub-area includes area outside of the pattern. This data was set to 0 MPa during the imaging analysis, as discussed, and thus will affect the average pressure. The second method involves more rigorously integrating across the pressure pattern. Firstly, since the resolution of the pressure films is 37.8 pixel/cm, the area encompassing one pixel is 0.07 mm^2 . Using the unfilled x, y and P data (the data for the pressure pattern only), at each pixel point the force on that point can be found by multiplying the pressure recorded at that pixel by 0.07 mm^2 to get the force on that pixel. The individual forces on each pixel can then be summed to get the total force, F_p , on the pressure film. Comparatively, the difference between each method is small.

The largest sub-area was carefully chosen to extend just beyond the pressure pattern. Thus, compared to the number of pixels inside of the pattern, the number of outside-of-pattern 0 MPa pixels is small and does not affect the average greatly. The comparison for FIT2 of both methods is shown in Table 8.

Table 8: Rigorous and Non-Rigorous Methods of Finding Total Pressure on Film

Non-Rigorous Pressure (MPa)	Rigorous Pressure (MPa)	% Error
19.54	19.81	1.36%
59.3	59.94	1.07%
53.92	54.2	0.52%

The error induced by calculating total force on a pressure pattern using the square sub-area rather than the actual contact area is clearly small enough that the less rigorous method is valid. The % Error between F_T and F_p using the less-rigorous method for FIT2 were found to be 583.2 %, 121.4 % and 284.6 %. Clearly the pressure films, at least for this test, did not predict the total force on the pressure film at a specific time with any accuracy, and this highlights the issues of the films recording a “history”, rather than an instantaneous measure. However, not all tests indicated errors as high as this test as shall be seen in Section 6.2. The nature of ice crushing within each step is not the same in all cases and depends upon other factors and this affects how much history is recorded in each test. The error between F_p and F_T for each test is listed in Table 12.

7.1.2: Treatment Combination bc

Treatment combination bc was -15°C , 5-10 mm grain size, 100 mm/s impact speed and 30° cone angle. The tests involved were F9T1, F24T1 and F28T1. However, problems occurred with the testing apparatus for both F9T1 and F24T1. As a result, only the pressure film test for treatment combination bc was recorded; no repeat run was made. Due to the much higher impact speed, it can be expected that the crushing will involve more small scale fracturing with less large spalls and thus less large load drops. The amount of data recorded will also be less, 138 data points versus 16677, and as a result the amount and amplitude of recorded load oscillations will be less [13]. The force-displacement curves for treatment combination bc are shown below in Figure 60.

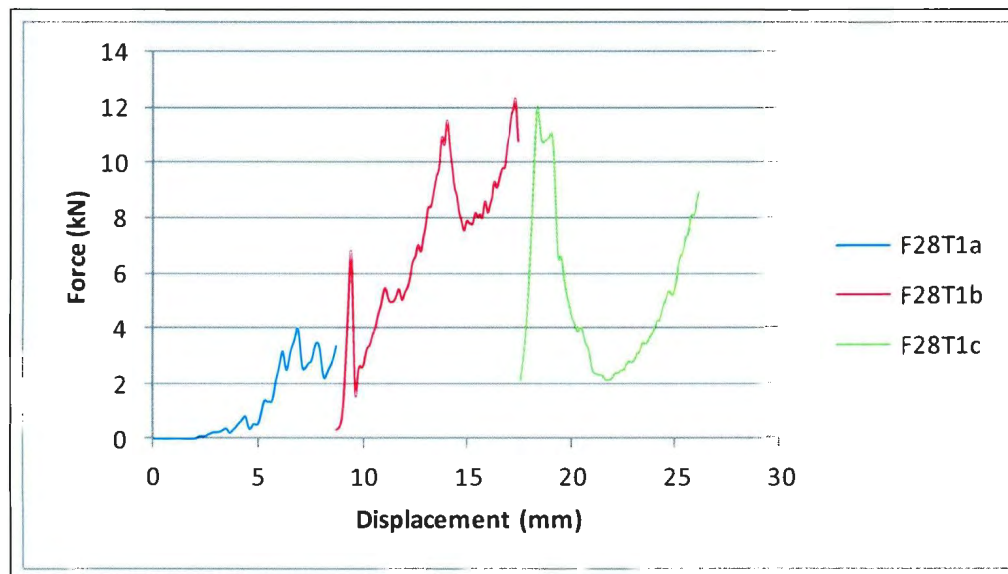


Figure 60 - Force-Displacement Curve, Treatment Combination bc

With this test, the loads at the beginning of each new crushing step were initially low but returned to expected levels in less than 0.01s. Interestingly, the force history for bc follows a very similar trend as that of F1T2, treatment combo (1), albeit with different load levels. F28T1 shows a force ramping relatively consistently, ignoring the force spikes, to a maximum before dropping significantly at 19 mm crushing depth. F1T2 showed (Figure 54) an overall ramping of load level before dropping significantly at 18 mm crushing depth. Both load drops were likely due to relatively significant ice failure and spalling events. By comparison, F28T1 indicated more significant fracturing events with two relatively significant events occurring at approximately 9 mm and 14 mm crushing depth. As expected, the level of load oscillations is less at the higher impact speed.

The pressure patterns for treatment combination bc are shown in Figure 61. In this test, the pattern after the first step of crushing is roughly circular. By the second stage of crushing, however, the pattern becomes much more complex. If one were to encircle the pattern with a circle, it would appear that notches had been cut out of the circle. The idea is detailed in Figure 62. These notches of "missing" data, clearly seen in *step b*, are due to ice fracturing away from the contact area which occurred throughout the course of the crushing step. Flakes of ice were broken off and extruded, altering the contact face. This is continued into *step c* where the notches have been widened and some material between notches has been completely removed.

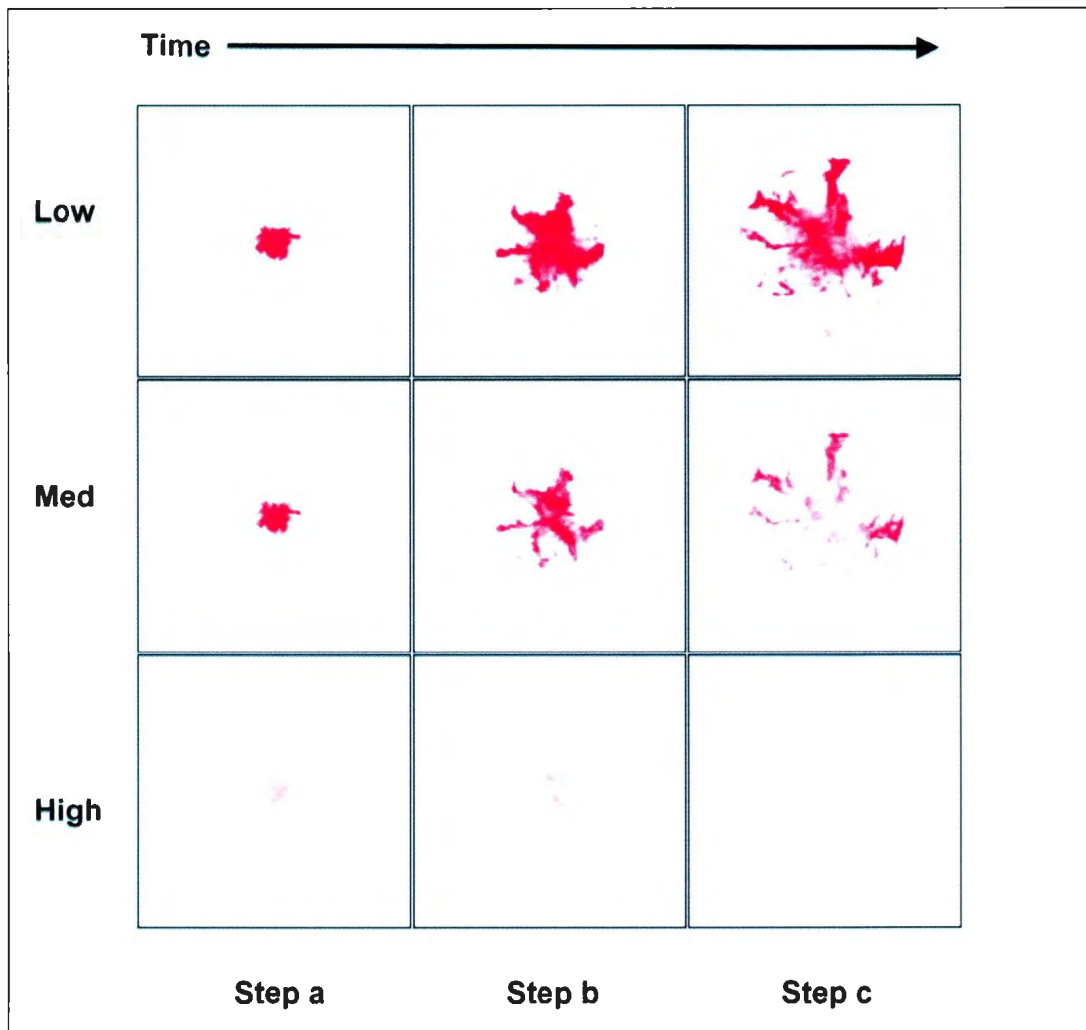


Figure 61 - Progression of Pressure Patterns, F28T1 (l-r: Step a, b, c, t-b: L, M, H)

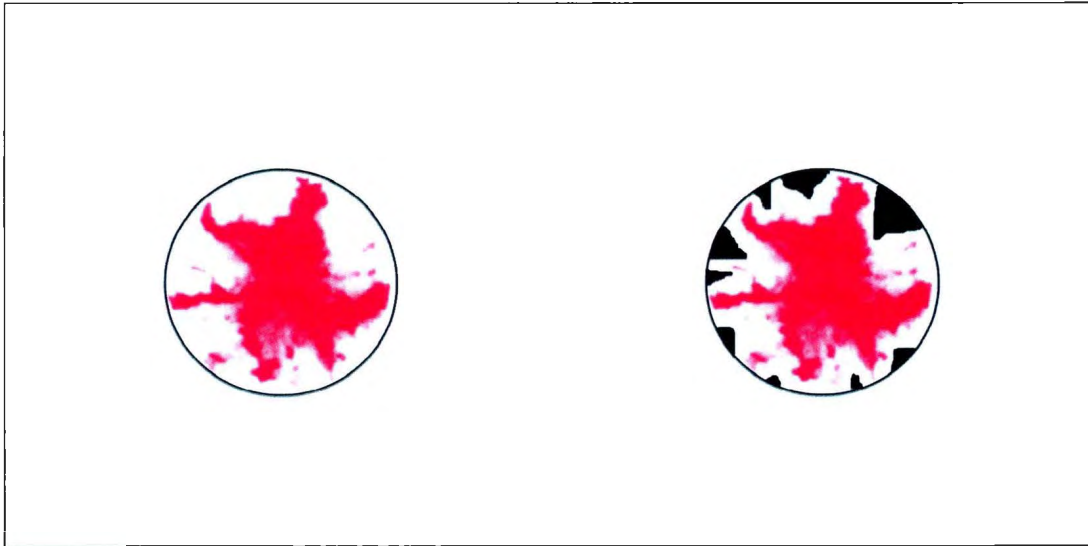


Figure 62 - "Missing" Spaces in Pressure Pattern

A visual comparison between the nominal contact area and the actual contact area is also of interest. Figure 63 shows the Low range contact film for Steps a, b and c encircled by a circular bounding encompassing the nominal contact area at the end of each step.

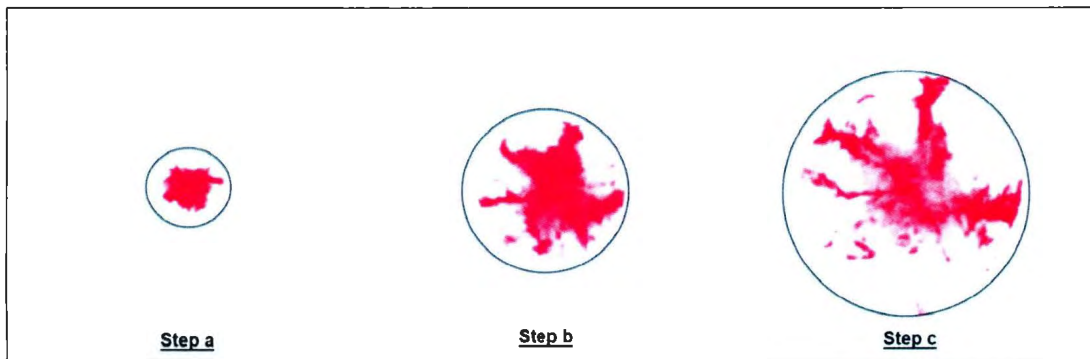


Figure 63 - Nominal and Actual Contact Areas, Low Range Film, F28T1

Recalling that the pressure films record a history rather than an instantaneous measurement, and thus extra data likely exists, the use of a simple geometry for contact

area does not accurately represent true ice contact and fracturing geometry. The numerical comparisons between nominal contact areas for all tests are shown in Table 9. For F28T1a (*step a*) the actual contact area was 236.916 mm^2 while the nominal contact area was 713.58 mm^2 at the conclusion of the test, resulting in an error of 201 %. For *step b*, the areas were 1080.023 mm^2 compared to 2900.8 mm^2 for an error of 169 %, and for *step c* they were 1620.875 mm^2 compared to 6464.0 mm^2 for an error of 299 %. With errors in contact area as high as 300%, the simplified geometry is clearly quite off. The 2D and 3D *spatial* maps are shown in Figure 64 and Figure 65 respectively. It is very clear from the 3D maps that the pressure is initially very uniformly high across the contact zone, but as the crushing event progresses pieces of ice flake and spall and are extruded, leaving smaller contact zones of high pressure.

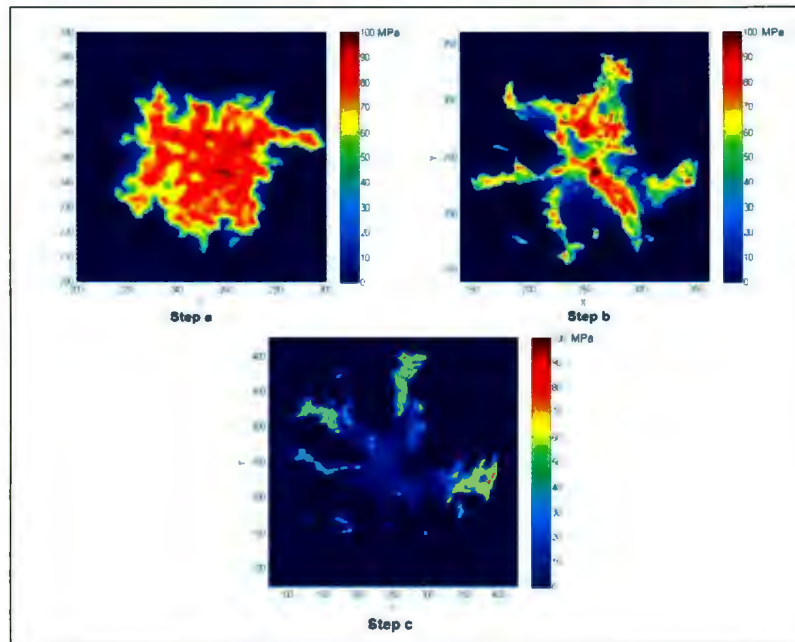


Figure 64 - 2D *Spatial* Pressure Maps, F28T1

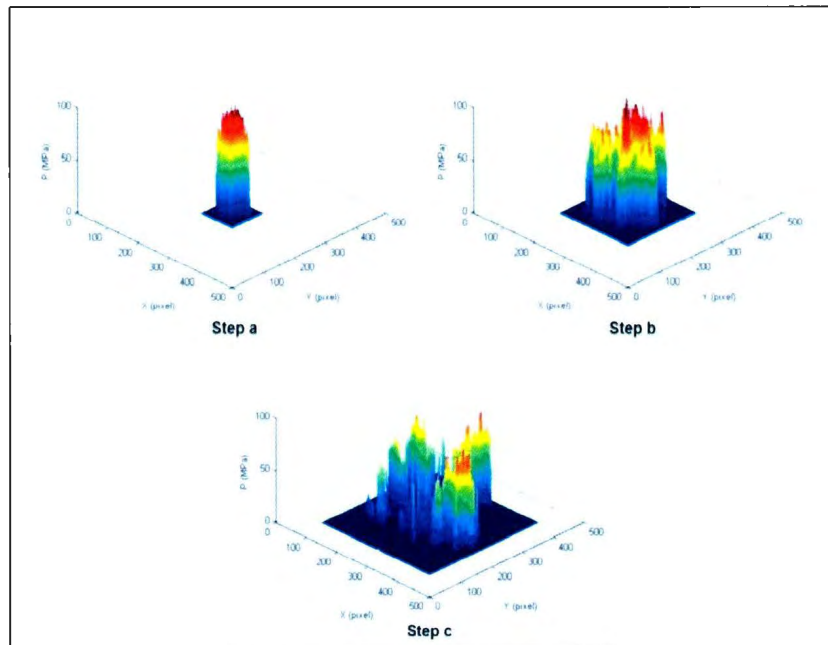


Figure 65 - 3D *Spatial* Pressure Maps, F28T1

The pressure-area curves for F28T1 are shown below in Figure 66. The *spatial* pressure-area curves terminate at pressures above the equivalent point on the process pressure-area curve. F28T1a terminates at a pressure of 21.6 MPa on the *spatial* curve, while the *process* curve reaches a pressure of only 4.4 MPa at the same area. In F28T1b, the *spatial* curve terminates at 13.7 MPa while the PPA curve reaches 3.2 MPa at the same contact area of 3449 mm², while F28T1c overshoots the contact area as expected, although it does come much closer to the *process* curve. The *spatial* curve of F28T1c terminates at approximately 3.8 MPa while the *process* curve terminates at 1.3 MPa. At the equivalent contact area as the end of the *process* curve, the *spatial* curve has descended to approximately 5.1 MPa. The deviations are again mainly due to the extra recorded pressure history throughout each crushing step.

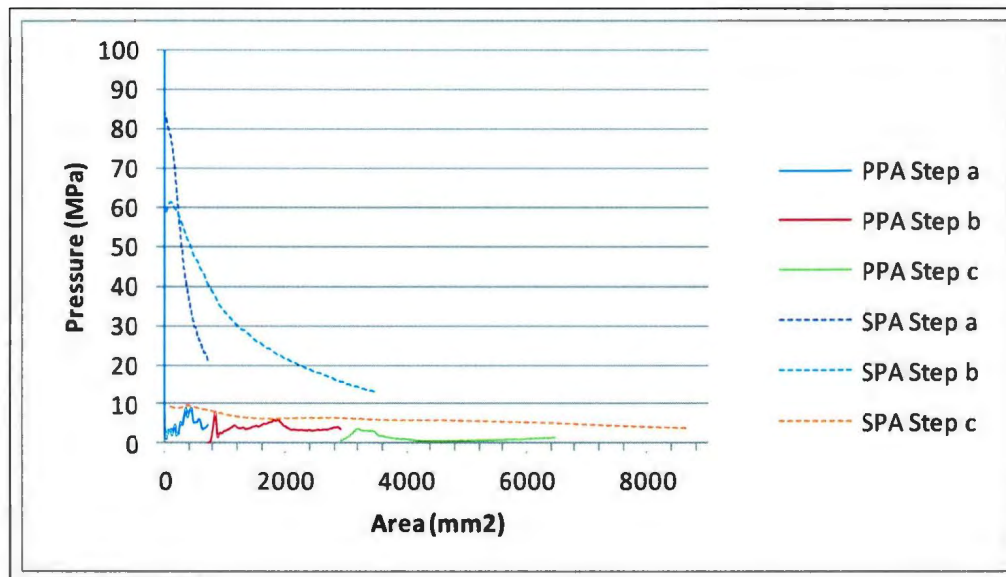


Figure 66 - Pressure-Area Curves, Treatment Combination bc

The high speed, large grain test resulted in average pressures across the contact face being much smaller than the slow speed, small grain tests of treatment combination (I). An enlargement of the *process* pressure-area curve is shown in Figure 67. The process pressure-area curve shows a sequence of sudden drops in pressure at approximately 443 mm², 833 mm², 1932 mm², and 3461 mm² nominal contact area. These drops indicate the likely timings of significant removal of ice from the contact surface. The first spalling event at 443 mm² can be readily approximated from the pressure film since the pressure pattern is relatively circular. It is possible that the extended “finger” of pressure on the right side of the F28T1a pattern is marking the position of ice which once existed alongside it.

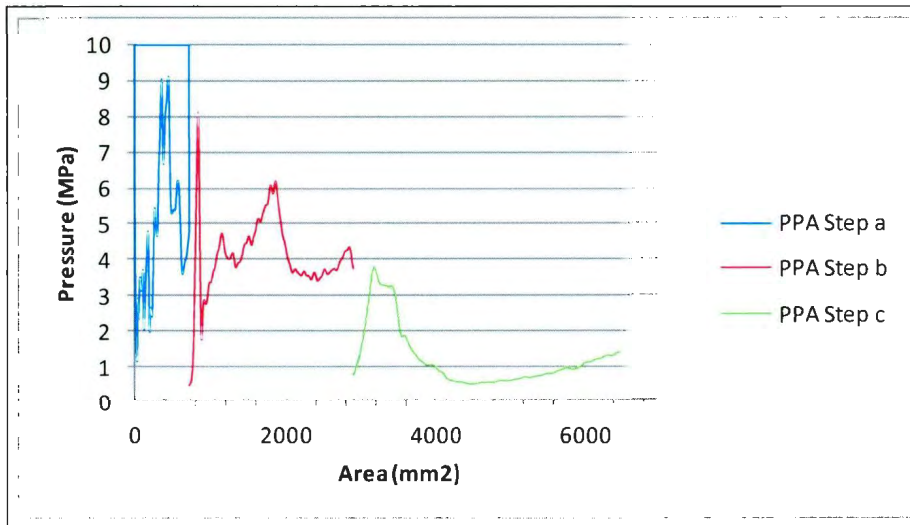


Figure 67 - *Process* Pressure-Area Plot, F28T1

As for F28T1b, the spalling events at 833 mm² and 1932 mm² nominal contact area may be the larger black areas marked in Figure 63. However, there were clearly numerous fractured points where ice was removed, so it cannot be determined for certain. The same interpretation can be applied to F28T1c.

Compared to the slower speed tests at Treatment Combination (1), the percentage of HPZs was higher for Treatment Combination *bc*, thus at the higher speed and larger grain size, high pressure regions made up a higher percentage of the overall contact area than at lower speed and small grain size for the same temperature and cone angle. The percentages were 58.9 % vs. 30.0 % for F28T1a, 33.7 % vs. 8.4 % for F28T1b and 10.1 % vs. 2.5 % for F28T1c. This indicates that either higher speed or larger grain size may affect creation of high pressure zones.

Lastly, the MTS load cell-measured total force, F_T , and the pressure-film predicted total force on the system, F_P , were respectively: for F28T1a 3.42 kN and 15.4 kN, for F28T1b 10.81 kN and 47.67 kN, and for F28T1c 8.94 kN and 33.23 kN. These

correspond to errors of 350.3 %, 341.0 % and 271.7 %- very high, much as for Treatment Combination (1), and indicative of a high degree of history, or activated, area recorded by the film and thus a high rate of ice fracture and spalling during each step. The more ice that fractured at a higher rate, the greater the amount of accrued activated area at the end of each crushing step, and so the degree of divergence between the actual and nominal areas and the difference in predicted loads can give a sense of the level and rate of fracturing during the collision.

*7.1.3: Treatment Combination *bd**

Treatment Combination *bd* was performed at a temperature of -15°C, 5-10 mm grain size, 1 mm/s impact speed and a cone angle of 50°. The corresponding tests were F13T1, for which pressure film was used, and the non-film replicate F9T2. However, as for treatment combination *bc*, there was an error during the tests of F9 which was not detected and the force data was not properly recorded. As a result, the force and pressure curves cannot be plotted for this test. The force-displacement history for F13T1 is shown below in Figure 68.

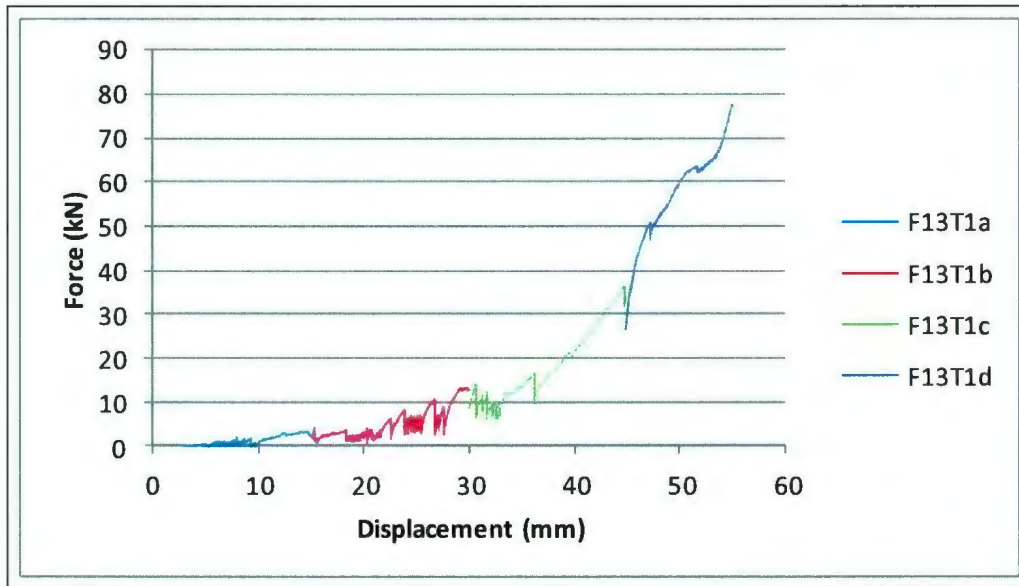


Figure 68 - Force-Displacement Curve, Treatment Combination bd

The force history for F13T1 is not remarkably different from those for Treatment Combination (1) and bc until the final stages of F13T1c and into F13T1d are reached. Prior to this, the force history displays the expected ramping sawtoothed pattern indicating spalling events and general breakup of the ice under load. However, beginning at approximately 36 mm impact distance, the force begins to increase with very little oscillation, and the rate of rising force increases even further during the final step of the impact up to almost 80 kN. Treatment combination (1) reached a force of 43 kN while Treatment Combination bc reached only 12 kN. The likely reason for this greatly increasing force and lack of oscillation is a combination of confinement and, most likely, boundary effects from the ice holder. The sharper cone resulted in more pieces of ice being spalled from the contact face earlier in the collision, but also resulted in these pieces building up at the periphery of the contact zone. Lack of complete extrusion therefore limited further fracture and allowed the forces to sharply increase. As ice was

crushed further and further, and more ice was entrapped by the already non-extruded ice, the steel ring from the ice holder began to enforce a structure to the crushing pattern. The pressure patterns are shown in Figure 69.

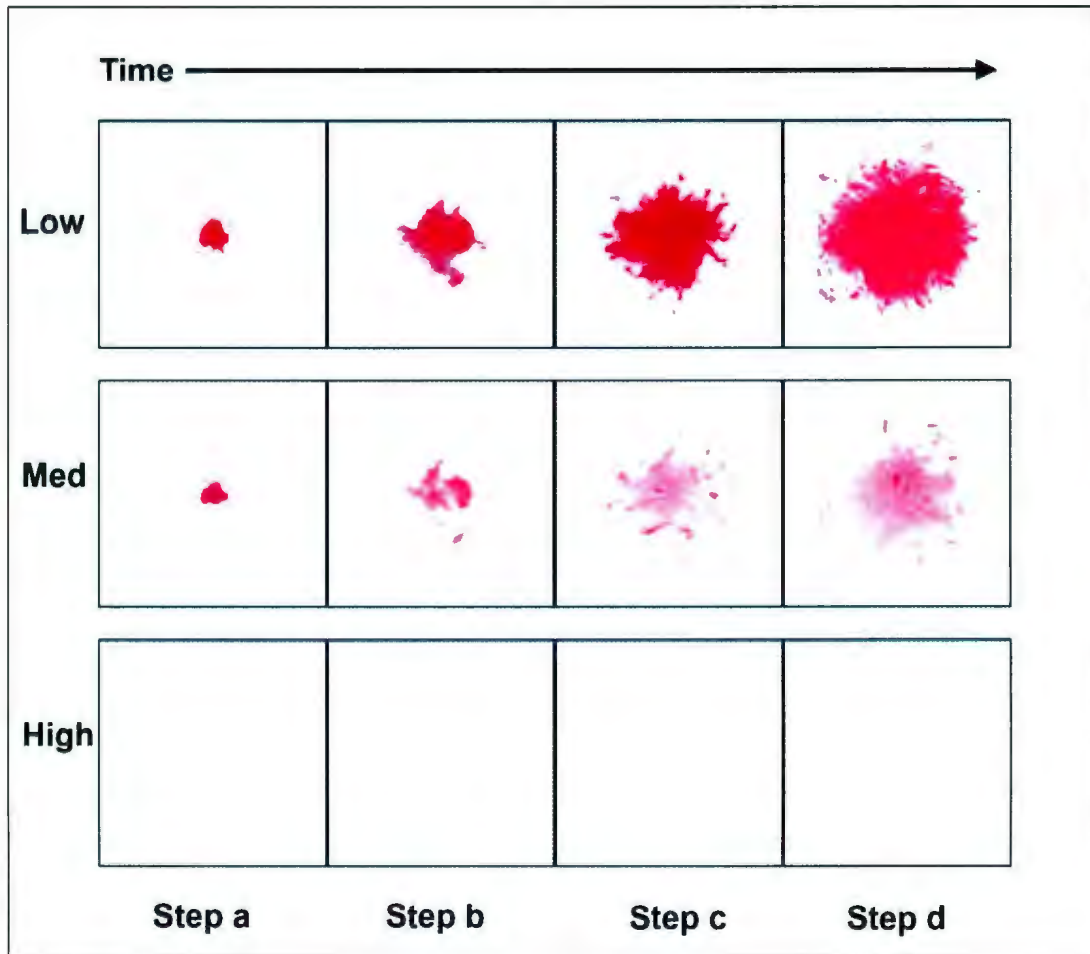


Figure 69 - Pressure Films for F13T1 (l-r: Step a, b, c and d, t-b: L, M and H)

Two things of immediate note are that a) the pressure patterns become almost circular over the course of the impact and b) there are almost no high pressure zones in F13T1b, F13T1c and F13T1d - indeed, they are essentially invisible to the eye, however they exist

and appear in the pressure maps. The circular pressure patterns in the last two stages and the lack of high pressure zones support the notion that confinement and boundary effects prevented spalling of large pieces of ice from the contact area. As has been discussed by Gagnon [8], the sudden reduction of contact area caused by a spalling event leads to an increase in pressure in the remaining contact zones. When there is less spalling, the amount of high pressure zones is reduced and the load is spread out over a larger contact face. However, as was seen in the force-displacement history, the overall load in this test increased greatly. Clearly the relationship between pressure and contact area in ice is a very complex one.

The actual and nominal contact areas are listed in Table 9. The comparison of contact area confirms that the actual contact area approached the idealized nominal circle as the crushing progressed. At the end of F13T1a the error between the nominal and the actual contact area was 116.9%, in line with the errors recorded in the previous tests. However, the error reduced in the subsequent steps to 87.3%, then 61.8%, and finally 30.9%- still off, but a much closer approximation.

The 2D and 3D *spatial* maps are shown in Figure 70 and Figure 71. The pressure maps clearly show the decrease in high pressure zones as the contact area approaches the idealized circular shape. This is demonstrated even more dramatically with the 3D *spatial* maps in Figure 71.

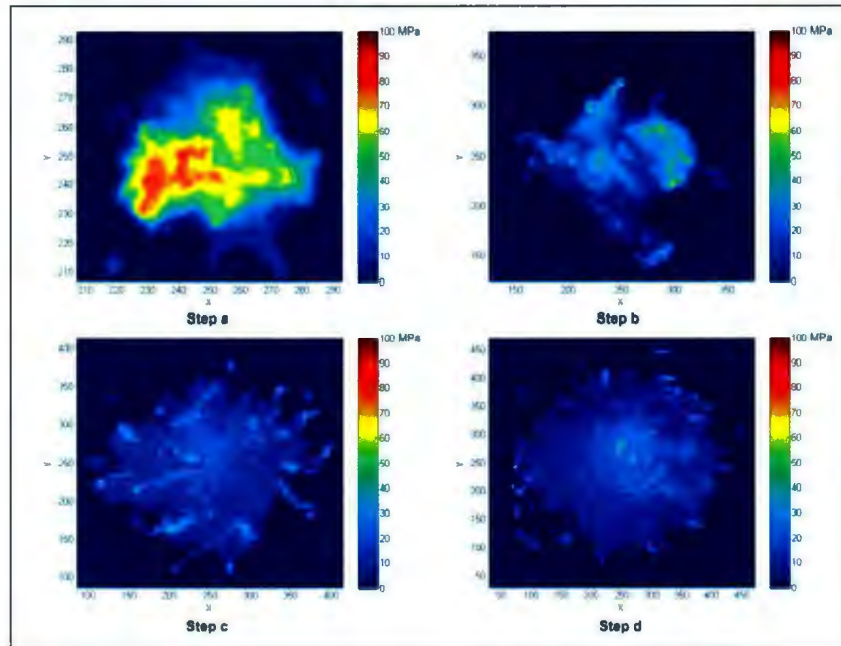


Figure 70 - 2D *Spatial* Pressure Maps, F13T1

The *spatial* and *process* pressure-area curves for F13T1 are shown in Figure 72. Unlike in the previous tests, the *spatial* pressure-area curves terminate at pressure below the nominal average, aside from F13T1a where the *spatial* pressure terminated above and showed similar results as the previous tests. F13T1b terminates at 4.8 MPa while the *process* curve reaches 8.0 MPa. It is unclear precisely why the *spatial* curves terminate at lower pressures than the *process* curve at equivalent areas, especially since the confinement experienced by the ice forced it into a shape approximating the nominal contact area. This is a matter which may require further investigation.

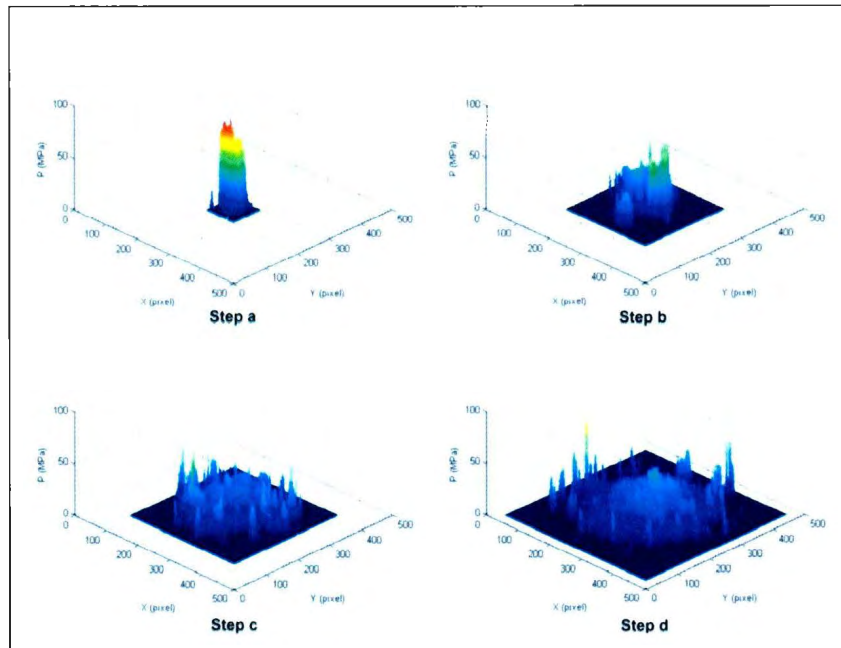


Figure 71 - 3D *Spatial* Pressure Maps, F13T1

The percentage of total contact area that was occupied by high pressure zones is listed in Table 10. The percentage greatly dropped as the crushing event proceeded and confinement began to affect the ice failure. After F13T1a, HPZs made up 22.0% of the total contact area and the shape was very irregular. After F13T1b HPZs made up 1.7% of the total contact area, while by F13T1c the contact area began to approximate the circular idealization and HPZs made up only 0.2% of the total contact area and by F13T1d less than 0.1% was made up of HPZs and the contact area was relatively circular. This provides further credence to the notion that confinement and boundary effects from the ice holder affected crushing, reducing the amount of spalling and irregular alteration of the contact area, thus reducing the amount of small area high pressure zones while allowing the load to build to a greater level over the entire contact area. The presence of

confinement can also be clearly seen in the *process* pressure-area curve of F13T1 as seen in Figure 73.

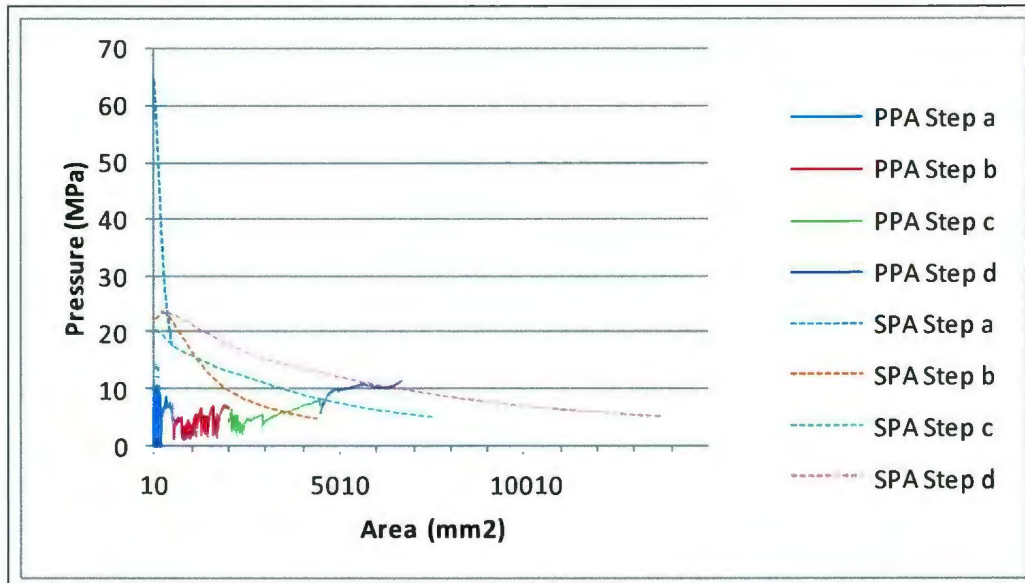


Figure 72 - *Spatial* and *Process* Pressure-Area Curves, F13T1

The curve initially shows an exponentially decreasing trend as predicted by Sanderson [22]. However, at 500 mm² nominal contact area the average pressure begins to rise. This rise in pressure as the impact continues is likely due to confinement of extruded ice as shown by Ulan-Kvitberg et al. [13] and Daley [10]. The previous tests did not indicate this behaviour. The deviations between pressure curves are likely due to these confinement and boundary effects and needs to be further investigated.

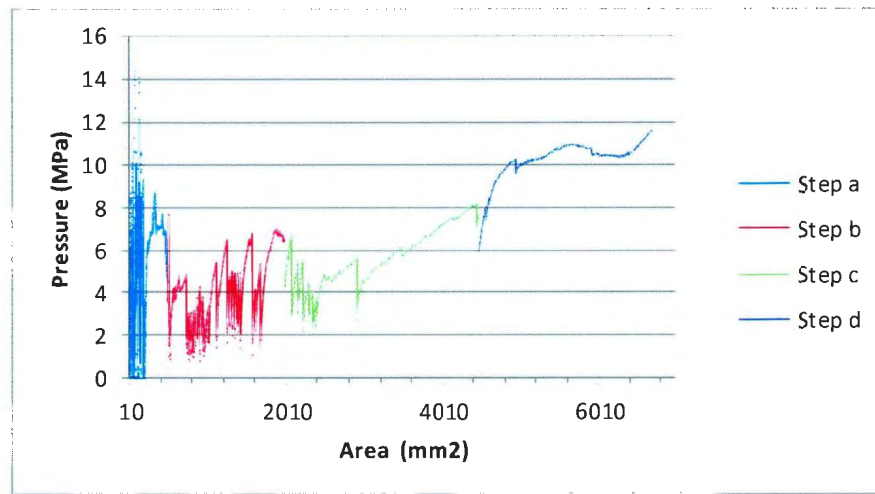


Figure 73 - Process Pressure-Area Curve Showing Effects of Confinement, F13T1

The total force values on the system as predicted by the pressure film, F_p , and recorded by the MTS machine, F_T , were found to be 9.1708 and 2.25 for F13T1a, 21.07 and 12.84 for F13T1b, 29.87 and 34.24 for F13T1c, and 69.58 and 77.66 for F13T1d, respectively.

7.1.4: Treatment Combination *cd*

Treatment combination *cd* was performed at a temperature of -15°C , grain size of 1-5 mm, cone angle of 50° and an impact speed of 100 mm/s. The tests were F9T3 and F9T4, which were both non-film tests but which were not recorded properly, and F13T2 which was a pressure-film test. The force-displacement history is shown in Figure 74.

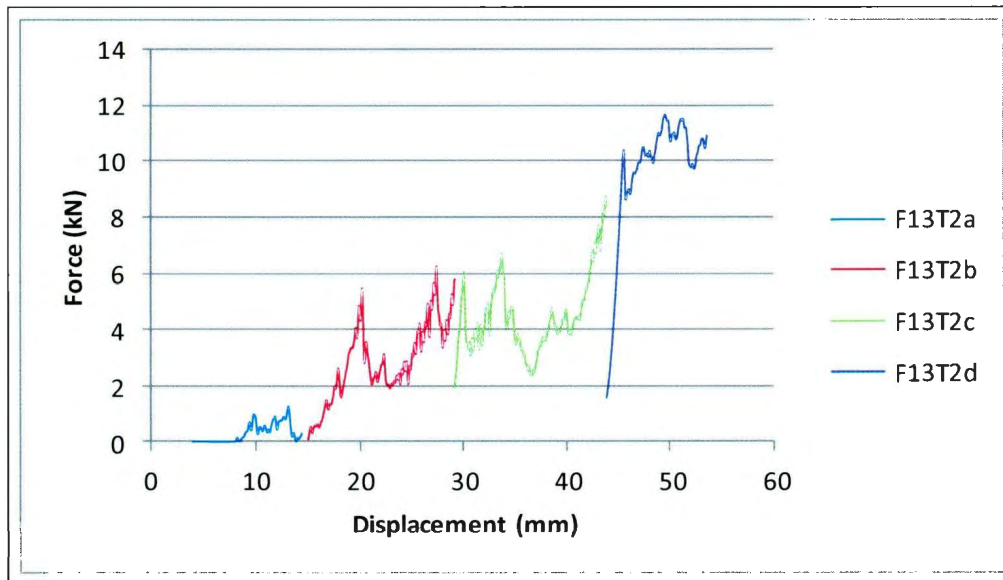


Figure 74 - Force-Displacement History, Treatment Combination cd

The load history for F13T2 shows a more ‘spiked’ and less sawtoothed behaviour than Treatment combination *bd* (also at 50° cone angle) but with much lower force levels. The forces do not reach above 12 kN, while for *bd* the forces reached to just under 80 kN (Figure 68) - likely confinement was not a major factor in this test. The load history is quite similar to that of test *bc* (Figure 60) which was also at 100 mm/s although without the extreme load drop in the final stages of the impact. The crushing event was therefore likely made up of many small fractures and spalls as the ice broke in a brittle manner but without the load buildup required to cause a large spall to occur. It is likely that cracks within the sample occurred, but boundary effects from the ice holder possibly prevented further spalling.

The pressure film patterns for F13T2 are shown in Figure 75.

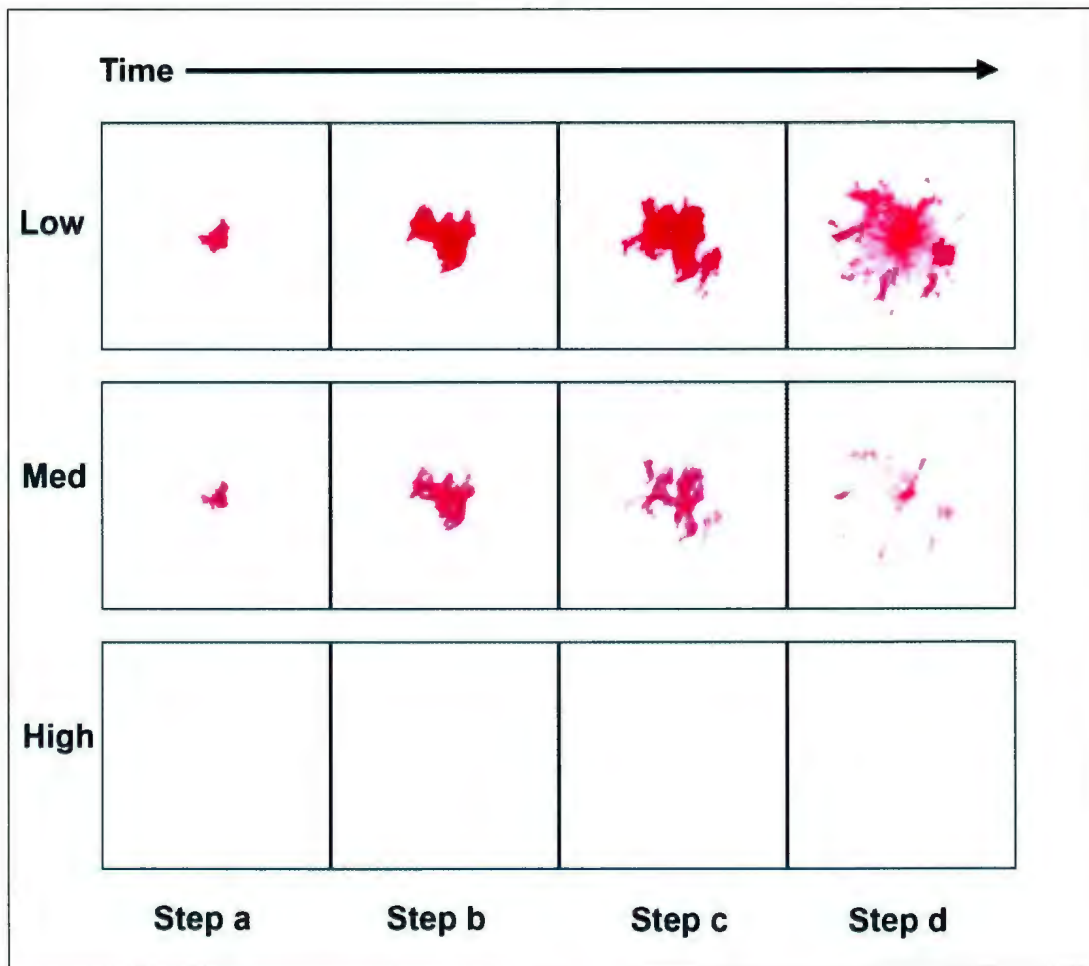


Figure 75 - Progression of Pressure Patterns, F13T2 (l-r: Step a, b, c, d t-b: L, M, H)

The sequence of pressure patterns for this test show the irregular shapes indicative of high levels of spalling and flaking from the contact surface and a low level of confinement. Ice failure at 100 mm/s is clearly a very brittle process and the overall force level does not reach as high as in the presence of confinement. Unlike the treatment combination *bc*, however, which was performed at the same speed, the number of high pressure regions appears to be low in spite of the irregular contact patterns.

The percent errors between actual and nominal contact areas for each step are 138.0%, 127.5%, 205.8%, and 212.8% for F13T2a, F13T2b, F13T2c, and F13T2d respectively. These numbers are high, but are in line with the percent errors in previous tests and further suggest that an assumption of simple geometry in the contact area may only be valid under very specific circumstances such as, potentially, high confinement or artificial boundary conditions.

The 2D and 3D *spatial* pressure maps are shown in Figure 76 and Figure 77 respectively. It is clear from these maps that the irregular contact patterns, caused by spalling and flaking, lead to high pressure zones within the contact area. As the impact continues, the amount of spalling decreases although confinement was not likely an issue.

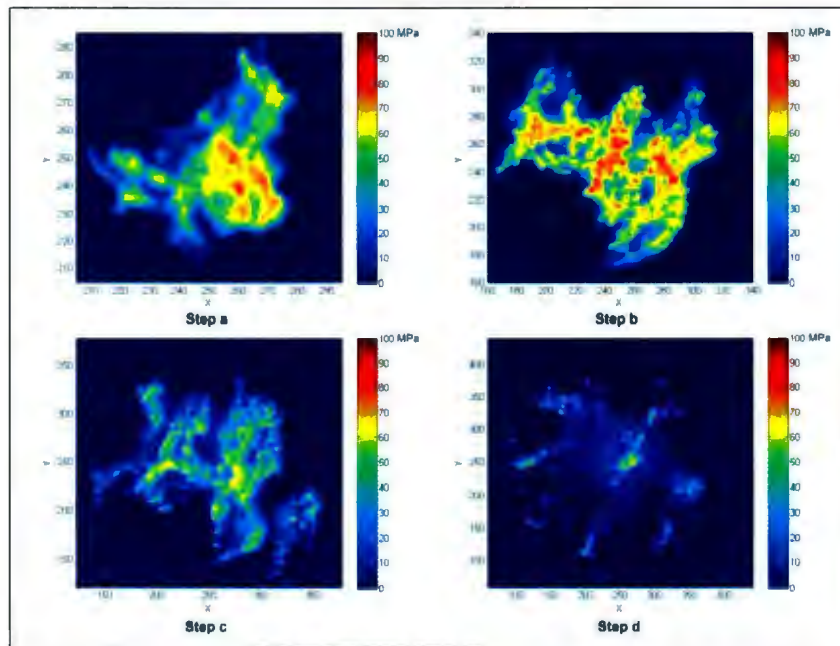


Figure 76 - 2D *Spatial* Pressure Maps, F13T2

Boundary effects from the ice holder may have affected the spreading of cracks and the formation of spalls past a certain point. If one were to, as a thought experiment, extend the ice out of the holder and allow the crushing to continue it can be expected that a crack would have caused a spall, leading to another change of the contact face and an increase in the number of HPZs.

The percentage of HPZs compared to the total contact area for each test was 24.0%, 34.5%, 14.7% and 2.0% for F13T2a, F13T2b, F13T2c, and F13T2d respectively. HPZs made up a relatively significant portion of the contact area at all steps except for F13T2d and showed similar percentages to other tests with irregular contact patterns.

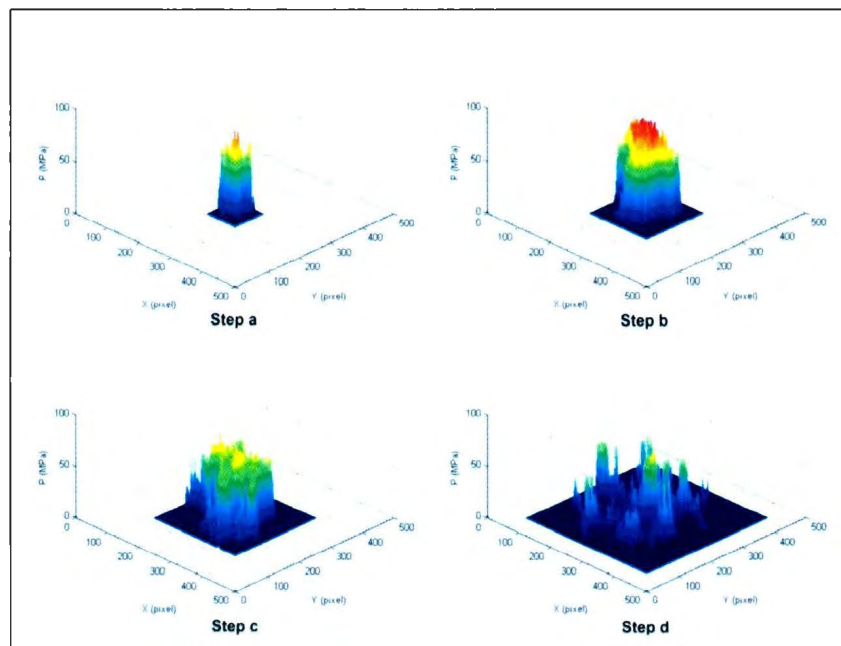


Figure 77 - 3D *Spatial* Pressure Maps, F13T2

The Pressure-Area curves are shown in Figure 78 and the Process Pressure-Area curve is highlighted in Figure 79. The *process* pressure-area curve shows that

confinement was indeed not present in any great extent in this test until approximately 2800 mm² nominal contact area and then into F13T2d. The pressure maps for F13T2d indicate a slightly more regular pattern and reduction in HPZs similar to Treatment Combination *bd* where confinement and boundary effects were clearly present. The terminal pressure values of the *spatial* curves and the corresponding pressures from the *process* curve are 12.94 MPa and 1.01 MPa, 16.86 MPa and 1.78 MPa, and 8.11 MPa and 2.05 MPa for F13T2a, F13T2b, and F13T2c while F13T2d extended beyond the nominal contact area.

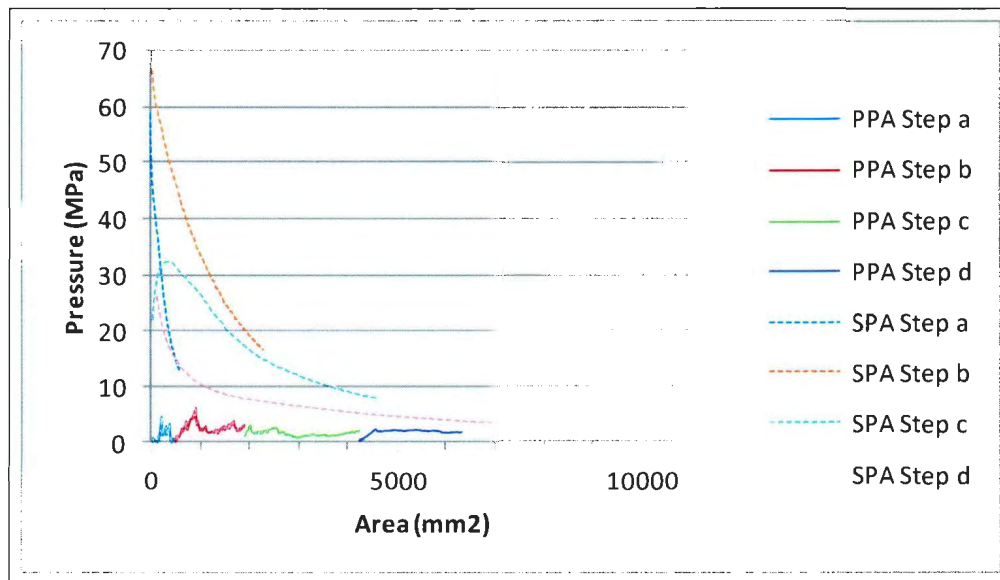


Figure 78 - *Spatial* and *Process* Pressure-Area Curves, F13T2

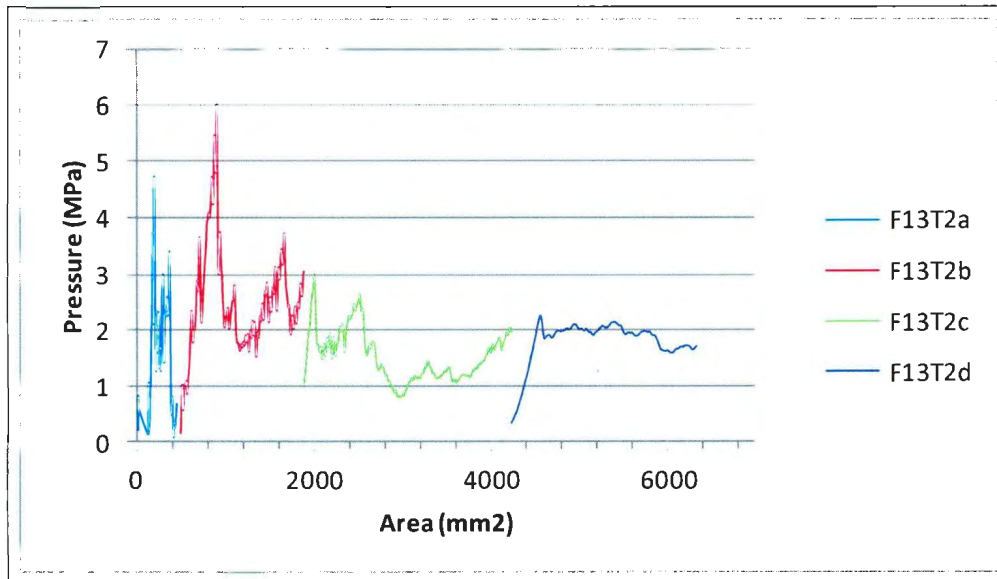


Figure 79 - Process Pressure-Area Curve, F13T2

The percentage errors between F_p and F_T were 2276%, 572%, 345% and 127% indicating that there was a large amount of rapid pressure change in the contact surface in the first step, all recorded as history, but that the rate of pressure change reduced as the test proceeded in the latter stages. The high errors in the load predictions are similar to those of Treatment Combinations *(1)* and *bc*, where confinement was likewise not readily apparent, while *bd* retained the lowest percentage errors in load prediction especially when confinement became a major factor in the event.

7.1.5: Treatment Combination *ad*

Treatment combination *ad* represents the first set of tests to be analyzed that were performed at higher temperature. It can be expected that less brittle ice failure and higher loads may be encountered due to the higher temperature. Treatment combination *ad* tests

were performed at -5°C at a speed of 1 mm/s with grains 1-5 mm in diameter and a cone angle of 50° . The tests performed with this factor combination were F13T3, with film, and F16T2 without film. The force-displacement histories are shown in Figure 80.

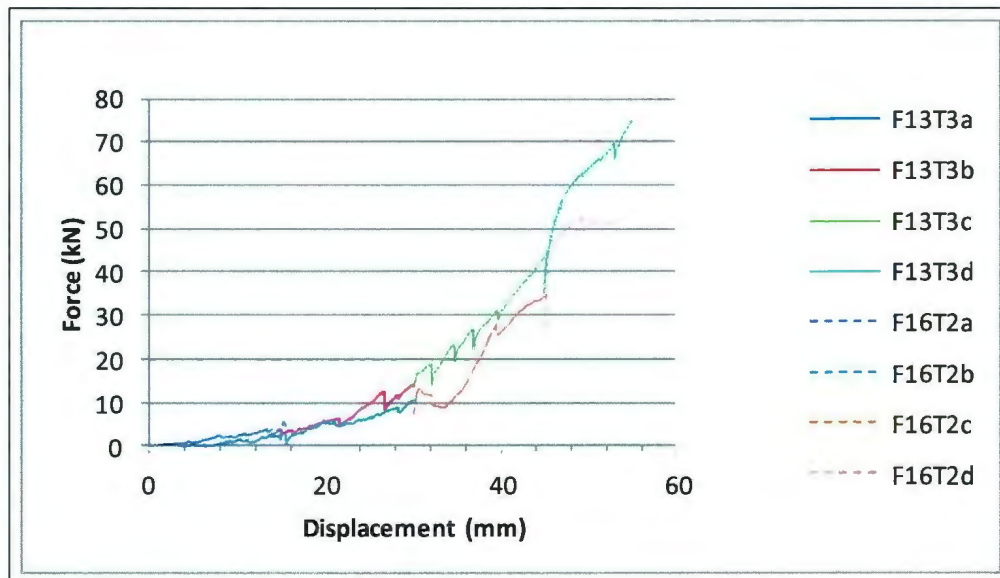


Figure 80 - Force Displacement Histories, Treatment Combination *ad*

The force histories follow a remarkably similar pattern for both tests. At approximately 21 mm displacement, the histories change slightly and F13T3 follows a more sawtoothed loading pattern while F16T2 shows more of a constant force rise after a slight drop. This difference can be explained by the chaotic behaviour of ice cracking and spalling under load. Two load traces of the same sample geometry under the same conditions can be expected to be similar but not the same, since exact cracking and flaking will not be the same. The maximum forces reached were 74.7 kN and 53.9 kN for F13T3 and F16T2 respectively. These values are comparable to Treatment Combination *bd*, F13T1, which

was performed at the same cone angle and speed. Interestingly, the warmer temperature did not result in higher load levels.

The pressure patterns are shown below in Figure 81.

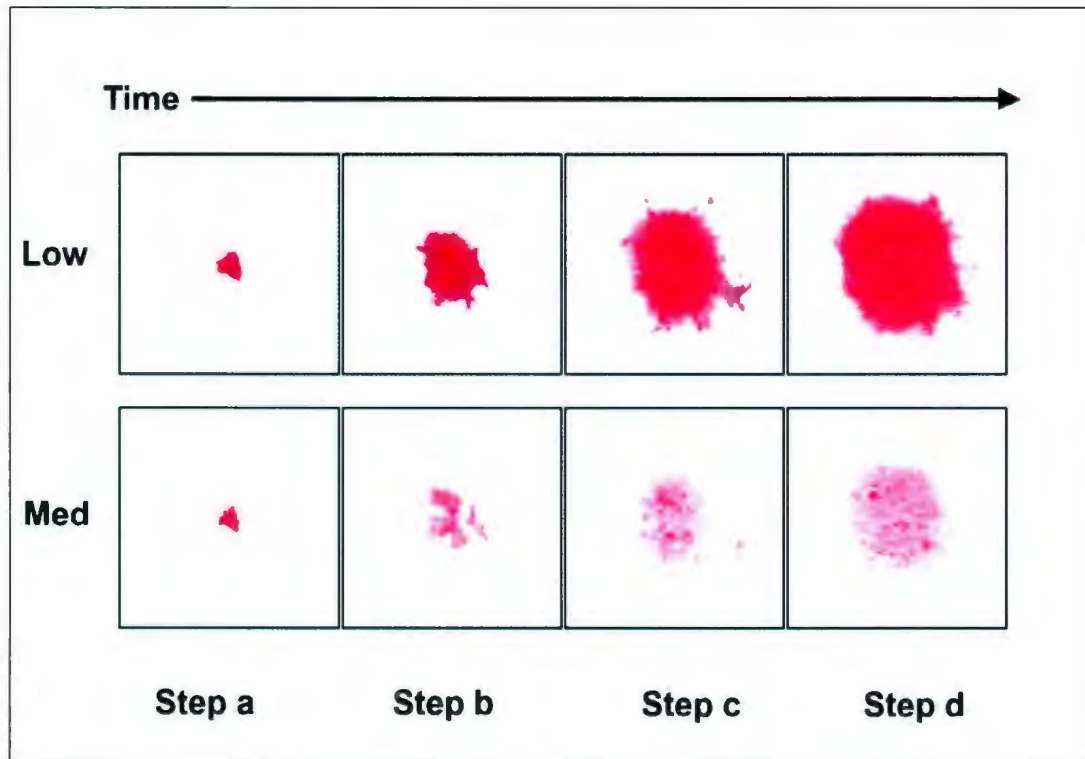


Figure 81 - Pressure Films for F13T3 (l-r: Step a, b, c and d; t-b: L and M)

High range films are not included in the figure because they were almost imperceptible in F13T3a and F13T3b, while F13T3c and F13T3d showed no high pressure patterns. Just as in Treatment Combination *bd*, the pressure patterns become very circular, approximating the nominal contact geometry and thus confinement and boundary effects were very likely present in the tests. In addition, and perhaps as a consequence, the presence of HPZs in the contact area are very low or non-existent. Also, much as with *bd* the load level became quite high and the amount of oscillation in the load pattern,

indicative of spalling and fracturing, was low in the last two steps of the impact. This was likely, then, were confinement began to become a factor in the impact and when the ice holder began to dominate the crushing mechanics. The percent errors between the actual and nominal contact areas for F13T3a, F13T3b, F13T3c and F13T3d for were 162.2%, 55.7%, 38.9% and 35.9%. Very clearly as confinement and boundary effects begin to drive fracturing the nominal contact area approximation becomes more valid. The *process* curve for F13T3 will provide clear evidence of whether confinement was present. The 2D and 3D *spatial* maps are shown in Figure 82 and Figure 83, respectively.

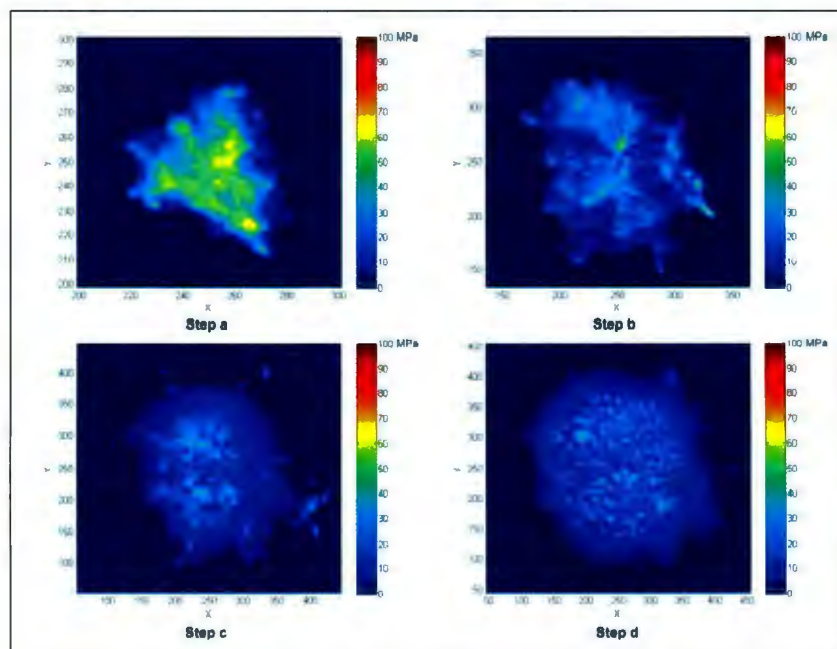


Figure 82 - 2D *Spatial* Pressure Maps, F13T3

The progression of pressure maps shows the pressure pattern to be initially very peaked and irregular but then flatten out and assume a more regular shape as the impact progresses.

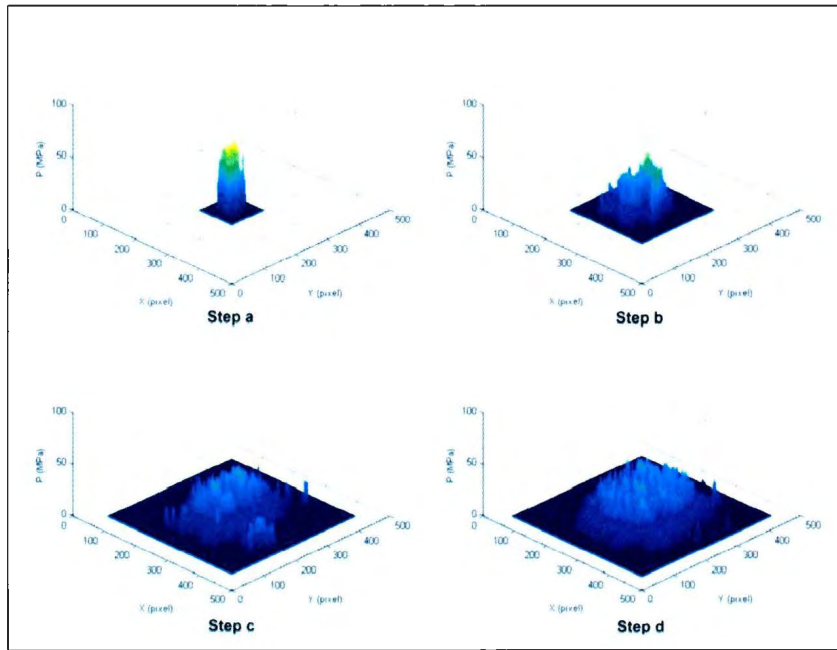


Figure 83 - 3D *Spatial* Pressure Maps, F13T3

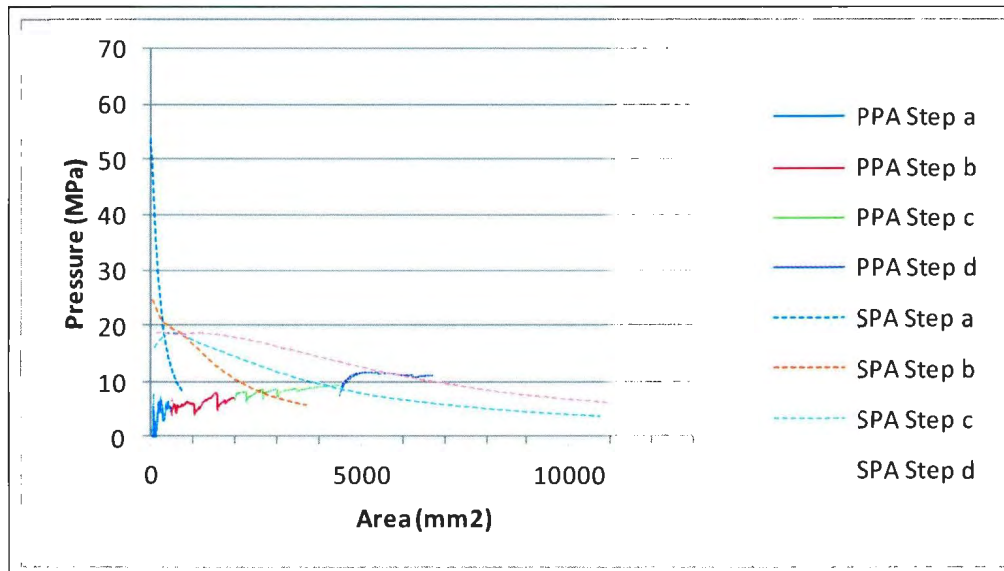


Figure 84 - *Spatial and Process* Pressure-Area Curves, F13T3

The *spatial* and *process* Pressure-Area curves for F13T3 and F16T2 are shown in Figure 84 and Figure 85. F13T3 shows the closest connection between the *spatial* and *process* pressure-area curves of all of the previous tests- this is due to the relatively close correlation between nominal contact area and actual contact area. As discussed in Section 6.1.1, the difference between the terminal pressures of the *spatial* curves and the actual average pressures across the contact areas is not substantially different, and indeed the actual average pressure is higher. The terminal pressures of F13T3c and F13T3d can easily be visually projected back to the *process* pressure-area curve and seen not to differ more than 5 MPa, while the terminal pressures of F13T3a and F13T3b are 8.35 MPa and 5.72 MPa. Compared to the nominal pressures at the same area, 5.61 MPa and 8.97 MPa respectively, the terminal *spatial* pressures do not differ greatly.

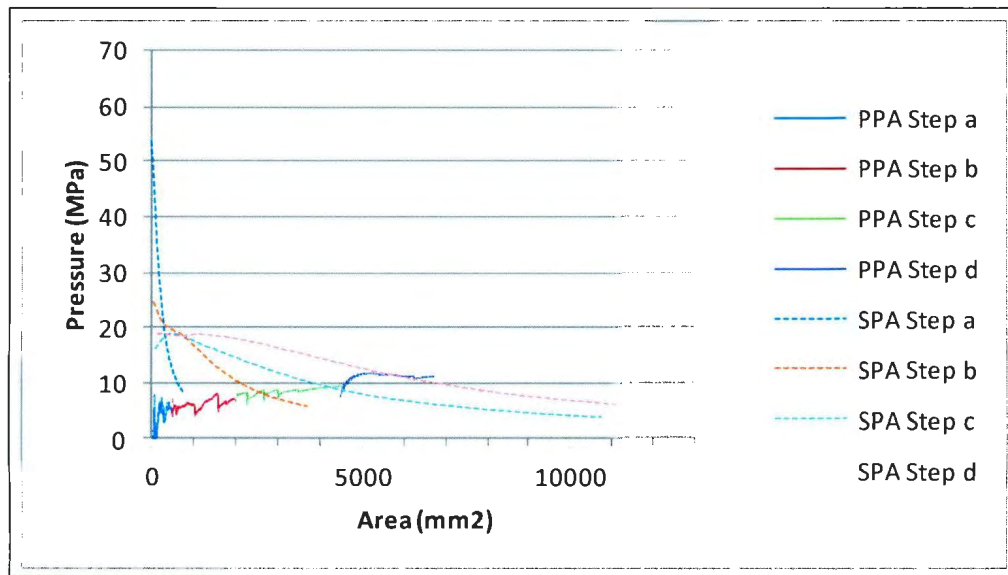


Figure 85 - Process Pressure-Area Curves, Treatment Combination *ad*

Both tests at treatment combination *ad* showed similar *process* pressure-area curves and both clearly indicate the presence of confinement and boundary-effects. In F13T3 the confinement begins to affect ice failure at approximately 575 mm² nominal contact area, while confinement begins to affect F16T2 at approximately 1054 mm² nominal contact area as seen in the *process* pressure-area curves shown in Figure 86.

The number of HPZs clearly dropped significantly as the test progressed down to 0% for both F13T3c and F13T3d, echoing similar behaviour in Treatment Combination *bd*. For F13T3a HPZs made up 18.3% of the total contact area, while for F13T3b they only made up 1.0%. This is further confirmation of the concept that confinement reduces cracking and spalling, thereby reducing high pressures over small areas while allowing overall loads to greatly increase, although the extent to which the confinement was driven by boundary-effects of the ice holder must be considered.

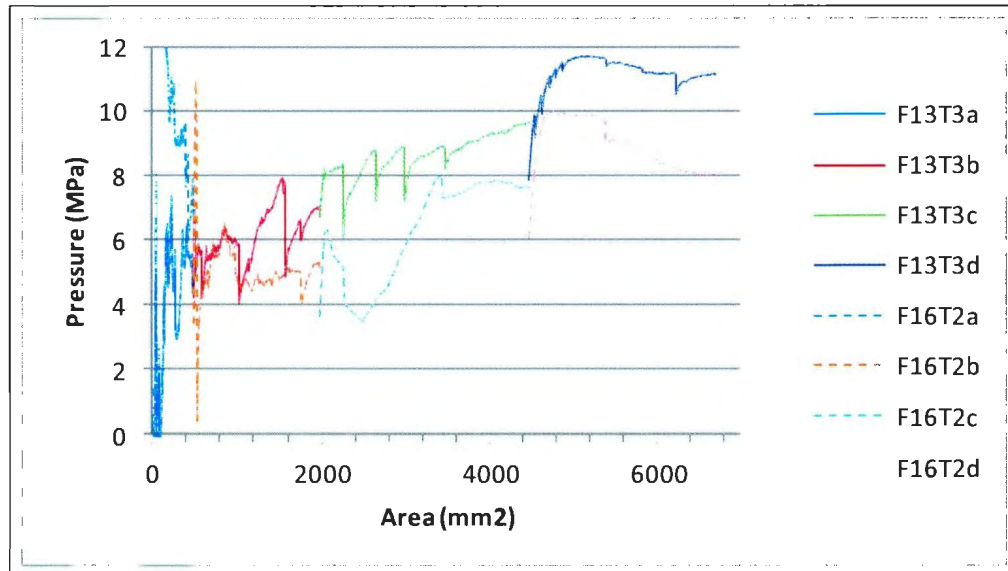


Figure 86 - *Process* Pressure-Are Curves, Treatment Combination *ad*

The predicted total loads on the contact area showed excellent correlation with the total loads detected by the MTS machine once confinement began to limit the fast spalling and cracking, much as for Treatment Combination *bd*. For F13T3a, where confinement was not yet a significant factor and the contact formed irregular geometry due to spalling, F_P differed from F_T by 175.3 % but by F13T3b the error was down to 55.4%. For F13T3c and F13T3d the error was very low, 0.4 % and 7.2 % respectively, and the pressure film became an excellent predictor of total load. This is further supporting evidence that a) confinement is an important factor to consider as it greatly affects the ice crushing process and both the associated total loads and local pressures, and b) that ice crushing is a complex process which can only be very rudely described by simple geometric forms and global considerations of pressure.

7.1.6: Treatment Combination *ac*

Treatment Combination *ac* tests were performed at -5°C , 1-5 mm grain size, 100 mm/s impact speed and 30° cone angle. From the factors involved, it can be predicted that the tests will likely involve a relatively high degree of fracturing and spalling with a low level of confinement, due to the high rate of impact and the shallow cone angle, and thus a low total load but a relatively significant percentage of HPZs in the contact surface. The tests performed at Treatment Combination *ac* were F16T1, which was performed with pressure film, and F16T3, which contained no film. The force-displacement curves for *ac* are shown in Figure 87.

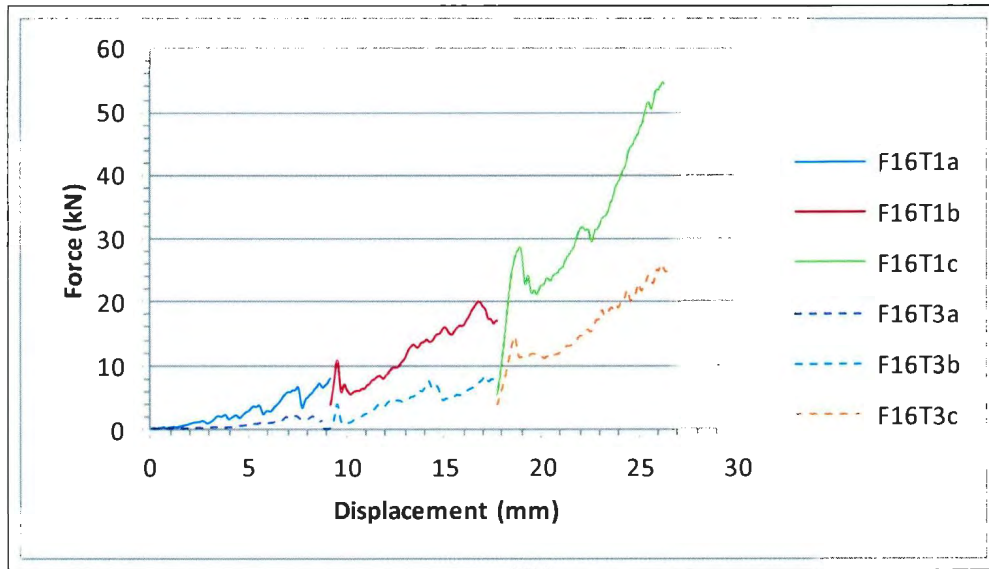


Figure 87 - Force-Displacement History, Treatment Combination *ac*

Both tests follow similar trends, except that load increases to a higher level and at a greater rate in F16T1 than F16T3. Force levels are much higher than expected, above 50 kN max, suggesting that confinement may have come into play in the interaction. The load variations occurred quickly and were small in amplitude, indicative of brittle behavior in the ice, which is expected given the colder temperature and higher impact speed.

The pressure film patterns are shown in Figure 88.

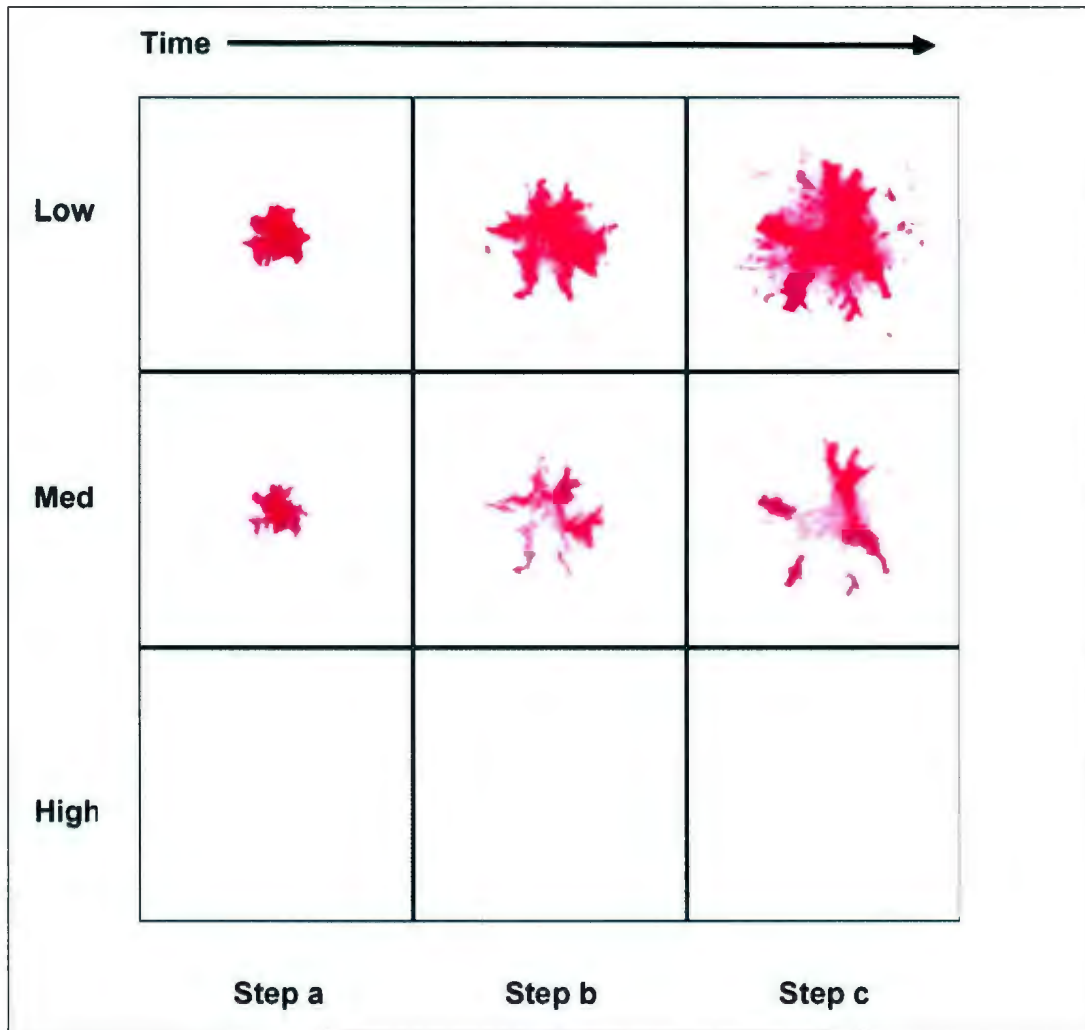


Figure 88 - Progression of Pressure Patterns, F16T1, (l-r: Step a, b, c, d; t-b: L, M, H)

The high pressure patterns are very difficult to distinguish in Figure 88, however they are present and show more clearly in the *spatial* pressure maps. What is immediately interesting about this sequence of pressure patterns, however, is that they show a combination of results from past experiments. The pressure patterns are highly variable, indicative of high levels of flaking and spalling, which was predicted. However, the very low level of high pressure patterning, and the relatively low pressures within those HPZs,

is potentially indicative of confinement as shown in previous tests and as suggested by the force-displacement curve for F16T1.

The percent errors between the actual and nominal contact areas are 41.0 %, 76.9 % and 123.9 %; the nominal contact area quickly outpaced the actual contact area in increasing area, as had been seen in other tests (eg. F1T2). If there was indeed confinement, it was not to a large degree as it did not appear to greatly limit the cracking and flaking of the ice contact surface.

The 2D and 3D *spatial* pressure maps are shown in Figure 89 and Figure 90.

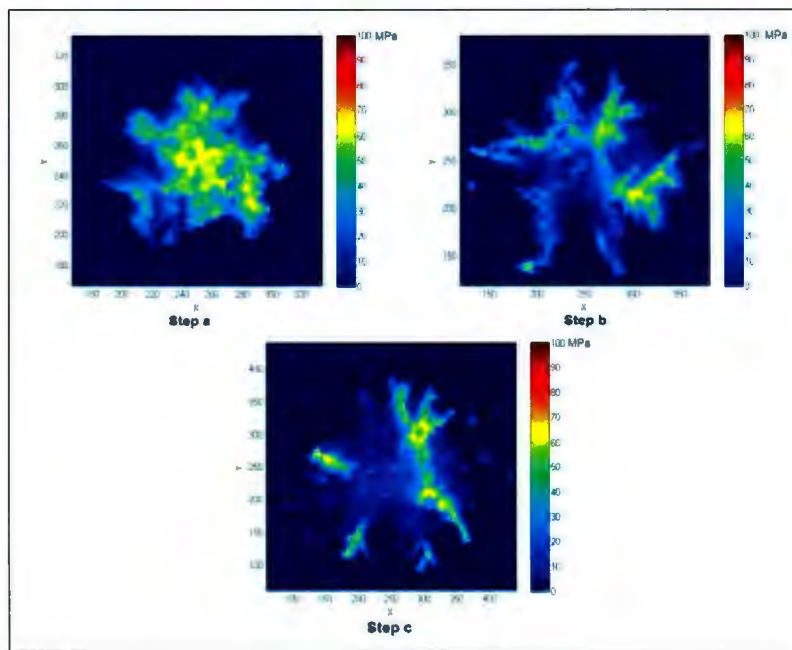


Figure 89 - 2D *Spatial* Maps, F16T1

Although the percentage of HPZs is reduced as the impact continues, they persist throughout the crushing event and the impact pattern retains the branched pattern indicative of spalling failure. Only the steep rise in load and high load-levels indicate the

potential existence of confinement as a factor. It is interesting to note that the initial pressure patterns in F16T1a are not as peaked as in previous tests, for example FIT2, with pressures reaching a plateau in the range of 60 MPa as opposed to 80 to 90 MPa.

The HPZ percentages for each test were 22.1 %, 10.5 % and 8.6 % for F16T1a, F16T1b, and F16T1c- while not high these percentages are similar to those of previous tests with low confinement and are much higher than the tests where confinement was clearly a factor. The *process* pressure-area curve will be needed to give a clearer indication of what occurred during the crushing test.

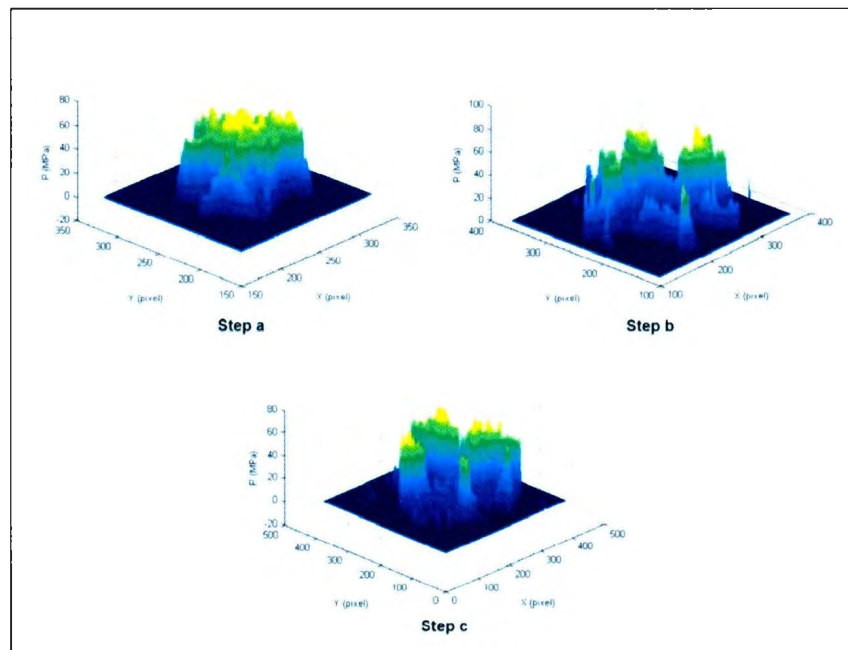


Figure 90 - 3D *Spatial* Pressure Maps, F16T1

The *spatial* and *process* Pressure-Area curves for F16T1 are shown in Figure 91. The *spatial* pressure-area curves for F16T1 appear to terminate at pressure values very close to the corresponding *process* pressure-area curve values, more so than previous

tests. F16T1a terminates at a pressure of 9.98 MPa compared 7.73 MPa on the *process* pressure-area curve, while F16T1b terminates at 7.65 MPa compared to 6.18 MPa. Even F16T1c, by roughly estimating the actual terminus pressure as occurring at the end of the *process* curve, terminates at 5.77 MPa while the roughly corresponding *process* pressure is 8.37 MPa.

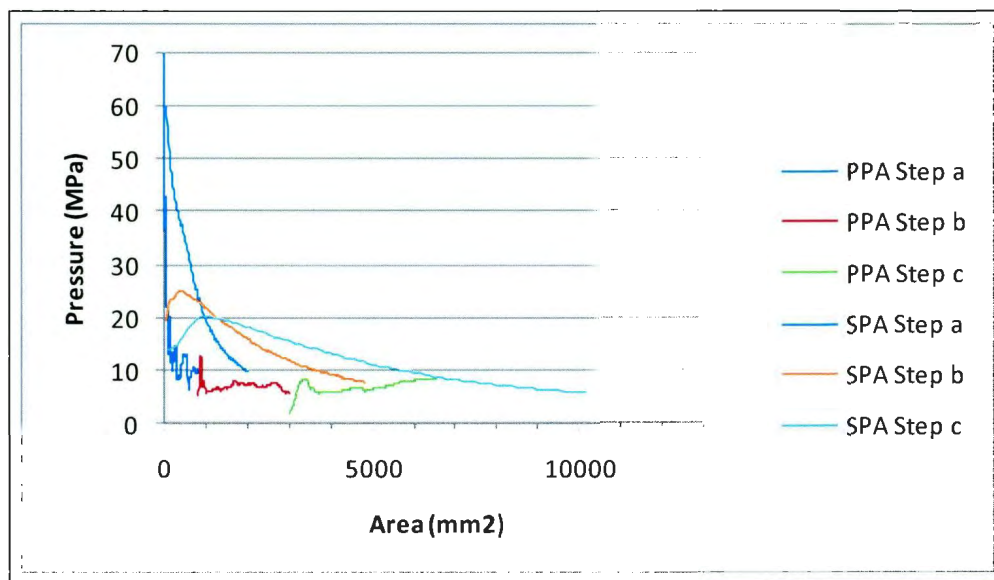


Figure 91 - *Spatial* and *Process* Pressure-Area Curves for F16T1

Recalling that the actual average pressures across the contact areas are slightly higher than those determined by the square sub-area method then F16T1c would lie even closer to *process* curve using a different method of *spatial* pressure-area curve creation which more accurately captures the exact contact area. It is interesting that this close correlation occurs in spite of the seemingly high rate of spalling and fracture that occurred, which would seemingly indicate that the error in the pressure film should be high based on

previous tests. The *process* pressure-area curves for both F16T1 and F16T3 are shown in Figure 92.

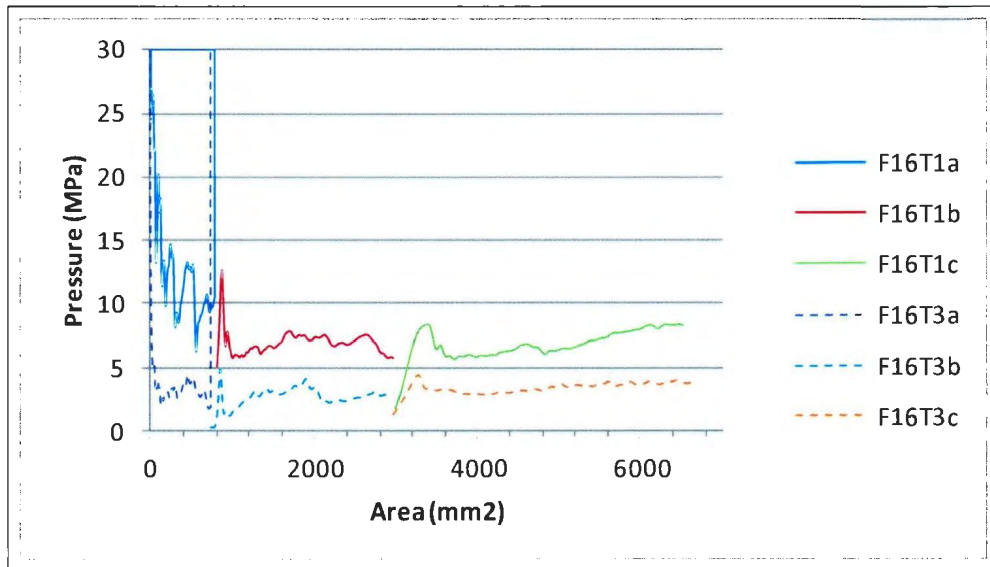


Figure 92 - *Process* Pressure-Area Curves, Treatment Combination *ac*

The *process* pressure-area curve for F16T1 does indicate some level confinement as the pressure levels out at approximately 1077 mm² before beginning to rise at approximately 4981 mm², however the confinement level does not appear to have been extreme based upon both the *process* curve and the pressure patterns. It is curious then why the load levels increased so greatly. The load of F16T1 didn't reach the close to 80 kN of say F13T1, however that previous test was performed at 1 mm/s impact speed versus 100 mm/s, so the 55 kN reached in F16T1 appears to be quite high. The reasons for the high force levels and the high rate of load increase in F16T1 are not entirely clear.

The percentage errors between F_p and F_T for F16T1 were 138.0 % for F16T1a, 117.5 % for F16T1b and a relatively low 7.6 % for F16T1c. The high errors in F16T1a

and F16T1b are to be expected because of the high level of spalling that appear to have occurred at these stages of the impact. The changes in the pressure pattern must not have been great during the final stage, perhaps due to the slight confinement that appears to have occurred, and so the history recorded by the pressure film for F16T1c is likely close to the actual final pressure pattern at the end of the test.

7.1.7: Treatment Combination abcd

Treatment Combination *abcd* tests were performed at -5°C with 5-10 mm diameter ice grains, 100 mm/s impact speed and a 50° cone angle. At high temperatures, it can be expected that the tests will exhibit higher loads due to less brittle behavior. However, the high speeds likely dominated the crushing and induced brittle behavior, enhanced by the sharper cone angle. From previous test results with 50° cone angle, it can also be expected that confinement played a role, although likely to a lesser degree than at slower impact speeds. The tests performed at this treatment combination were F20T1, performed with pressure film, and F24T2 which was performed film-free. The force-displacement curves are shown in Figure 93.

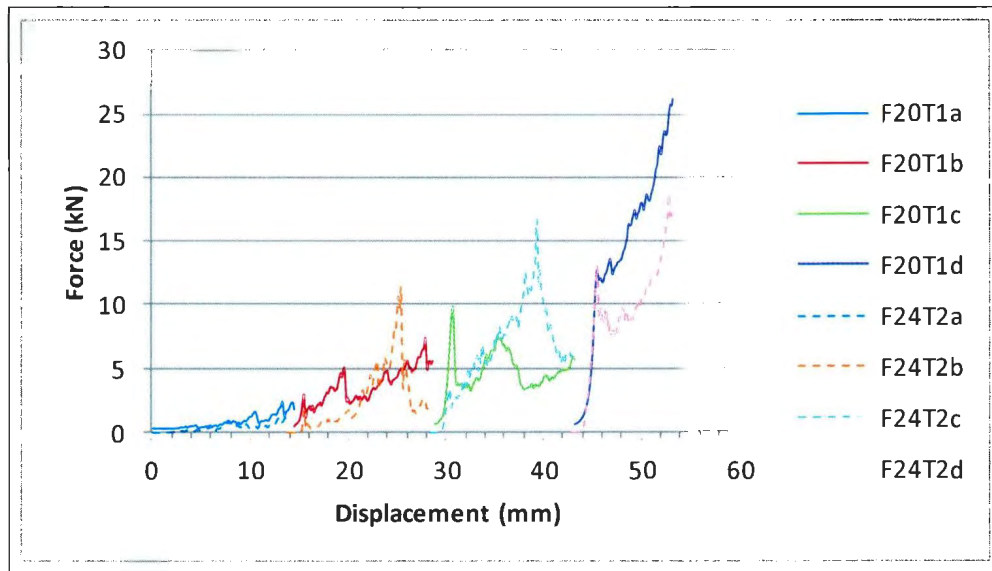


Figure 93 - Load History, Treatment Combination *abcd*

Interestingly, F24T2 shows a sequence of fairly substantially ice failure events, indicated by the force peaks at 25 mm, 40 mm and 53 mm. F20T1 does not show the same degree of spiked force history, and therefore did not likely face the same degree of relatively large-scale contact surface failure and extrusion, although there is a fairly significant force spike at approximately 30 mm crushing depth. It is unfortunate that pressure film was not used during F24T2 since fairly complex pressure patterns were likely to have occurred. The peak force of 26.22 kN in F20T1 is quite high compared to the previous 100 mm/s tests and indicates that confinement may have played a role in dictating ice failure in the latter stages of the interaction.

The pressure film patterns for F20T1 are shown in Figure 94. The pressure films show a series of highly geometrically irregular contact surfaces which fit with the prediction of high levels of flaking and cracking from the load history. By F20T1d the pressure pattern does become somewhat more circular, which may predict confinement or

more likely boundary-effects, but there is still a high degree of pressure variation across the pressure pattern which differs from previous tests with confinement effects. HPZs for this test account for 54.3 %, 29.7 %, 24.2 % and 10.9 % of the total contact area for F20T1a, F20T1b, F20T1c and F20T1d respectively. These percentages are in keeping with the results of previous tests where there was little confinement as the contact face appears to have been free to spall and fracture, thus altering the contact geometry and inducing regions of high pressure. The 2D *spatial* pressure maps are shown in Figure 95.

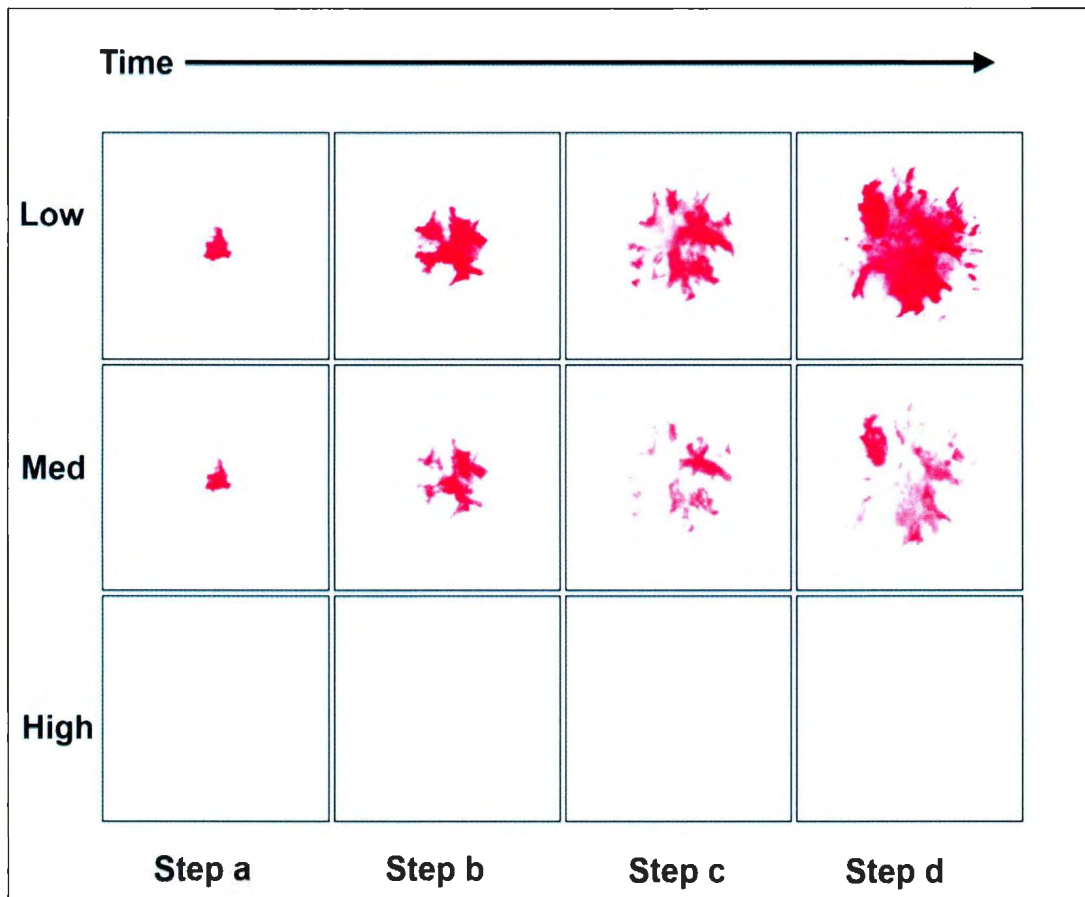


Figure 94 - Progression of Pressure Patterns, F20T1 (l-r: Step a, b, c, d; t-b: L, M, H)

What is immediately clear is that HPZs appear throughout the impact to a significant level. But what is more interesting is the appearance of the spot of high pressure in the upper left region of F20T1d. This HPZ appears to have developed from nothing, as there was hardly any pressure in this region in the preceding step. Was this due to a large entrapped piece of ice that had dislodged between steps and become trapped, or is this clear indication that localized regions of high pressure can develop anywhere across a contact face, dependant entirely upon previous fracturing and spalling behavior? 3D *spatial* pressure maps are shown in Figure 96.

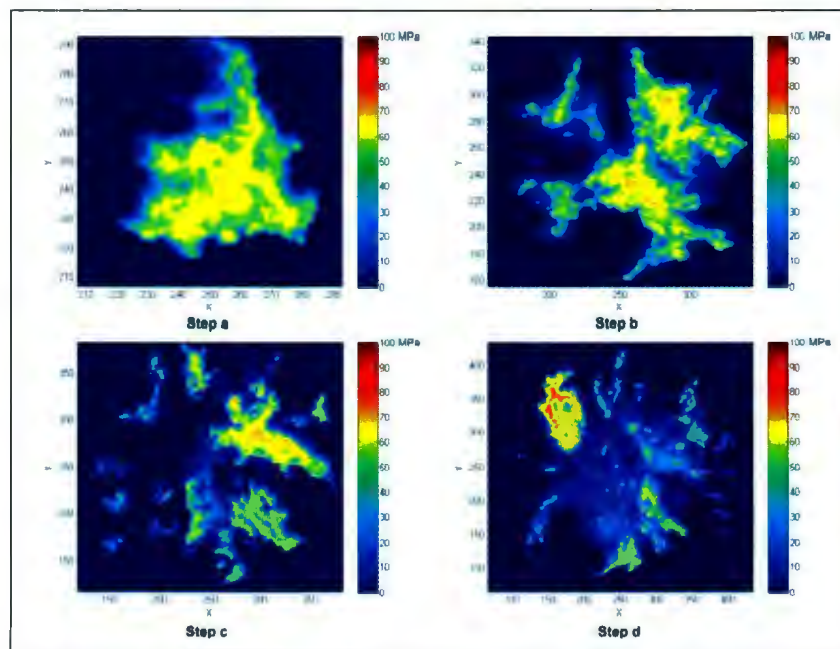


Figure 95 - 2D *Spatial* Pressure Maps, F20T1

It is very clear from these maps the removal of ice from spalling and the resulting changes to the contact area and pressures. The distinctive HPZ in F20T1d is very elegantly shown in Figure 97.

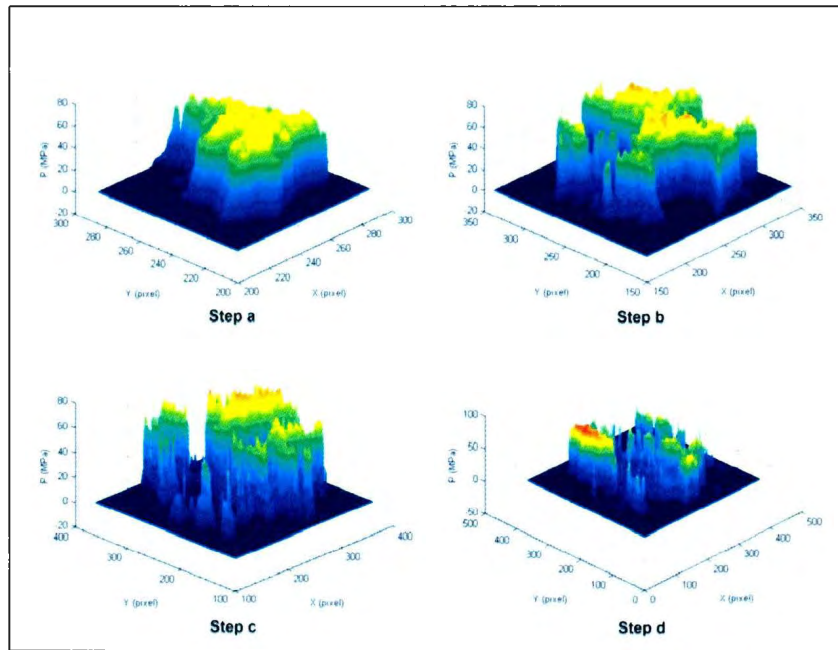


Figure 96 - 3D *Spatial* Pressure Maps, F20T1, Treatment Combo *abcd*

It is not clear if this HPZ could have been predicted from the previous pressure patterns. The fact that it appears so late in the crushing test is very intriguing and further highlights the complexities of the true contact and ice failure physics that occur during and ice-structure interaction.

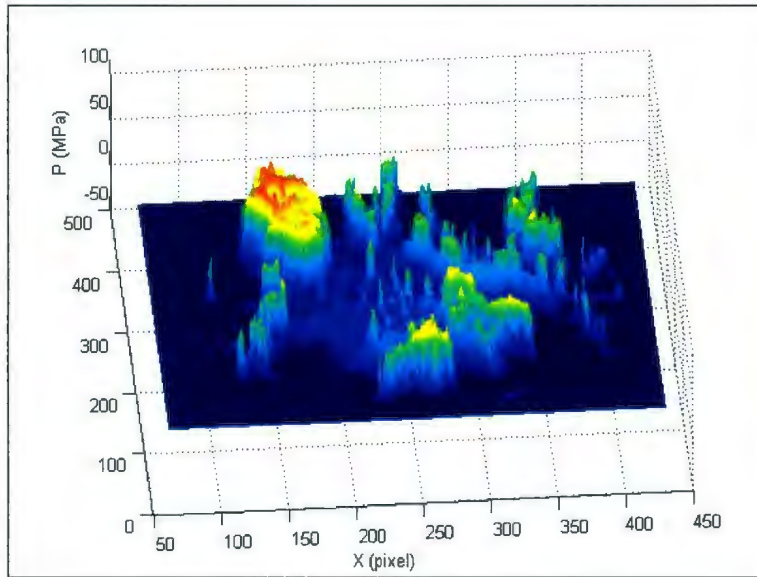


Figure 97 - Distinctive High Pressure Zone, F20T1d

The pressure-area curves for F20T1 are shown in Figure 98.

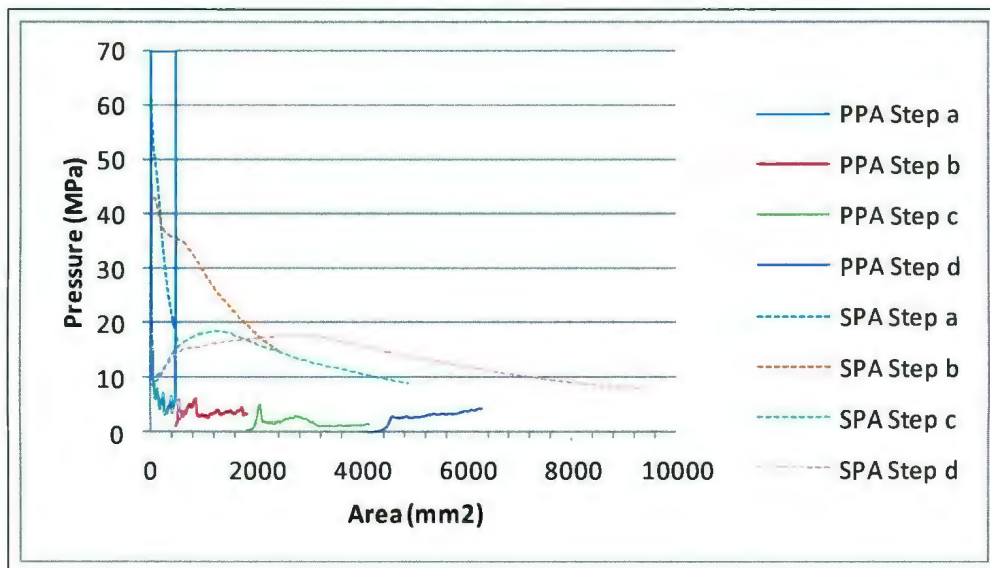


Figure 98 - Spatial and Process Pressure-Area Curves, F20T1

The *spatial* pressure-area curves clearly terminate at pressures higher than the equivalent *process* pressures, and this is indicative that the ice behavior under load was of fast spalling and flaking, greatly increasing the amount of accumulated pressure history in the pressure patterns. The *spatial* curve for F20T1a terminates at 16.88 MPa compared to 3.59 MPa at 516.62 mm² contact area, while for F20T1b the pressure was 14.80 MPa compared to 1.71 MPa, and for F20T1c 8.76 MPa and 2.79 MPa. F20T1b terminates at 7.77 MPa while the *process* curve reaches no greater pressure than 4.17 MPa in the last step of the test. It can be expected that the predicted forces will also be off as was seen in previous tests with high rates of contact area change. The *process* pressure-area curves for both tests at Treatment Combo *abcd* are shown in Figure 99 and interestingly indicate confinement at the latter stages of the interaction.

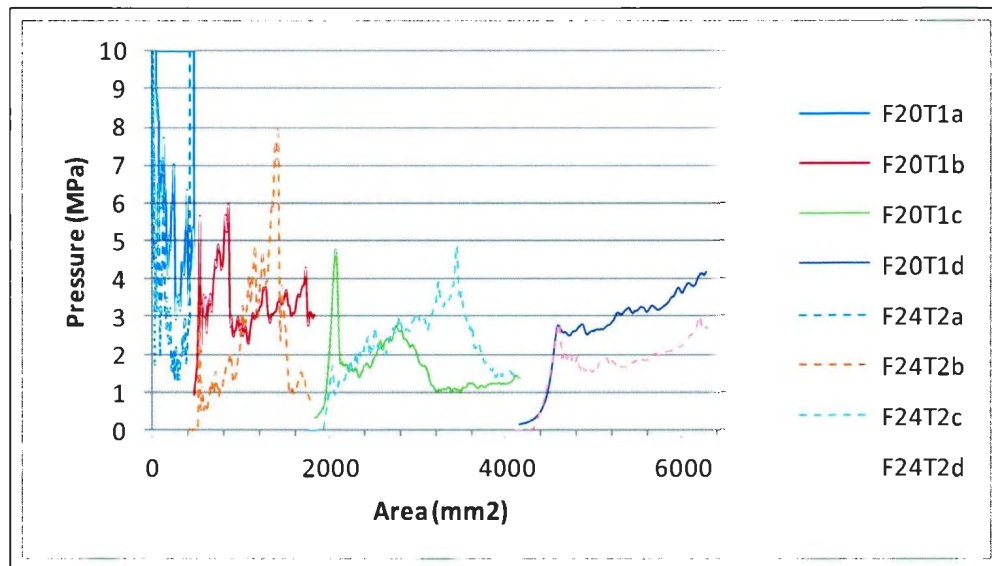


Figure 99 - Process Pressure-Area Curves, Treatment Combo *abcd*

While not severe, the upswing of pressure in Step d for both tests beginning at approximately 4000 mm^2 is indicative of confinement being a potential factor in the interactions, although likely it was artificial boundary effects caused by the circular ice holder at the latter stages of impact. This upswing could also be solely due to the HPZ that appeared in F20T1d seemingly from nowhere. F24T2 also showed some very distinctive behavior, namely large pressure spikes, which indicate that the behavior of that test was one of very small scale flaking allowing stresses to build in the sample contact face until large scale cracking and spalling occurred. It is unfortunate that pressure film was not used in this test as the results would have been extremely interesting to analyze. What is highlighted is the level of variability in repeated tests, all performed under the same conditions, with results similar overall but very different in the details. Neither *process* curve follows the general exponential decline predicted by Sanderson except as a general trend.

As discussed, given the high rate of variation in the contact areas during the tests of *abcd* and the lack of correlation between the end pressures of *spatial* curves and the *process* curves, it is to be expected that the predicted total loads on the film will not correlate well with the loads measured by the MTS machine load cell. For F20T1a the error between F_P and F_T was 375.7 %, for F20T1b it was 562.8 %, 655.9 % for F20T1c, and 178.3 % for F20T1d. These are very high errors and match, for example, those found in Treatment Combo *bc* where high rates of spalling and fracture were present. Clearly for subsequent tests, especially those at high loading rates, the time length between steps and thus between replacement of pressure films must be reduced in order to get a clearer representation of true pressure patterns at a given time in the interaction.

7.1.8: Treatment Combination *ab*

The final Treatment Combination tested was *ab*. The tests were performed at -5°C, 5-10 mm ice grain diameter, impact speed of 1 mm/s and a cone angle of 30°. The tests performed under this set of factors were F20T2, which was performed with pressure film, and F20T3, which was not. The high temperature and slow impact speed indicate that loads should be relatively high and spalling and fracturing relatively limited, while confinement may also be a factor, although the highest confinement effects were seen with the 50° cones. The force-displacement curves for *ab* are shown in Figure 100.

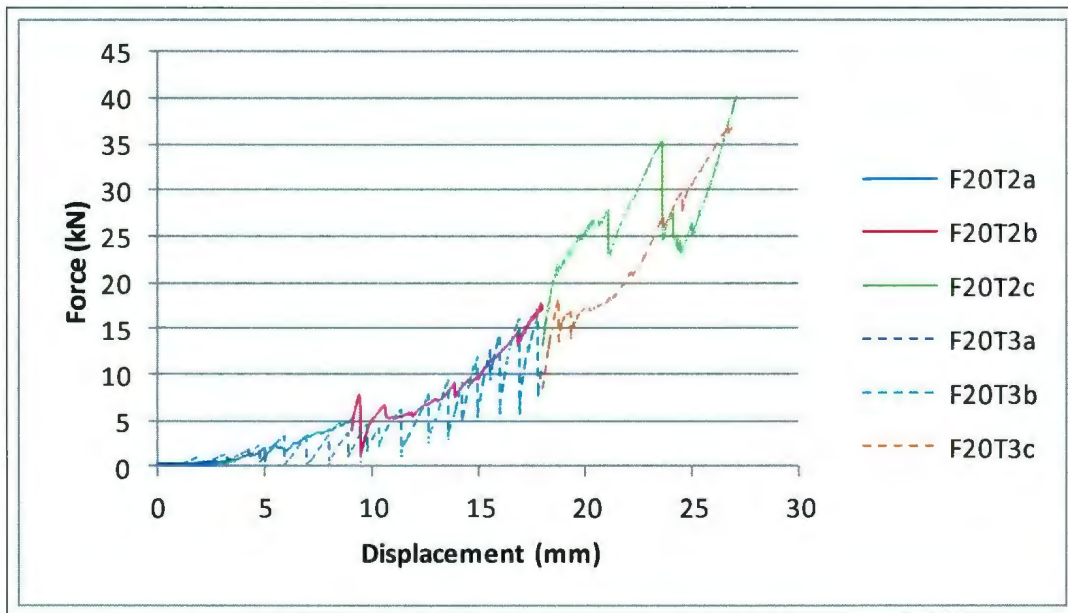


Figure 100 - Force-Displacement Curves, Treatment Combo *ab*

Both tests show a similar trend of exponentially increasing force to a maximum of 40.2 kN and 37.1 kN in F20T2 and F20T3 respectively. These loads are on the same order as those detected in previous tests such as Treatment Combo (1). However, beyond the

overall trend each test displayed very different behavior from each other. F20T2 followed a sawtoothed pattern of very small amplitude pressure drops, indicating very small fractures occurring at the contact surface at a high rate but no major fracturing events. The force-displacement curve for F20T2a to F20T2b is highlighted in Figure 101 and shows clearly the very small amplitude load oscillations.

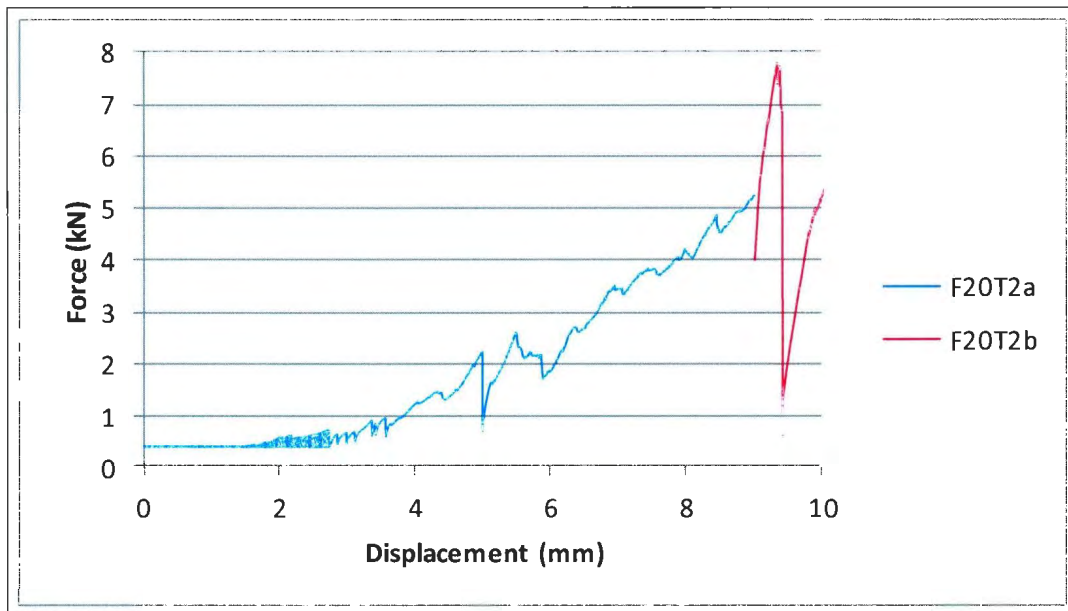


Figure 101 - Force-Displacement for F20T2a and F20T2b

During the entire crushing event of F20T2 there were two relatively substantial load drops at first at approximately 9.4 mm and again at 23 mm crushing depth which is indicative of fracture and extrusion of a relatively substantial piece of ice from the contact face. By contrast, F20T3 followed a sawtoothed pattern of fairly substantial, and exponentially increasing in amplitude, load drops up to 19 mm depth, at which point the load variations drop off almost completely while the load itself continues to rise. Since the load continued rising, it is evident that some form of confinement was occurring to

prevent cracks from travelling to a free edge and forming a spall. This could have been due to extruded ice confinement or due to boundary effects from the ice holder, or a combination of both. Unfortunately, without the pressure film one can only conjecture as to what occurred.

The pressure film patterns for F20T2 are shown in Figure 102.

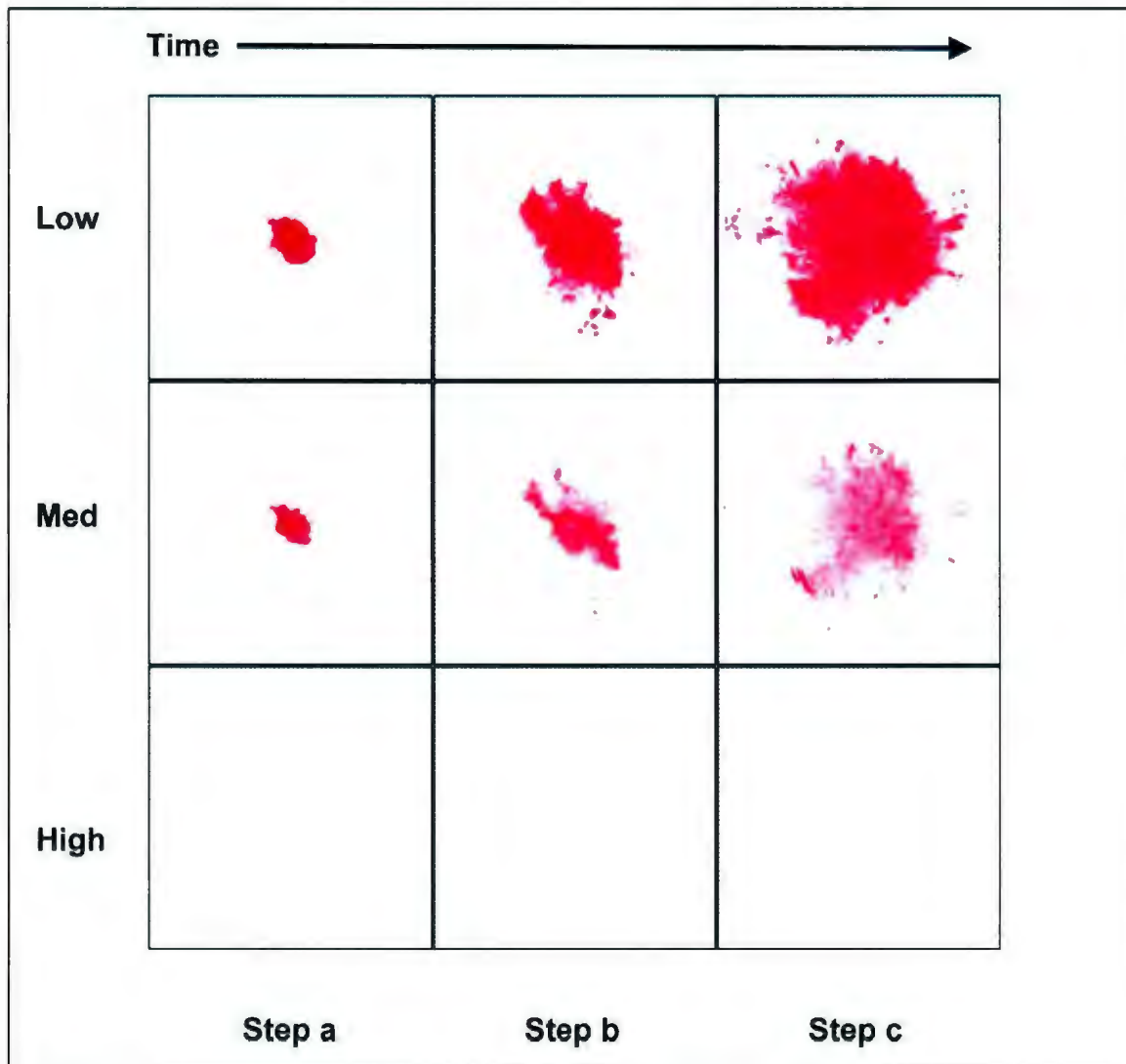


Figure 102 - Progression of Pressure Patterns, F20T2 (l-4: Step a, b, c; t-b: L, M, H)

The progression of pressure patterns shows an increase in pressure pattern area from step to step, but no great alteration to the shape, which would have been indicative of fracturing and spalling. The pressure patterns tell much the same tale as the load history: that the ice surface did not undergo great levels of fracturing and that loads were allowed to build with only the two relatively substantial spalling events during the impact. What is very clear from the pressure patterns of F20T2 is that the contact area appears to greatly increase from F20T2b to F20T2c. At the same time, it was during F20T2c that the most significant spalling event occurred in the load history. The possible sequence of events is that load built up in the sample and no major cracks grew to the surface of the ice, which would have resulted in spalling, and that all changes in contact area were due to small scale flaking. During F20T2c, however, a crack (or sequence of cracks) was able to reach a free surface causing a large amount of ice extrusion which was then trapped in the at that point small space between plate and ice, therefore being crushing and confined and ultimately becoming part of the ice pressure pattern.

The actual contact areas of the pressure patterns varied from the nominal contact areas for F20T2a, F20T2b and F20T2c by 121.9 %, 79.1 %, and 43.8 %. While still high, these errors are similar to the errors seen in tests with high confinement and low spalling, indicating that in some way fracture and extrusion was indeed being limited.

The 2D *spatial* pressure maps for F20T2 are shown in Figure 103.

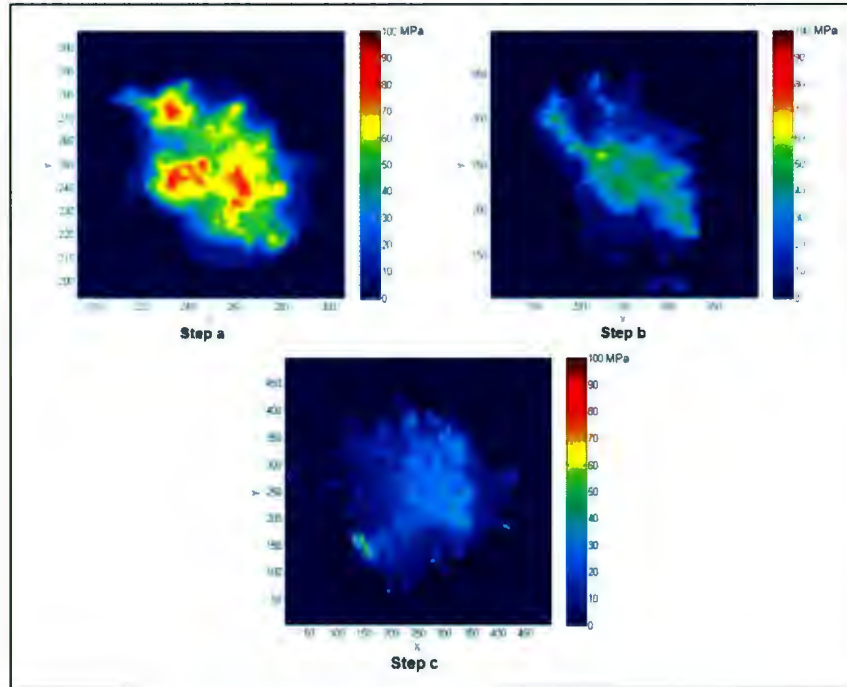


Figure 103 - 2D *Spatial* Pressure Maps, F20T2

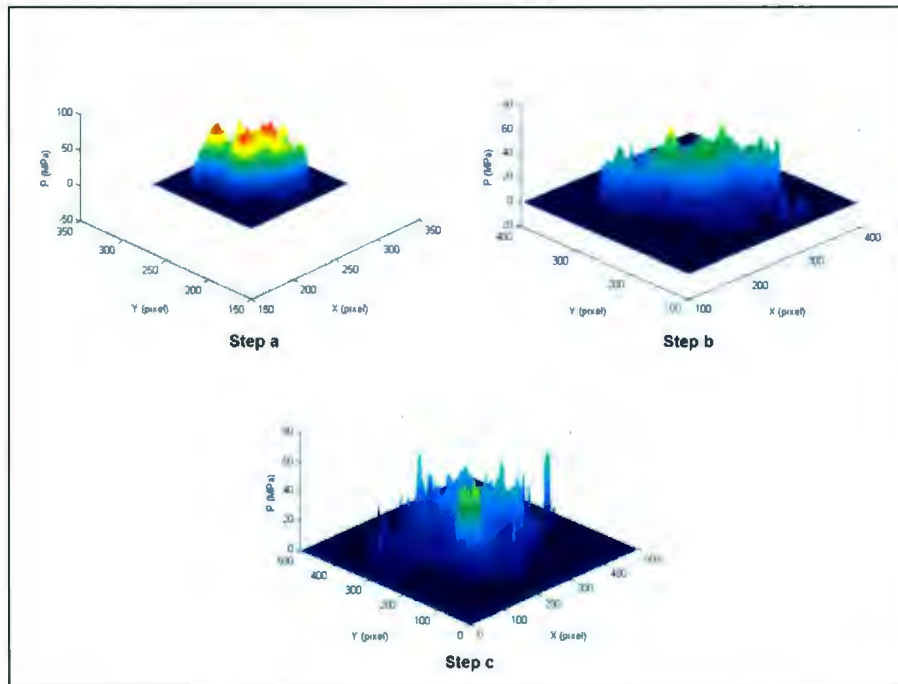


Figure 104 - 3D *Spatial* Pressure Maps, F20T2

There is a definite reduction in High Pressure zones from F20T2a to F20T2b to F20T2c but without the extreme alteration of the contact area; as previously discussed, the contact area appears to be built upon without pieces being removed due to spalling. The 3D *spatial* pressure maps are shown in Figure 104.

The number of high pressure regions is clearly reduced as the process continues, becoming very localized to tiny regions in the last stage of the impact. The HPZs account for 23.9 %, 1.8 % and 0.5 % of the total contact area in F20T2a, F20T2b and F20T2c. The low percentage of HPZs in F20T2b and F20T2c indicate that confinement may indeed have been a major factor in the experiment, or else some other form of driving behavior was in existence to limit spalling and subsequent alteration of the contact surface.

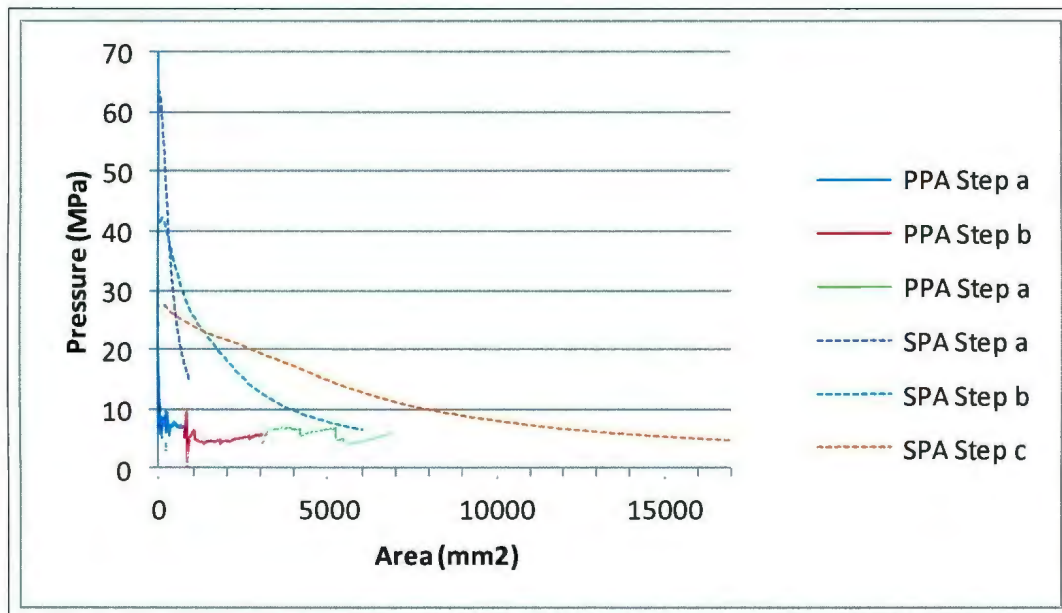


Figure 105 - *Spatial* and *Process* Pressure-Area Curves, F20T2

The *spatial* pressure-area curve for F20T2a shown in Figure 105 does not come very close to the *process* curve, dropping to only 15.21 MPa while the process pressure at that area is 4.96 MPa. The subsequent steps are closer, however, with F20T2b dropping to 6.59 MPa compared to 4.56 MPa on the *process* curve, while the final step, F20T2c, can be compared to the final pressure of the *pressure* curve: 4.79 MPa compared to 5.84 MPa. The reason for the close correlation of F20T2b is not entirely clear, as the pressure film area did not greatly match the nominal contact area, although it was relatively closer than in other tests with high rates of spalling. For F20T2c the close correlation between the terminal *spatial* pressure and the *process* curve is likely due to a combination of the large spall at 23 mm being entrapped and overall boundary effects from the ice holder. If the ice was fractured and then trapped, rather than extruded, then the pressure film of F20T2c does indeed indicate more of the active area rather than the activated area.

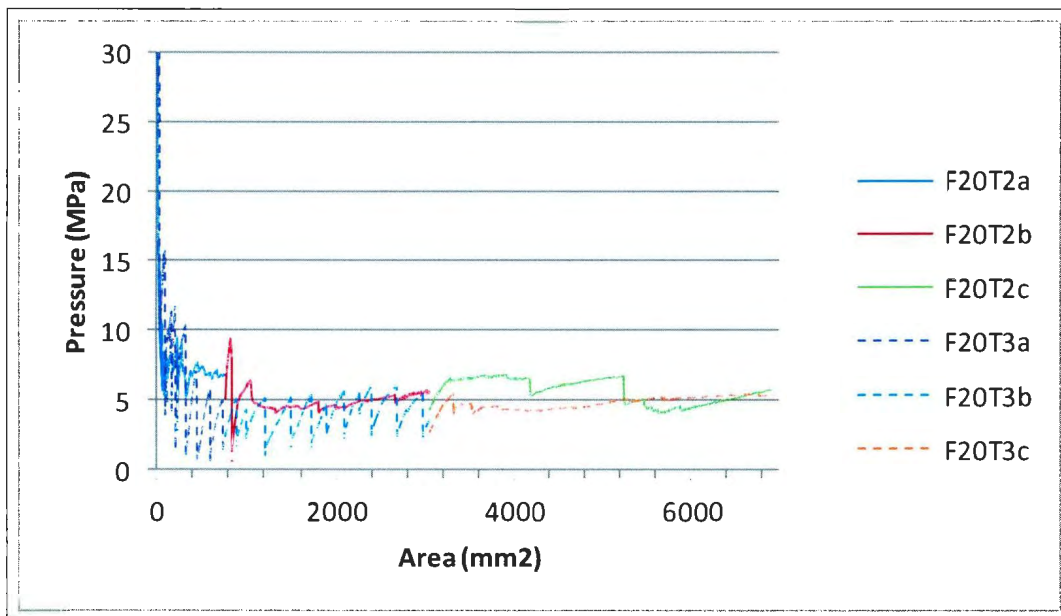


Figure 106 - *Process* Pressure-Area Curves, Treatment Combo *ab*

The *process* curves for both tests confirm a level of confinement marked by the upswings in pressure at approximately 1200 mm². The pressure plateau and drop in the *process* curve of F20T2 during F20T2c marks the spalling event. The continuing rise in pressure past 6000 mm² contact area may mark the point where the spalled ice was trapped and pressed against the pressure film.

The errors between F_P and F_T for F20T2 were 167.8 %, 134.2 %, and 104.3 % for F20T2a, F20T2b and F20T2c respectively. The errors are fairly large, more in line with the high-spalling tests than those with confinement, contradicting the suggestion that the recorded history at F20T1c is low.

Treatment Combination *ab* proved to be a very complicated set of experiments, challenging the findings from the previous tests and definitely challenging, as all of the tests have done, the widely held notions about ice interactions and ice failure processes.

7.2: Data Tables

In Section 6.1 numerous values were calculated for each test. These included the actual and nominal contact areas at the end of each step, the percentage of contact area at high pressure for each step, the correlation between the terminal pressures of each *spatial* pressure-area curve and the corresponding pressure of the *process* pressure-area curve, and both the maximum load predicted by the pressure film and the actual maximum load measured by the load cell on the MTS machine. These values and the percentage error between them are collected in this section in Table 9 to Table 12.

The percentage errors calculated in Table 9 clearly show the discrepancies between actual and nominal contact area. In the initial steps of interaction the actual contact area varied from the nominal contact area by upwards of 200 %. In subsequent steps, the difference either increased or decreased. As was discussed in Section 6.1, the treatment combinations which likely saw the highest level of confinement saw the largest drop in area discrepancy; this is to be expected, since the circular holder imposes a circular shape under confinement and the diameter of the ice inside the cylinder is the nominal contact area at full penetration. Treatment combinations *bd*, *ad* and *ab* appeared to show the highest level of confinement based upon their pressure patterns and showed decreases in percent error of nominal contact area down to as low as 30.9 %. The treatment combinations that showed significant variations between nominal and actual contact area, however, such as *bc* and *cd*, are much more interesting. The pressure patterns did not appear to indicate boundary effects of the ice holder being a major influence on the formation of pressure patterns and on cracking and extrusion. The

differences between nominal and actual pressure throughout the entire crushing event of these tests strongly supports the notion that assumed simple geometries for contact patterns may not be valid in all but very specific cases.

Table 9: Comparison of Nominal Contact Area to Actual Contact Area

Test No.	Factor Combo	Step	Actual Area (mm ²)	Nominal Area (mm ²)	% Difference
F1T2	(1)	a	460.0	765.9	66.5
		b	2094.5	3059.5	46.1
		c	2906.3	6879.4	136.7
F24T1	bc	a	237.3	713.6	200.7
		b	1080.0	2900.8	168.6
		c	1620.9	6464.0	298.8
F13T1	bd	a	230.1	498.9	116.9
		b	1063.9	1993.2	87.3
		c	2771.3	4483.0	61.8
		d	5116.0	6696.1	30.9
F13T2	cd	a	191.9	456.7	138
		b	826.4	1880.4	127.5
		c	1386.0	4238.6	205.8
		d	2022.8	6328.2	212.8
F13T3	ad	a	190.2	498.8	162.2
		b	1279.8	1993.2	55.7
		c	3228.2	4483.2	38.9
		d	4928.1	6695.7	35.9
F16T1	ac	a	566.3	798.3	41
		b	1679.9	2972.4	76.9
		c	2910.0	6516.1	123.9
F20T1	abcd	a	187.6	464.8	147.8
		b	963.9	1828.9	89.7
		c	1462.0	4148.6	183.8
		d	3326.9	6284.3	88.9
F20T2	ab	a	345.3	766.2	121.9
		b	1708.1	3059.8	79.1
		c	4786.6	6881.1	43.8

Table 10: Percentage of Total Area Occupied by High Pressure Zones

Test No.	Factor Com bo	Step	Actual Area (mm ²)	HPZ Area (mm ²)	% of Actual Area
F1T2	(1)	a	460.0	138.1	30.0
		b	2094.5	175.5	8.4
		c	2906.3	72.9	2.5
F24T1	bc	a	237.3	139.7	58.9
		b	1080.0	364.0	33.7
		c	1620.9	163.1	10.1
F13T1	bd	a	230.1	50.6	22.0
		b	1063.9	18.3	1.7
		c	2771.3	4.4	0.2
		d	5116.0	1.5	0.0
F13T2	cd	a	191.9	46.1	24.0
		b	826.4	285.4	34.5
		c	1386.0	203.2	14.7
		d	2022.8	41.2	2.0
F13T3	ad	a	190.2	34.8	18.3
		b	1279.8	16.5	1.0
		c	3228.2	0.0	0.0
		d	4928.1	0.0	0.0
F16T1	ac	a	566.3	124.9	22.1
		b	1679.9	177.2	10.5
		c	2910.0	251.3	8.6
F20T1	abcd	a	187.6	101.9	54.3
		b	963.9	286.0	29.7
		c	1462.0	353.9	24.2
		d	3326.9	362.9	10.9
F20T2	ab	a	345.3	82.5	23.9
		b	1708.1	30.0	1.8
		c	4786.6	22.1	0.5

The percentage of HPZs in the contact face appeared to be inversely correlated to confinement or boundary effects. As was discussed in Section 6.1 when ice breaks free of the contact face while under load, the remaining contact area suddenly decreases. The load drops but immediately begins to increase again. There is an immediate increase in pressure, as discussed by Gagnon [8], since the entirety of the load is immediately transferred to the now reduced contact area. Although the pressures and loads then drop

before subsequently rising again, the pressure films will record that pressure spike caused by fracture and extrusion and carry that activated area throughout the crushing step. The percentage of HPZs present during a crushing step gives an indication as to the level of fracturing and spalling. The tests which featured irregular shapes, caused by fracturing and extrusion, showed the highest percentages of HPZs throughout the tests, such as F20T1. As a contrast, the tests which seemed to be dominated by a combination of ice confinement, perhaps due to ice build-up during slow impact speed and a steep cone angle, and boundary-effects due to entrapment by the steel ice holder, typically showed the lowest levels of HPZs, such as F13T1. In these tests, the macrocracking throughout the sample leading to flaking and extrusion was suppressed through some mechanism during the impact.

The terminal points of the *spatial* curves, listed in Table 11 rarely matched the *process* curves as predicted by Daley [10] and as predicted by theory, but this is primarily a causation of the history recording nature of the pressure films. In order to improve the analysis of the interrelationship between *spatial* and *process* pressure-area curves using the pressure films an improved test design with more crushing steps, each covering as small of a distance as possible, is required.

Table 11: Correlation between SPA Curve End Pressures and PPA Pressures

Test No.	Factor Combo	Step	SPA End P (MPa)	PPA P (MPa)	Nominal Area (mm ²)
F1T2	(1)	a	11.77	4.99	1659.8
		b	14.71	2.06	4031.2
		c	4.81	/	11197.9
F28T1	bc	a	21.6	4.4	699.9
		b	13.7	3.2	3449.2
		c	3.8	/	8671.6
F13T1	bd	a	17.31	2.66	517.6
		b	4.78	8.01	4374.2
		c	5.26	/	7529.5
		d	5.07	/	13672.9
F13T2	cd	a	12.94	1.013	566.9
		b	16.86	1.78	2267.6
		c	8.11	2.05	4586.7
		d	2.44	/	10103.1
F13T3	ad	a	8.35	5.61	728.1
		b	5.72	8.97	3702.3
		c	3.98	/	10754.5
		d	5.86	/	11764.8
F16T1	ac	a	9.98	7.33	1975.3
		b	7.65	6.18	4804.2
		c	5.77	/	10106.1
F20T1	abcd	a	16.88	3.59	517.6
		b	14.8	1.71	2473.6
		c	8.76	2.79	4877.8
		d	7.66	/	9477.9
F20T2	ab	a	15.21	4.96	909.6
		b	6.59	4.56	6049.4
		c	4.79	/	17079.3

Table 12: Comparison of Predicted and Measured Maximum Load

Test No.	Factor Combo	Step	FP	FT	% Error
F1T2	(1)	a	19.54	2.86	583.2
		b	59.30	26.78	121.4
		c	53.92	14.02	284.6
F24T1	bc	a	15.40	3.42	350.3
		b	47.67	10.81	341
		c	33.23	8.94	271.7
F13T1	bd	a	9.17	2.25	307.6
		b	21.07	12.84	64.1
		c	39.87	34.24	16.4
		d	69.58	77.66	10.4
F13T2	cd	a	7.52	0.32	2276.5
		b	38.66	5.75	572.2
		c	37.55	8.44	344.8
		d	24.78	10.93	126.8
F13T3	ad	a	6.20	2.25	175.3
		b	21.39	13.77	55.4
		c	43.08	43.24	0.4
		d	69.33	74.74	7.2
F16T1	ac	a	19.95	8.38	138
		b	37.11	17.06	117.5
		c	58.68	54.52	7.6
F20T1	abcd	a	8.94	1.88	375.7
		b	37.02	5.59	562.8
		c	43.06	5.70	655.9
		d	72.98	26.22	178.3
F20T2	ab	a	14.08	5.53	167.8
		b	40.40	17.25	134.2
		c	82.13	40.20	104.3

The correlation between MTS load cell-predicted max load and pressure film predicted max load appears to match the level of confinement and therefore level of activated area. As has been discussed, the more confinement in the test (and especially the higher the degree of influence from the ice holder), the lower the level of fracturing and extrusion, and therefore the lower the level of activated area accrual. F13T1 is a primary example of

this: the error between F_p and F_T became lower as the impact became more circular and the amount of HPZs decreased. After F13T1a the error was 308%, a number in line with previous tests. However, during F13T1b the error had reduced to 64%, by F13T1c it is was down to 16% and by F13T1d, where the contact area most closely approximated the nominal contact area and the % of HPZs was minimal, the error in max force predictions was down to only 10%. This indicates that the change in pressure patterns across the contact face over the course of F13T1b, F13T1c and especially F13T1d, where confinement was present and fracture and extrusion was reduced, was minimal and therefore the negative effects of the pressure films history recording was minimal. By comparison, F20T1 maintained high levels of HPZs and very irregular crushing patterns, indicating low level of confinement and high rate of fracturing, and the correlation between F_p and F_T was off with as much as 655.9% error.

The low level of correlation between load cell and the pressure film-predicted loads, and between the *spatial* and *process* curves, is not necessarily indicative of failure in the test plan or of the pressure-sensing film. What it does indicate is that a) the test design needs to be refined to fit the limitations of the pressure film, but more importantly b) that ice crushing is incredibly complex and is an interrelated system where speed, entrapment, temperature and geometry all play a role.

7.3 Curve Fitting

As was discussed in Chapter 2 many ice researchers have attempted curve fitting of pressure-area curves. A standard equation used by many is of the form:

$$P = P_0 A^c \quad [10]$$

Frederking [9] reported values of 2.35 and 3.46 for P_0 for the Louis St. Laurent and the Oden icebreakers, and -0.42 and -0.51 for c . It is therefore of interest to determine what the parameters c and P_0 are for the *spatial* and *process* curves developed during these tests using the pressure films, keeping in mind that the history-accumulating effects of the pressure film will affect the *spatial* plots and therefore the resulting parameters.

An example of curve fitting the *spatial* curve of F1T2b is given in Figure 107. Curve fitting was performed by firstly excluding initial data that did not follow an exponentially decreasing trend, for example the plateau beginning at approximately 300 mm² contact area, and then plotting the \log_{10} of both area and pressure. A linear curve plotted to this data of the form $y = mx + b$ will therefore result in an equation of the form [Eq. 9] where $P_0 = 10^b$ and $c = m$. The parameters for F1T2b were found to be 0.72 for P_0 and -0.57 for c .

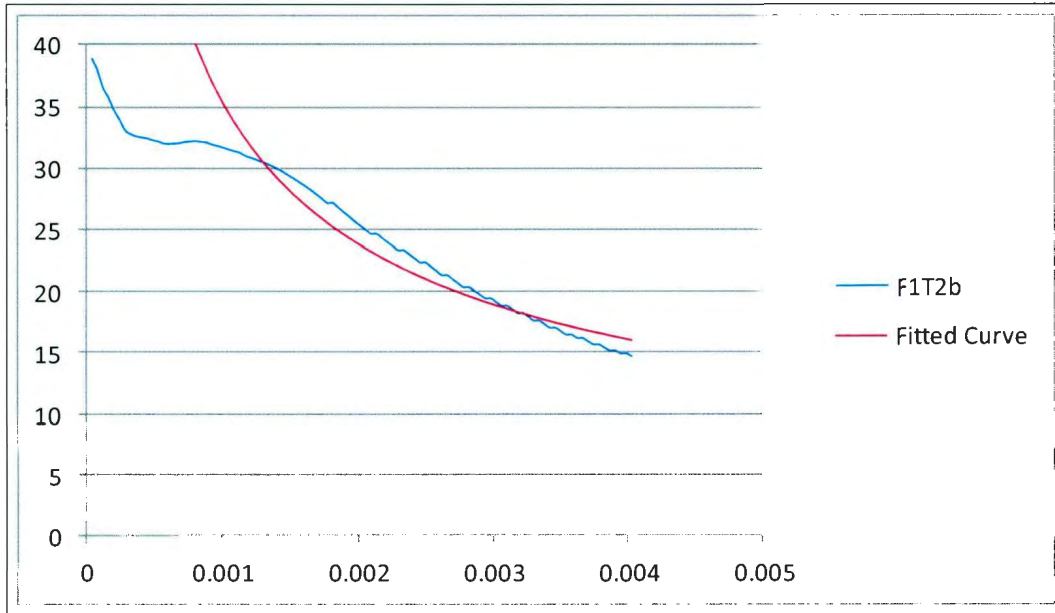


Figure 107 - Curve Fitting F1T2b

The rest of the pressure-area curves were fitted using the same method. The parameters for each spatial pressure-area curve are gathered in Table 13 . The values of c fall within the range of -0.24 to -0.80, with an average value of -0.52 which is in keeping with the results obtained by other researchers. The values of P_o fall within the range of 0.11 to 3.25 with an average value of 0.72. These values are typically quite below the values reported by other ice researchers, and this is likely due to the pressure history-recording nature of the pressure films.

It was not quite as straightforward to fit the *process* pressure-area data as it is the *spatial* pressure-area data. Typically, the *process* curves follow highly oscillating paths with only a very generally exponentially decreasing trend. Therefore, it was decided to plot a pressure ‘envelope’, similar to that done by Sanderson [22]. The envelope was found by plotting the \log_{10} of pressure and area and then finding the straight line which represents the ceiling of the data. This is shown for F1T2 in Figure 108.

Table 13: Curve Fitting Parameters, $P = PoA^c$, Spatial Curves

Test	Po	c
F1T2a	0.45	-0.54
F1T2b	0.72	-0.57
F1T2c	0.58	-0.50
F13T1a	0.21	-0.60
F13T1b	0.11	-0.71
F13T1c	1.02	-0.39
F13T1d	0.91	-0.46
F13T2a	0.72	-0.42
F13T2b	2.04	-0.39
F13T2c	0.23	-0.68
F13T2d	0.22	-0.56
F13T3a	0.16	-0.57
F13T3b	0.71	-0.42
F13T3c	0.24	-0.65
F13T3d	1.08	-0.44
F16T1a	0.47	-0.53
F16T1b	0.44	-0.56
F16T1c	0.28	-0.68
F20T1a	1.25	-0.38
F20T1b	3.25	-0.30
F20T1c	0.36	-0.61
F20T1d	0.20	-0.80
F20T2a	0.44	-0.54
F20T2b	0.37	-0.60
F20T2c	0.72	-0.53
F28T1a	0.84	-0.48
F28T1b	0.83	-0.52
F28T1c	1.45	-0.24

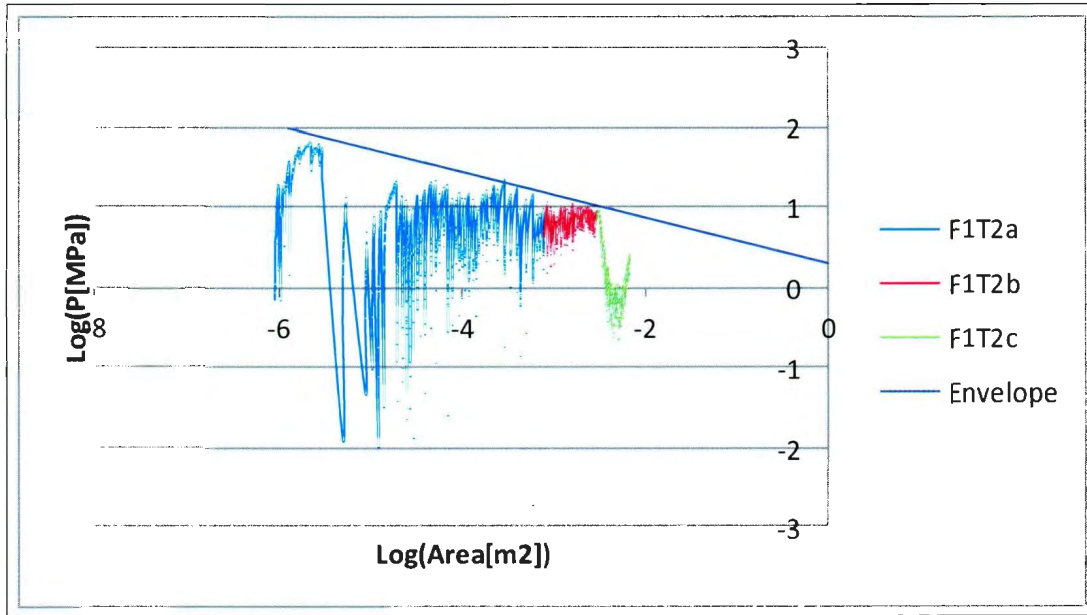


Figure 108 - Curve Fitting 'Envelope', F1T2

Converting the slope and y-intercept of the envelope equation in the same method as described above results in a P_0 of 2.00 and a c of -0.29. The parameters for each *process* pressure-area curve are gathered in Table 14

Table 14: Curve Fitting Parameters, $P = P_0 A^c$, Process Curves

Test	P_0	c
F1T2	2.00	-0.29
F1T3	5.01	-0.09
F13T1	10.00	-0.05
F13T2	0.10	-0.60
F13T3	15.85	0.05
F16T1	0.50	-0.56
F16T2	0.25	-0.76
F16T3	0.20	-0.61
F20T1	0.16	-0.69
F20T2	0.13	-0.81
F20T3	0.13	-0.79
F24T2	0.50	-0.45
F28T1	0.32	-0.49

It is interesting to note that F13T3 has c parameter with a positive value. This test indicated a high degree of confinement and boundary-effects during the collision as could be seen in Figure 73. For the *process* pressure-area curves, the enveloping curve parameters had a high value of 15.85 for P_o and 0.05 for c , both from F13T3, and a minimum value of 0.10 and -0.81 for P_o and c , respectively. The average values were 2.70 and -0.47. The averages are in keeping with those numbers found by other ice researchers and the differences may be attributed the inevitable differences between laboratory ice, however carefully grown, and natural ice and, more significantly, the boundary-effects likely induced by the ice holders.

8. Conclusions and Recommendations

The purpose of this study was to determine how to properly adapt pressure-sensing chemical films for use in ice-crushing experiments, and then to use the films in a series of uniaxial steel-ice impact experiments under a range of factors in order to obtain a clearer picture of the presence and temporal evolution of spatial pressure variations across the ice-steel contact surface. The films were successfully adapted for use in cold environments and a method for in-house analysis of the films post-test was developed. Ice was successfully grown in the lab and shaped into reproducible geometries, and a test plan involving a range of factors including ice grain size, impact speed, atmospheric temperature and ice geometry was implemented. From the resulting force data and pressure film patterns, 2D and 3D spatial pressure maps were created and a method for developing spatial pressure-area curves as an expanding set of square areas across the pressure patterns was developed. From the resulting process and spatial pressure-area curves and force-time histories, the link between spatial and process pressure-area curves was investigated as well as the changing percentages of high pressure zones across the contact area, the correlation between the actual contact area and the nominal contact area, and the ability for the pressure films to predict the maximum load incurred by the system during the collision. Curves were fitted to both the spatial and process pressure-area curves to determine the correlation with previous ice research.

Based on the results of the study, the following conclusions can be made:

1. The pressure-sensing chemical film can be adapted for use in investigating ice-structure interactions, however they have several restrictions. Firstly, the conversion curves from colour density to pressure must be adapted for the specific working environment. Secondly, the films record a pressure-history and not an instantaneous pressure, thus in order to reduce the error from spurious data the ice must be crushed in steps with the film replaced at each step. The shorter the step, the lower the error from accrued pressure history. Thirdly, a method of securing the alignment of the films during the test must be developed so that proper alignment during film analysis can be ensured.
2. Ice does not crush in simple geometric patterns, as is assumed in current design codes. Ice patterns are complex and chaotic, determined primarily by cracking, flaking and extrusion processes.
3. Ice pressures vary greatly across the contact surface and, in regions as small as 500 mm^2 can reach pressure of up to 90 MPa or higher.
4. Confinement appears to greatly alter the mechanics of ice cracking and spalling, and as a result greatly affects the pressure patterns, the overall contact geometry, and the percentage of high pressure zones in the contact face. Boundary-effects from the ice holder appeared to dominate confinement at slow speed and steeper cone angles, but it is not hard to imagine similar confinement occurring in the field due to structure geometry or even ice-pack geometry. This is an issue that necessitates further investigation.

5. Assumptions of nominal geometry do not appear to accurately model actual contact patterns and ignoring spatial pressure patterns in favour of global average pressures may exclude important information. Given the risks associated with operations in the arctic offshore, and the significantly higher load levels experienced in the field, these effects need to be more thoroughly studied at high spatial and temporal resolution to determine their importance.

There are a number of recommendations for future ice research using pressure films.

- To ensure alignment of the layered films one could create a specifically designed holding apparatus for the films, however a simple solution would have been to mark alignment dots on the film once they were in place on the apparatus by simply pressing on the films near the edges with a hard, object of small contact area. This would place a mark on all levels of film in the same spot, allowing for easy alignment afterwards using imaging software.
- Running a repeat of the tests with a much larger cone with a much larger number of steps would be of great interest. This would allow for a greater non-boundary-affected crushing depth, while the greater number of crushing steps would reduce the error due to accrued pressure history or activated area.
- Improvement of the ice growth and shaping technique would allow for the proper performance of a Design of Experiments-method testing scheme, thereby allowing for the statistical significance of factors to be properly determined.

References

- [1] H. Kim, C. Daley and C. Ulan-Kvitberg, "Reappraisal of Pressure Distribution Induced by Ice-Structure Interaction Using High-Precision Pressure Measurement Film," in *ICETECH 2012*, Banff, 2012.
- [2] US Geological Survey, "US Geological Survey," 23 July 2008. [Online]. Available: http://www.usgs.gov/newsroom/article.asp?ID=1980&from=rss_home/#.UENnMtaPUIN. [Accessed 17 July 2012].
- [3] C. Daley, "The Role of Discrete Failures in Local Ice Loads," *Cold Regions Science and Technology*, vol. 27, pp. 197-211, 1998.
- [4] D. E. Kheisin, V. A. Likhomanov and V. A. Kurdyumov, "Determination of Specific Breakup Energy and Contact Pressures Produced by the Impact of a Solid Against Ice," in *Symposium on Physical Methods in Studying Snow and Ice*, Leningrad, 1975.
- [5] C. Daley, "Ice Edge Contact and Failure," *Cold Regions Science and Technology*, vol. 21, pp. 1-23, 1992.
- [6] A. Joensuu and K. Riska, "Contact Between Ice and Structures," Helsinki University of Technology, Laboratory of Naval Architecture and Marine Engineering, Helsinki, 1989.
- [7] R. Frederking, I. J. Jordaan and J. S. McCallum, "Field Tests of Ice Indentation at Medium Scale Hobson's Choice Ice Island, 1989," in *IAHR Ice Symposium*, Espoo, 1990.
- [8] R. E. Gagnon, "Analysis of Visual Data from Medium Scale Indentation Experiments at Hobson's Choice Ice Island," *Cold Regions Science and Technology*, vol. 28, pp. 45-58, 1998.
- [9] R. Frederking, "The Local Pressure-Area Relation in Ship Impact with Ice," *Proceedings 15th International Conference on Port and Ocean Engineering under Arctic Conditions, POAC '99*, vol. 2, pp. 687-696, 1999.
- [10] C. G. Daley, "Reanalysis of Ice Pressure-Area Relationships," *Marine Technology*, vol. 44, no. 4, pp. 234-244, 2007.
- [11] R. Ritch, R. Frederking, M. Jonston, R. Browne and F. Ralph, "Local Ice Pressures Measured on a Strain Gauge Panel During the CCGS Terry Fox Bergy Bit Impact Study," *Cold Regions Science and Technology*, vol. 52, pp. 29-49, 2008.
- [12] A. B. Liggins, J. C. E. Stranart, J. B. Finlay and C. H. Rorabeck, "Calibration and Manipulation of Data from Fuji Pressure-Sensitive Film," in *Experimental Mechanics: Technology Transfer Between High Tech Engineering and Biomechanics (Clinical Aspects of Biomedecine)*, Elsevier Science, 1992.

- [13] C. Ulan-Kvitberg, H. Kim and C. Daley, "Comparison of Pressure-Area Effects for Various Ice and Steel Indenters," in *International Society of Offshore and Polar Engineers 2011*, Maui, 2011.
- [14] H. Kim, C. Ulan-Kvitberg and C. Daley, "Crushing Characteristics of Dry, Wetted and Submerged Ice," in *International Society of Offshore and Polar Engineers 2011*, Maui, 2011.
- [15] S. Bruneau, A. Dillenburg and S. Ritter, "STEPS-RP001-2011 Ice Specimen Fabrication Techniques and Indentation Experiments, A STePSS Pilot Laboratory Investigation of Ice-Structure Interaction," Memorial University of Newfoundland, Sustainable Technology for Polar Ships and Structures, St. John's, 2011.
- [16] G. W. Oehlert, *A First Course in Design of Experiments*, W. H. Freeman, 2000.
- [17] Fujifilm, "Fujifilm Prescale FAQ," Fujifilm Canada, [Online]. Available: <http://www.fujifilm.ca/products/prescale/faqs/index.html>. [Accessed 3 September 2012].
- [18] Sensor Products Incorporated, *Fujifilm Prescale Product Information*, Madison, New Jersey: Sensor Products Incorporated, 2011.
- [19] Paint.Net, "Paint.Net," Paint.Net, [Online]. Available: <http://www.getpaint.net/>. [Accessed 3 September 2012].
- [20] ImageJ, "ImageJ," ImageJ, [Online]. Available: <http://rsbweb.nih.gov/ij/>. [Accessed 3 September 2012].
- [21] Rapid Tables, "RGB Color Codes Chart," [Online]. Available: http://www.rapidtables.com/web/color/RGB_Color.htm. [Accessed 3 September 2012].
- [22] T. J. O. Sanderson, *Ice Mechanics: Risks to Offshore Structures*, London: Graham and Trotman Ltd., 1988.

Appendix A

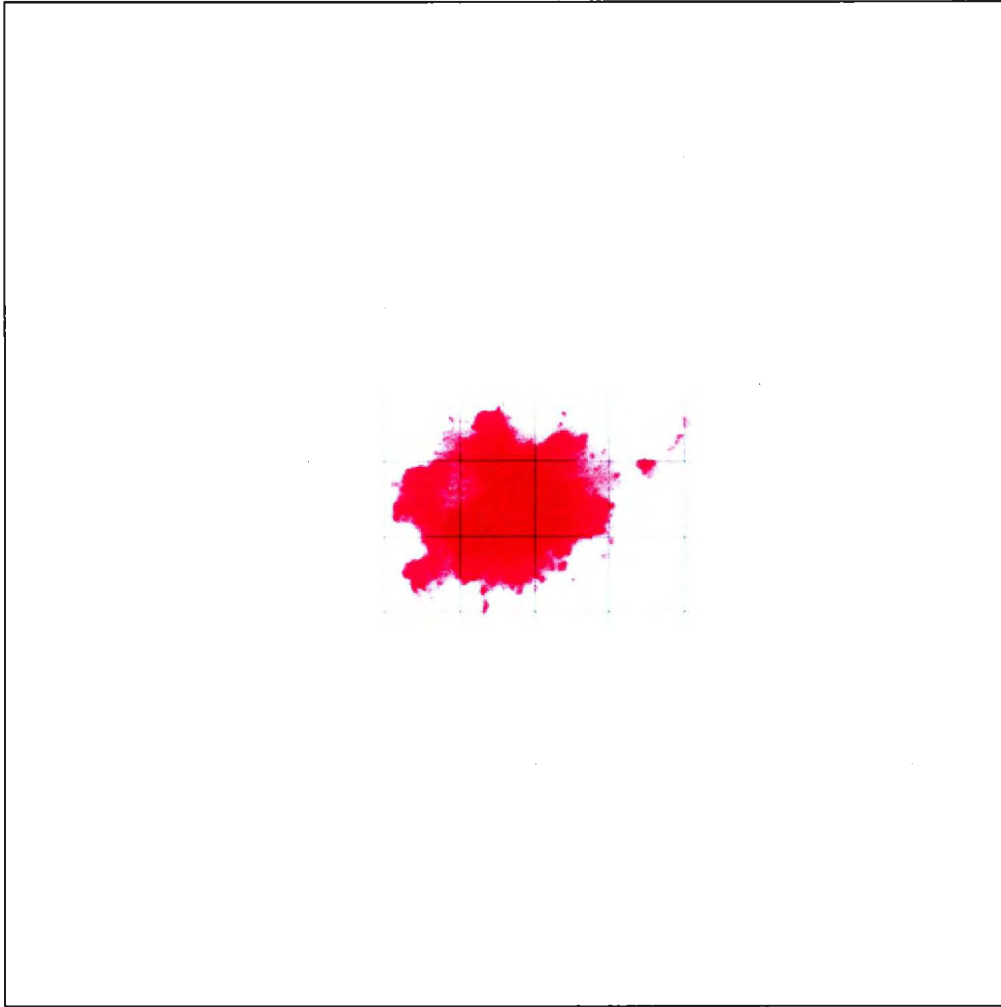


Figure 109 - FIT2a Low (1cm x 1cm Grid Spacing)

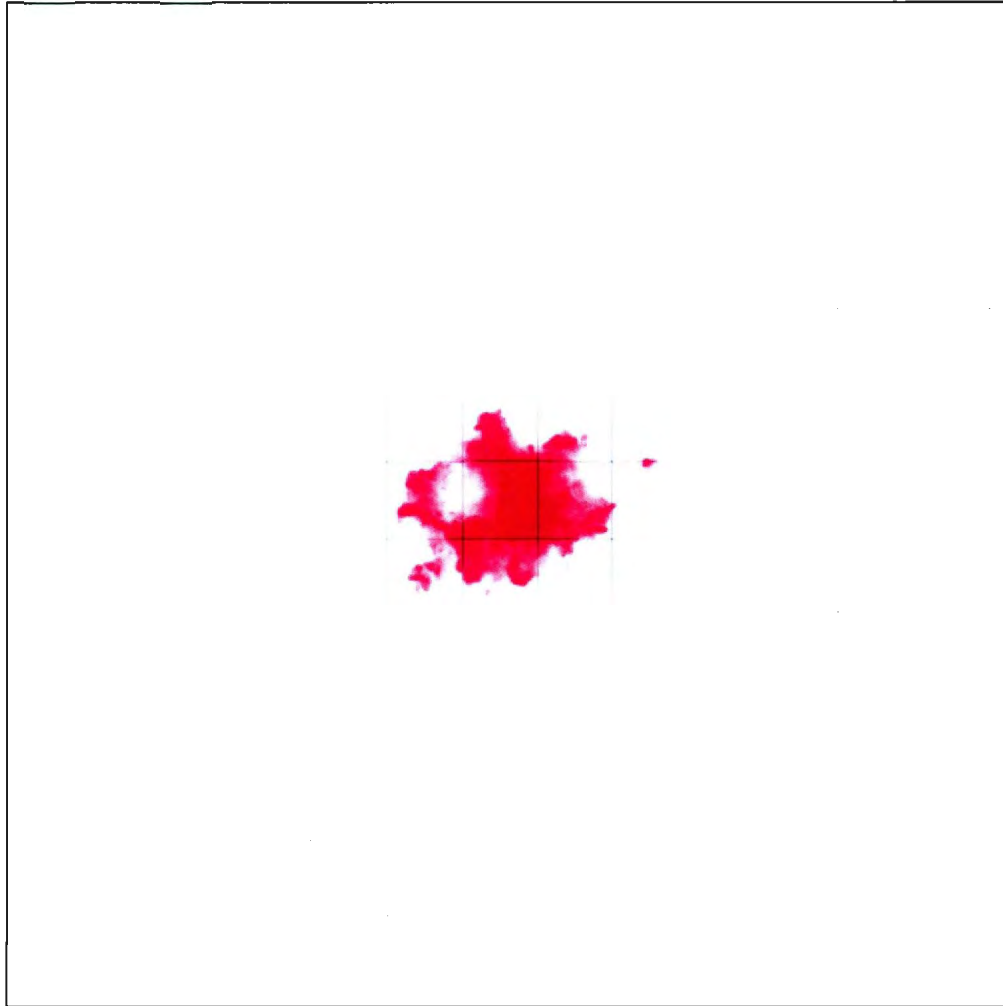


Figure 110 - F1T2a Medium (1cm x 1cm Grid Spacing)

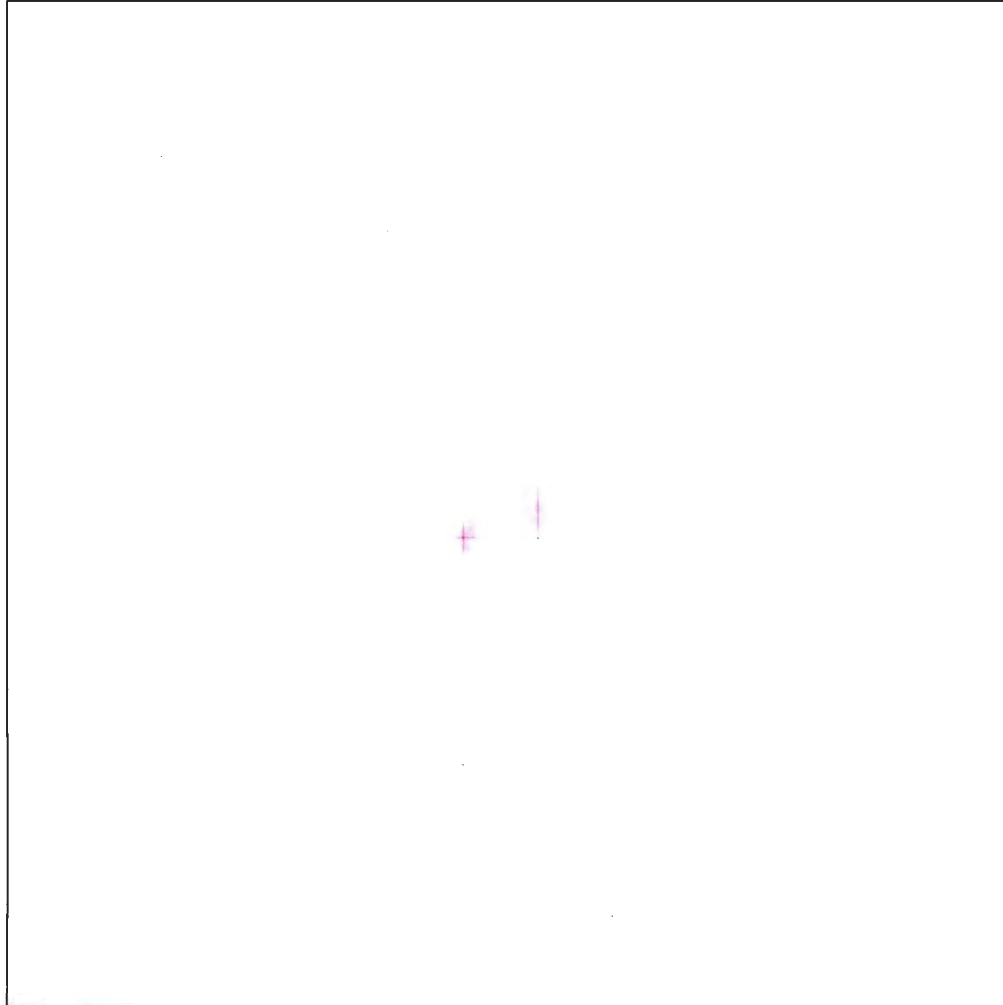


Figure 111 - F1T2a High (1cm x 1cm Grid Spacing)

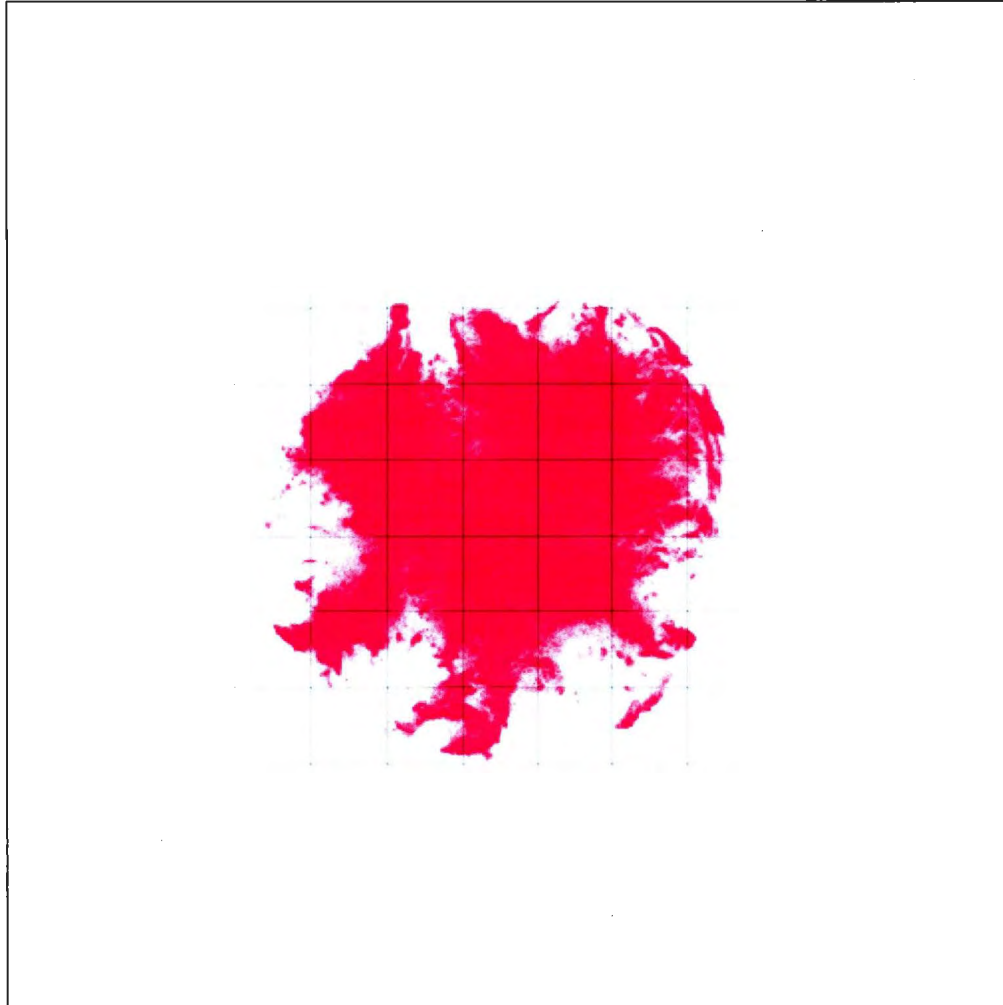


Figure 112 - F1T2b Low (1cm x 1cm Grid Spacing)

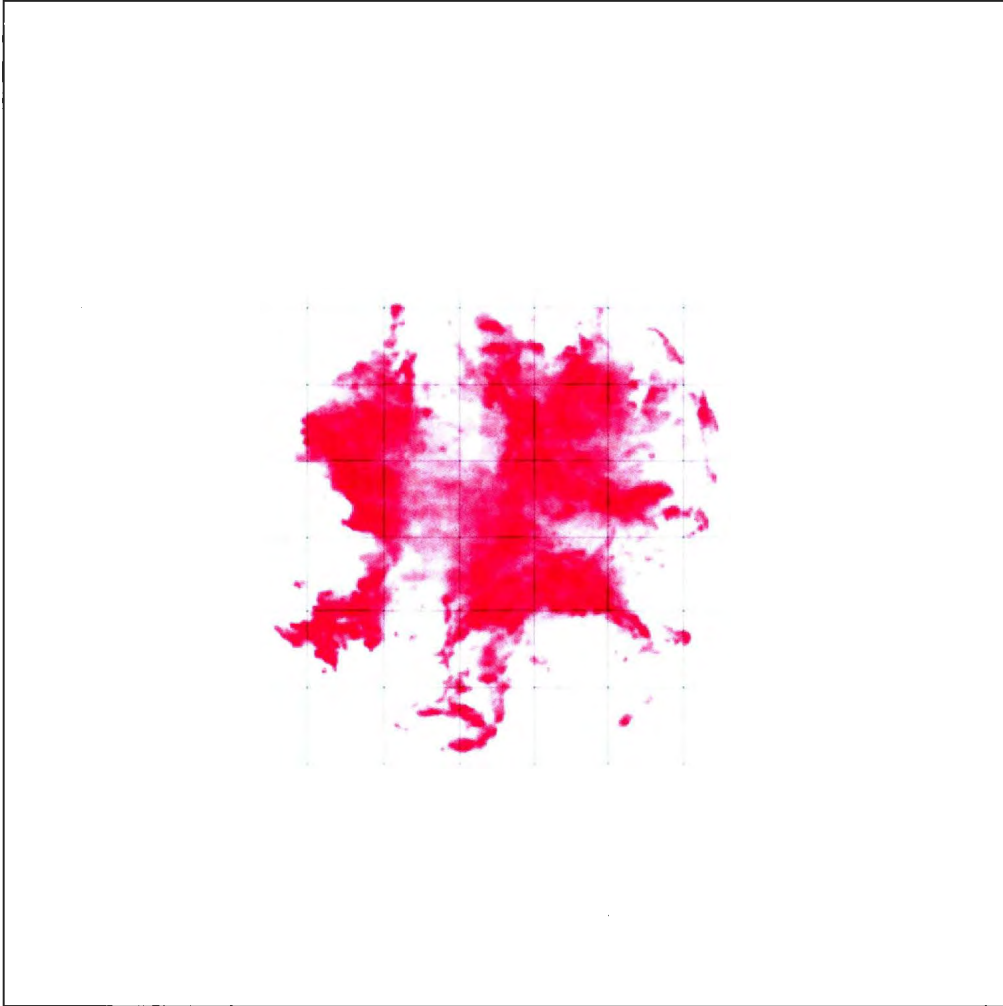


Figure 113 - F1T2b Medium (1cm x 1cm Grid Spacing)

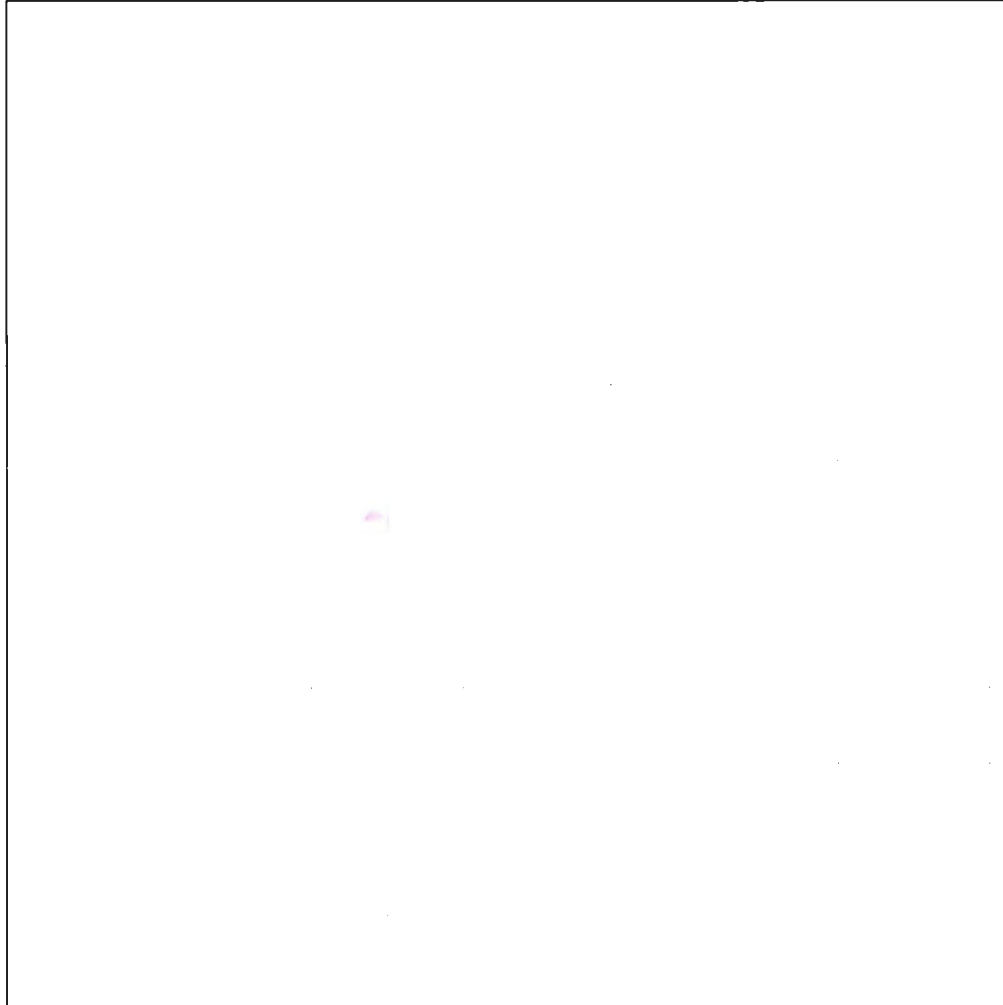


Figure 114 - F1T2b High (1cm x 1cm Grid Spacing)



Figure 115 - FIT2c Low (1cm x 1cm Grid Spacing)

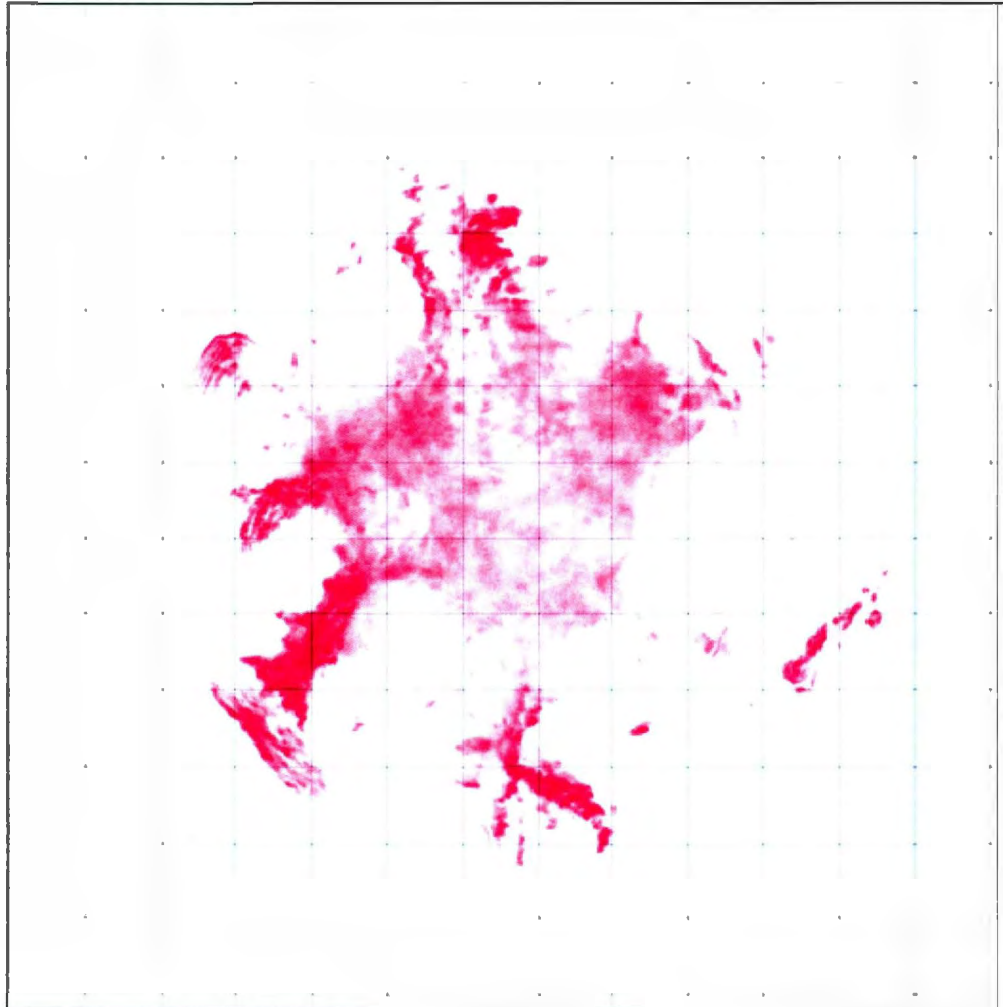


Figure 116 - F1T2c Medium (1cm x 1cm Grid Spacing)

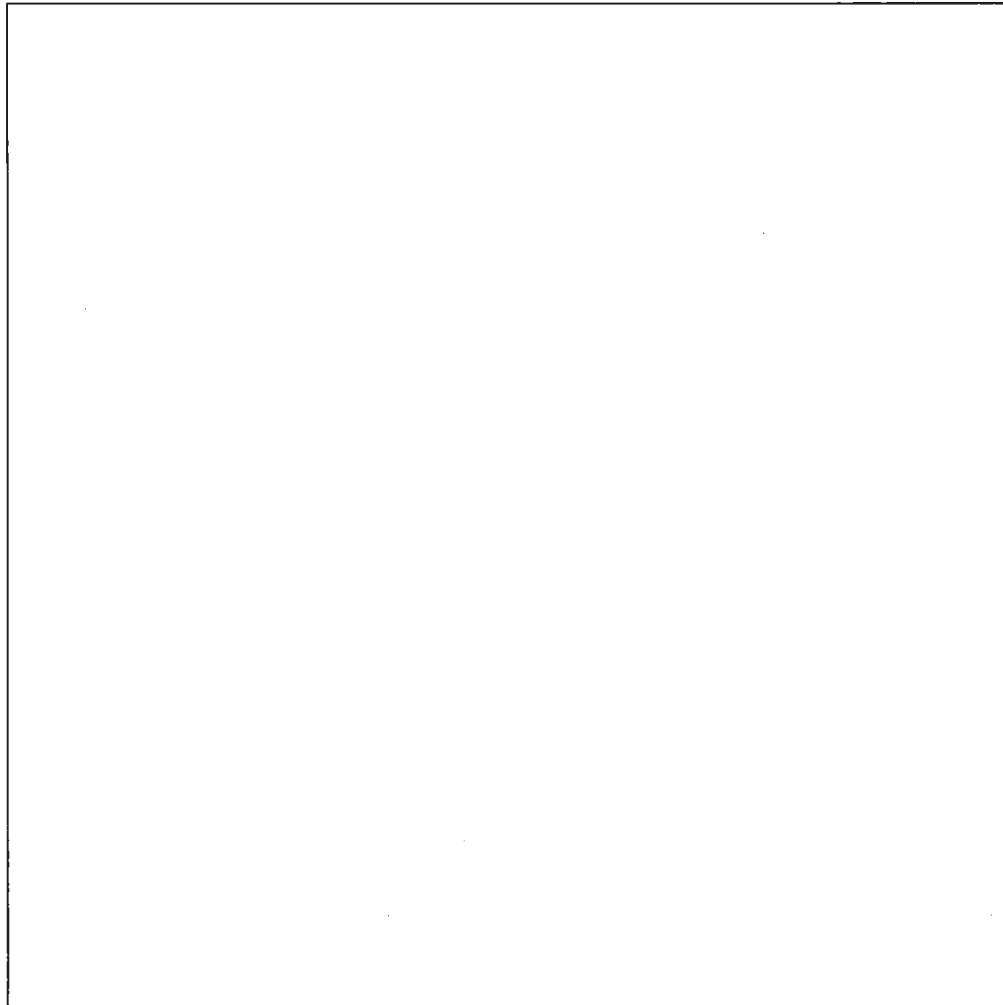


Figure 117 - F1T2c High (1cm x 1cm Grid Spacing)

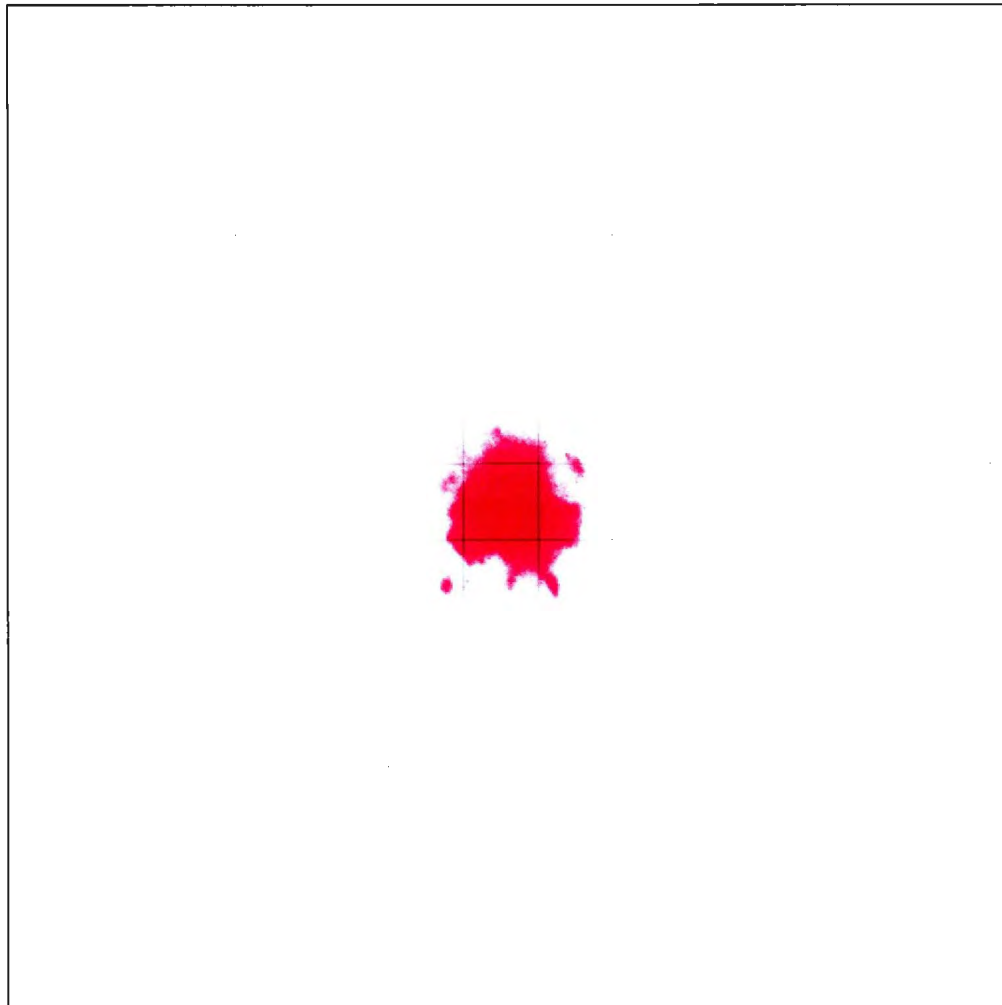


Figure 118 - F13T1a Low (1cm x 1cm Grid Spacing)

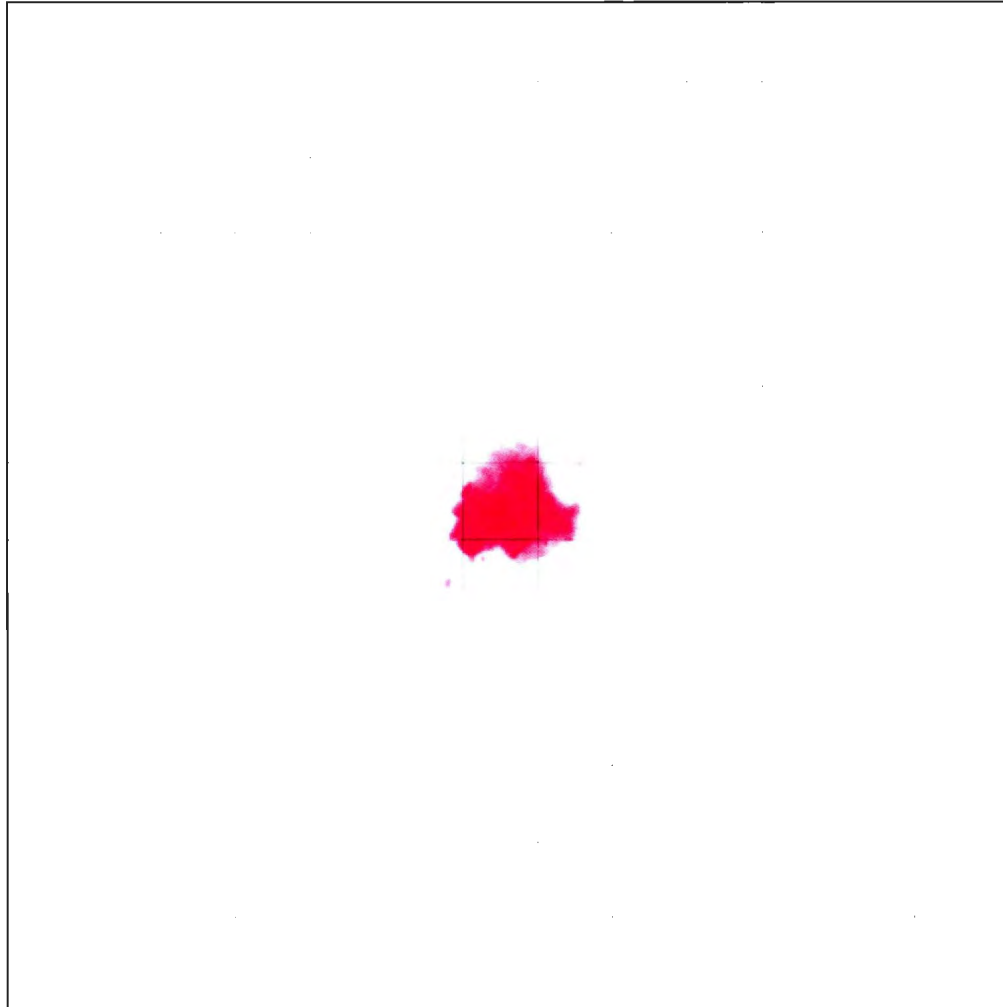


Figure 119 - F13T1a Medium (1cm x 1cm Grid Spacing)

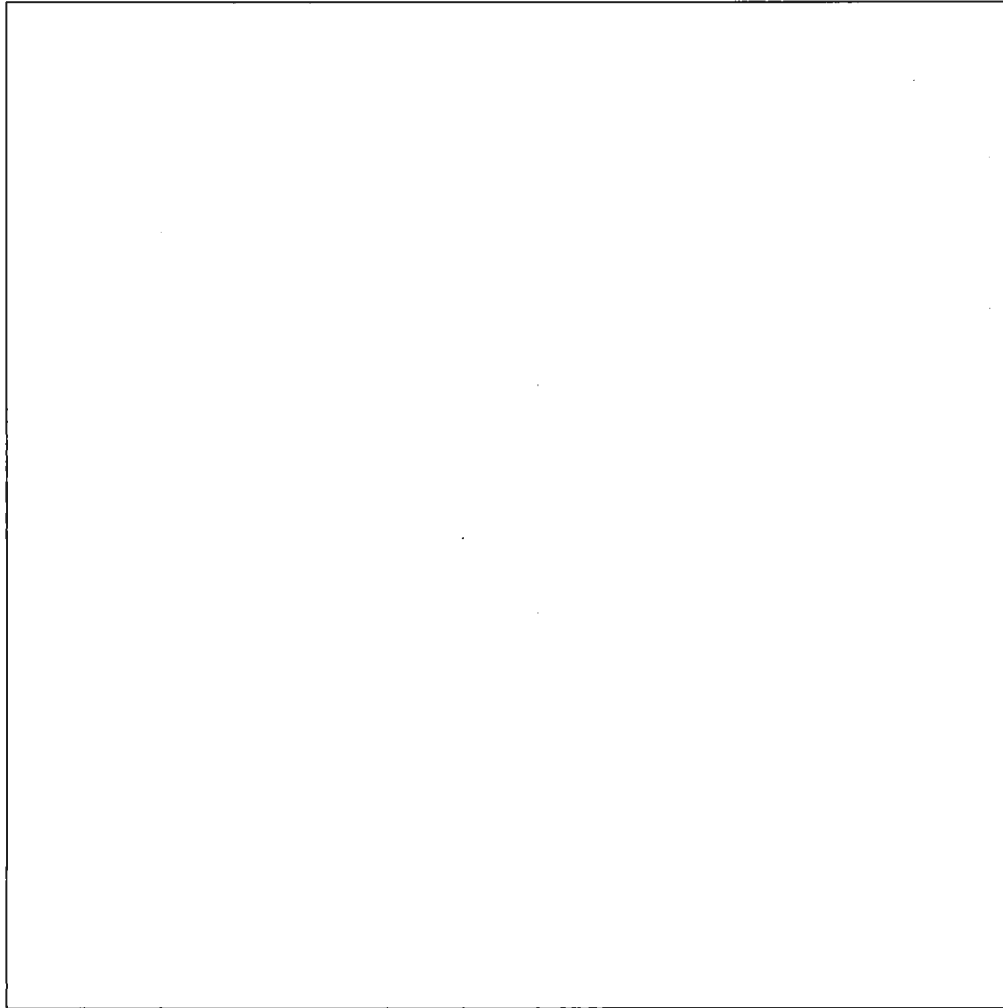


Figure 120 - F13T1a High (1cm x 1cm Grid Spacing)

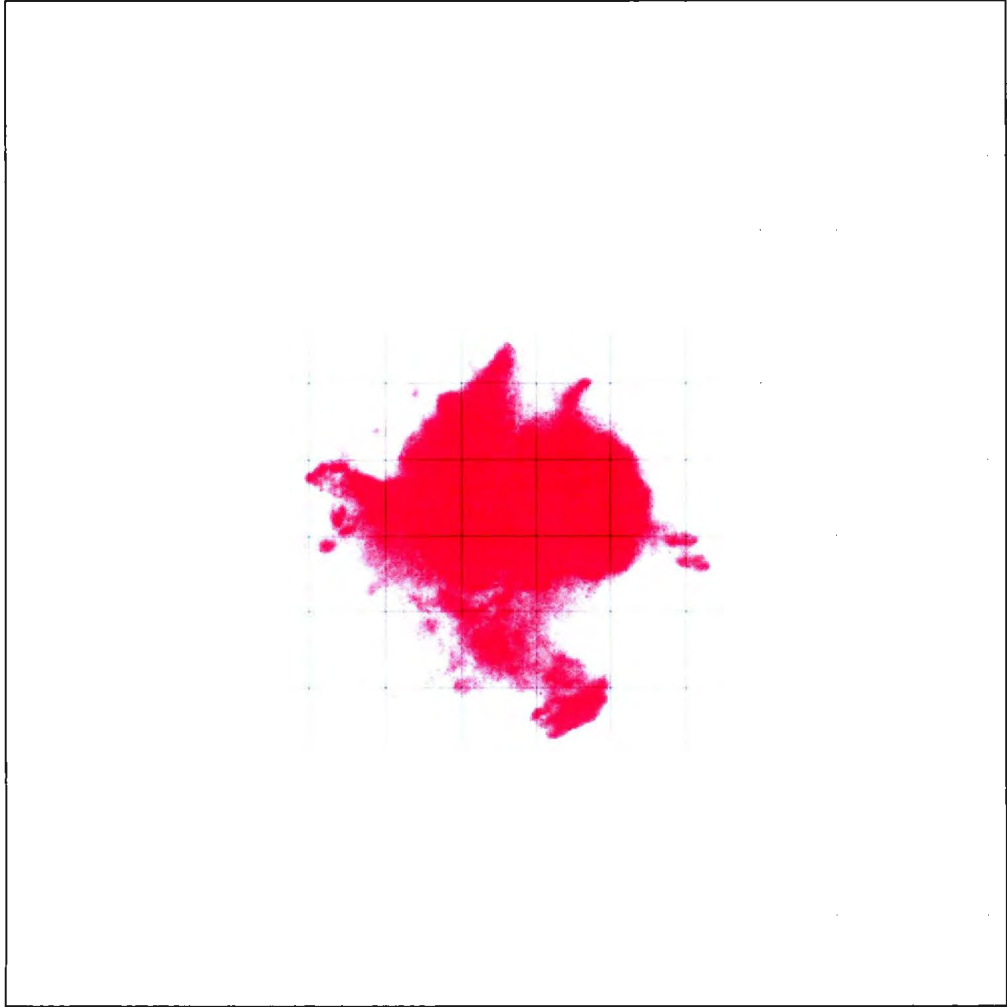


Figure 121 - F13T1b Low (1cm x 1cm Grid Spacing)

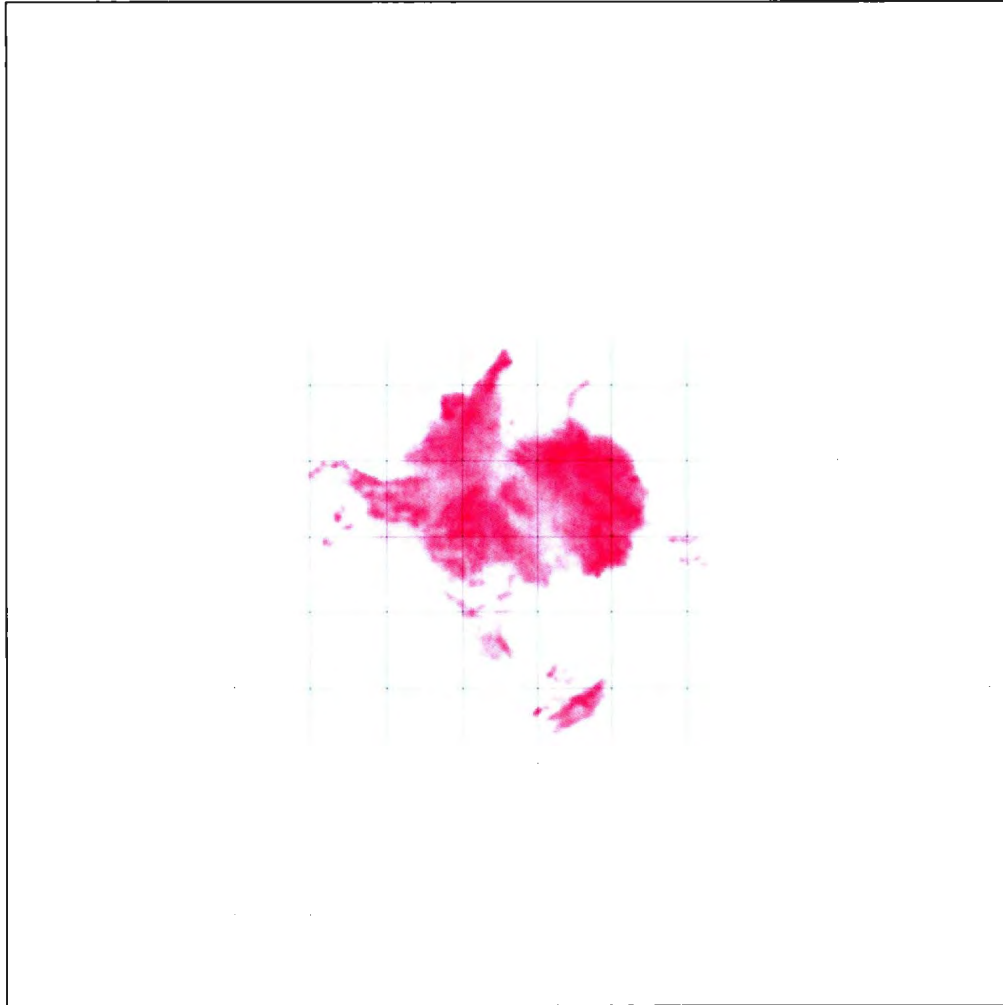


Figure 122 - F13T1b Medium (1cm x 1cm Grid Spacing)

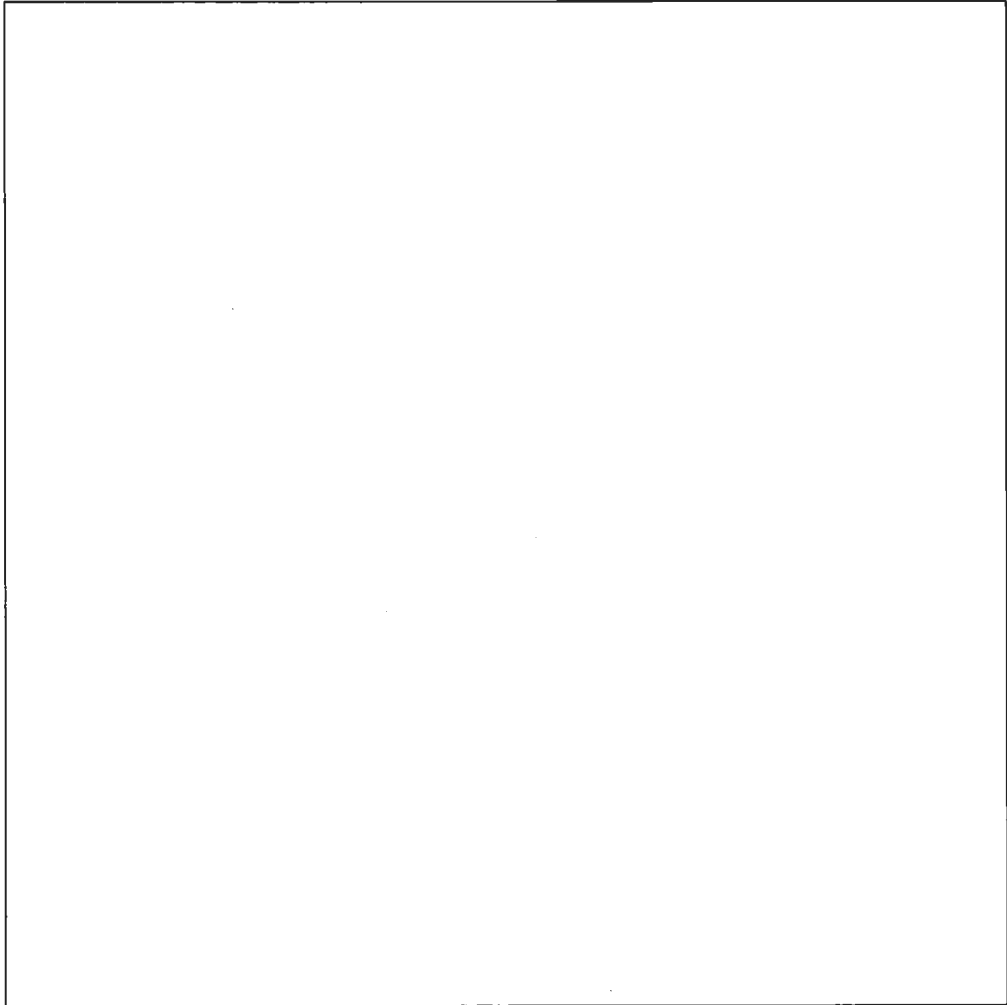


Figure 123 - F13T1b High (1cm x 1cm Grid Spacing)

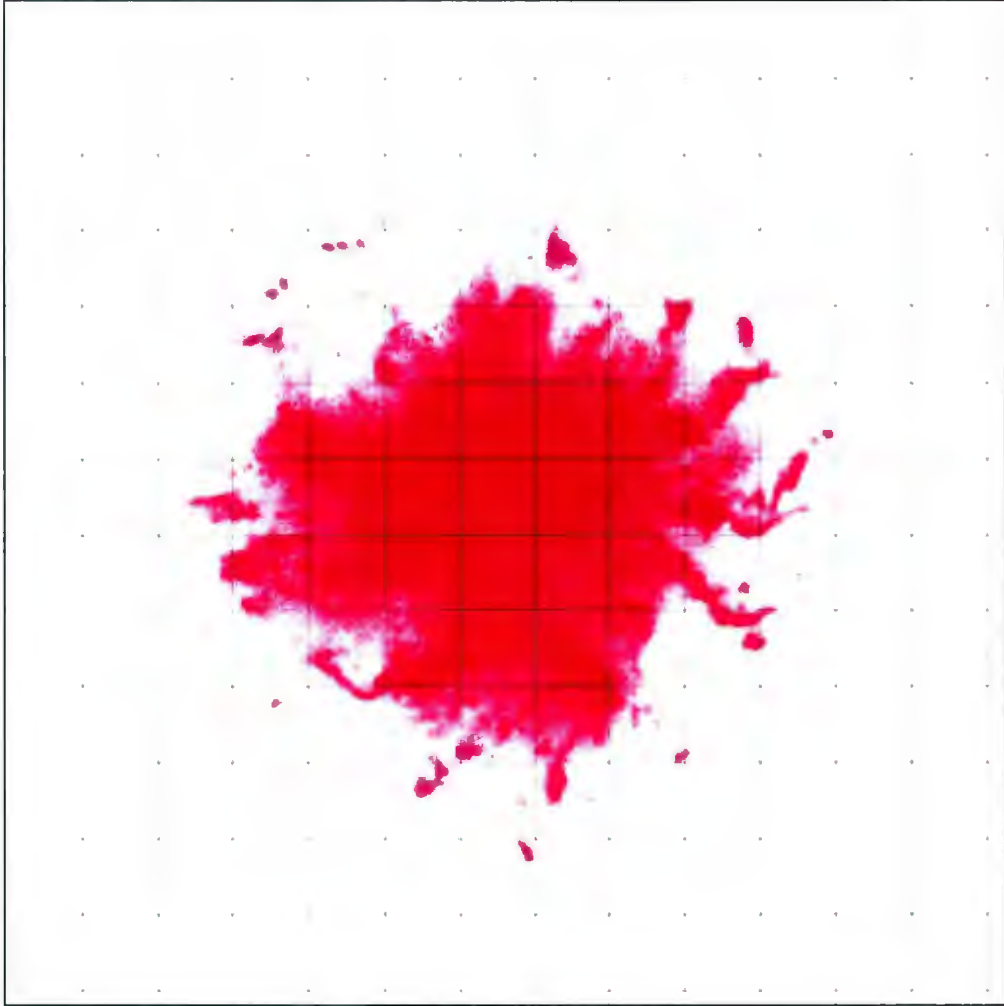


Figure 124 - F13T1c Low (1cm x 1cm Grid Spacing)

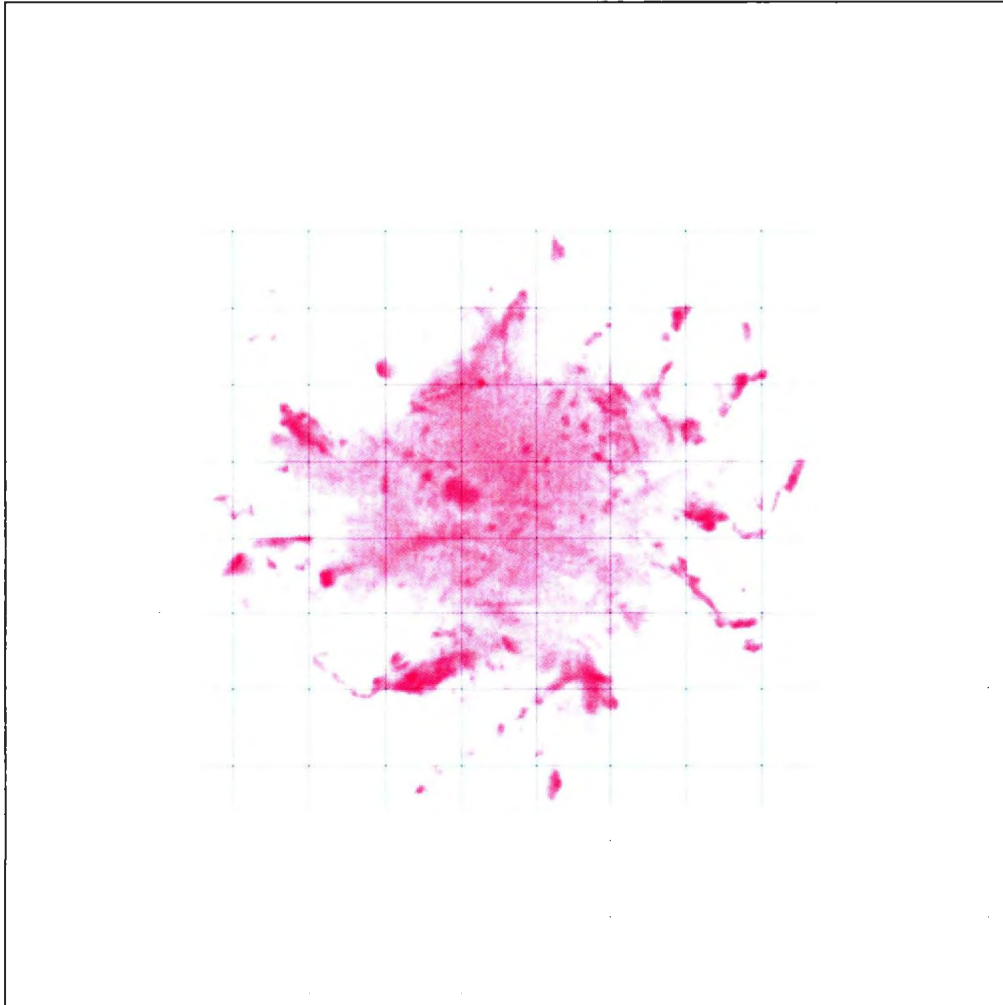


Figure 125 - F13T1c Medium (1cm x 1cm Grid Spacing)

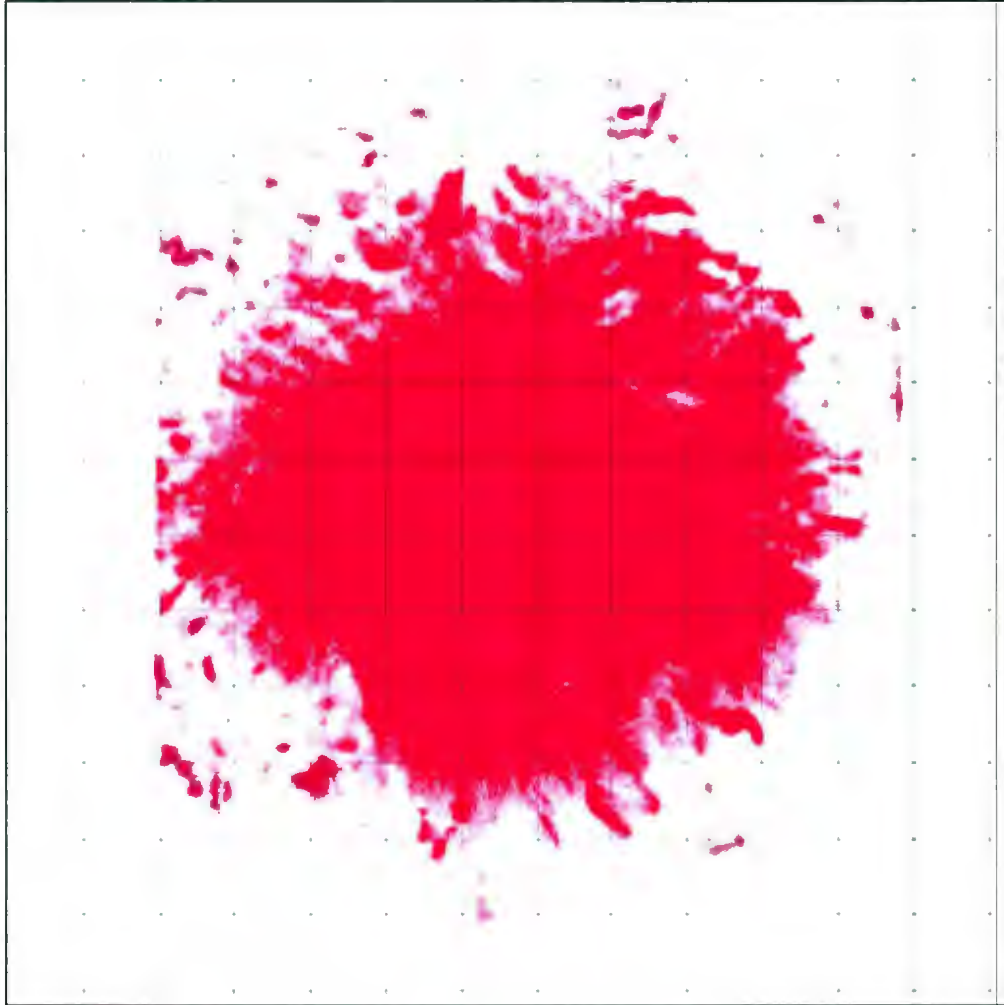


Figure 126 - F13T1d Low (1cm x 1cm Grid Spacing)

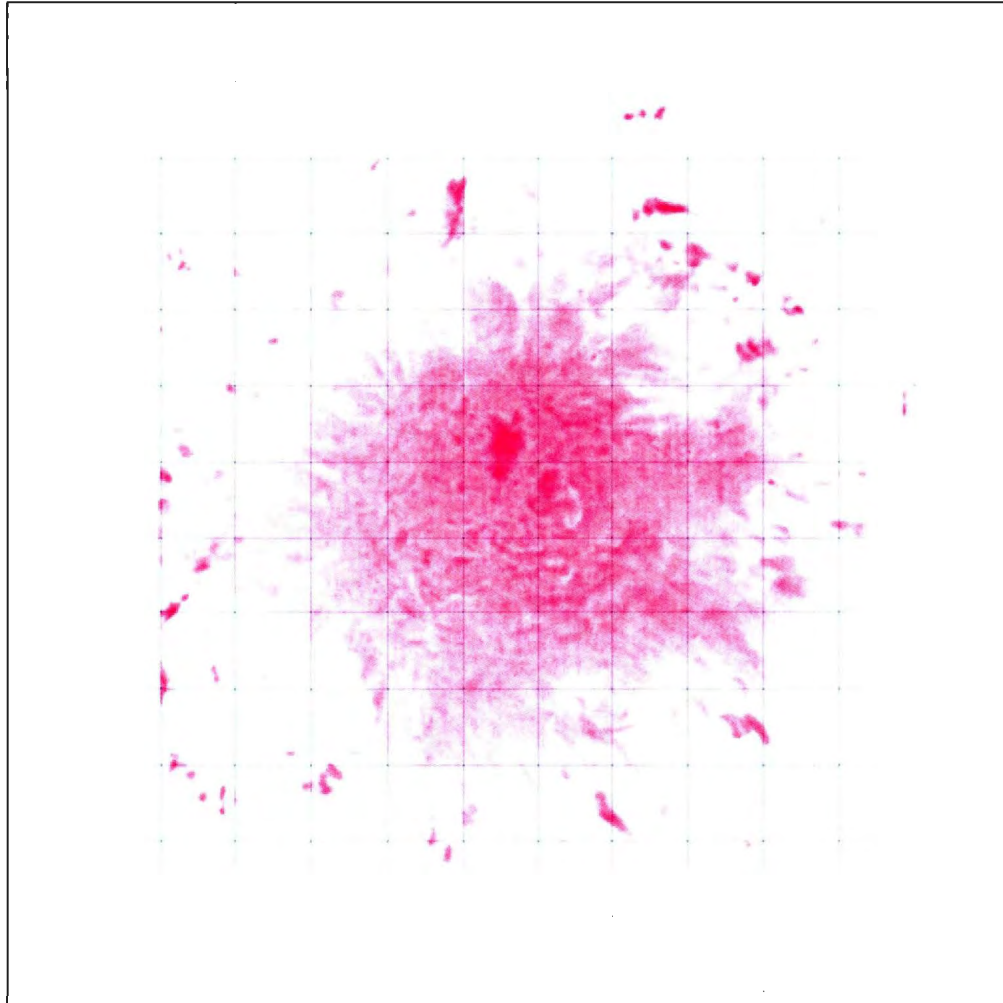


Figure 127 - F13T1d Medium (1cm x 1cm Grid Spacing)

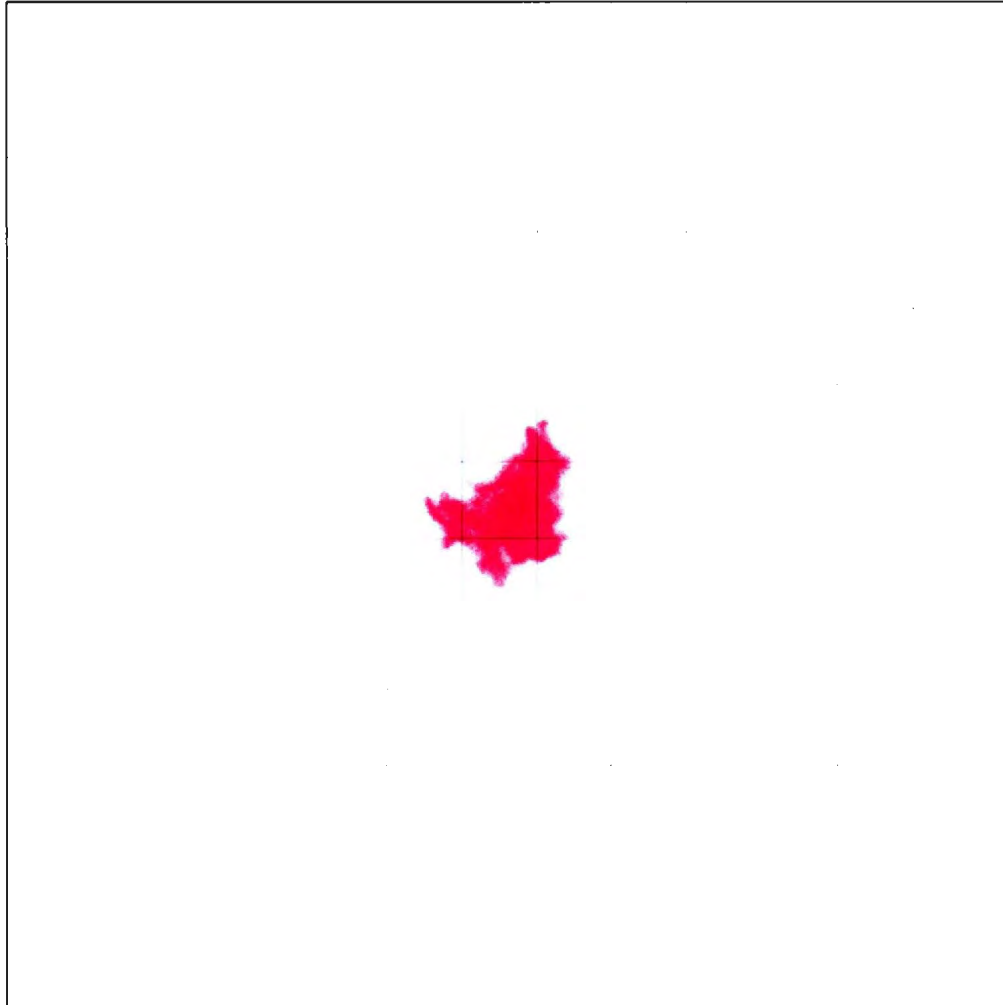


Figure 128 - F13T2a Low (1cm x 1cm Grid Spacing)

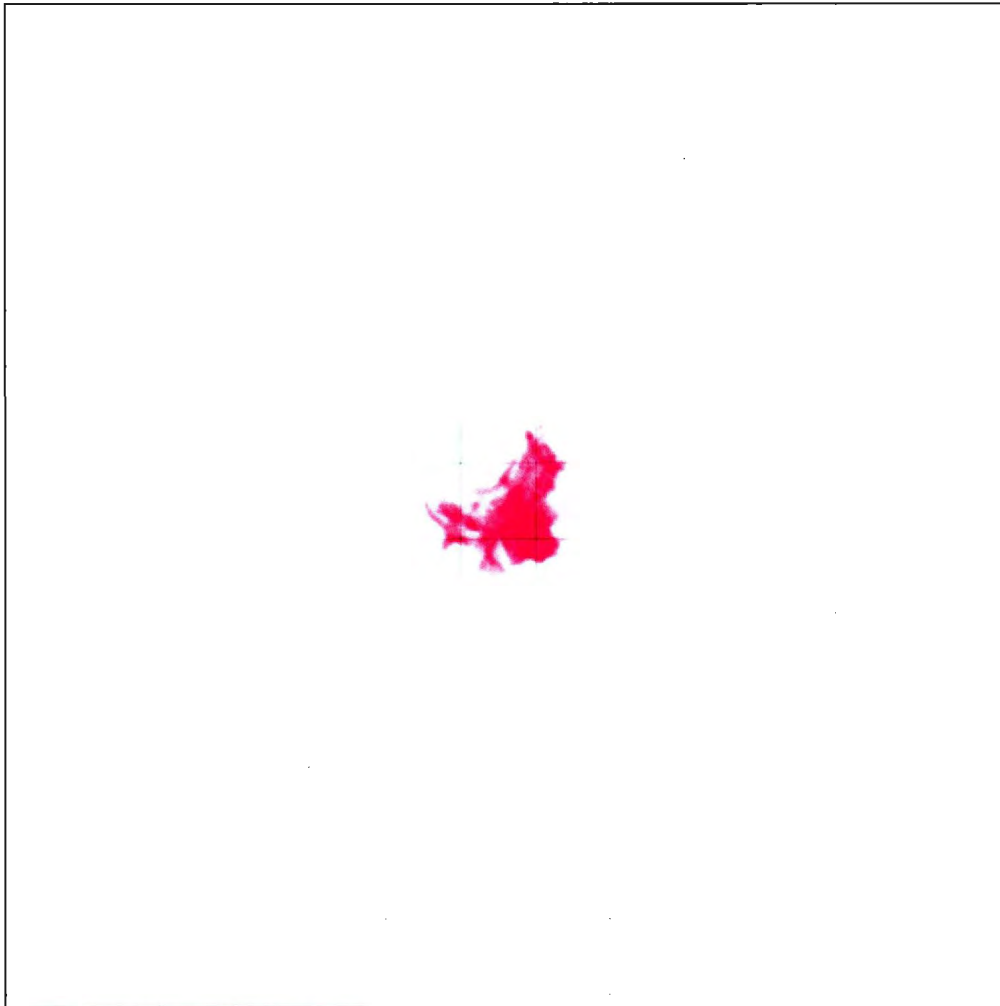


Figure 129 - F13T2a Medium (1cm x 1cm Grid Spacing)

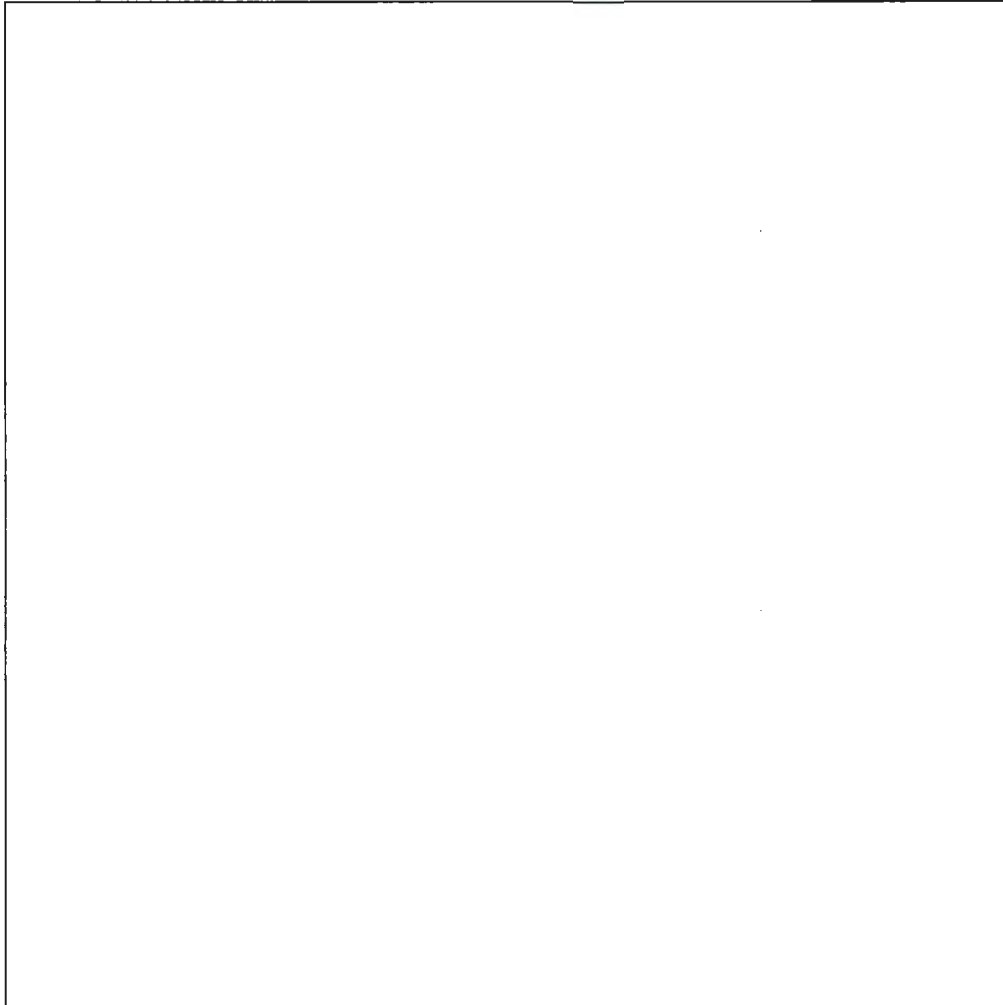


Figure 130 - F13T2a High (1cm x 1cm Grid Spacing)

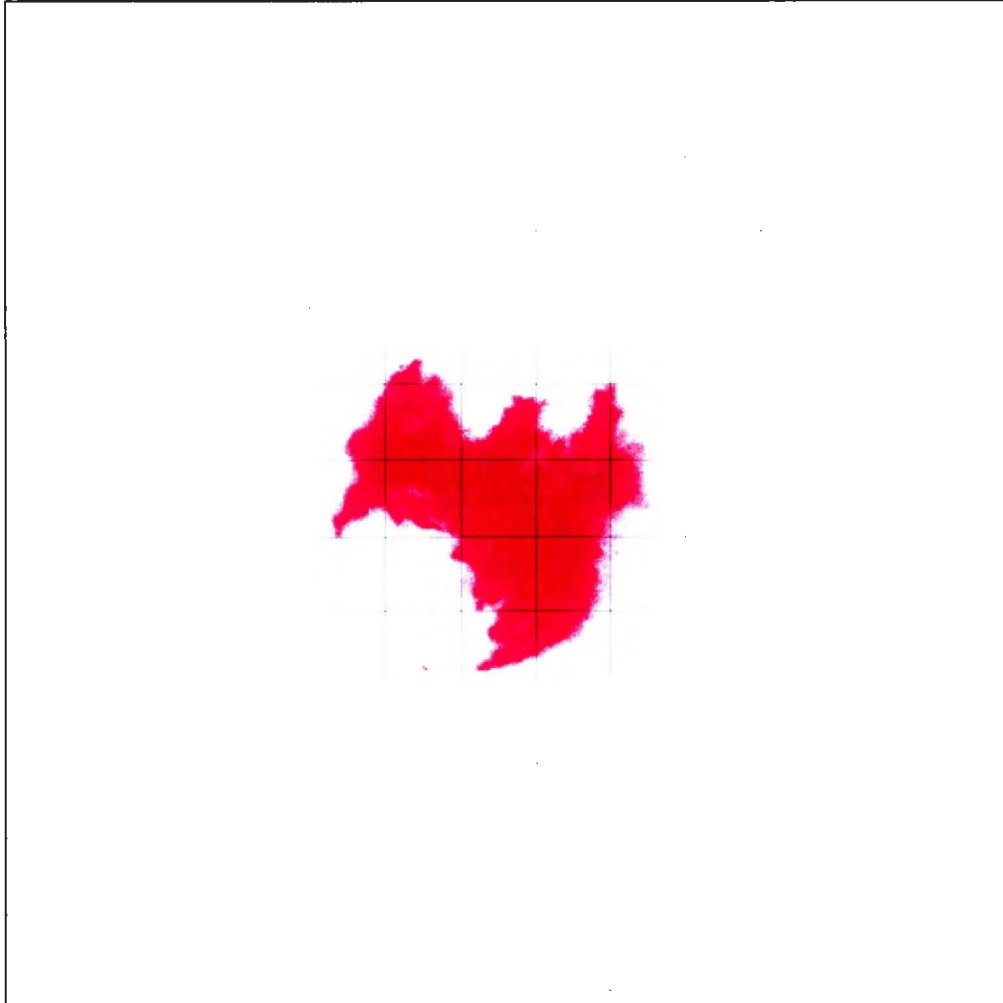


Figure 131 - F13T2b Low (1cm x 1cm Grid Spacing)

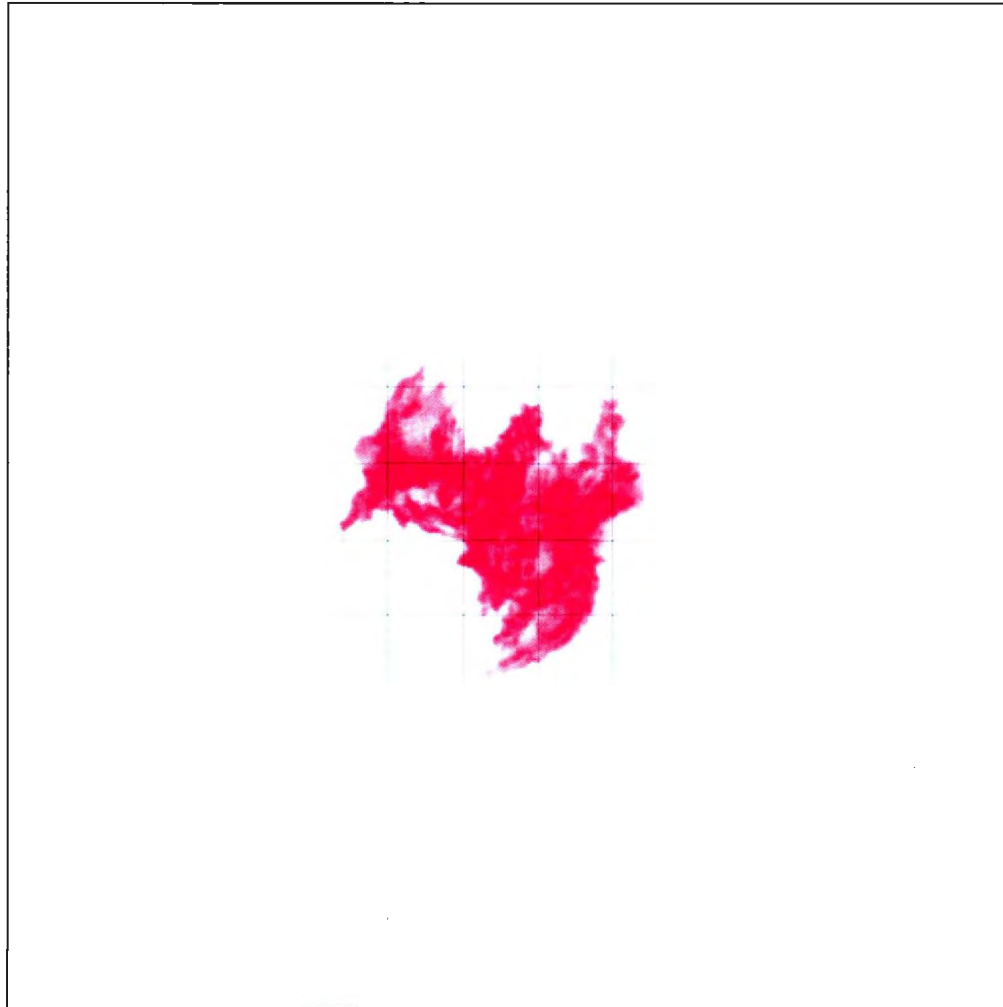


Figure 132 -F13T2b Medium (1cm x 1cm Grid Spacing)

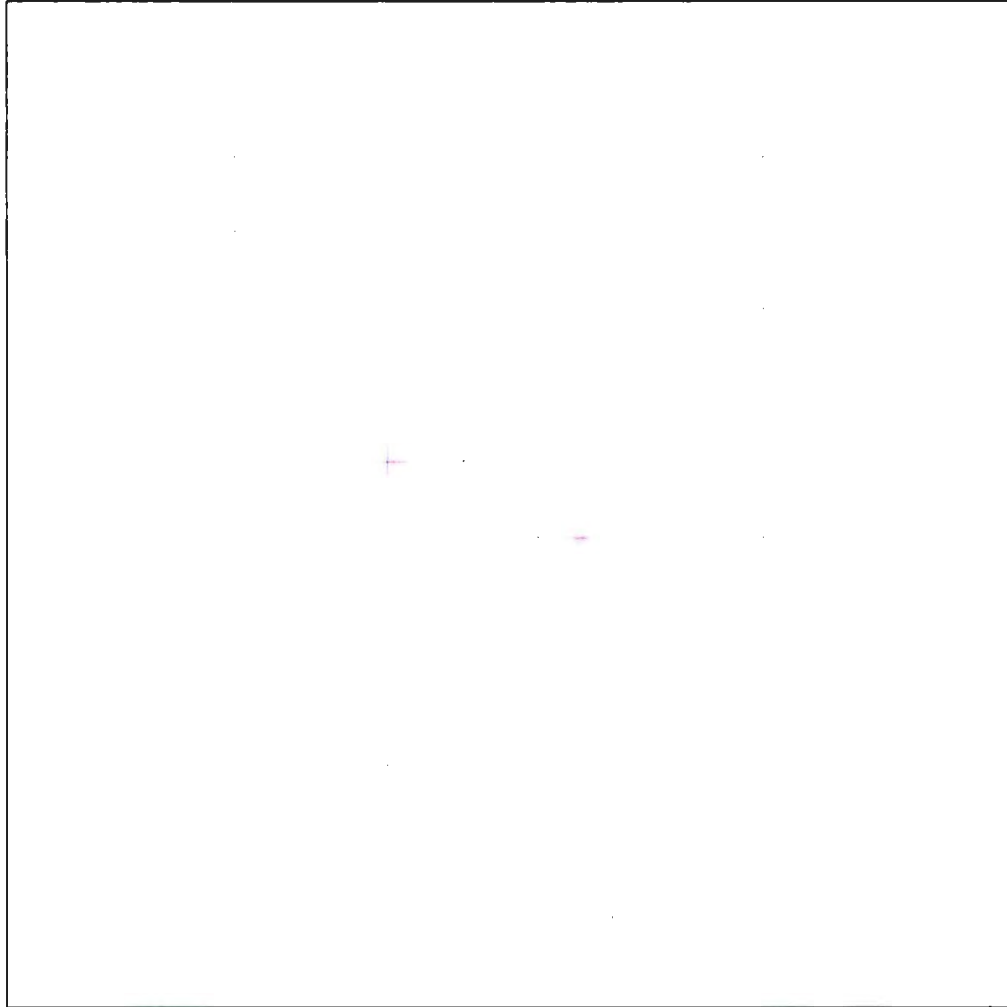


Figure 133 - F13T2b High (1cm x 1cm Grid Spacing)

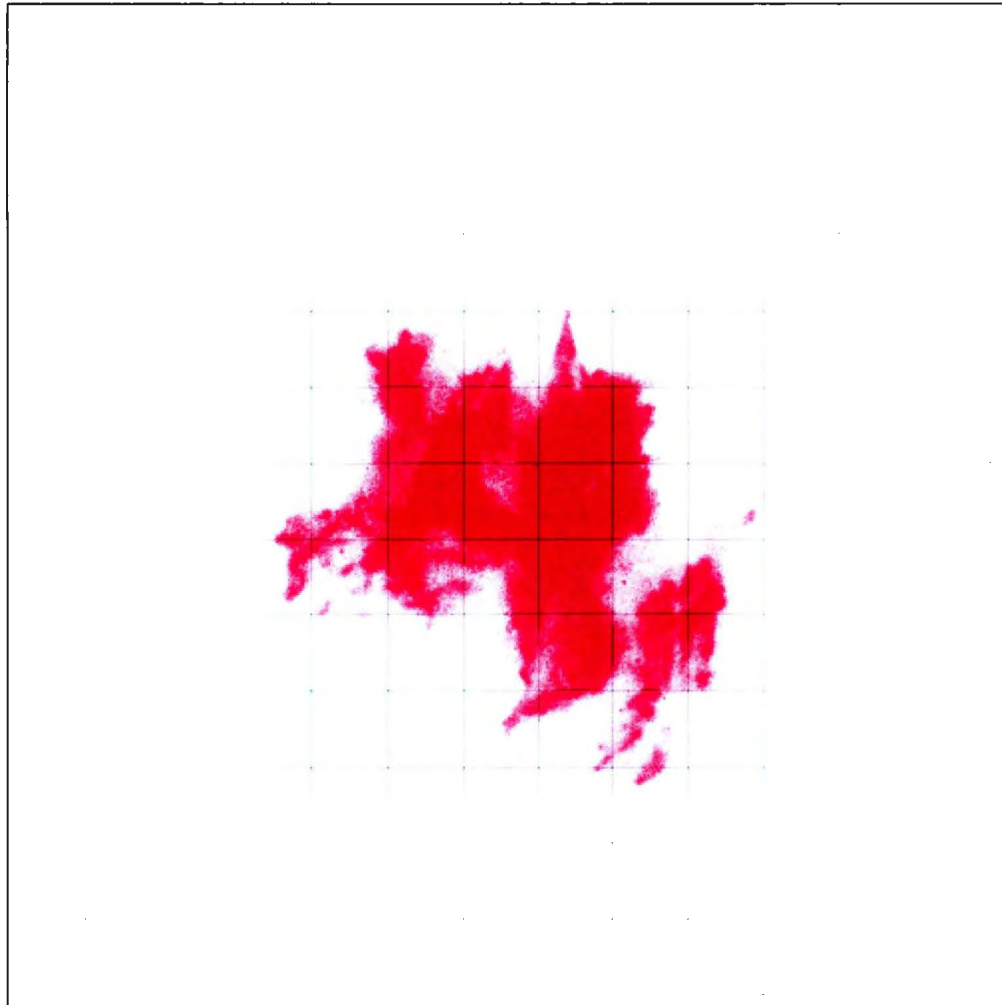


Figure 134 - F13T2c Low (1cm x 1cm Grid Spacing)

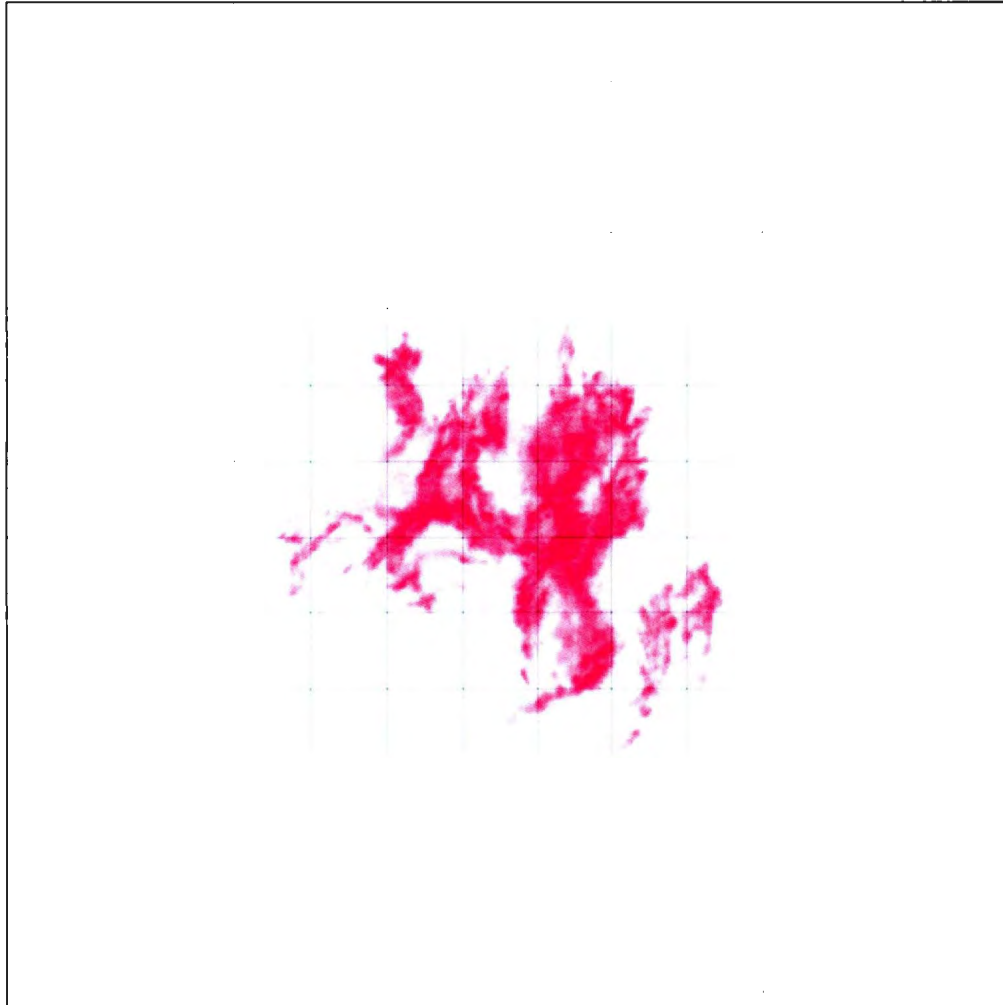


Figure 135 - F13T2c Medium (1cm x 1cm Grid Spacing)

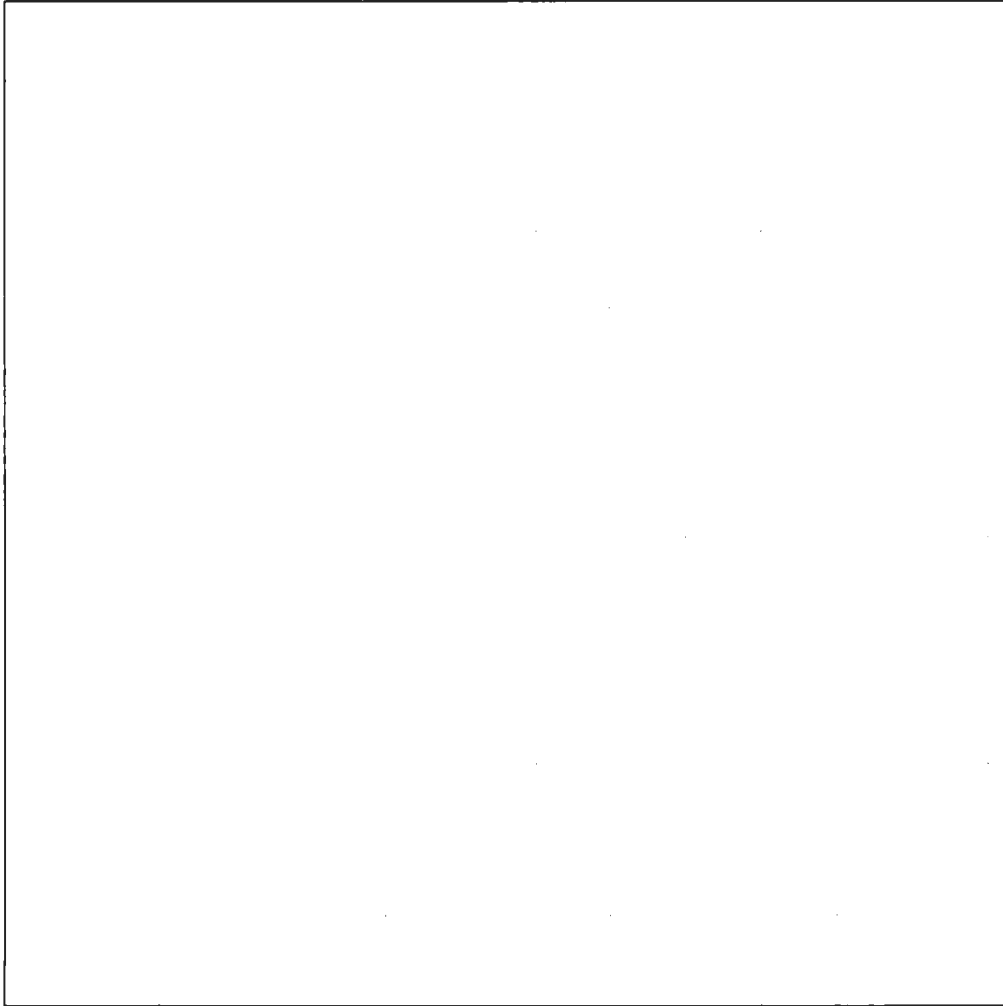


Figure 136 - F13T2c High (1cm x 1cm Grid Spacing)

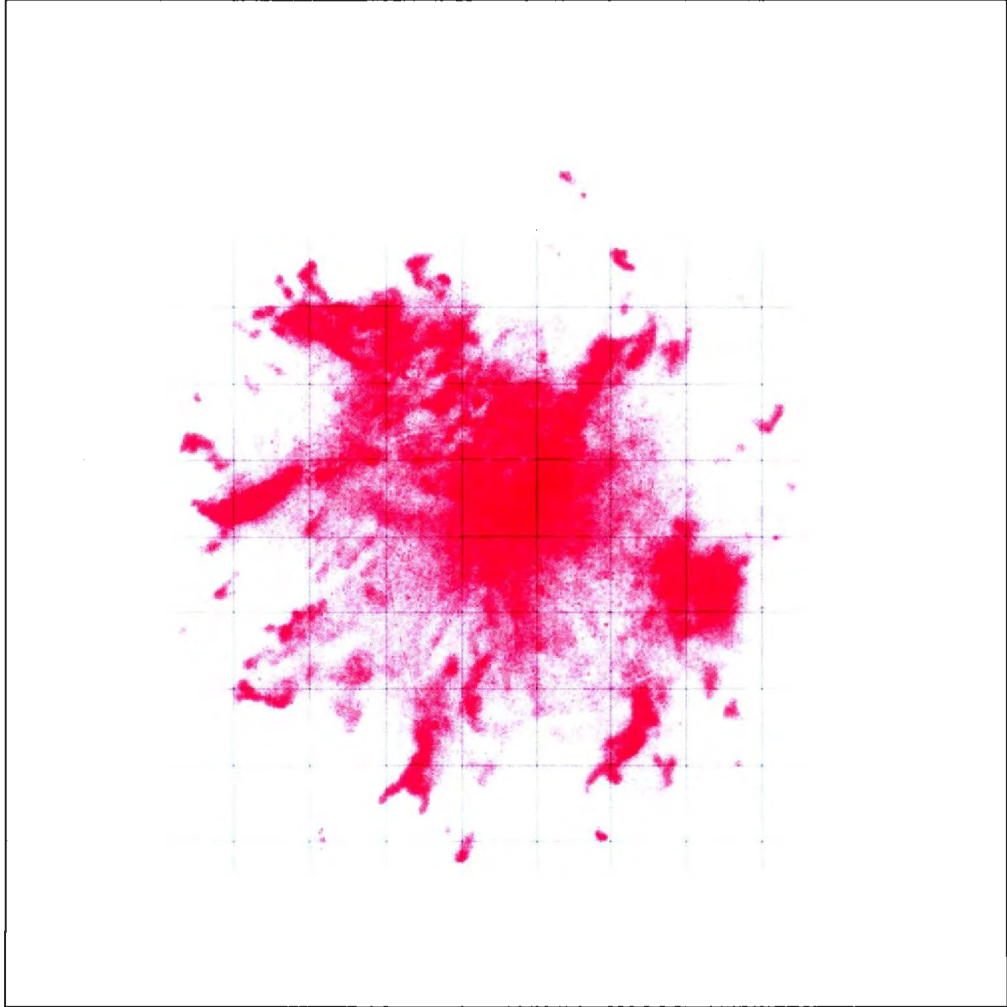


Figure 137 - F13T2d Low (1cm x 1cm Grid Spacing)

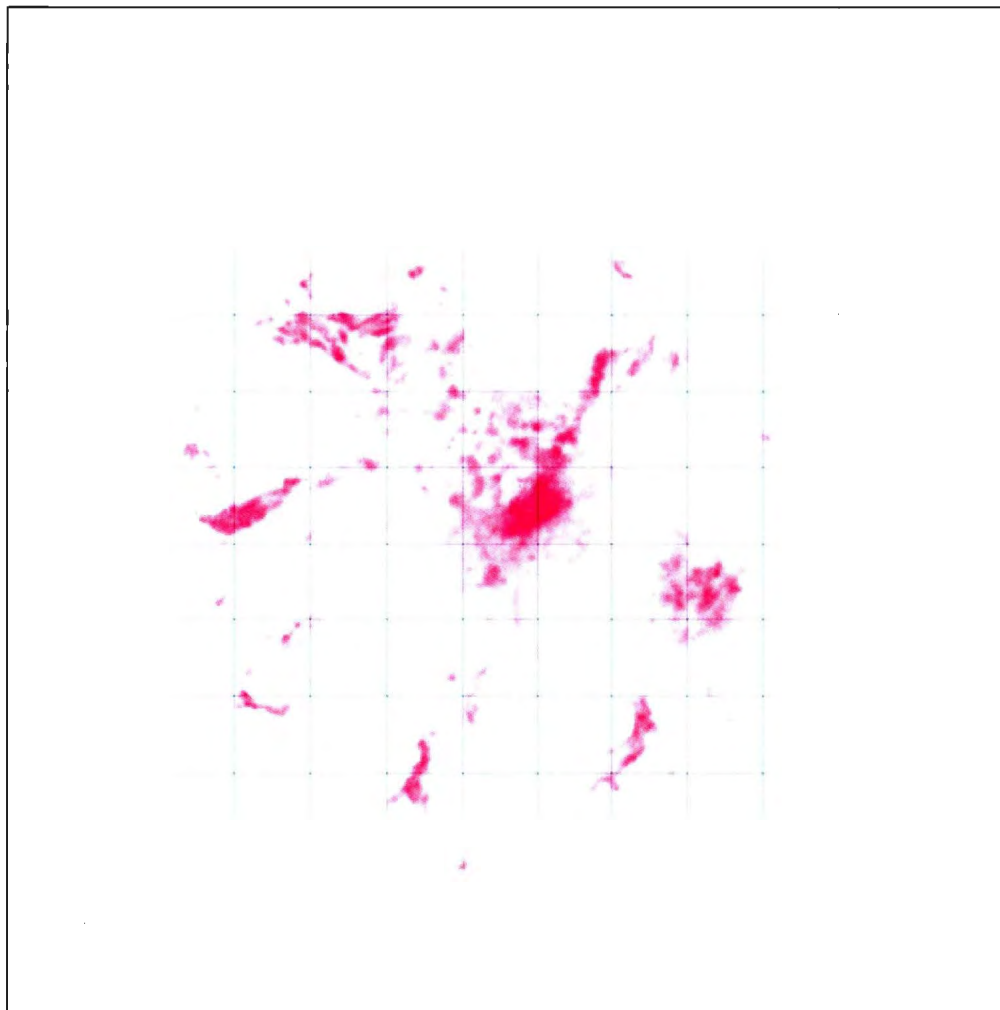


Figure 138 - F13T2d Medium (1cm x 1cm Grid Spacing)

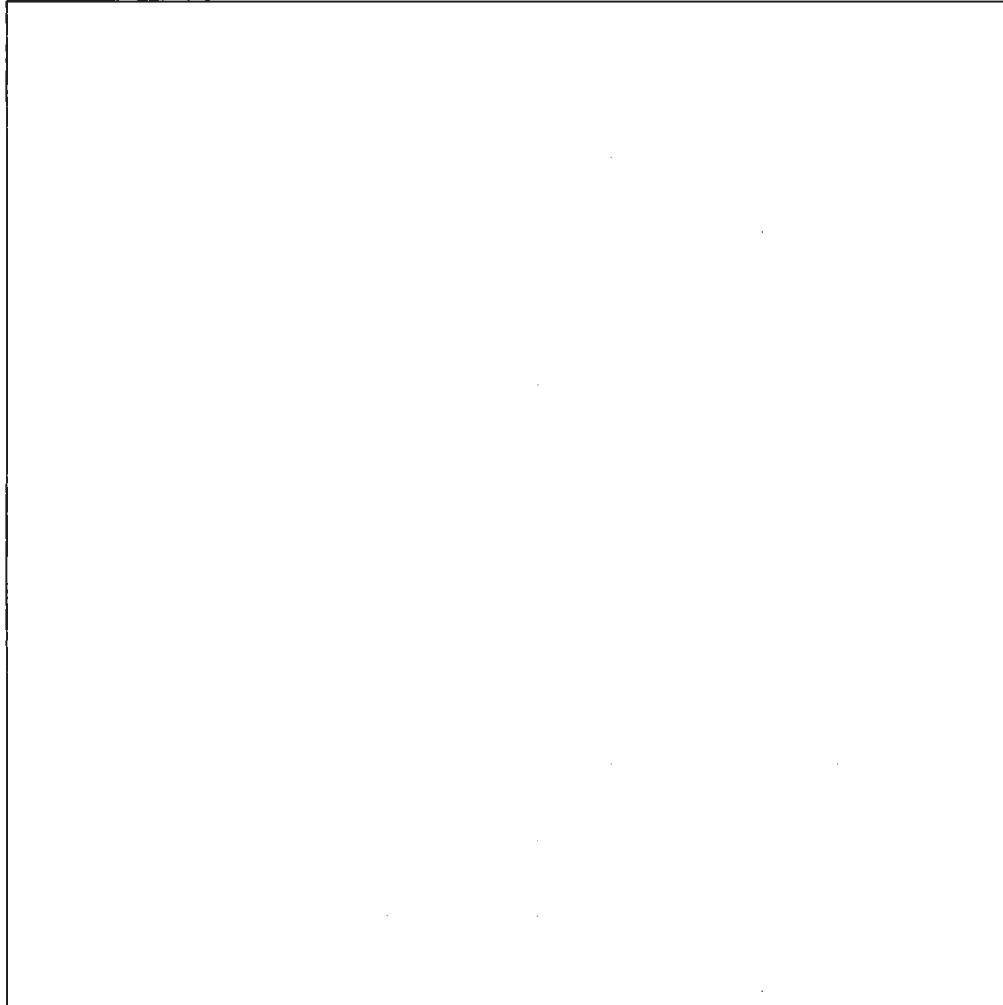


Figure 139 - F13T2d High (1cm x 1cm Grid Spacing)

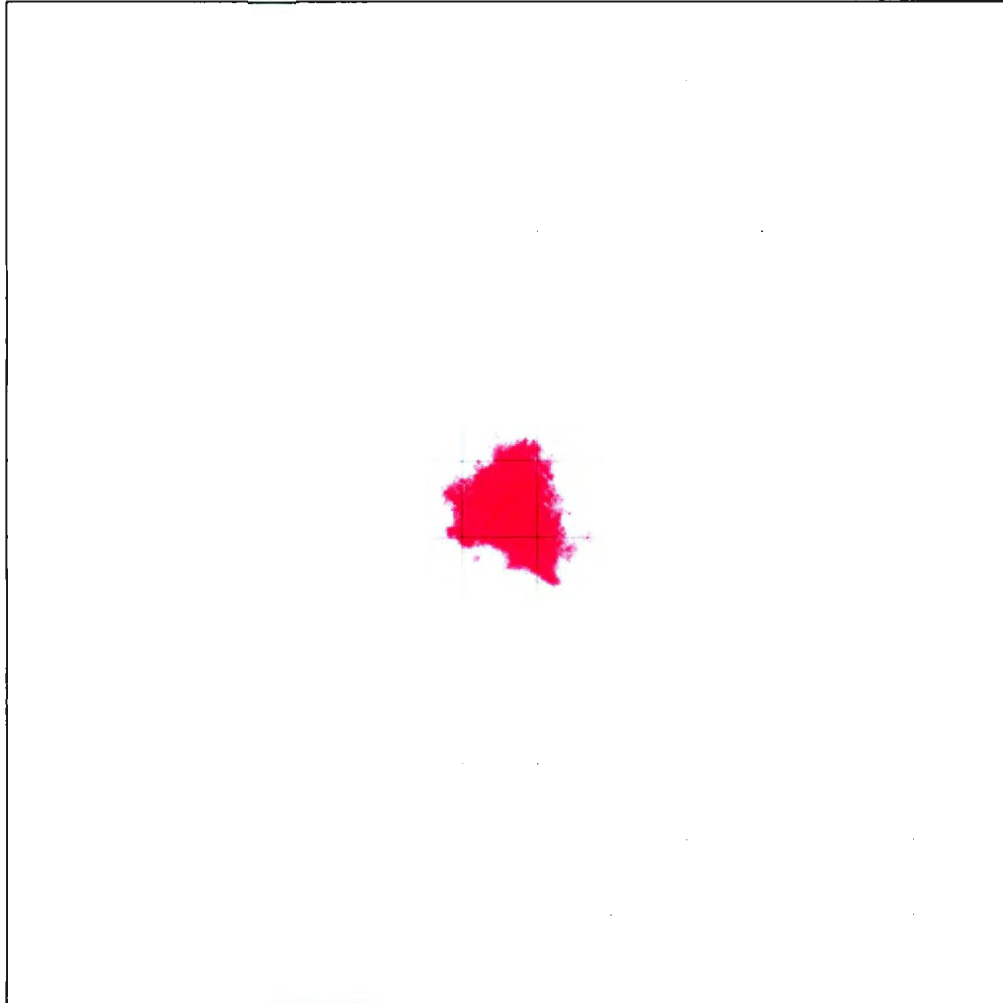


Figure 140 - F13T3a Low (1cm x 1cm Grid Spacing)

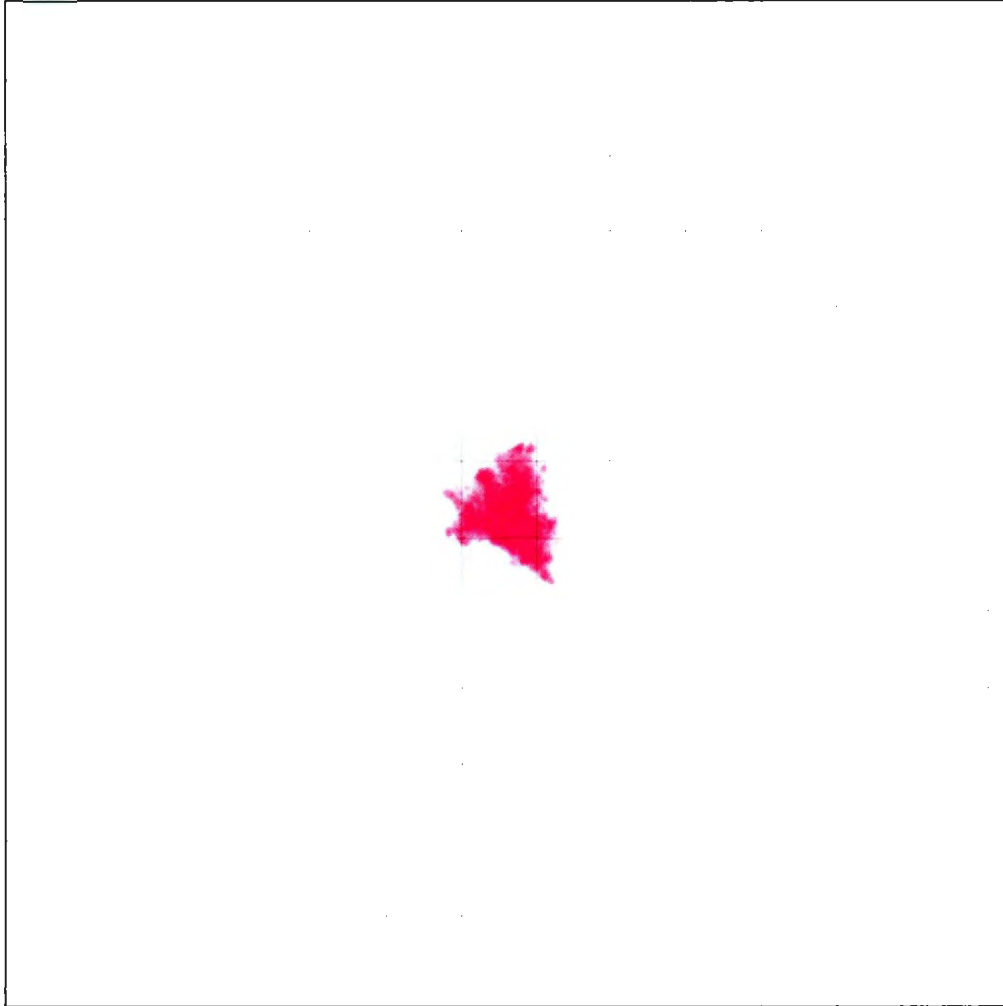


Figure 141 - F13T3a Medium (1cm x 1cm Grid Spacing)

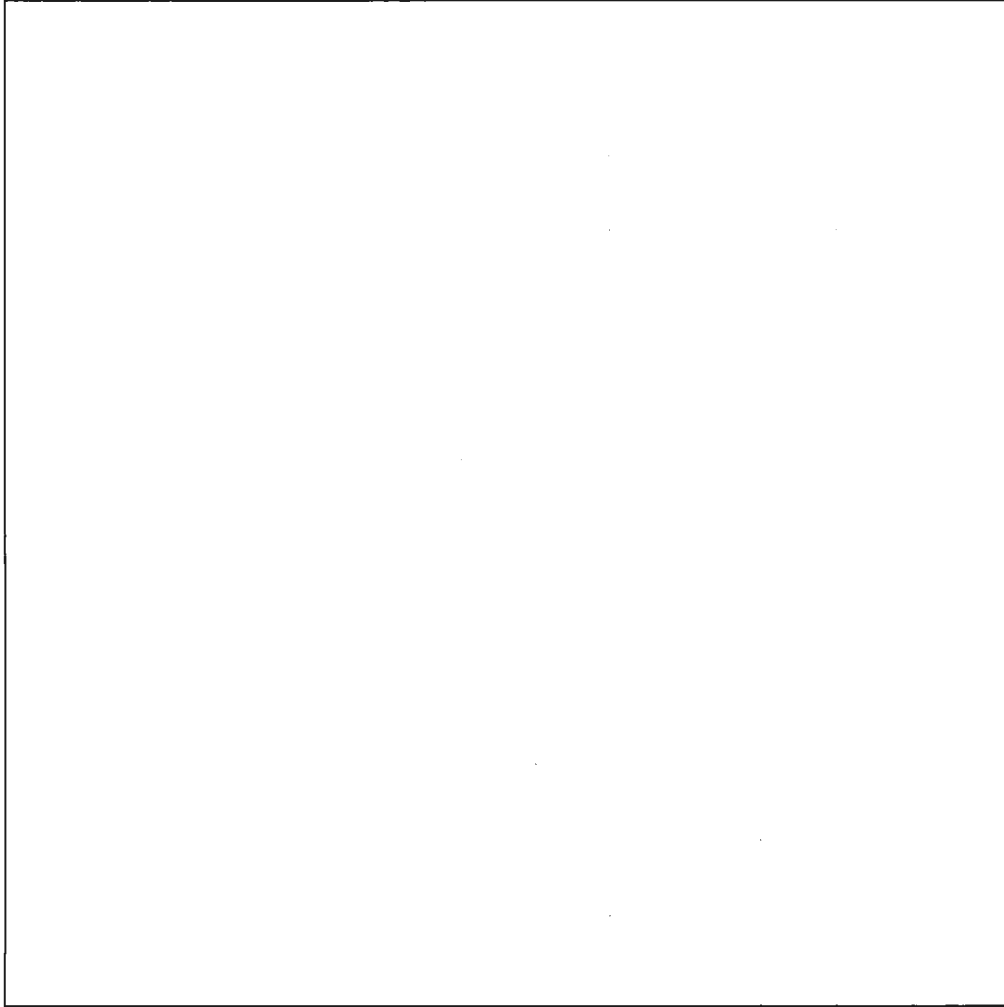


Figure 142 - F13T3a High (1cm x 1cm Grid Spacing)

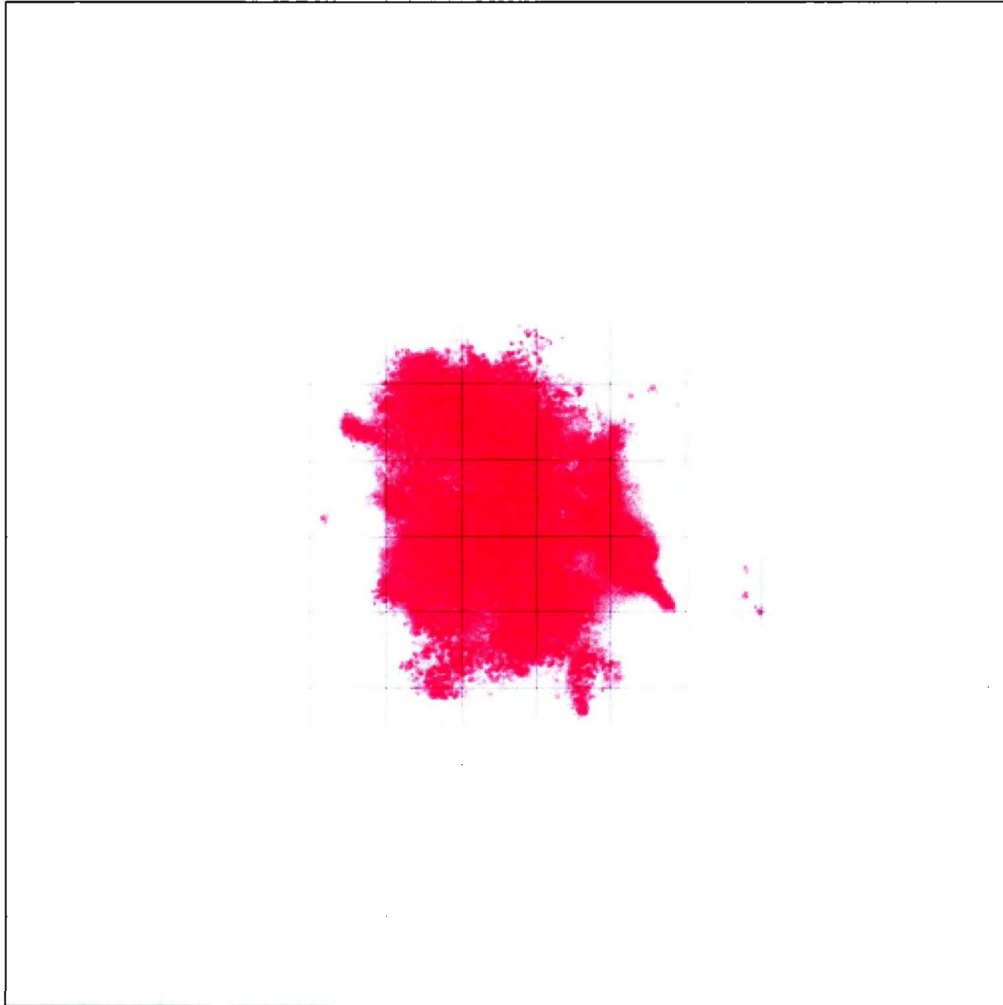


Figure 143 - F13T3b Low (1cm x 1cm Grid Spacing)

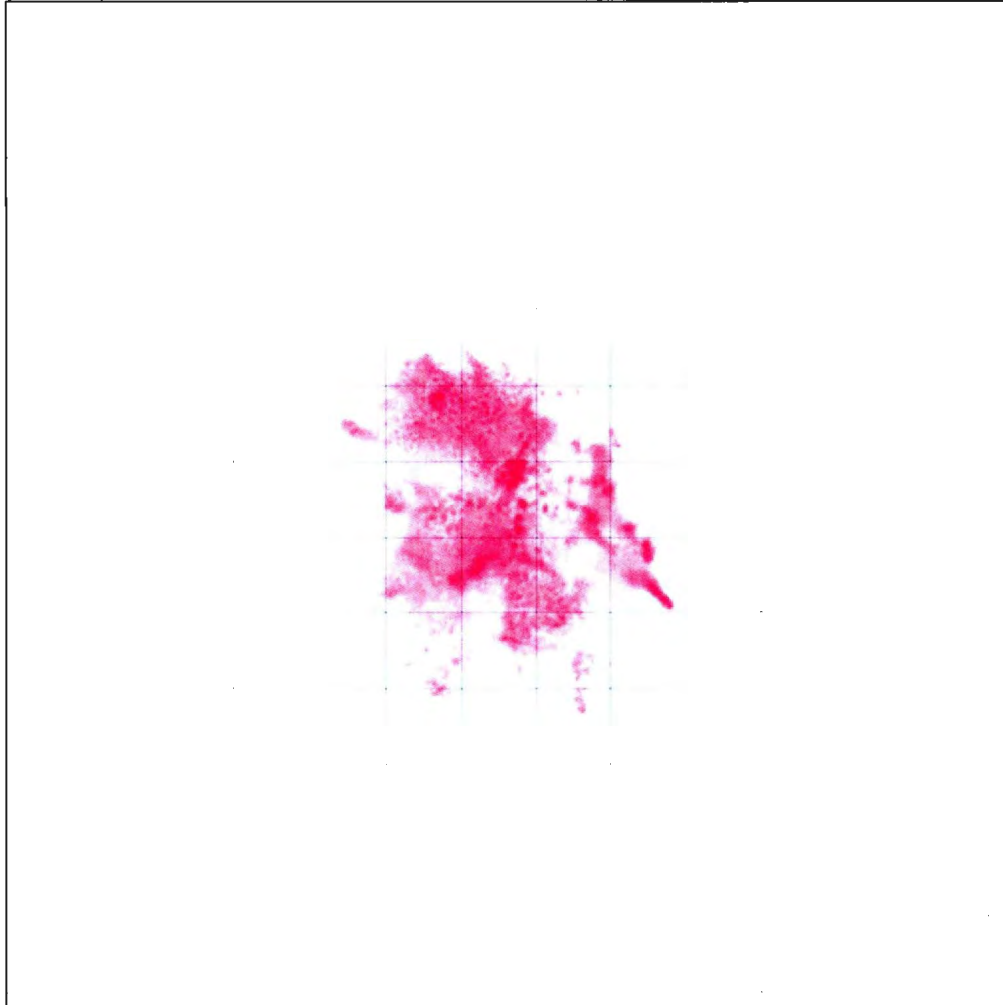


Figure 144 - F13T3b Medium (1cm x 1cm Grid Spacing)

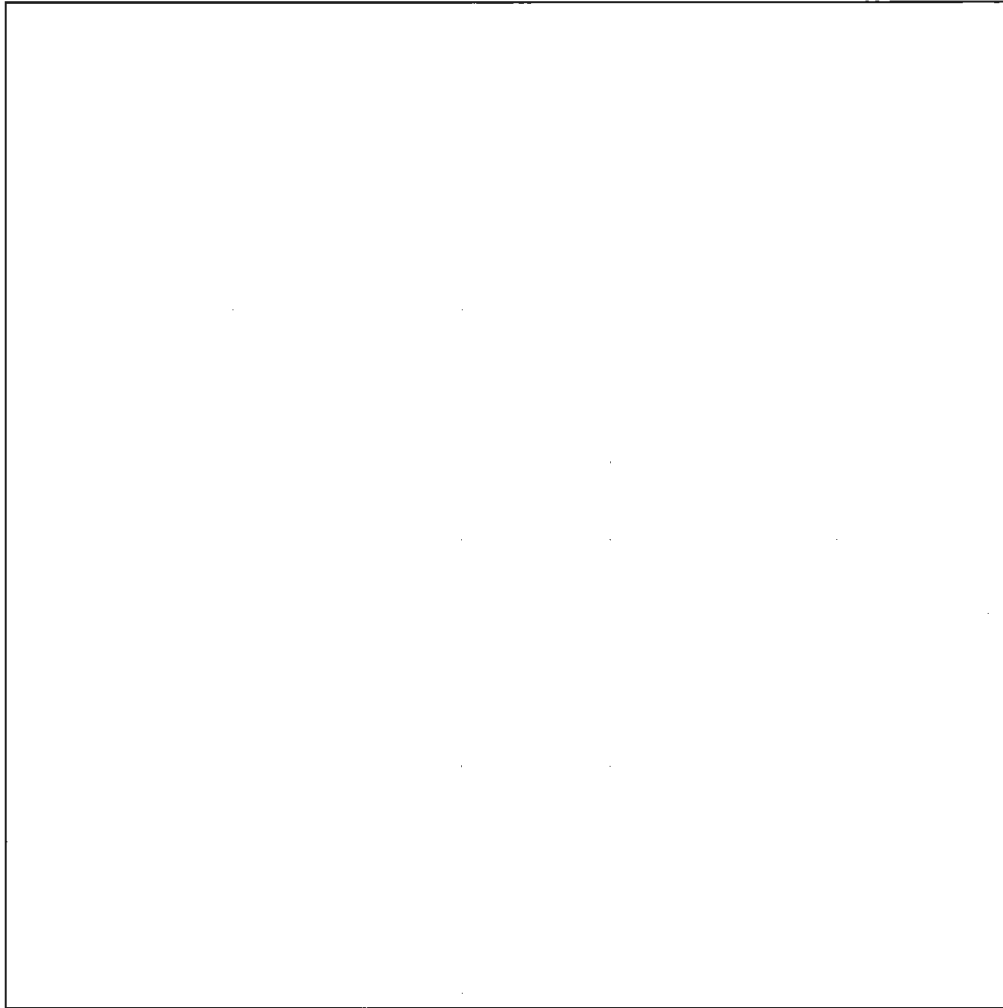


Figure 145 - F13T3b High (1cm x 1cm Grid Spacing)

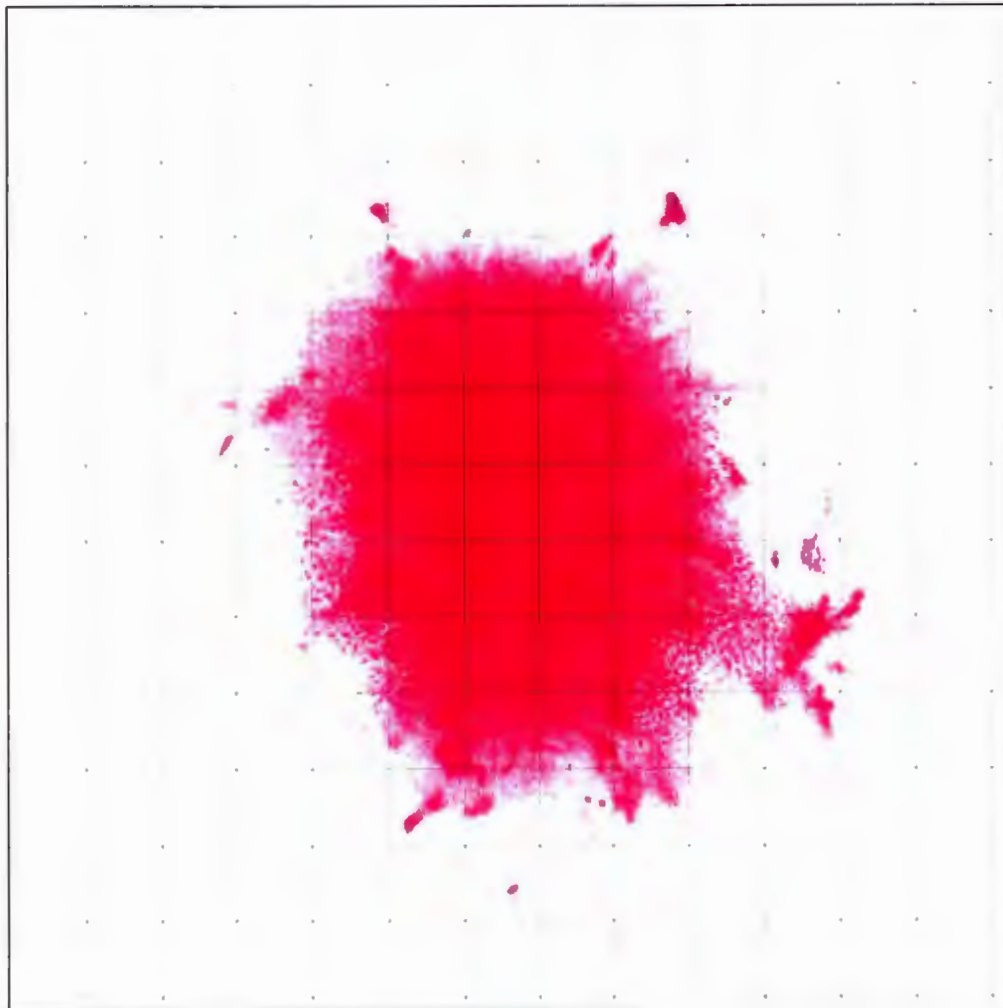


Figure 146 - F13T3c Low (1cm x 1cm Grid Spacing)

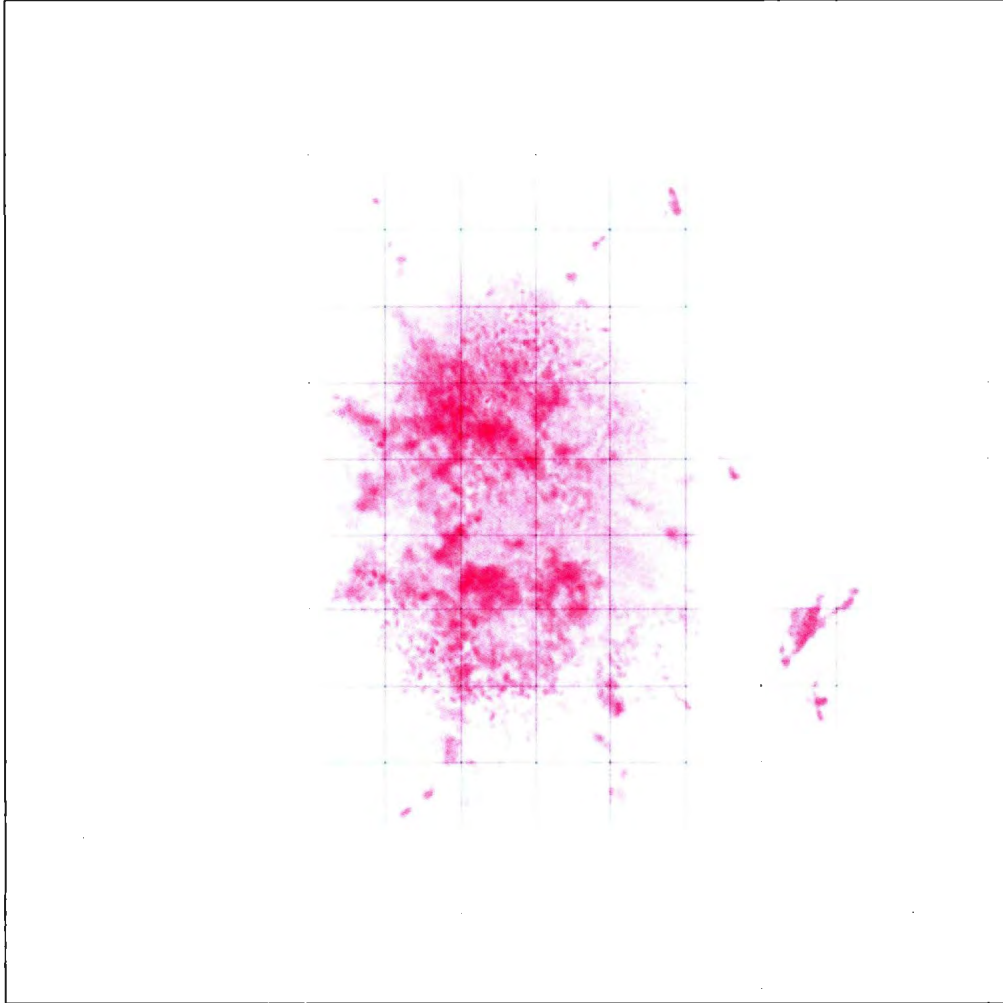


Figure 147 - F13T3c Medium (1cm x 1cm Grid Spacing)

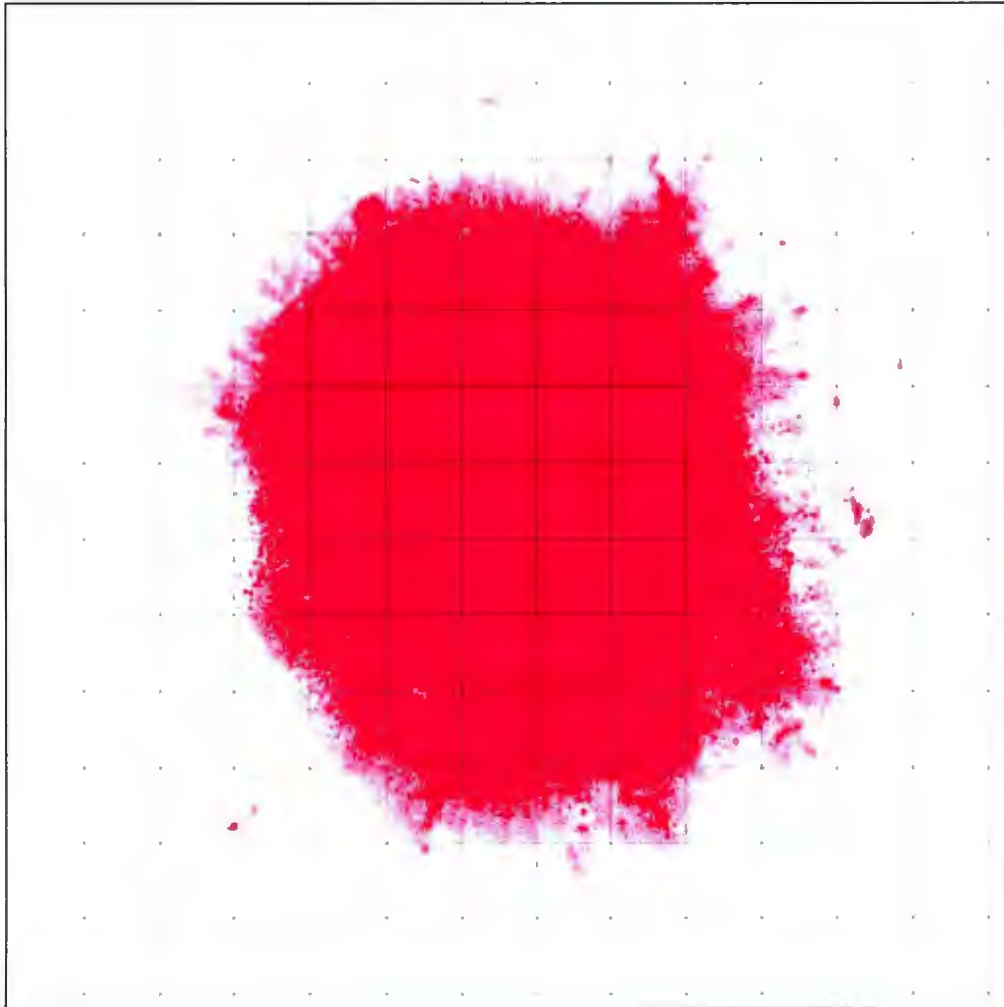


Figure 148 - F13T3d Low (1cm x 1cm Grid Spacing)

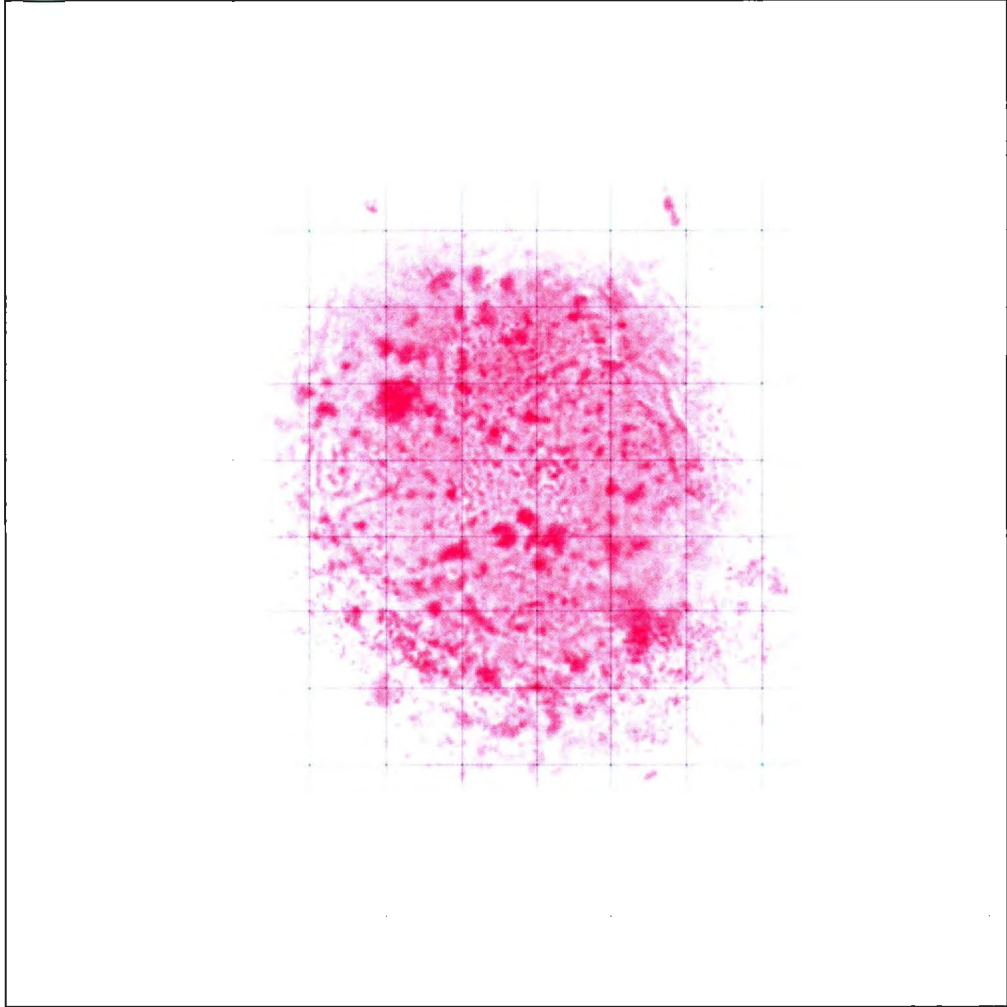


Figure 149 - F13T3d Medium (1cm x 1cm Grid Spacing)

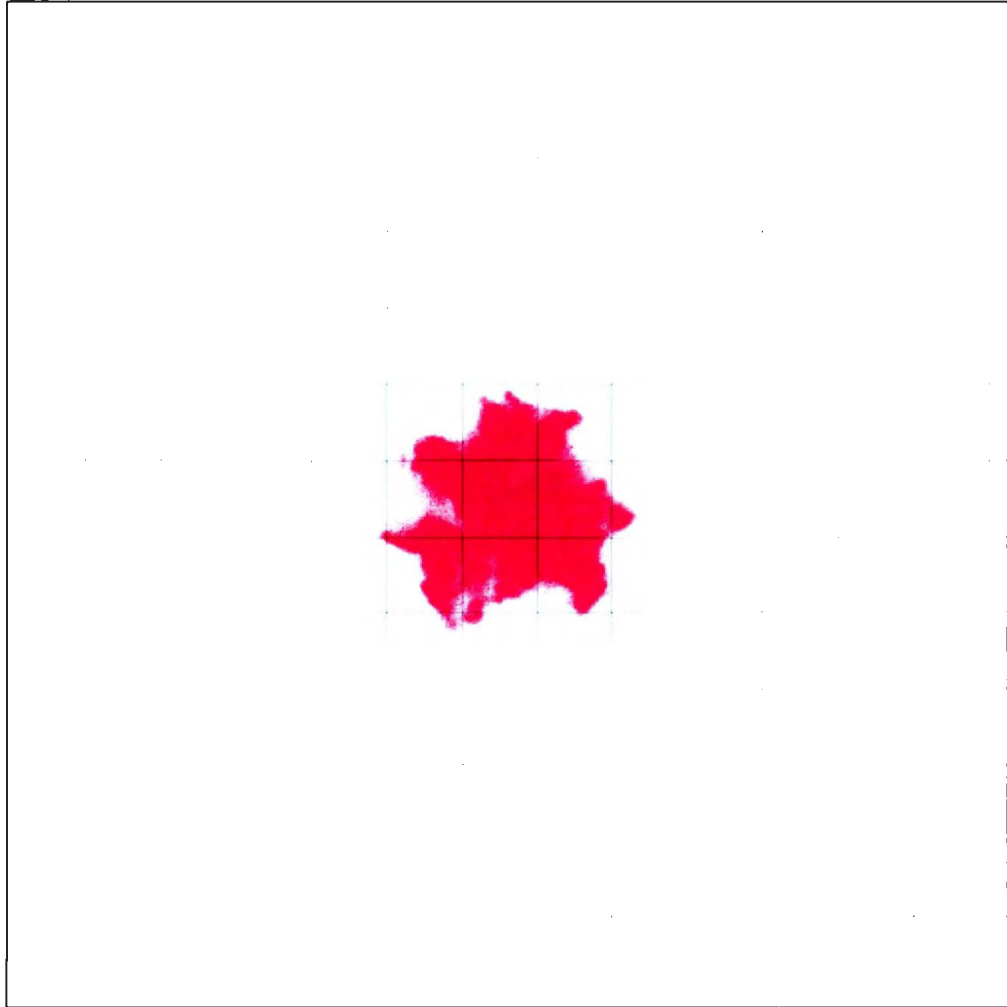


Figure 150 - F16T1a Low (1cm x 1cm Grid Spacing)

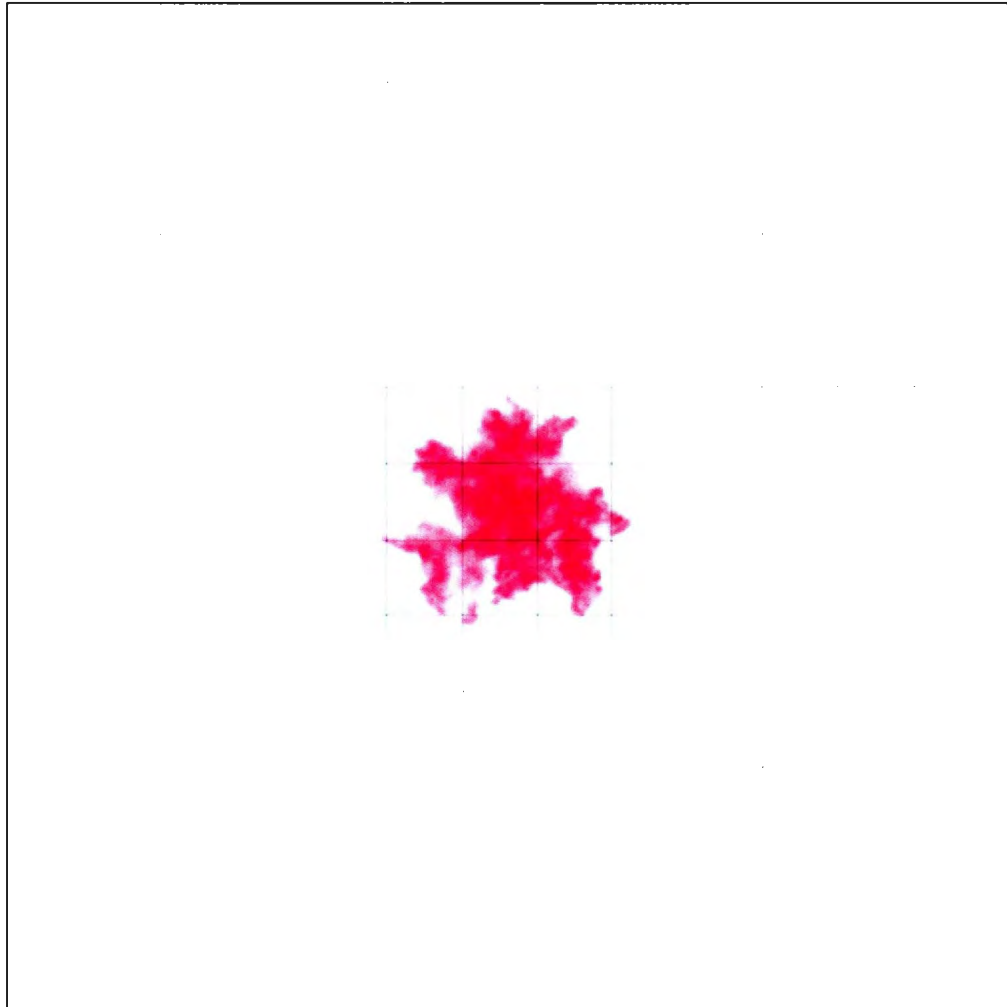


Figure 151 - F16T1a Medium (1cm x 1cm Grid Spacing)

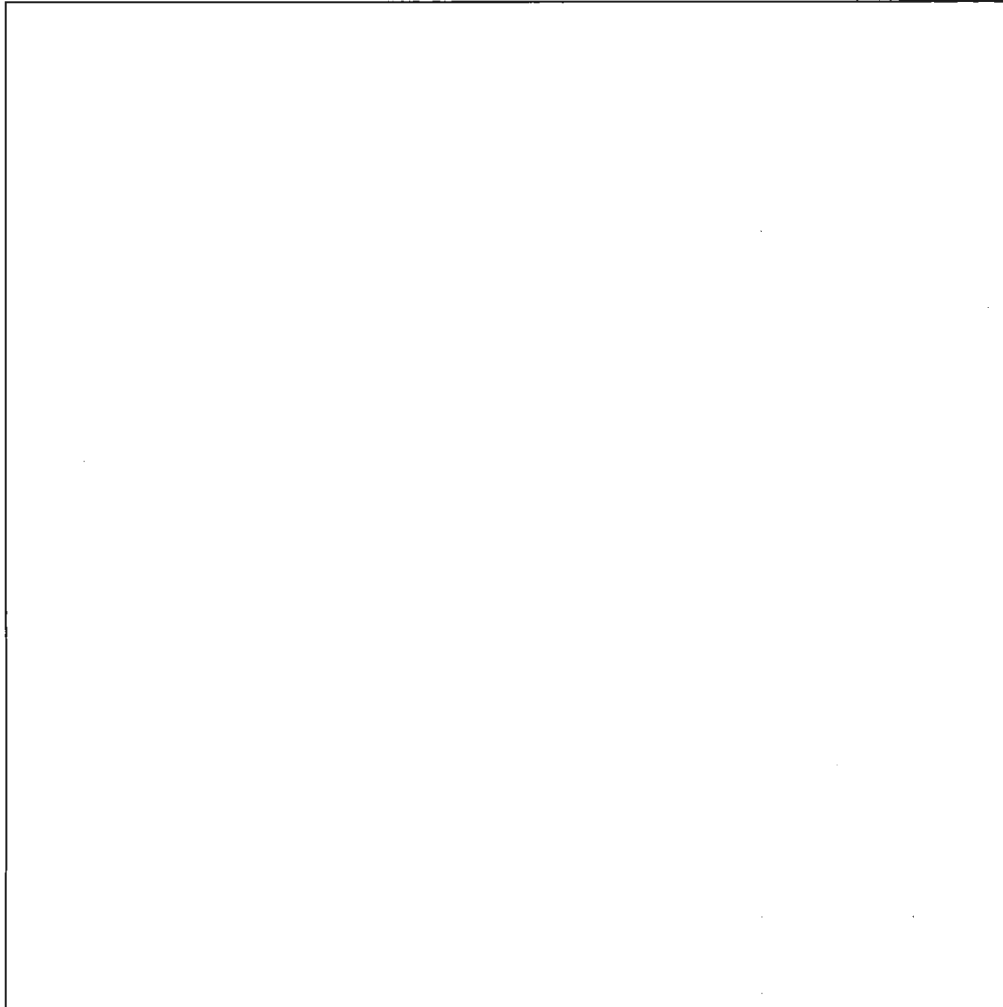


Figure 152 - F16T1a High (1cm x 1cm Grid Spacing)

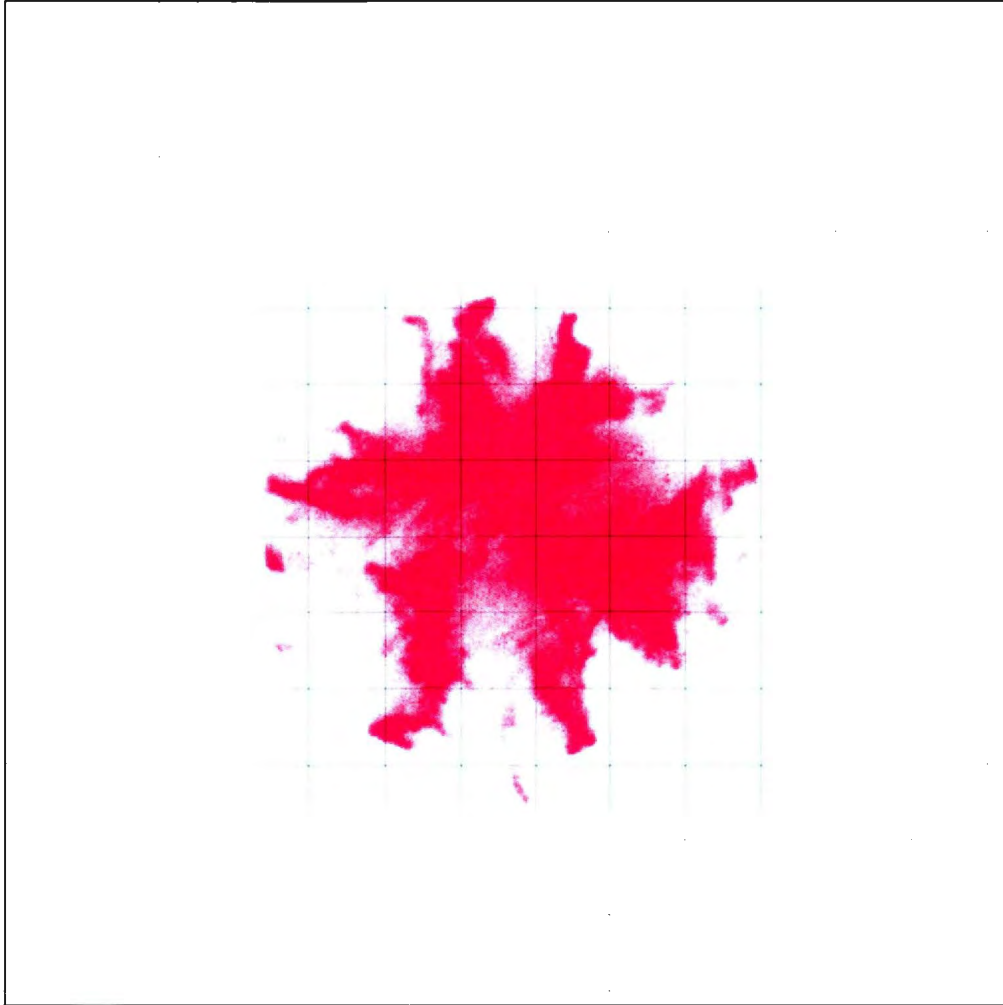


Figure 153 - F16T1b Low (1cm x 1cm Grid Spacing)

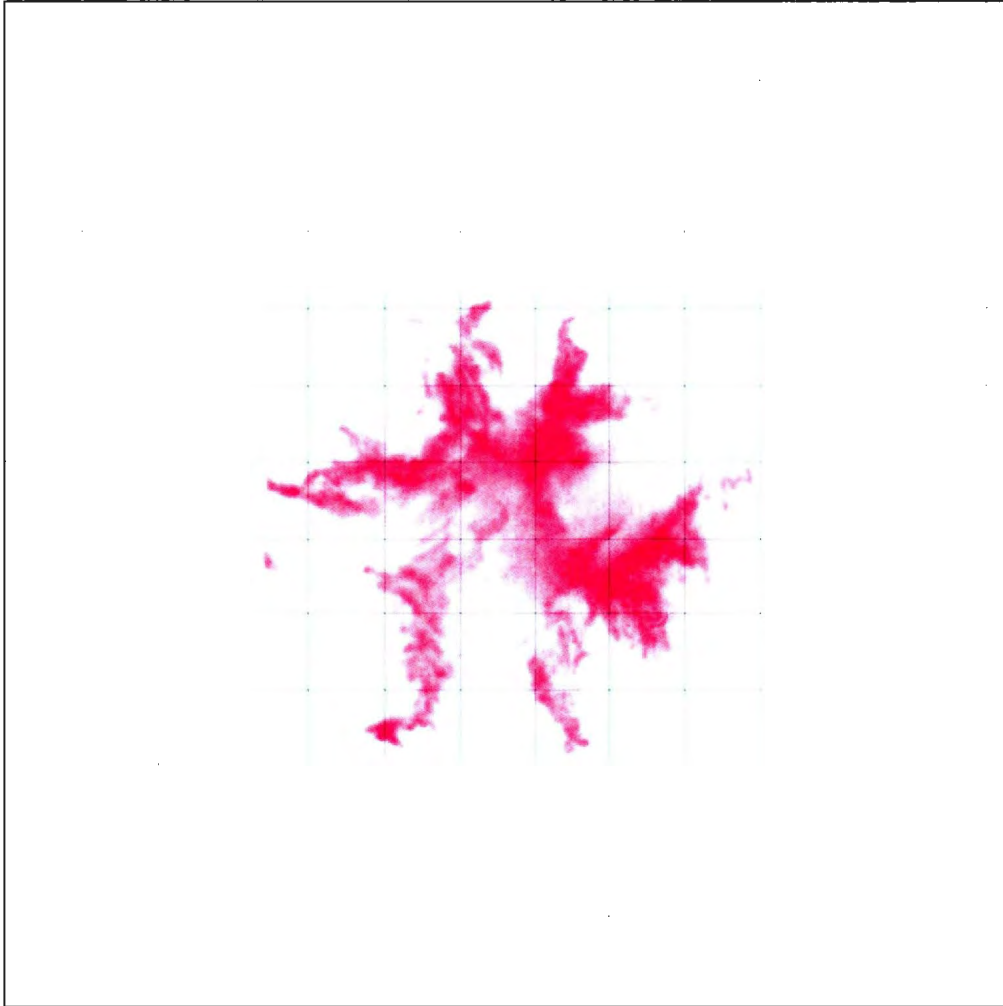


Figure 154 - F16T1b Medium (1cm x 1cm Grid Spacing)

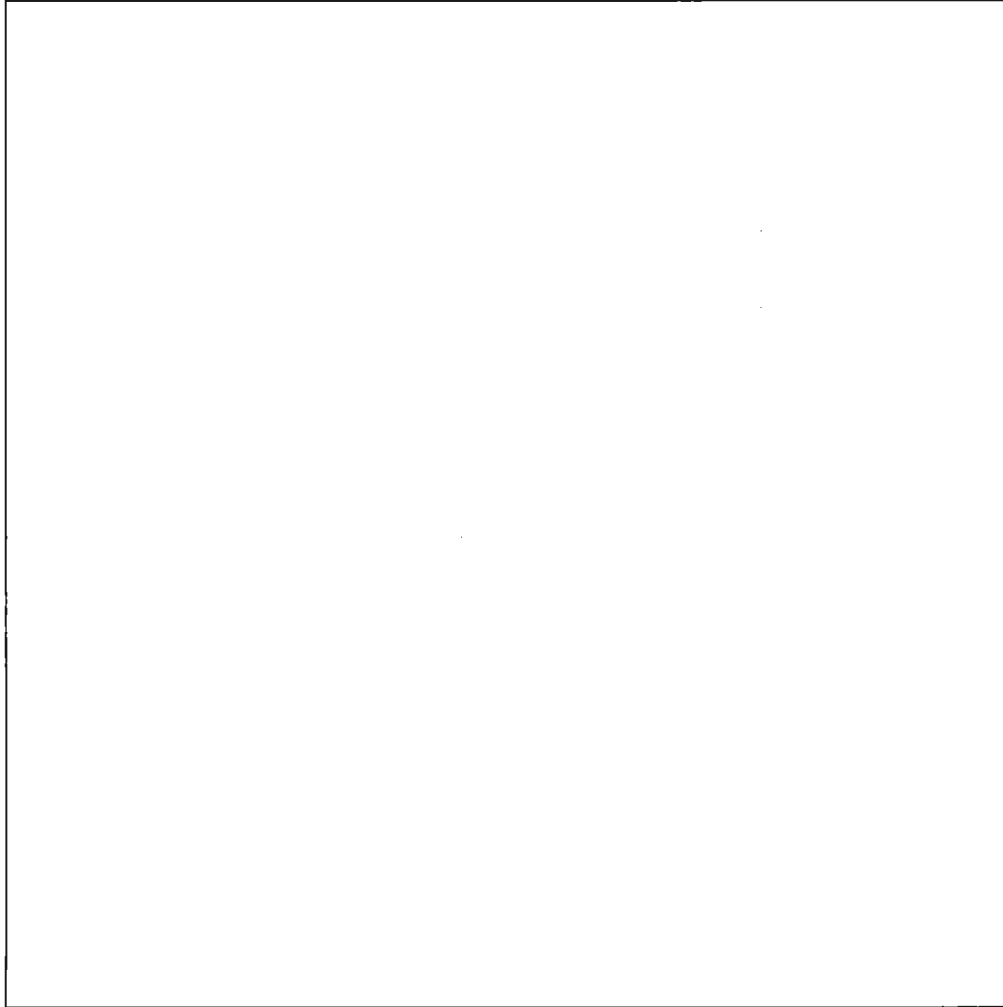


Figure 155 - F16T1b High (1cm x 1cm Grid Spacing)

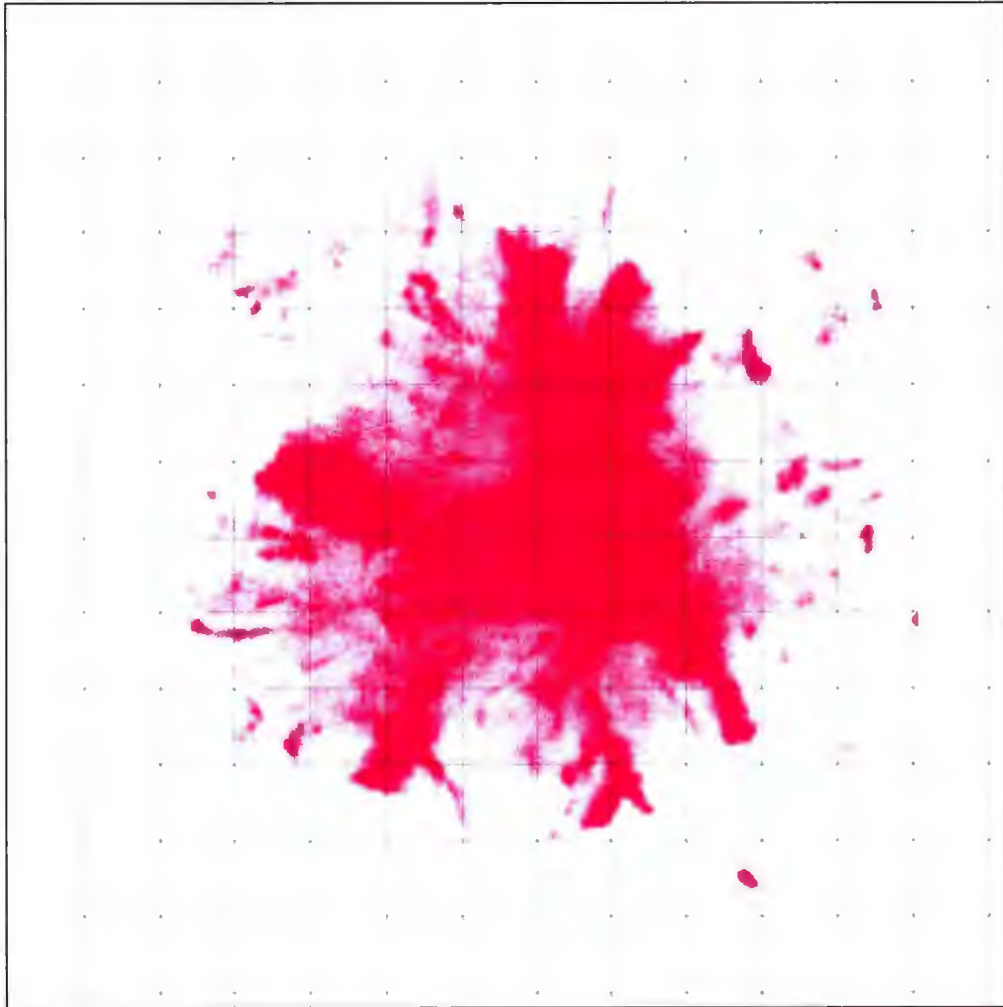


Figure 156 - F16T1c Low (1cm x 1cm Grid Spacing)

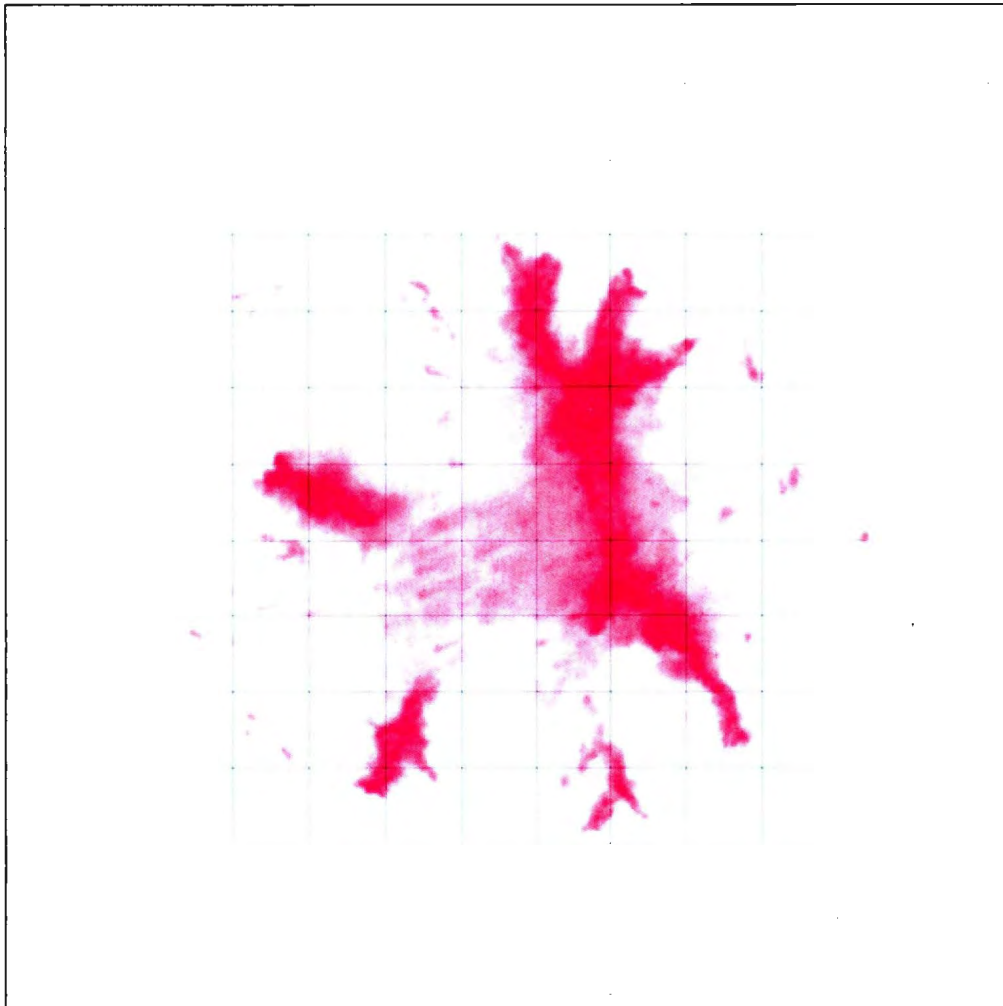


Figure 157 - F16T1c Medium (1cm x 1cm Grid Spacing)

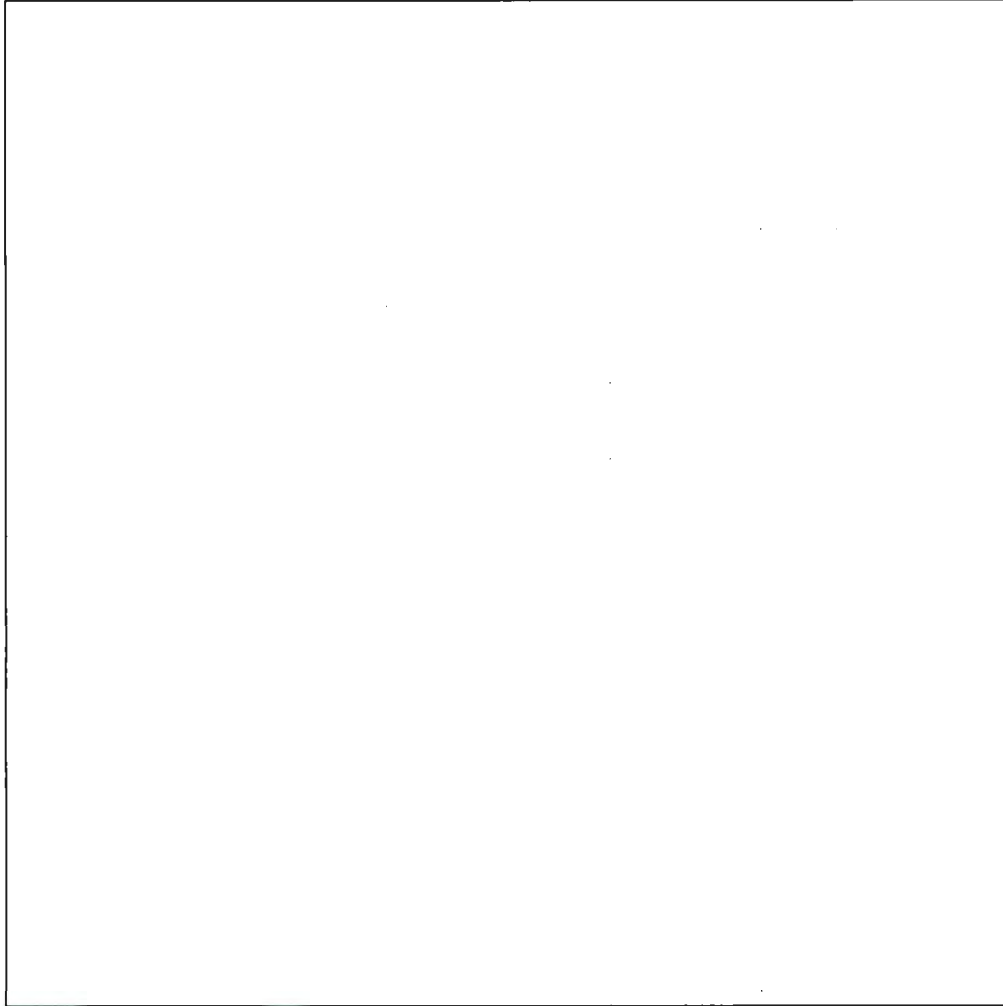


Figure 158 - F16T1c High (1cm x 1cm Grid Spacing)

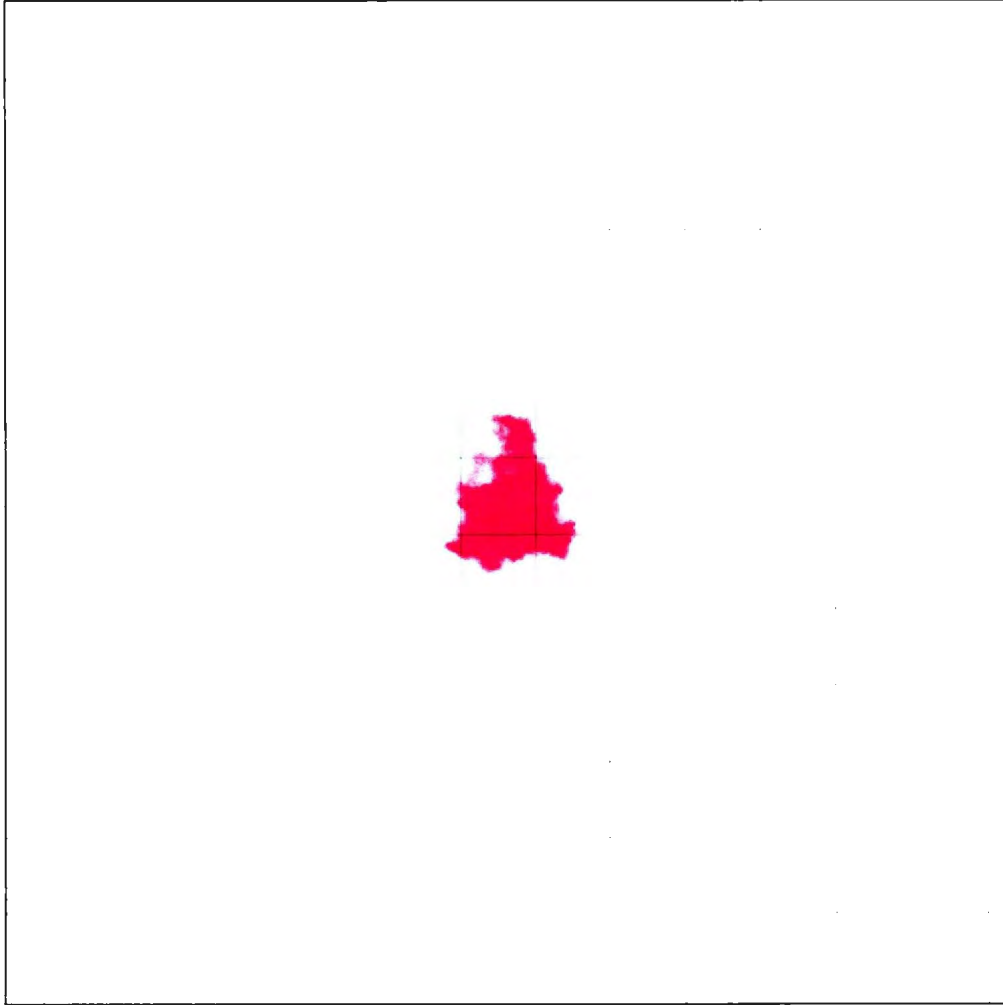


Figure 159 - F20T1a Low (1cm x 1cm Grid Spacing)

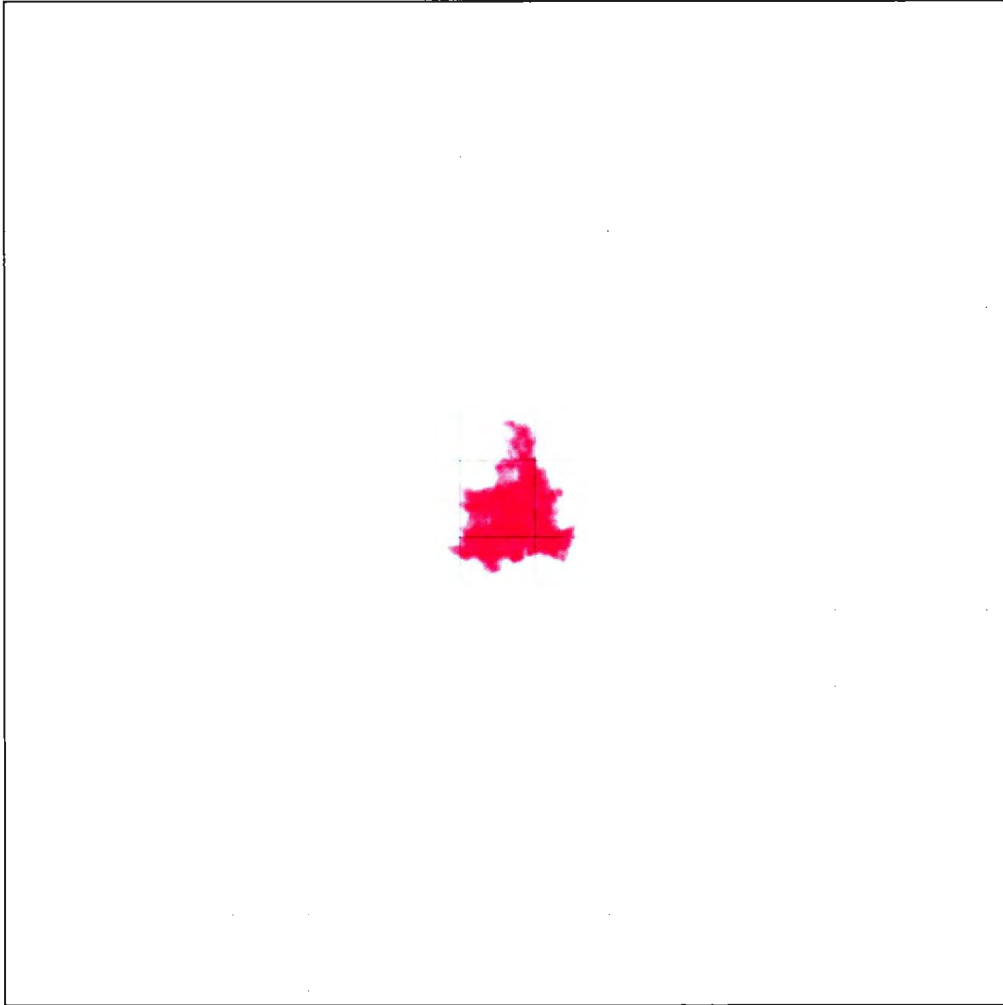


Figure 160 - F20T1a Medium (1cm x 1cm Grid Spacing)

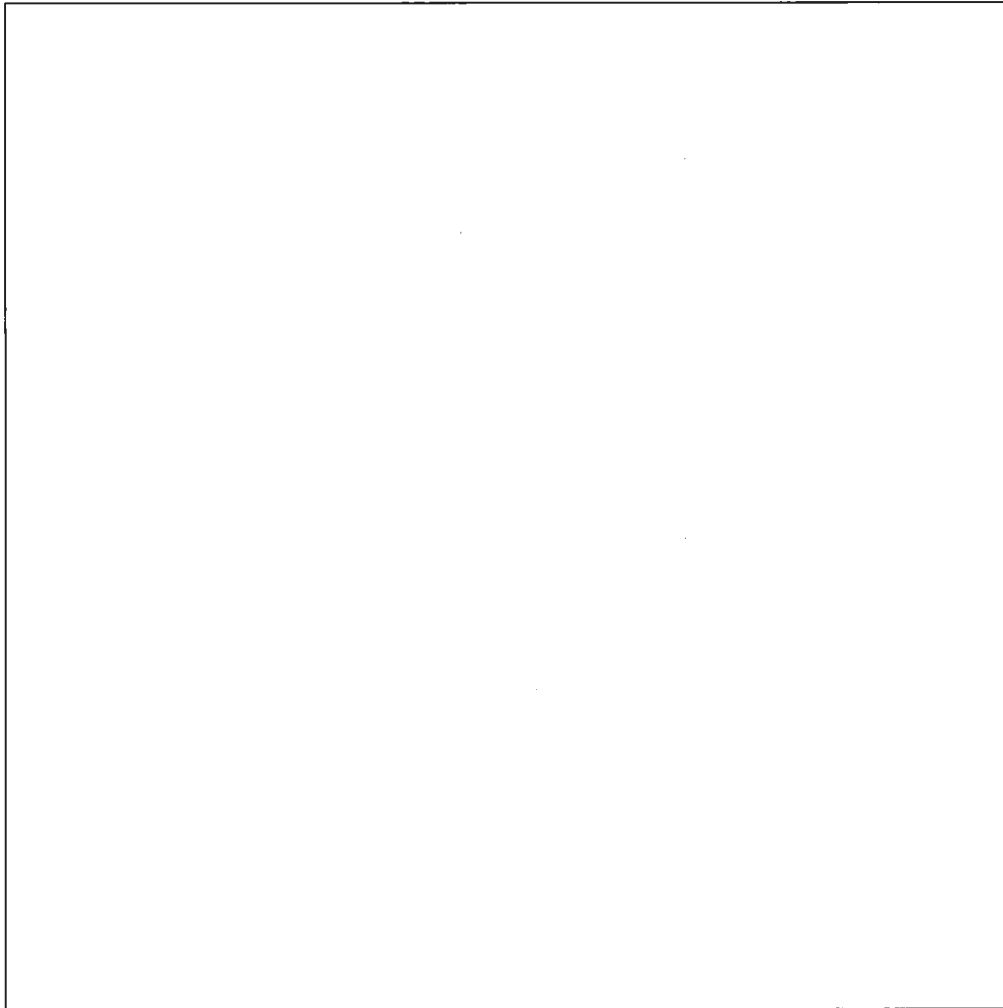


Figure 161 - F20T1a High (1cm x 1cm Grid Spacing)

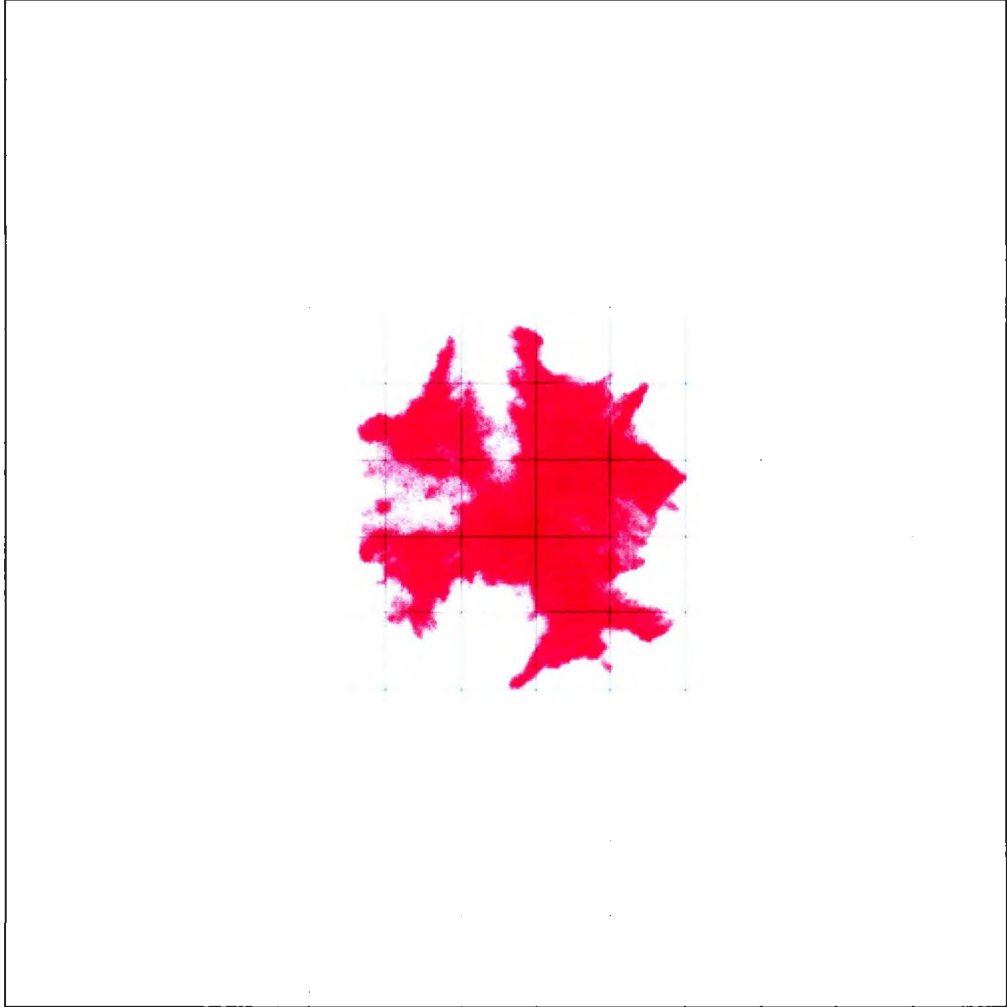


Figure 162 - F20T1b Low (1cm x 1cm Grid Spacing)

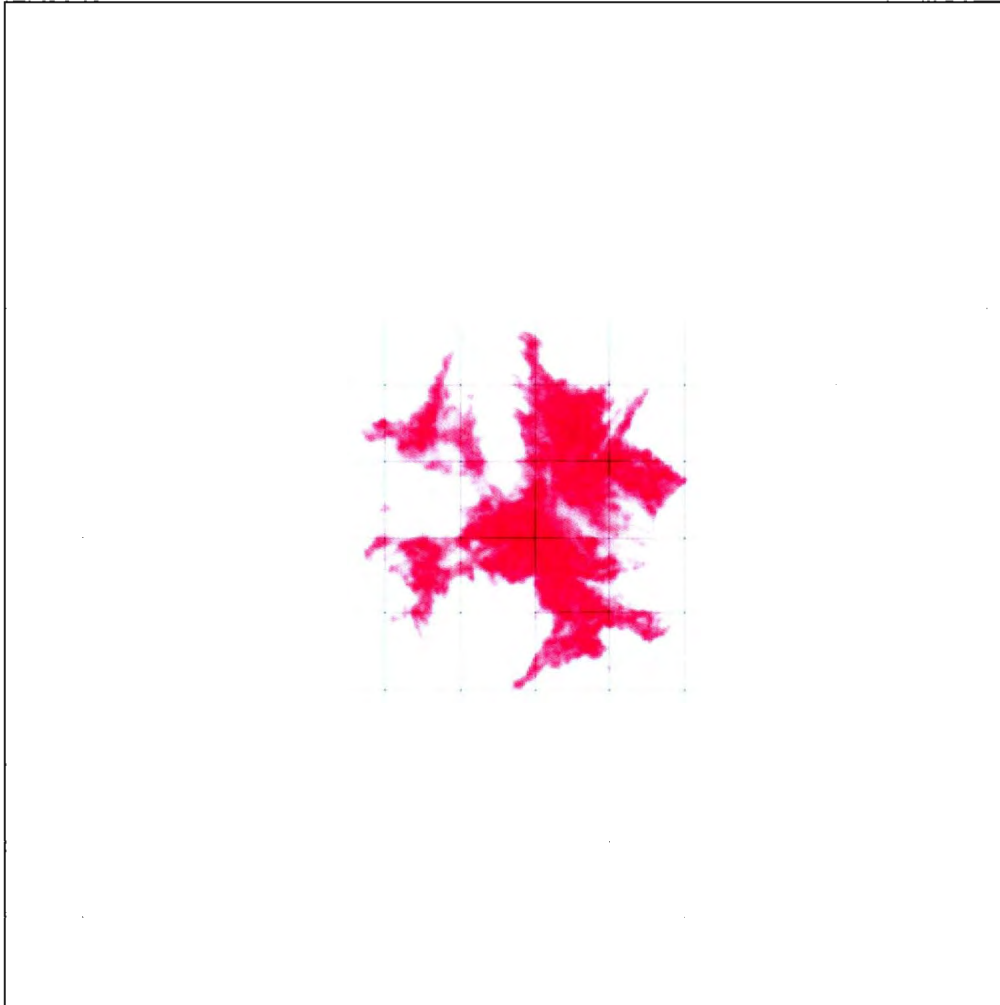


Figure 163 - F20T1b Medium (1cm x 1cm Grid Spacing)

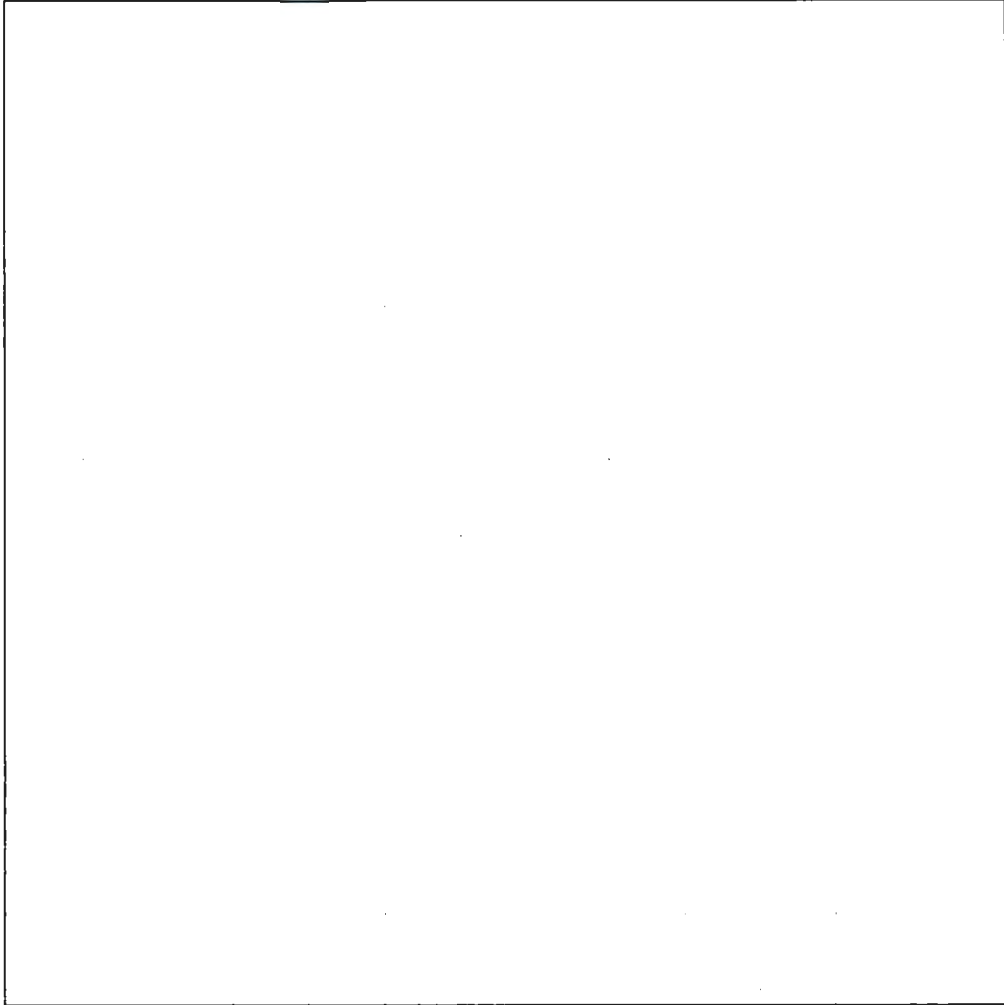


Figure 164 - F20T1b High (1cm x 1cm Grid Spacing)

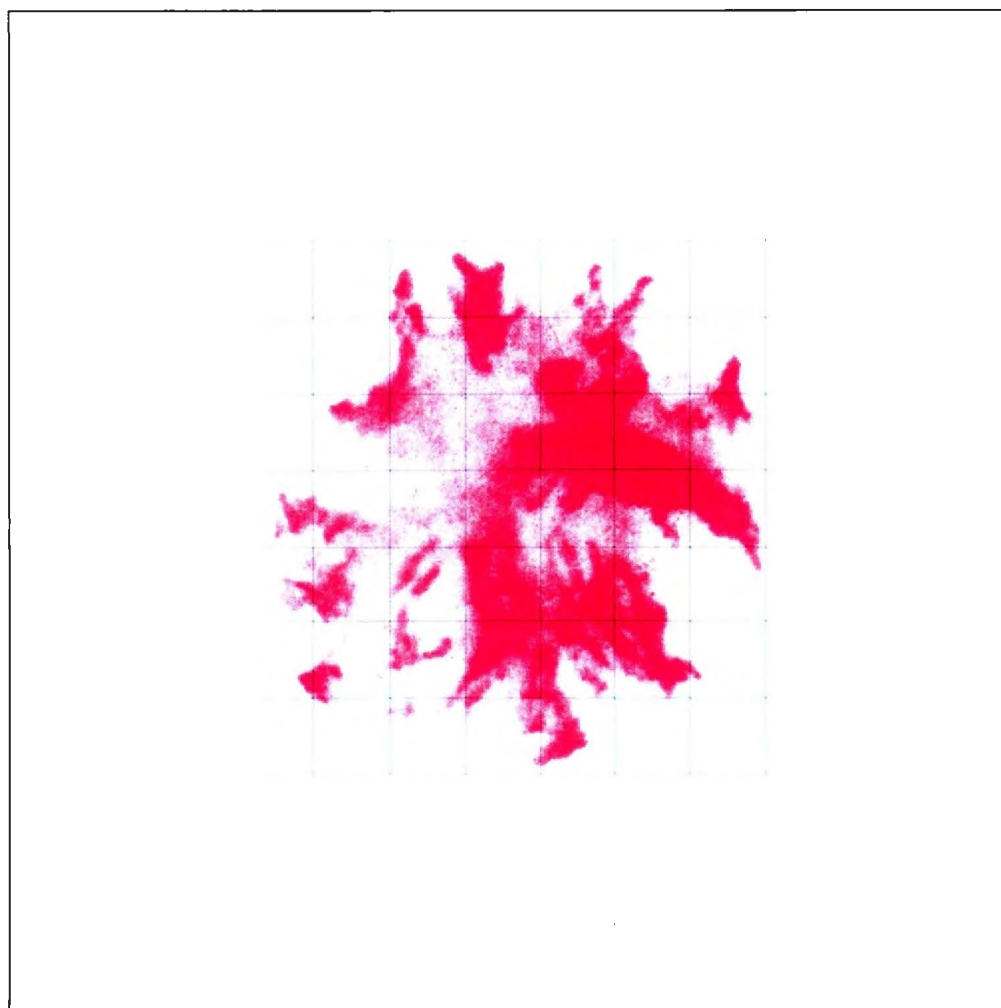


Figure 165 - F20T1c Low (1cm x 1cm Grid Spacing)

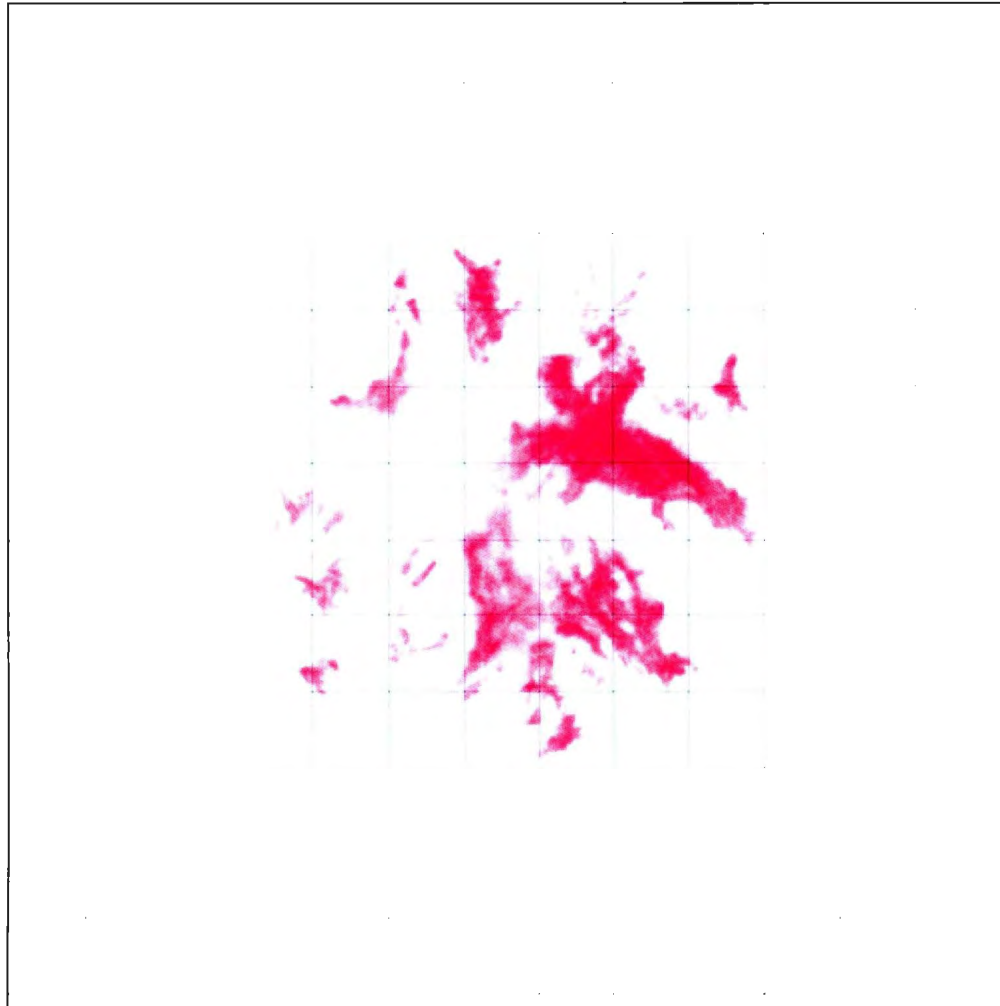


Figure 166 - F20T1c Medium (1cm x 1cm Grid Spacing)

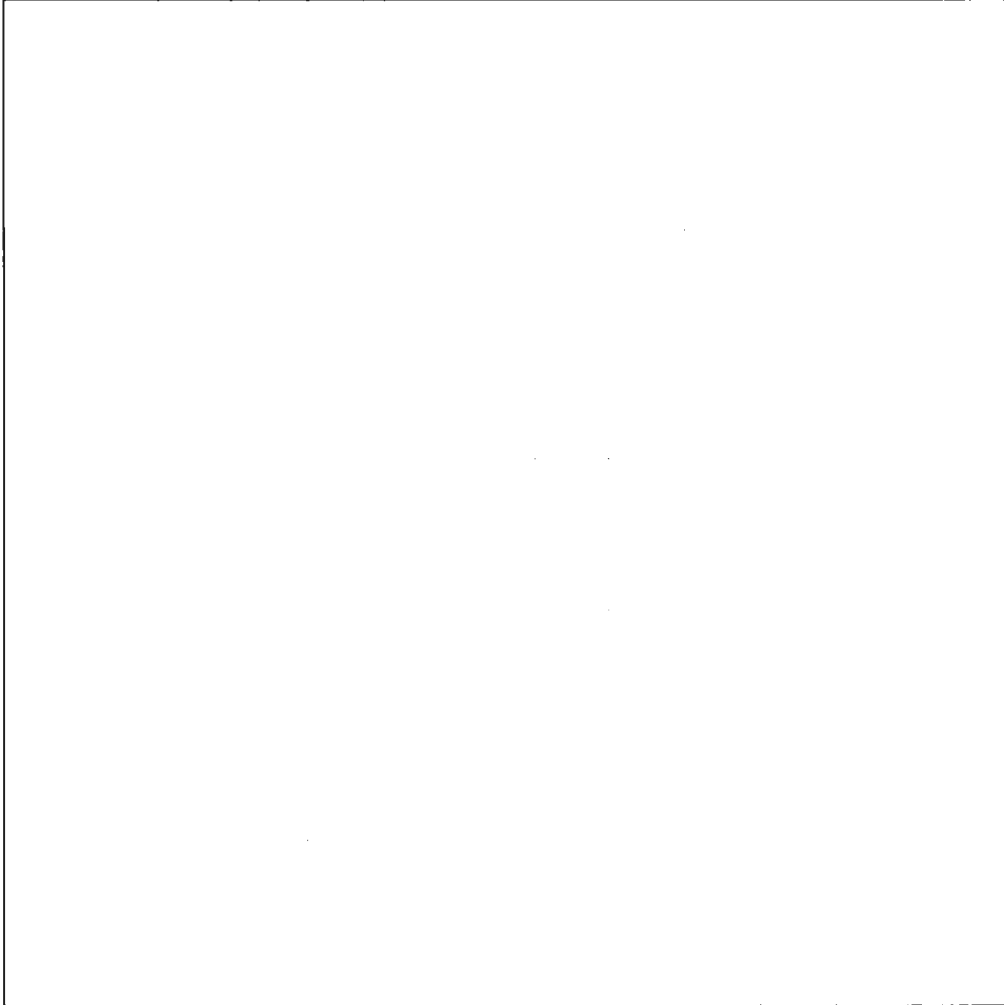


Figure 167 - F20T1c High (1cm x 1cm Grid Spacing)

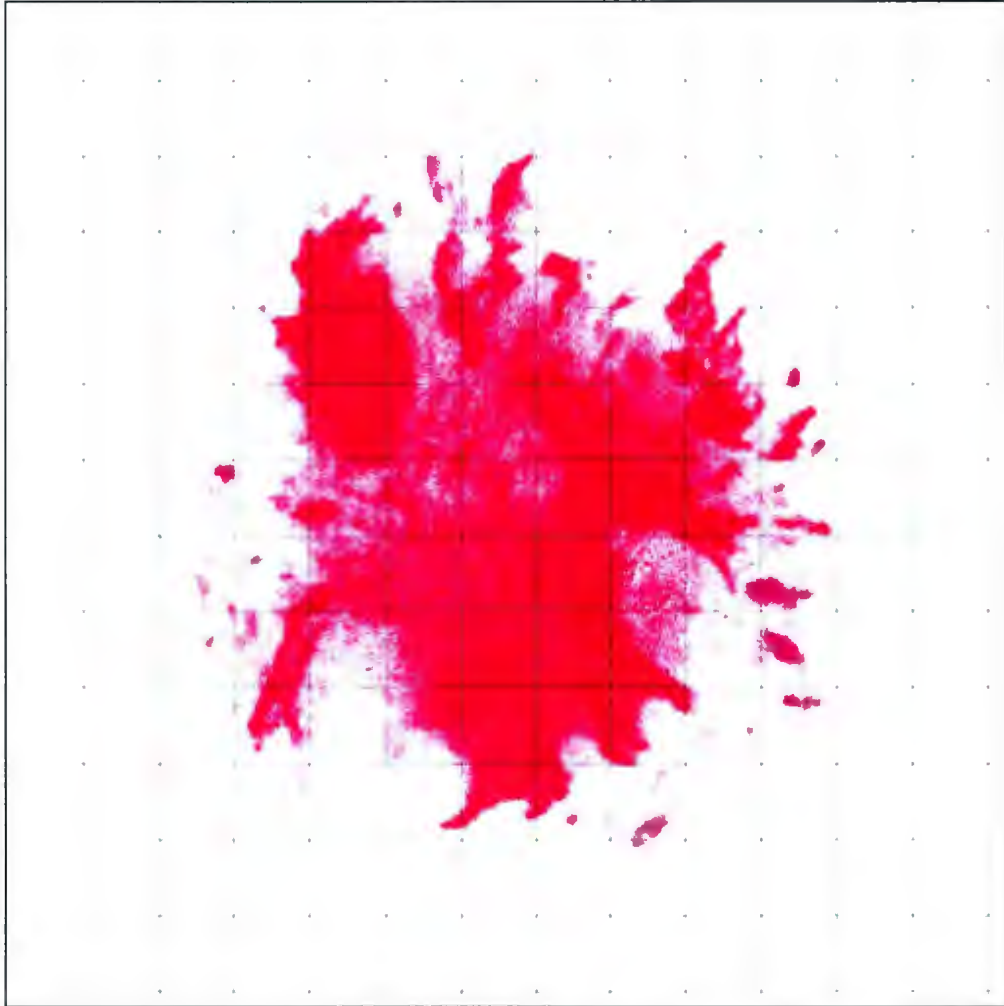


Figure 168 - F20T1d Low (1cm x 1cm Grid Spacing)

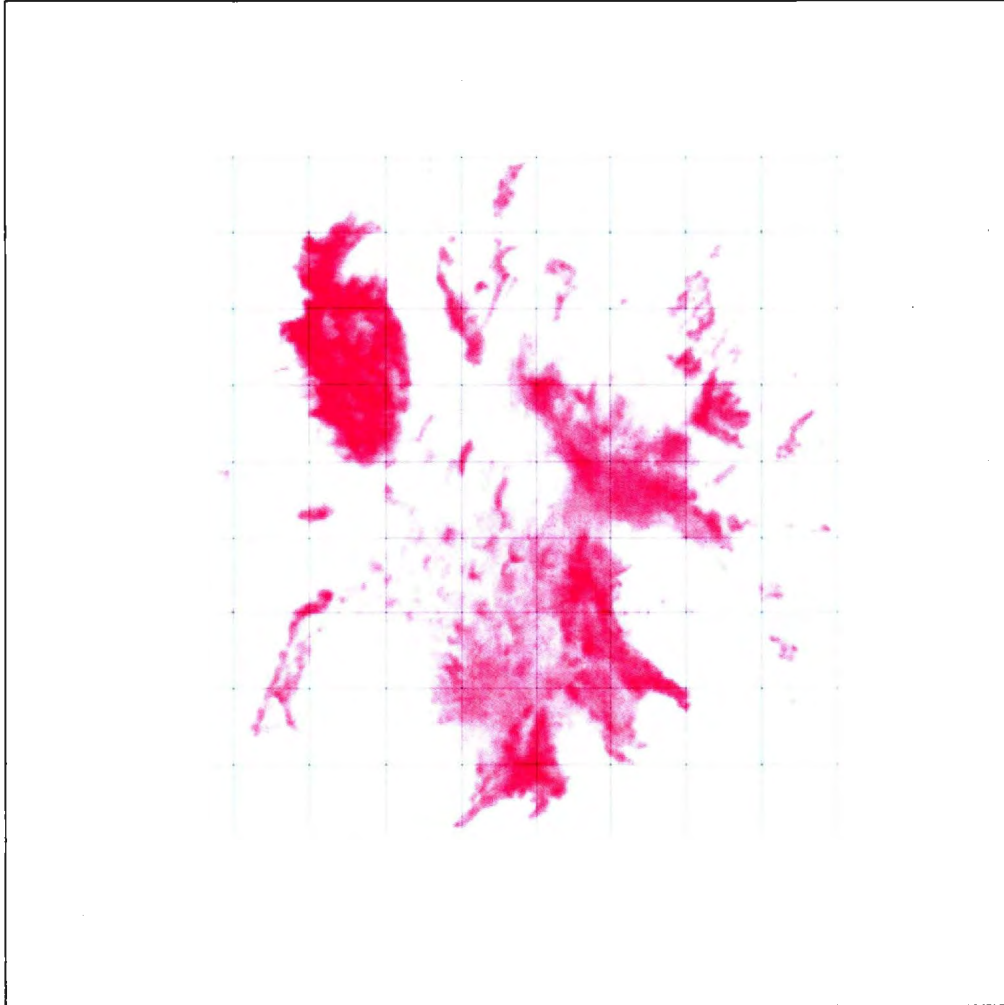


Figure 169 - F20T1d Medium (1cm x 1cm Grid Spacing)

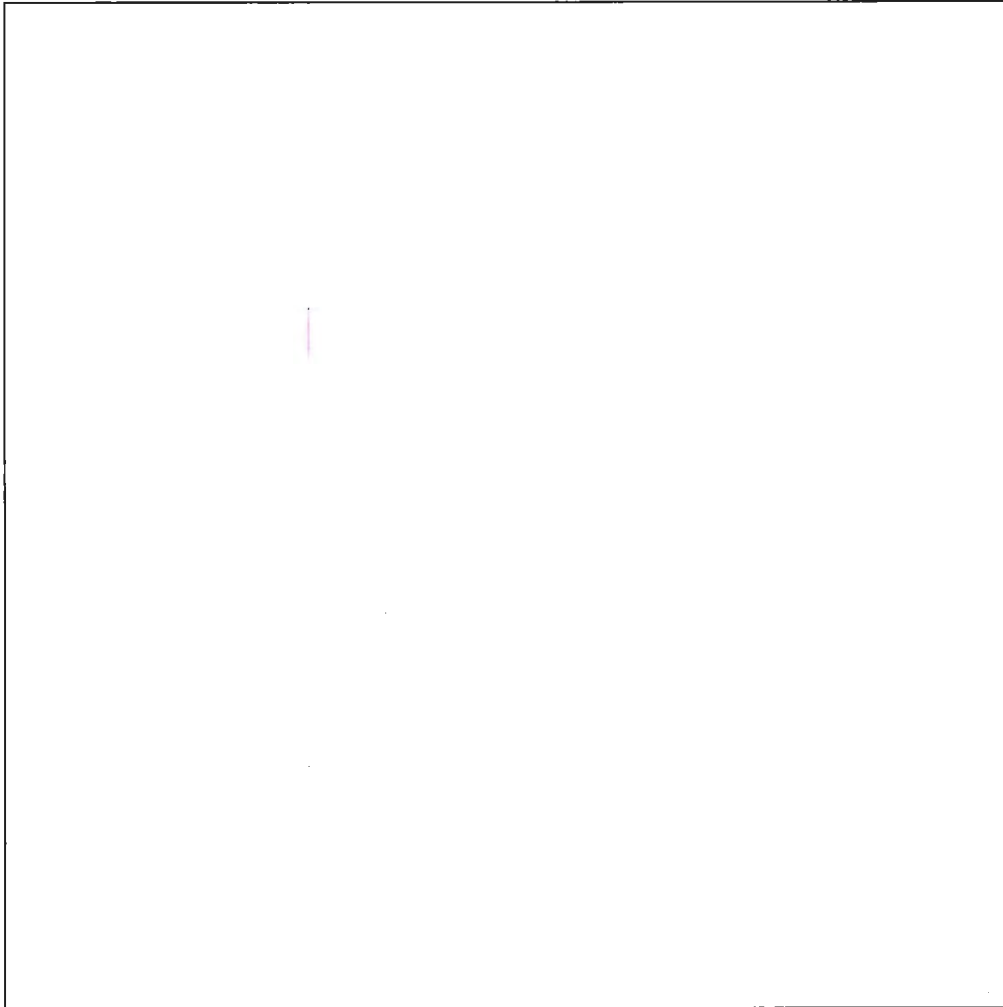


Figure 170 - F20T1d High (1cm x 1cm Grid Spacing)

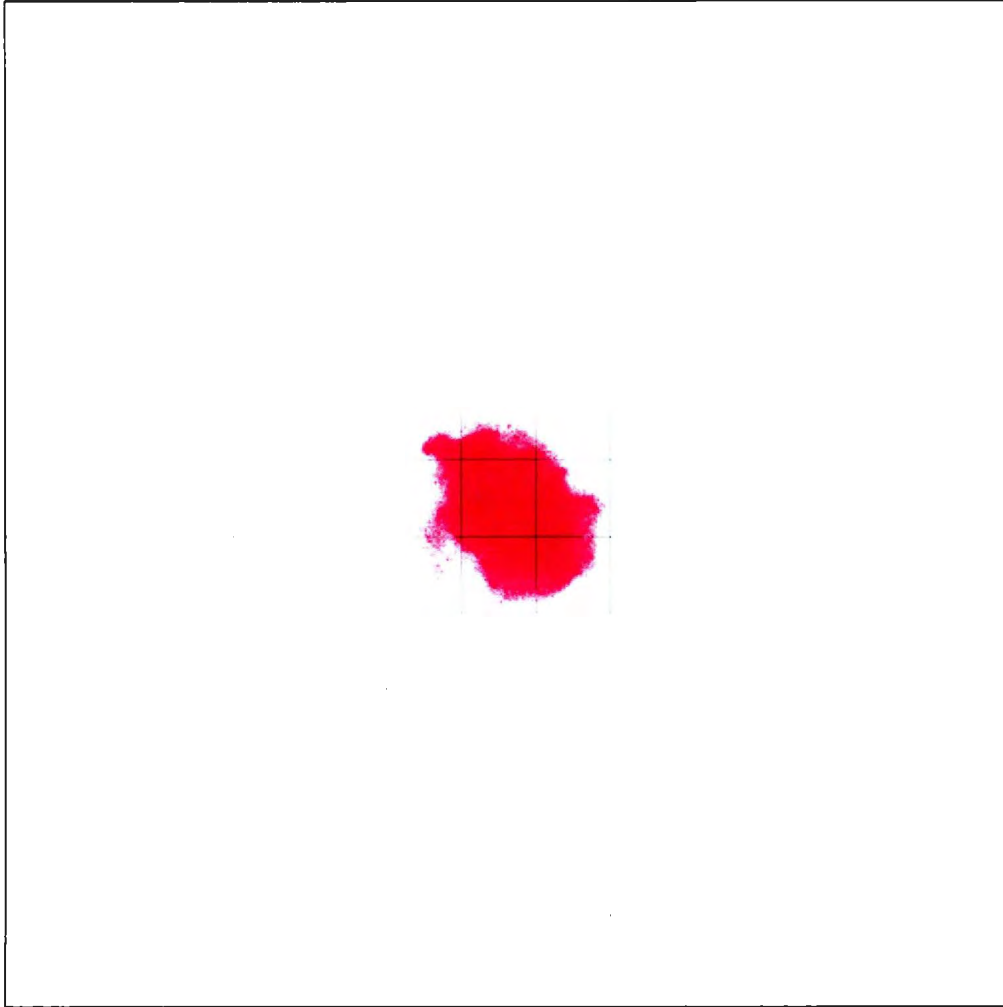


Figure 171 - F20T2a Low (1cm x 1cm Grid Spacing)

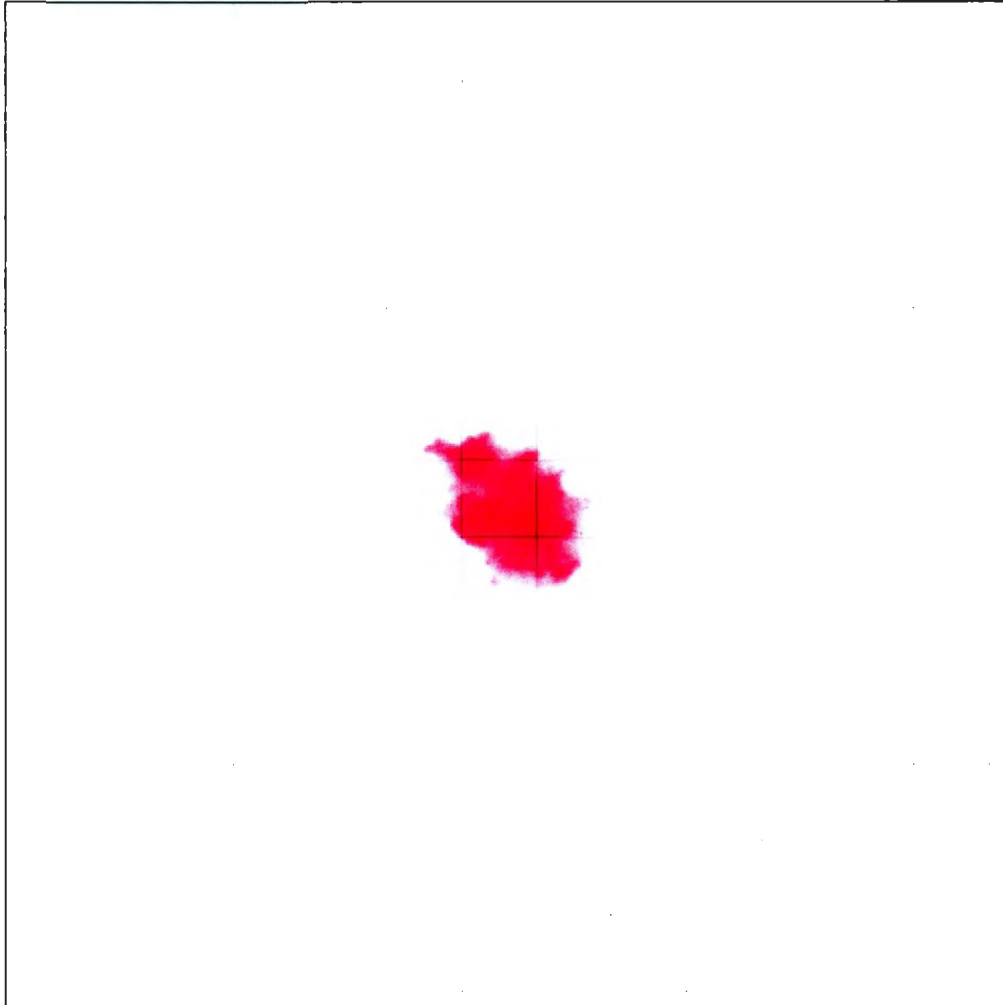


Figure 172 - F20T2a Medium (1cm x 1cm Grid Spacing)

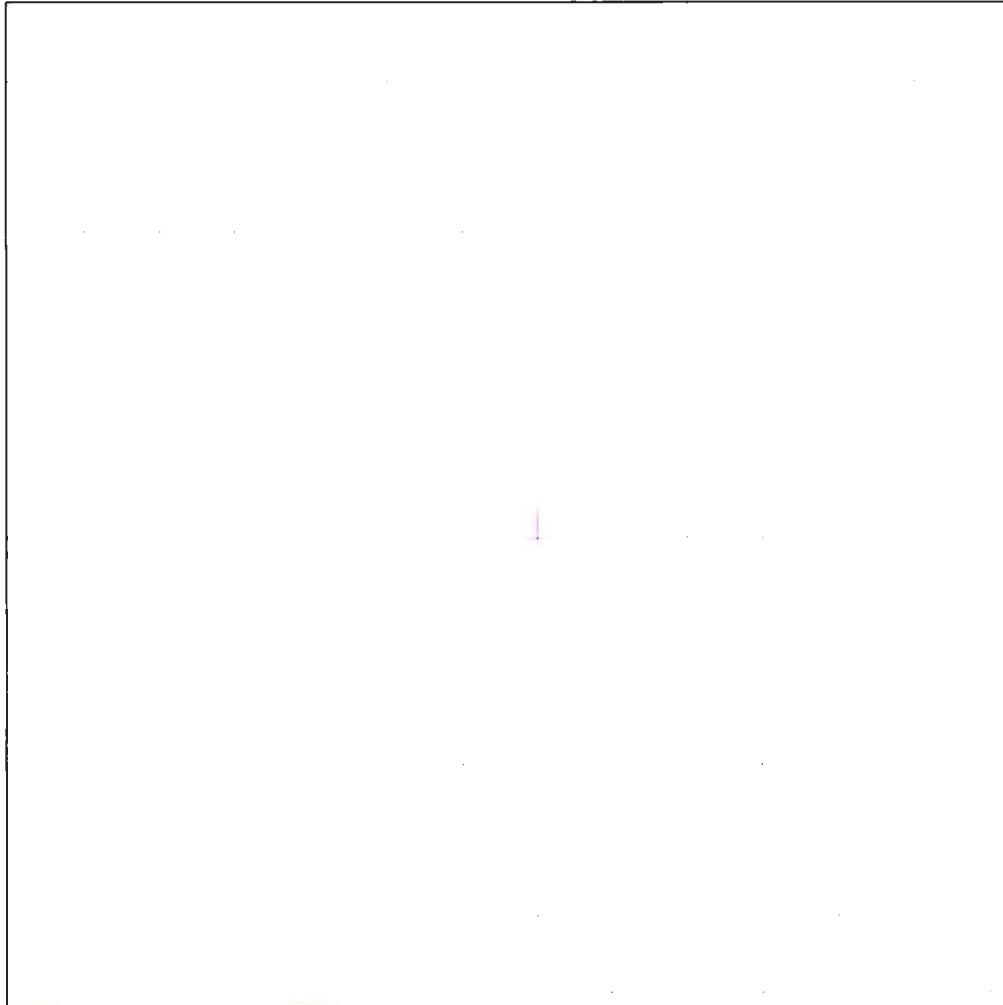


Figure 173 - F20T2a High (1cm x 1cm Grid Spacing)

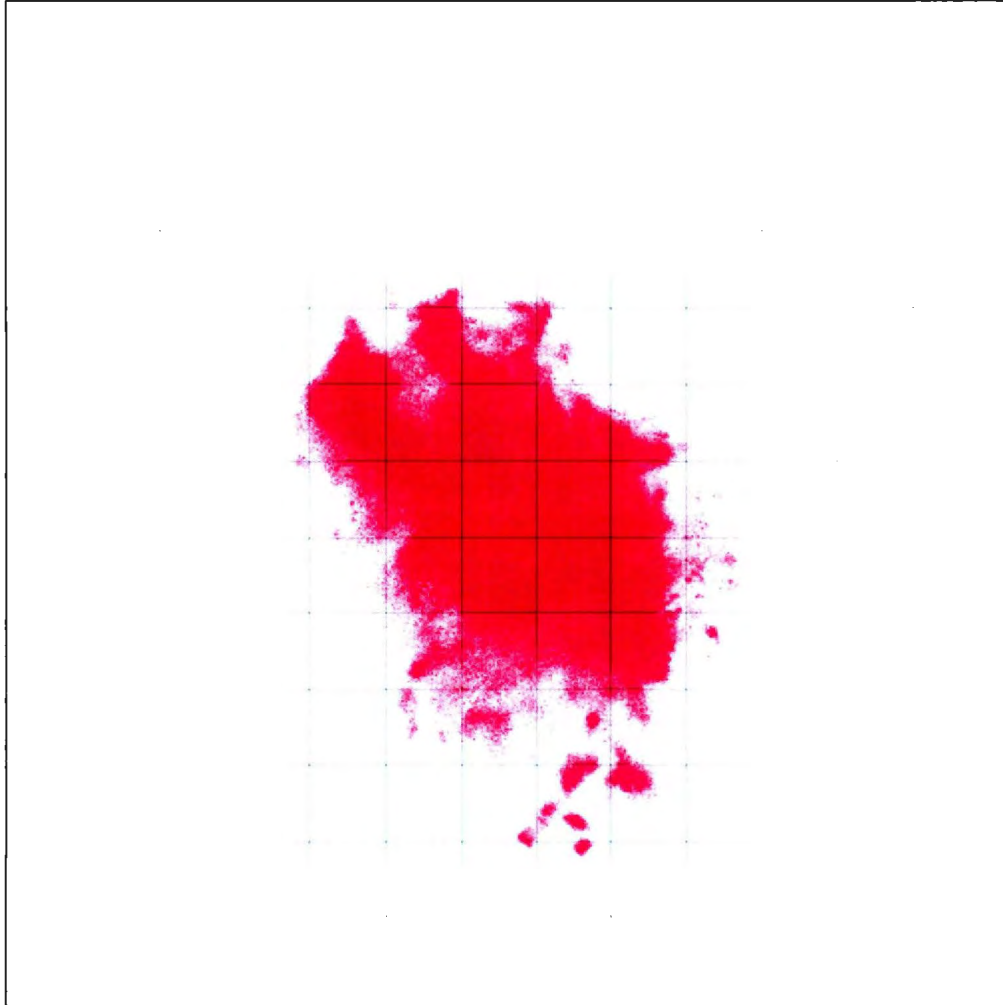


Figure 174 - F20T2b Low (1cm x 1cm Grid Spacing)

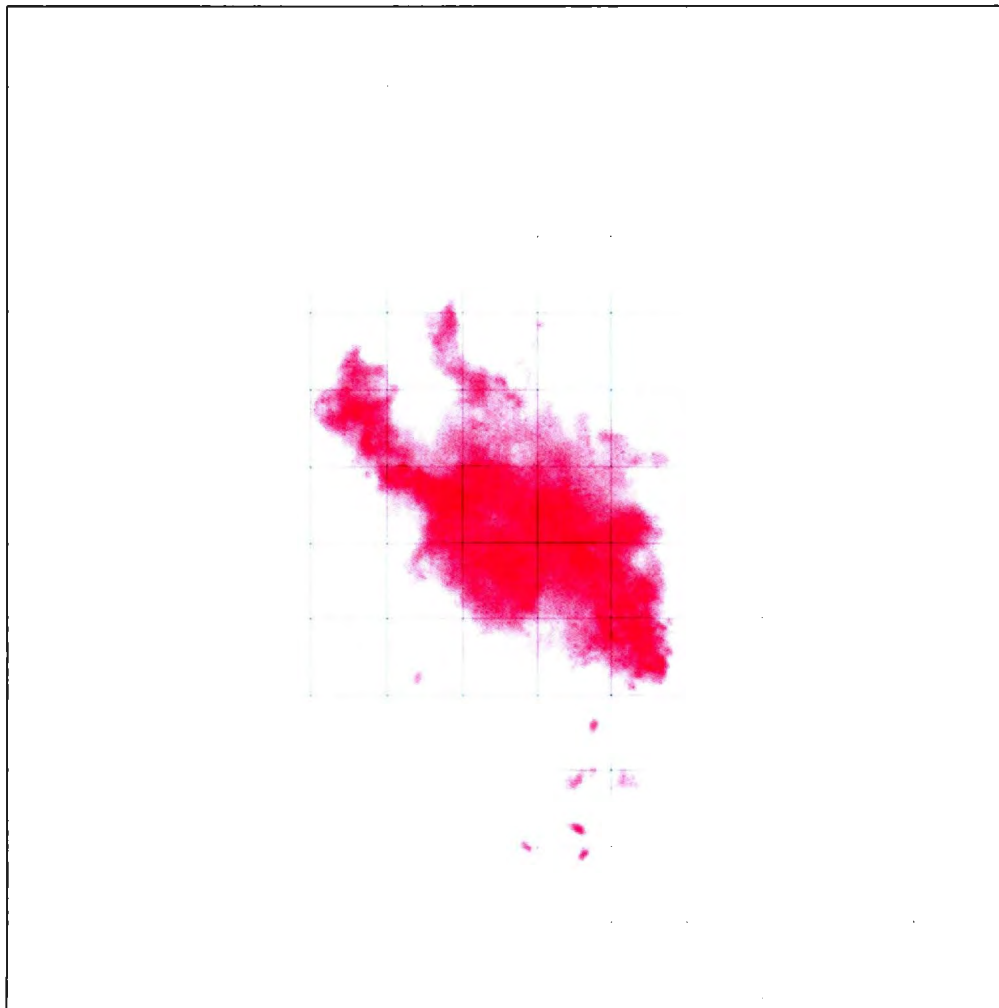


Figure 175 - F20T2b Medium (1cm x 1cm Grid Spacing)

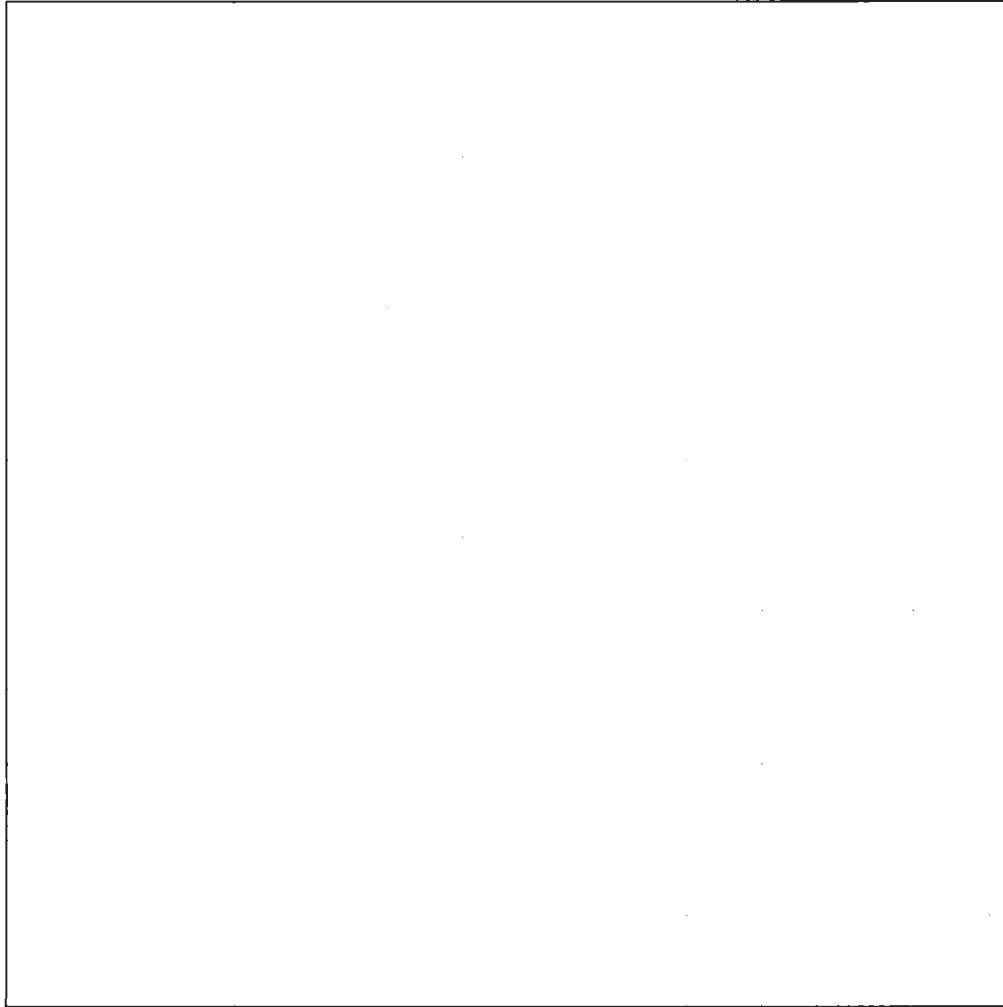


Figure 176 - F20T2b High (1cm x 1cm Grid Spacing)

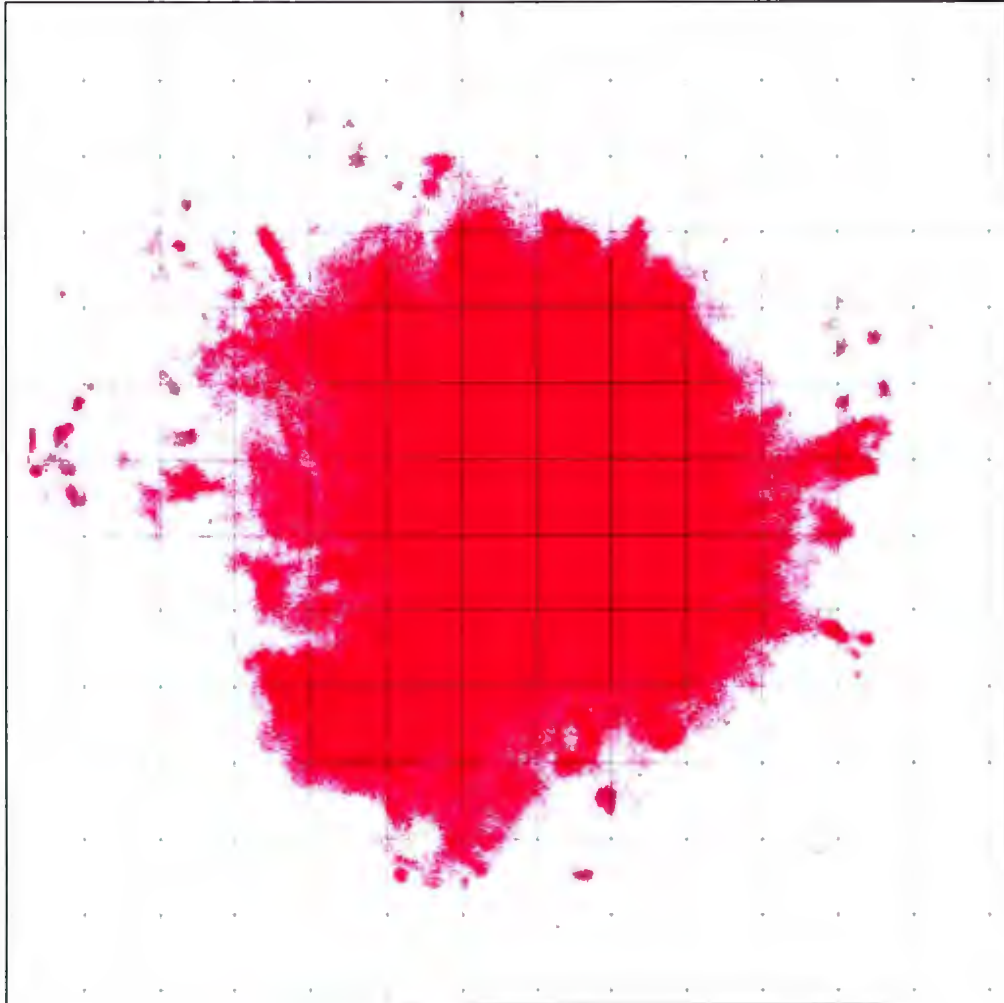


Figure 177 - F20T2c Low (1cm x 1cm Grid Spacing)

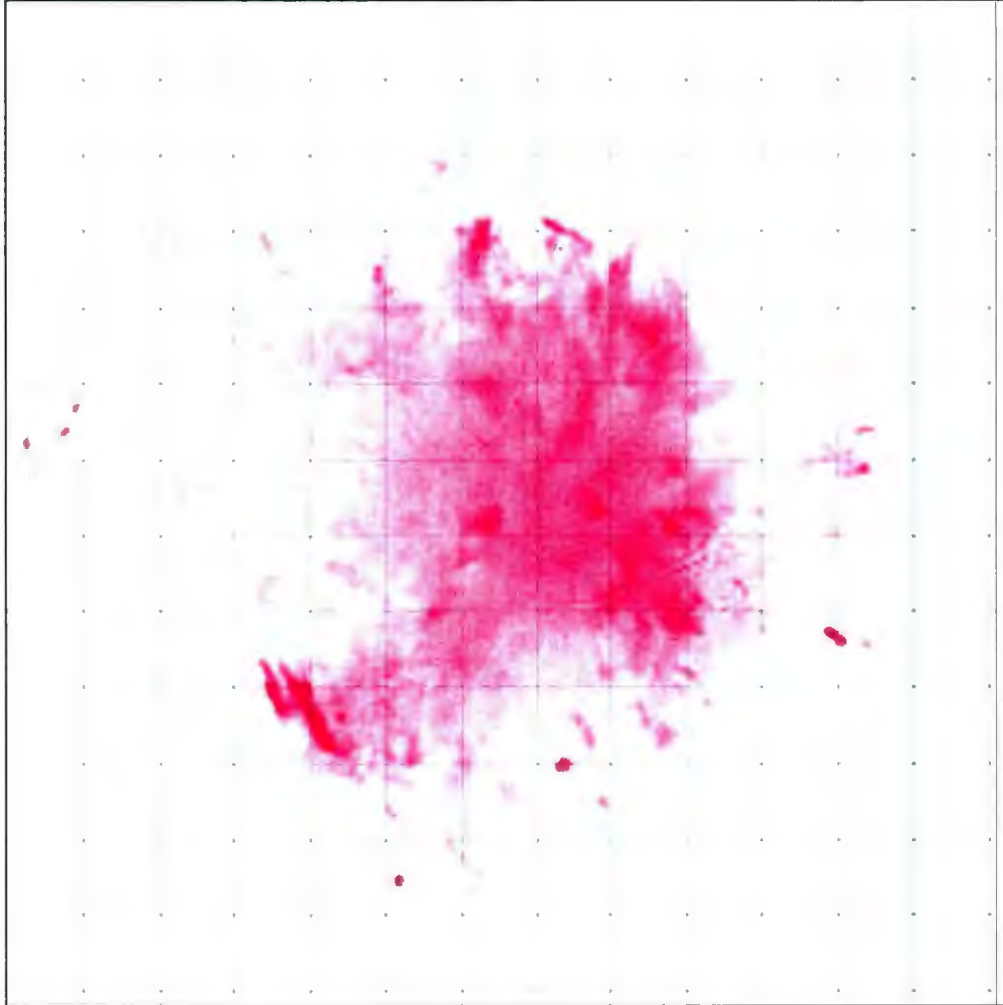


Figure 178 - F20T2c Medium (1cm x 1cm Grid Spacing)

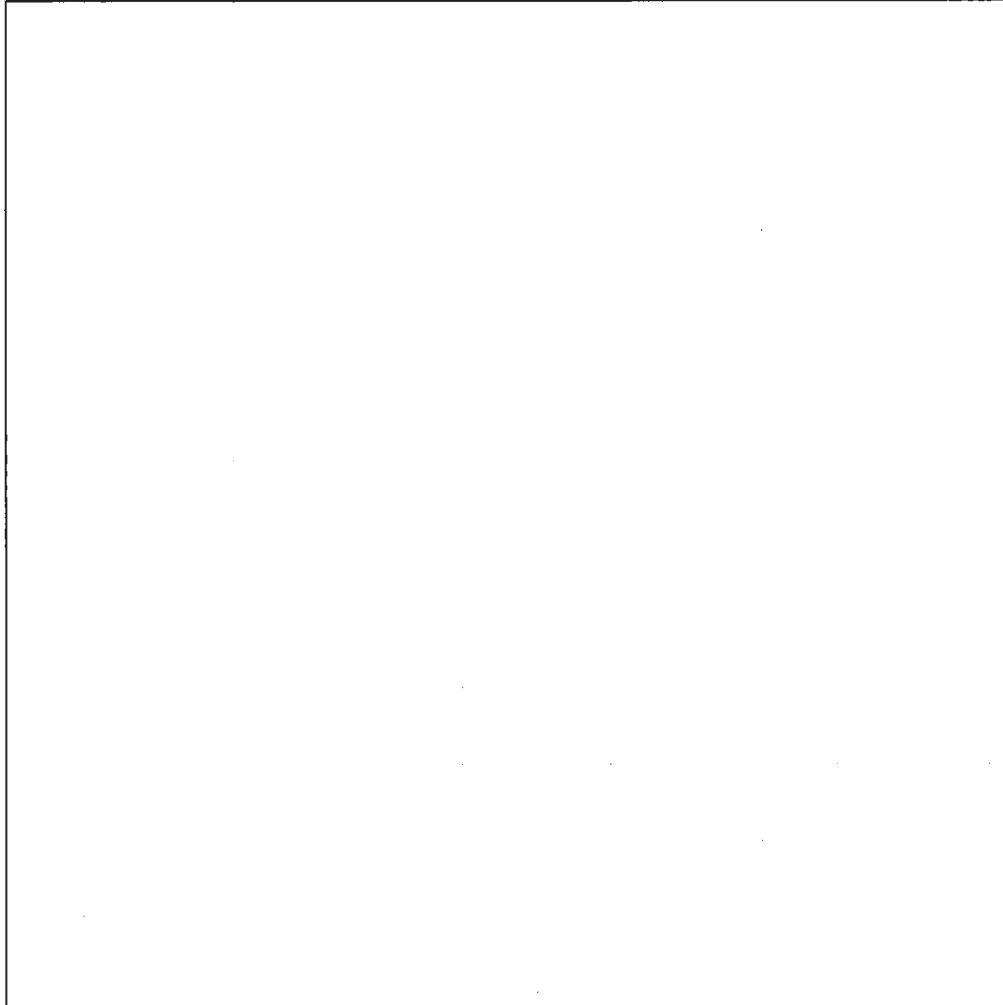


Figure 179 - F20T2c High (1cm x 1cm Grid Spacing)

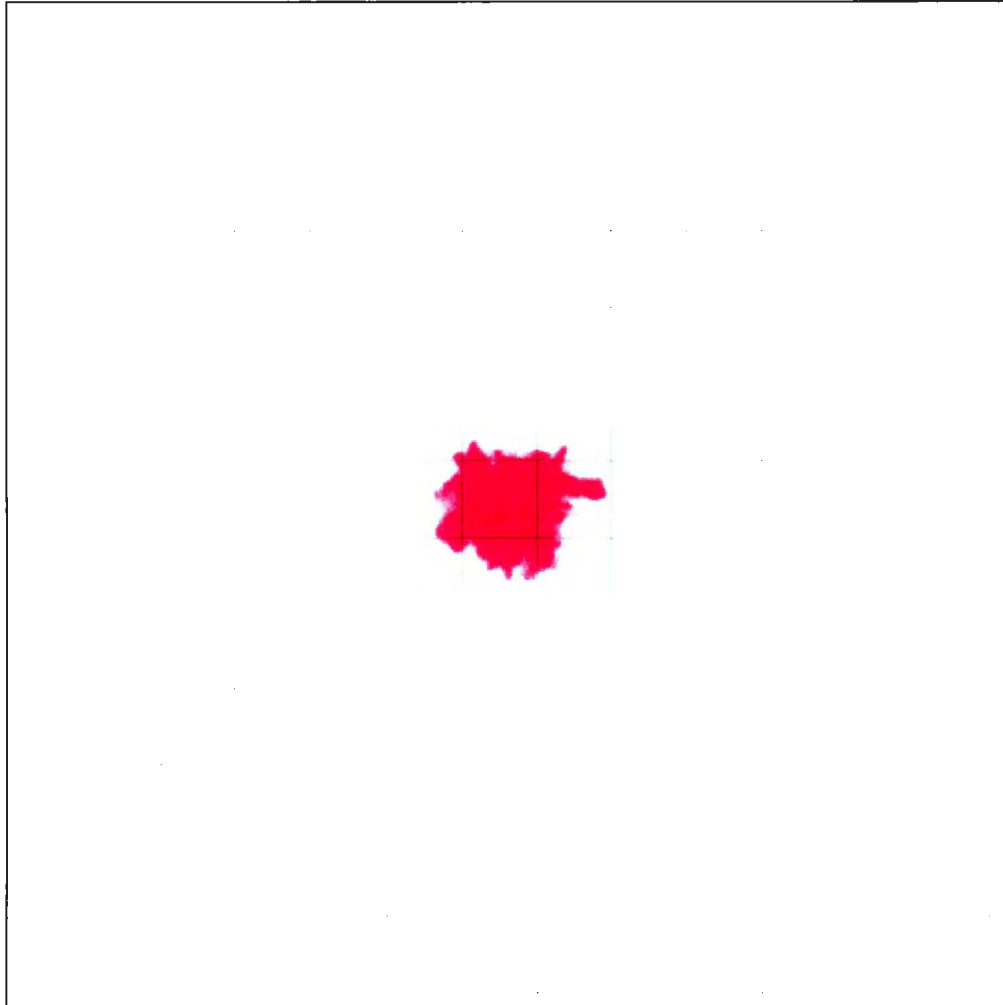


Figure 180 - F281a Low (1cm x 1cm Grid Spacing)

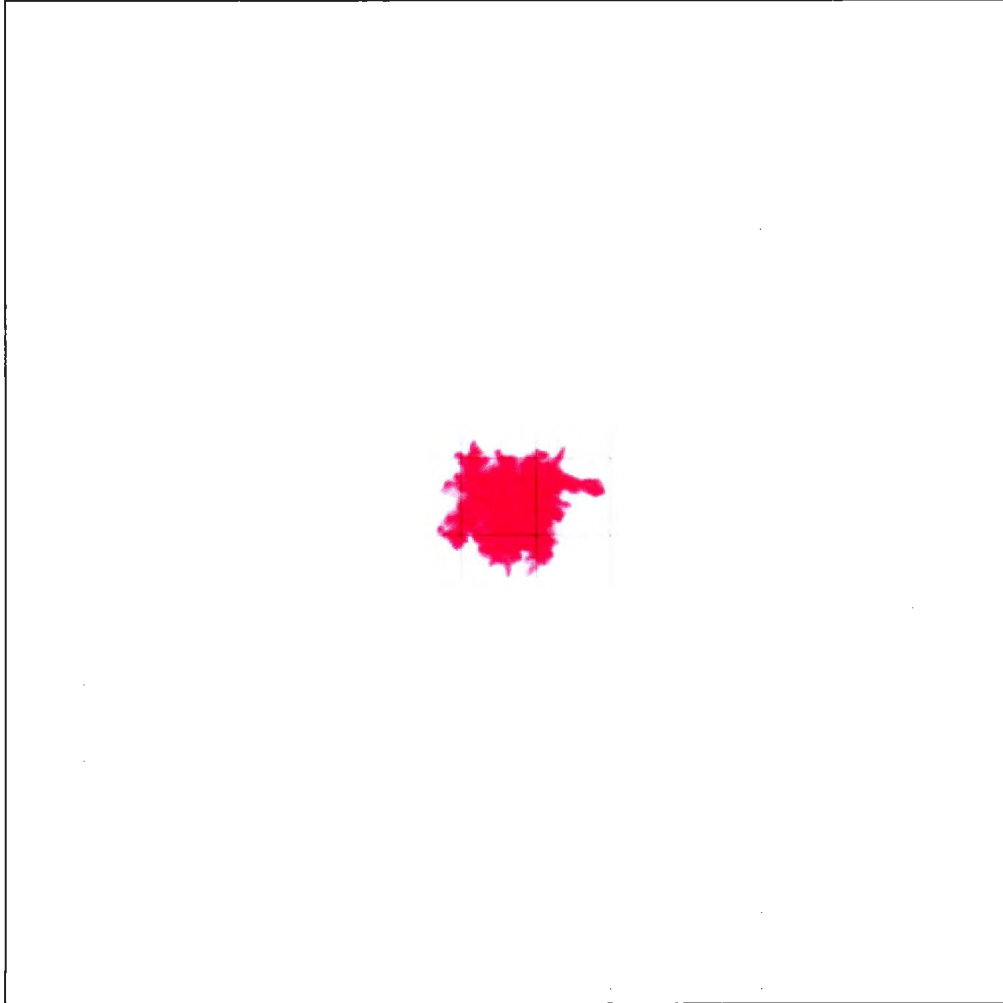


Figure 181 - F28T1a Medium (1cm x 1cm Grid Spacing)

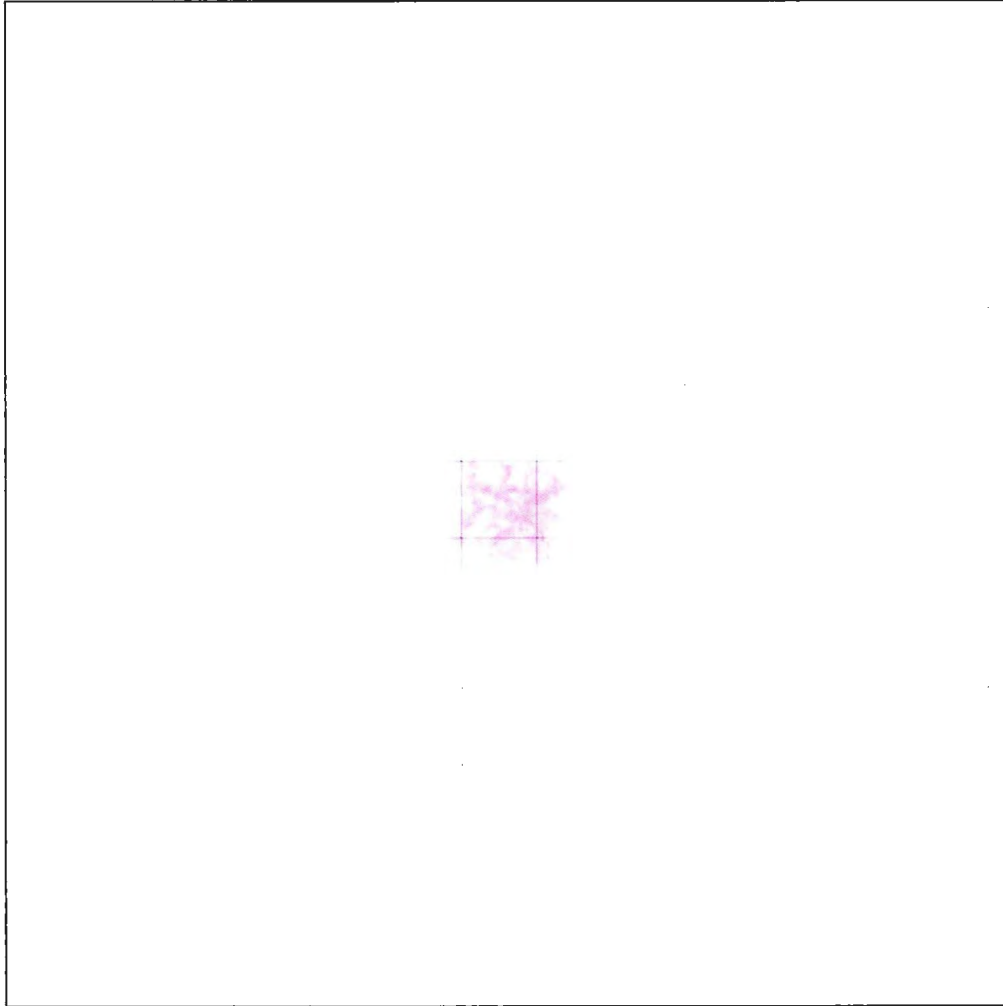


Figure 182 - F28T1a High (1cm x 1cm Grid Spacing)

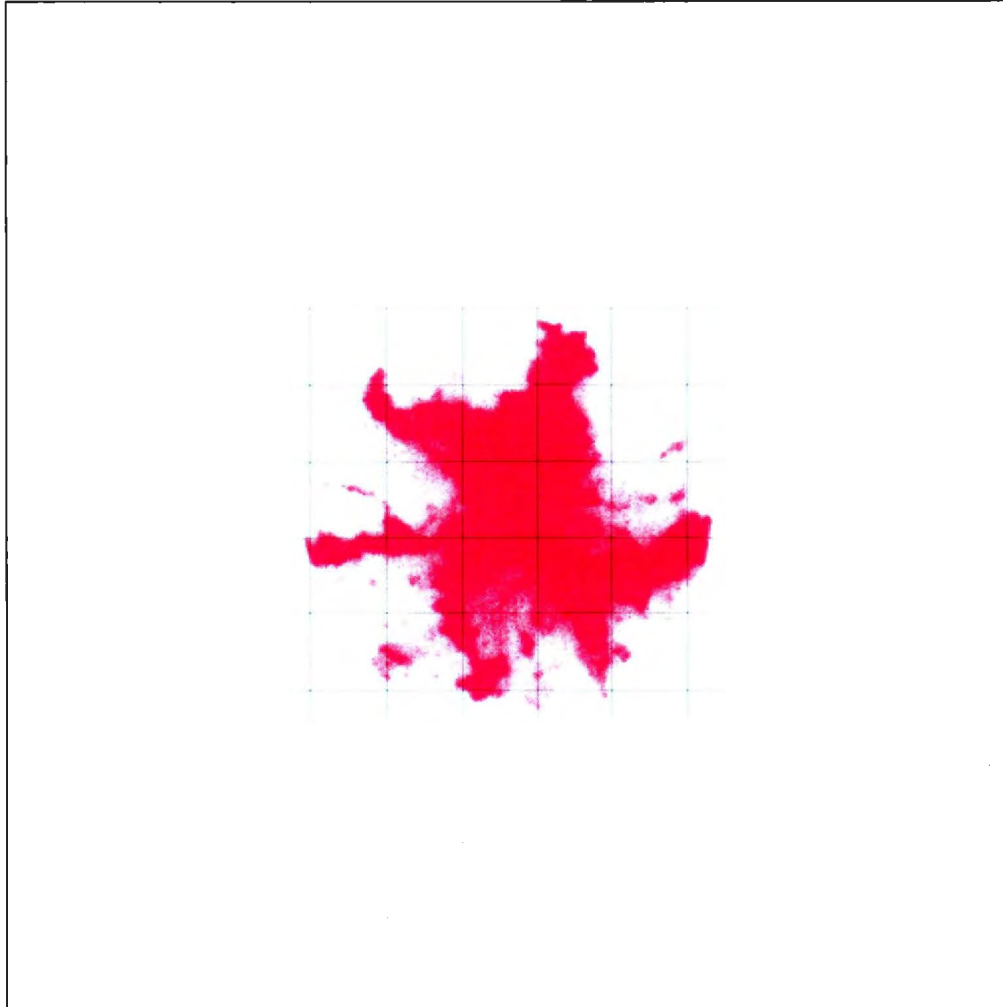


Figure 183 - F28T1b Low (1cm x 1cm Grid Spacing)

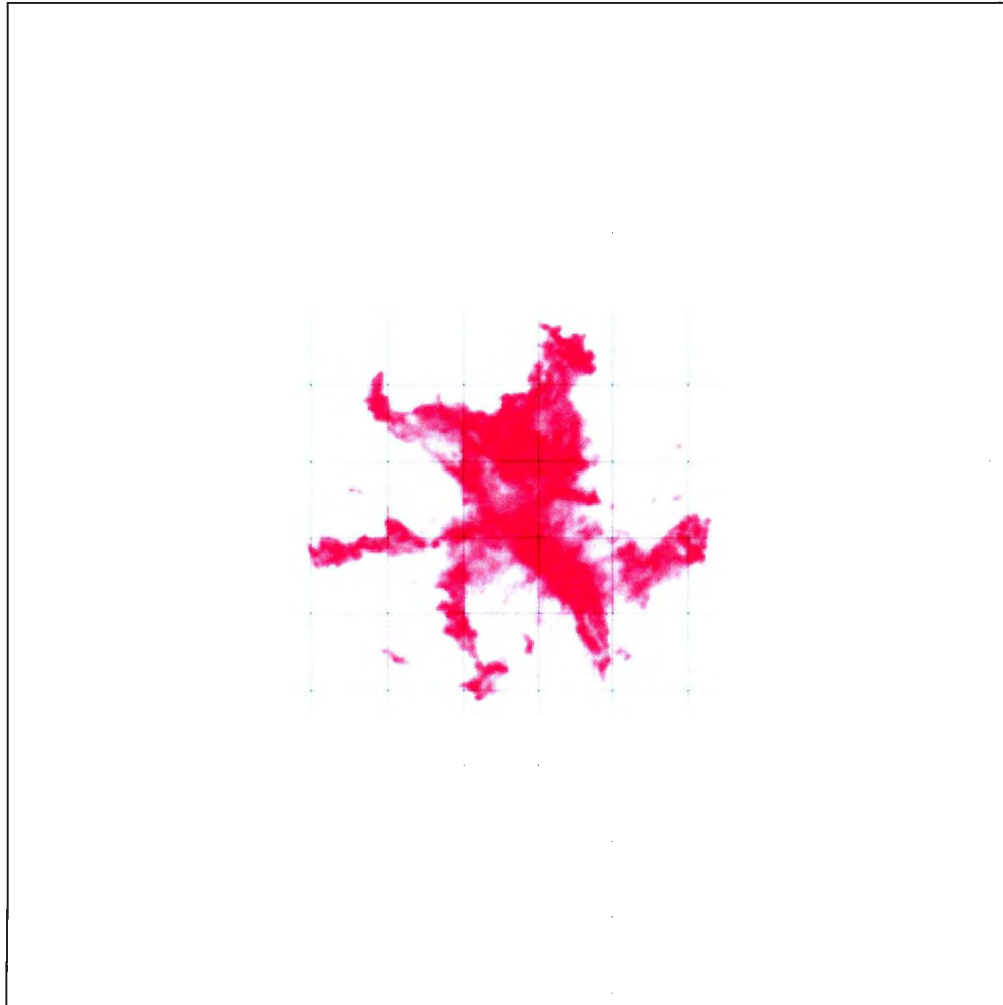


Figure 184 - F28T1b Medium (1cm x 1cm Grid Spacing)

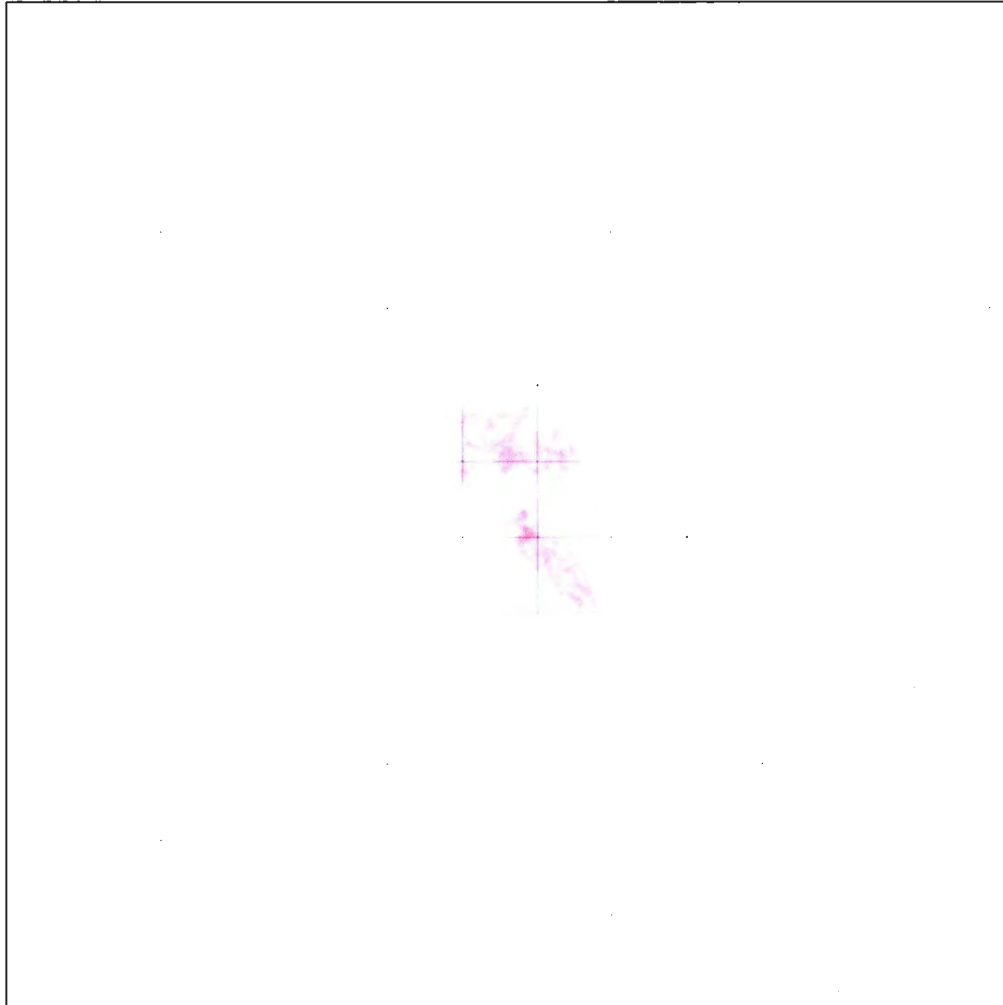


Figure 185 - F28T1b High (1cm x 1cm Grid Spacing)

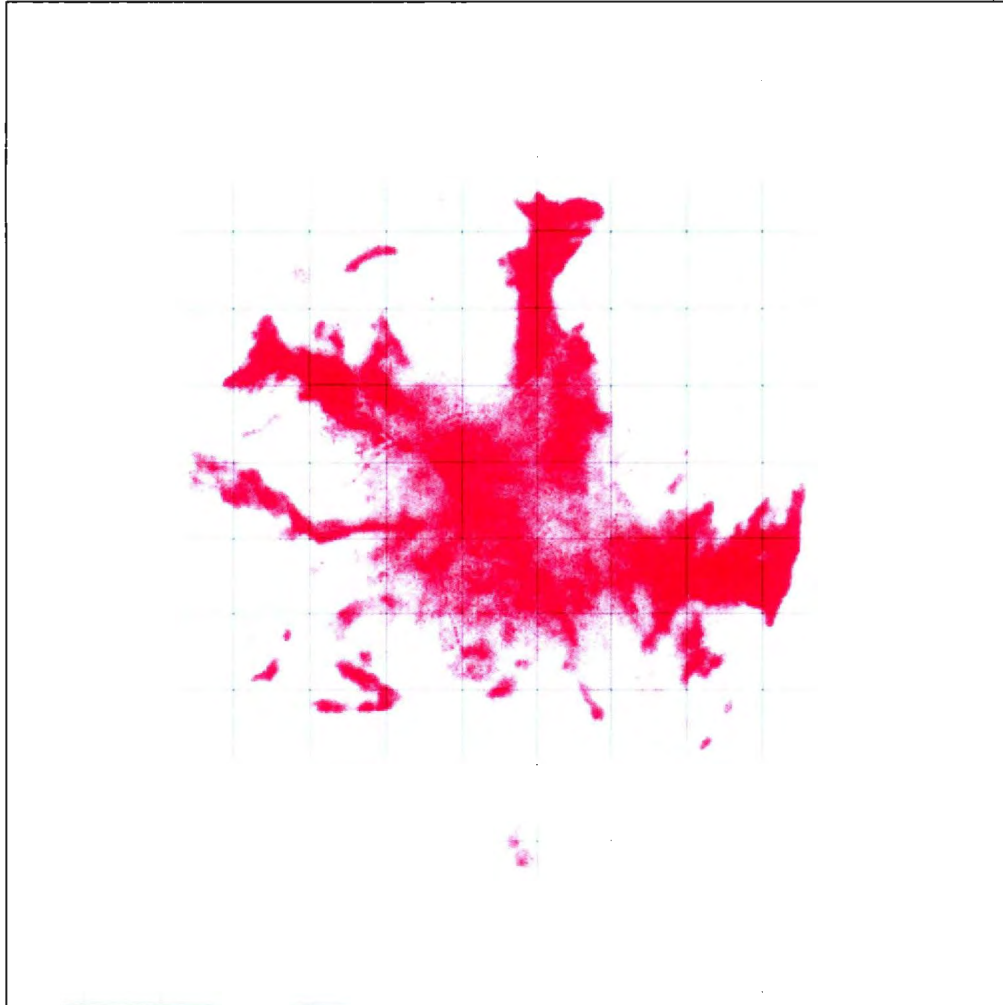


Figure 186 - F28T1c Low (1cm x 1cm Grid Spacing)

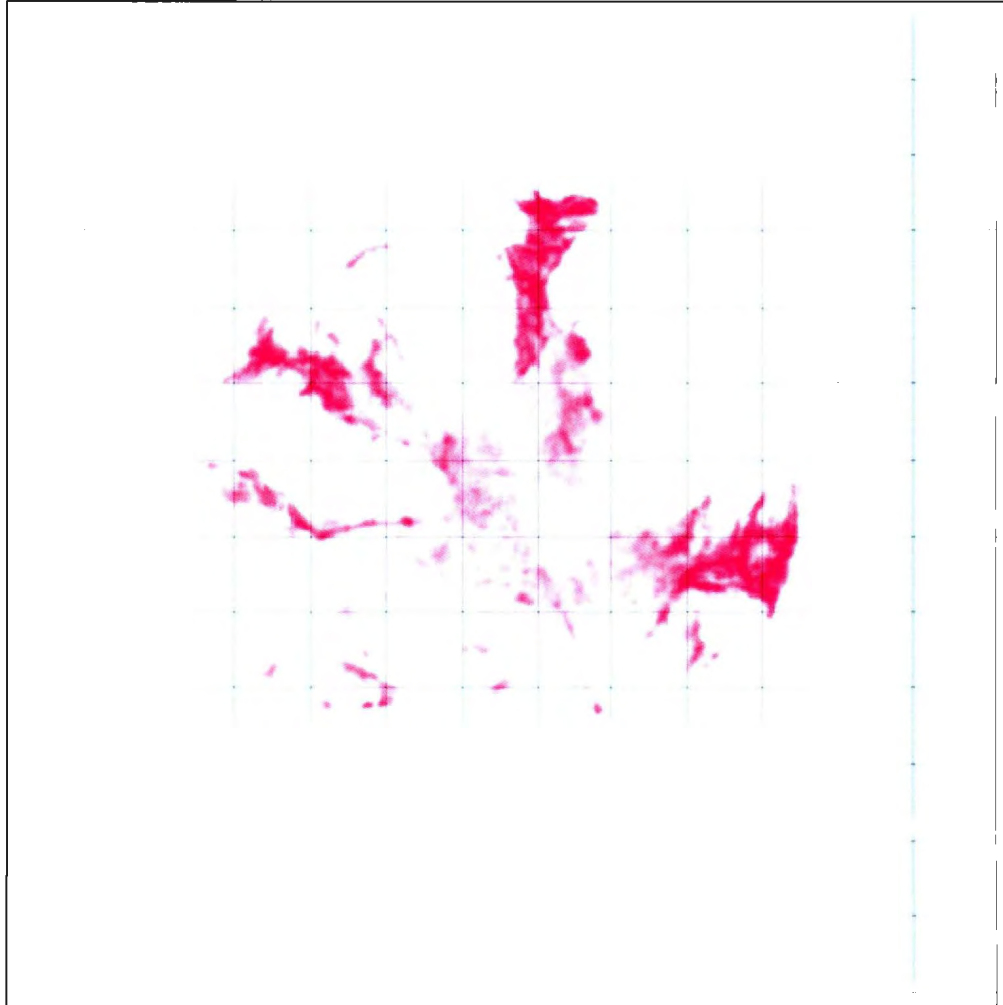


Figure 187 - F28T1c Medium (1cm x 1cm Grid Spacing)

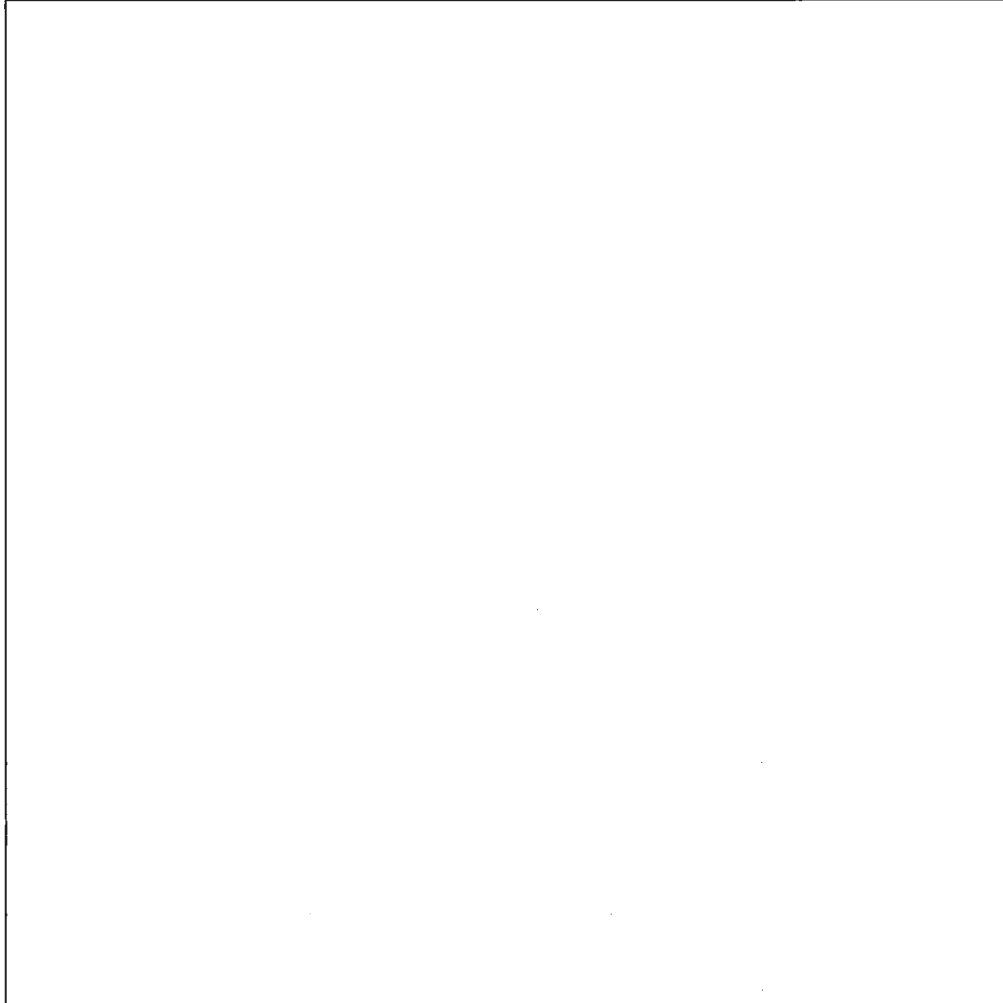


Figure 188 - F28T1c High (1cm x 1cm Grid Spacing)

Appendix B

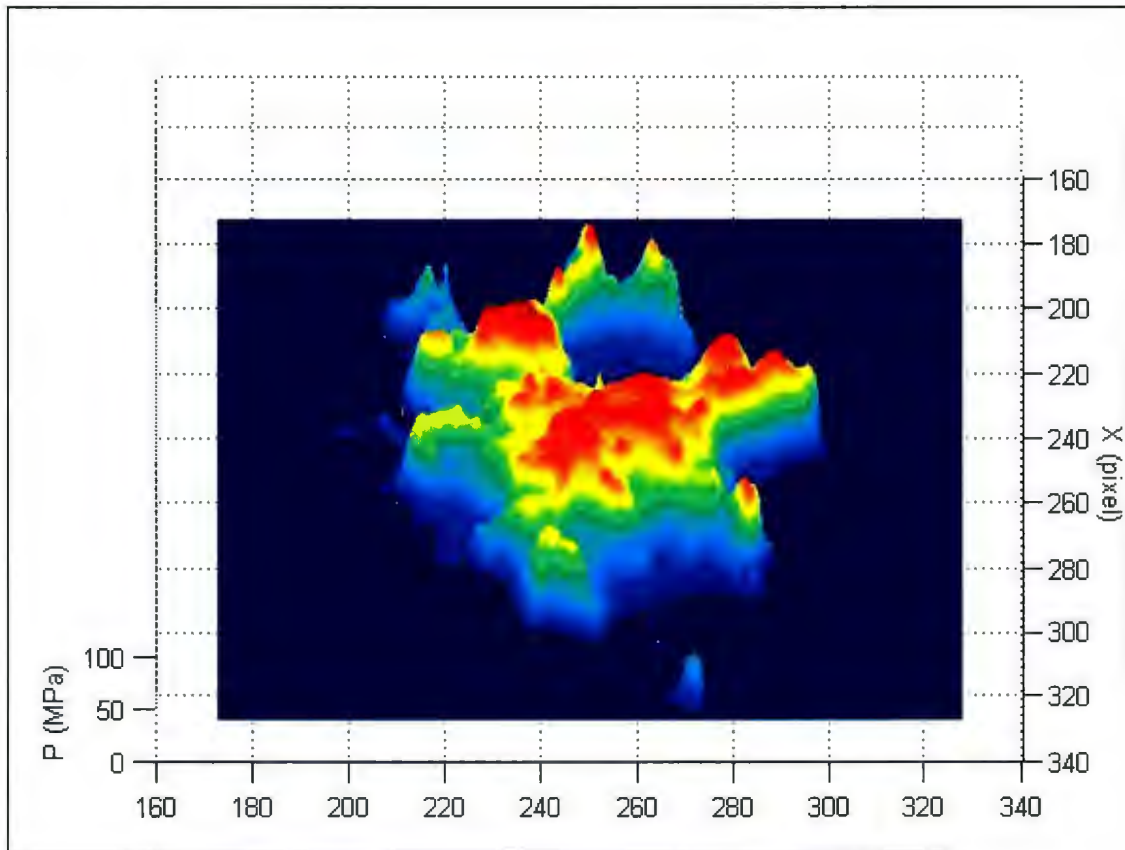


Figure 189 - F1T2a

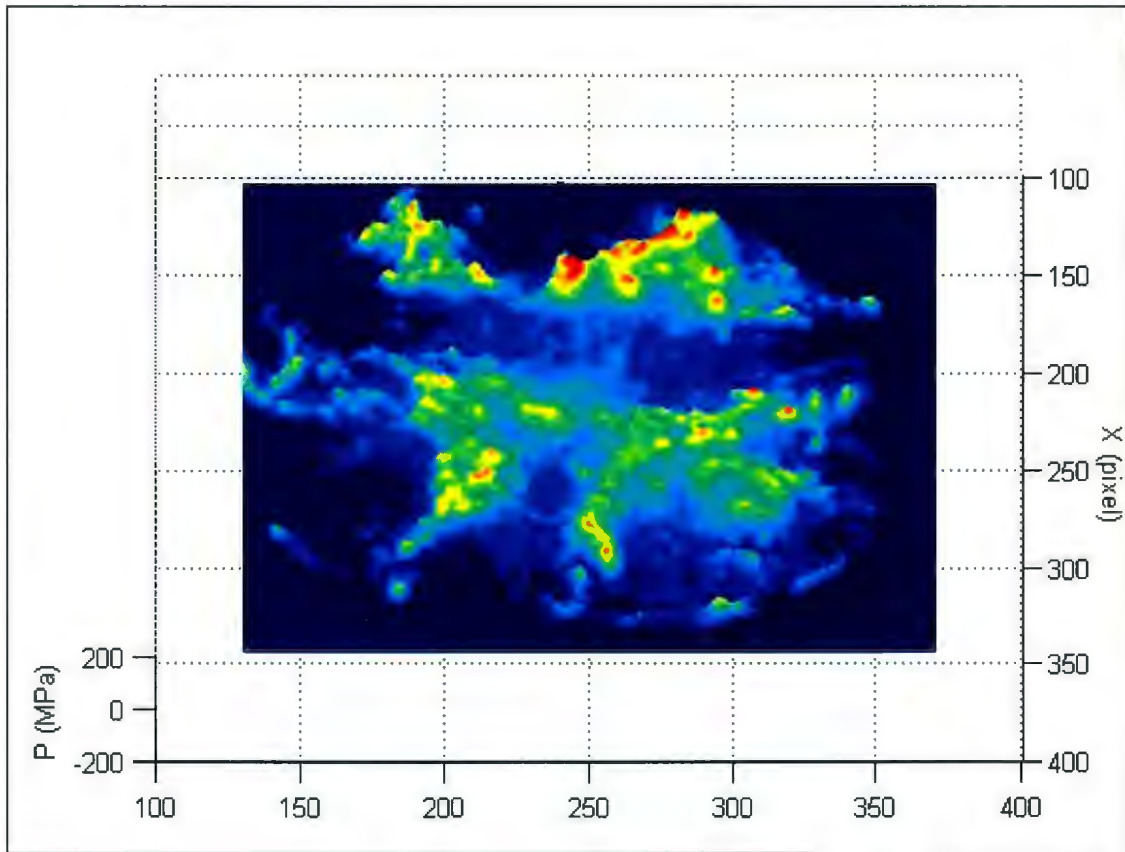


Figure 190 - F1T2b

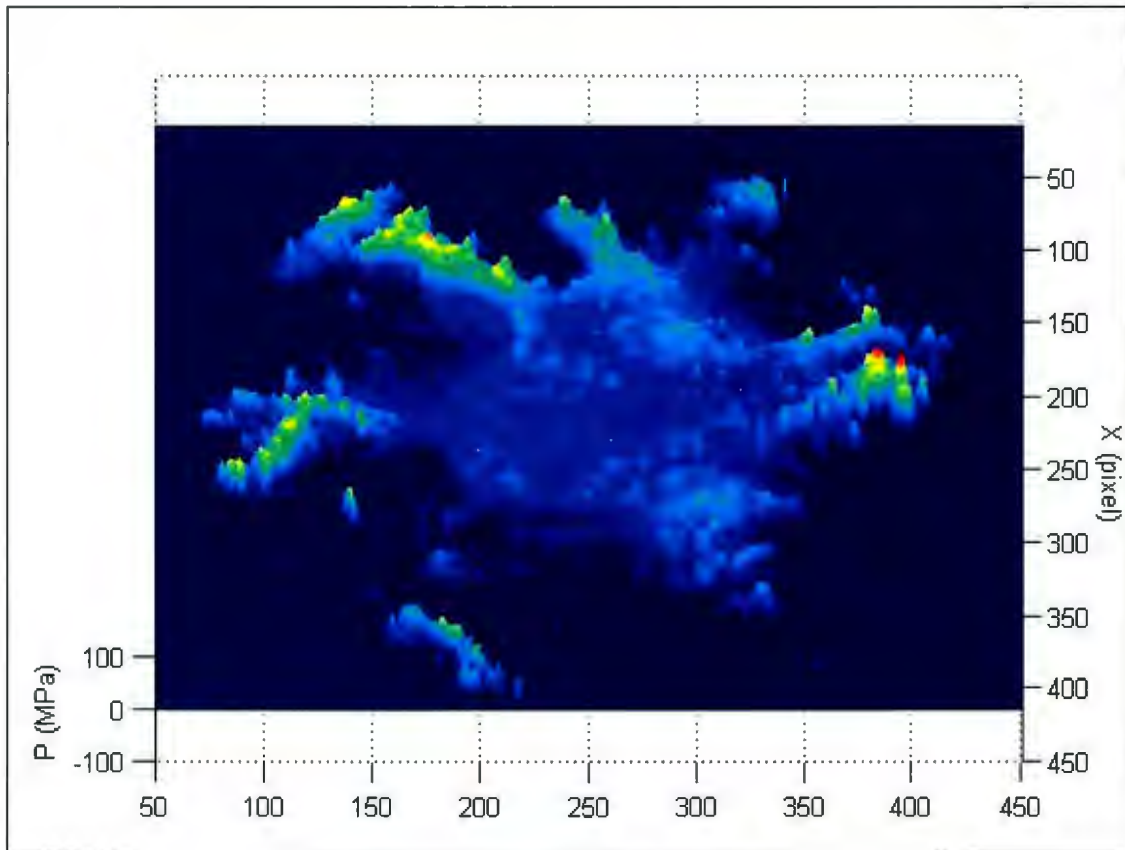


Figure 191 - F1T2c

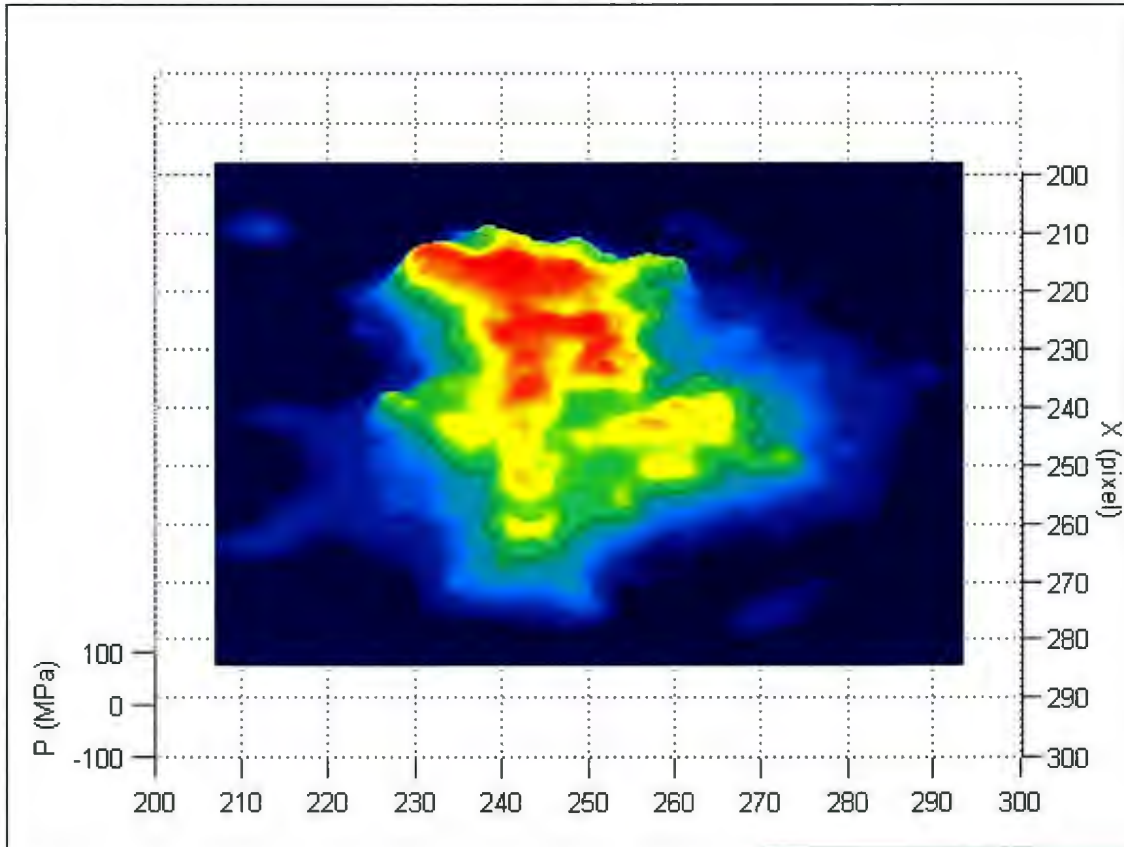


Figure 192 - F13T1a

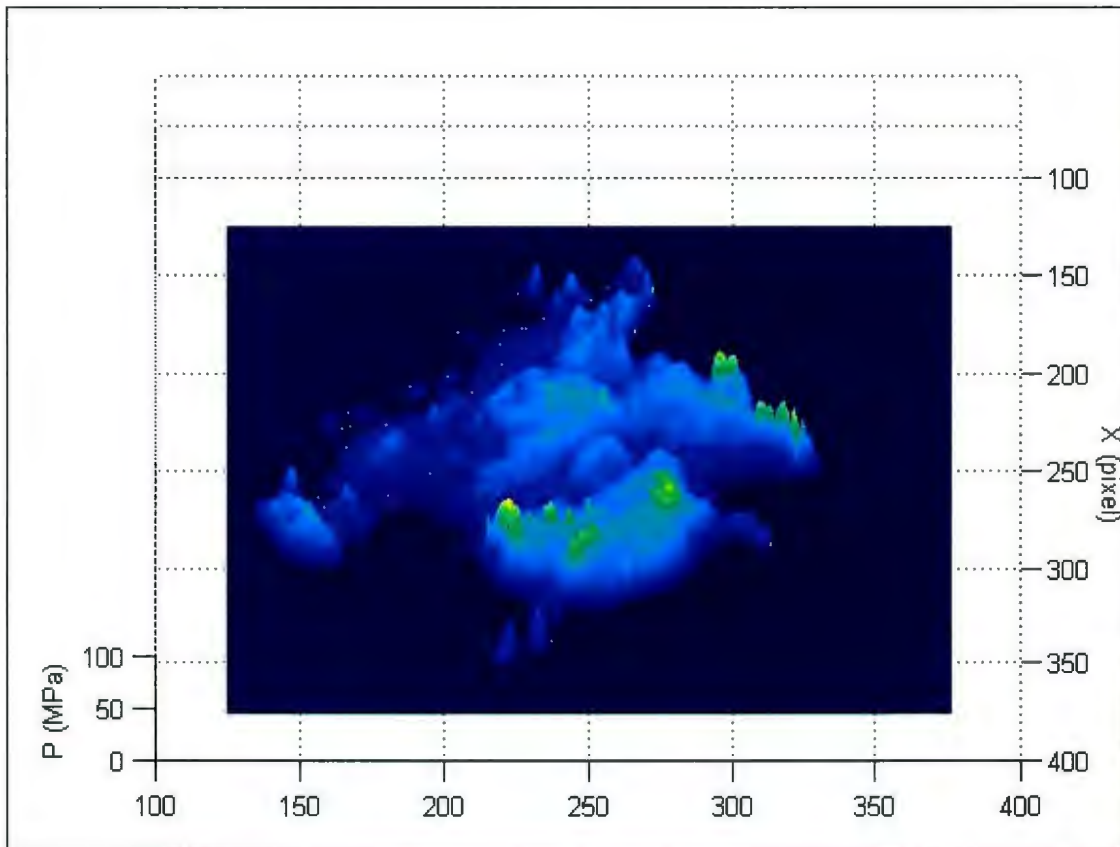


Figure 193 - F13T1b

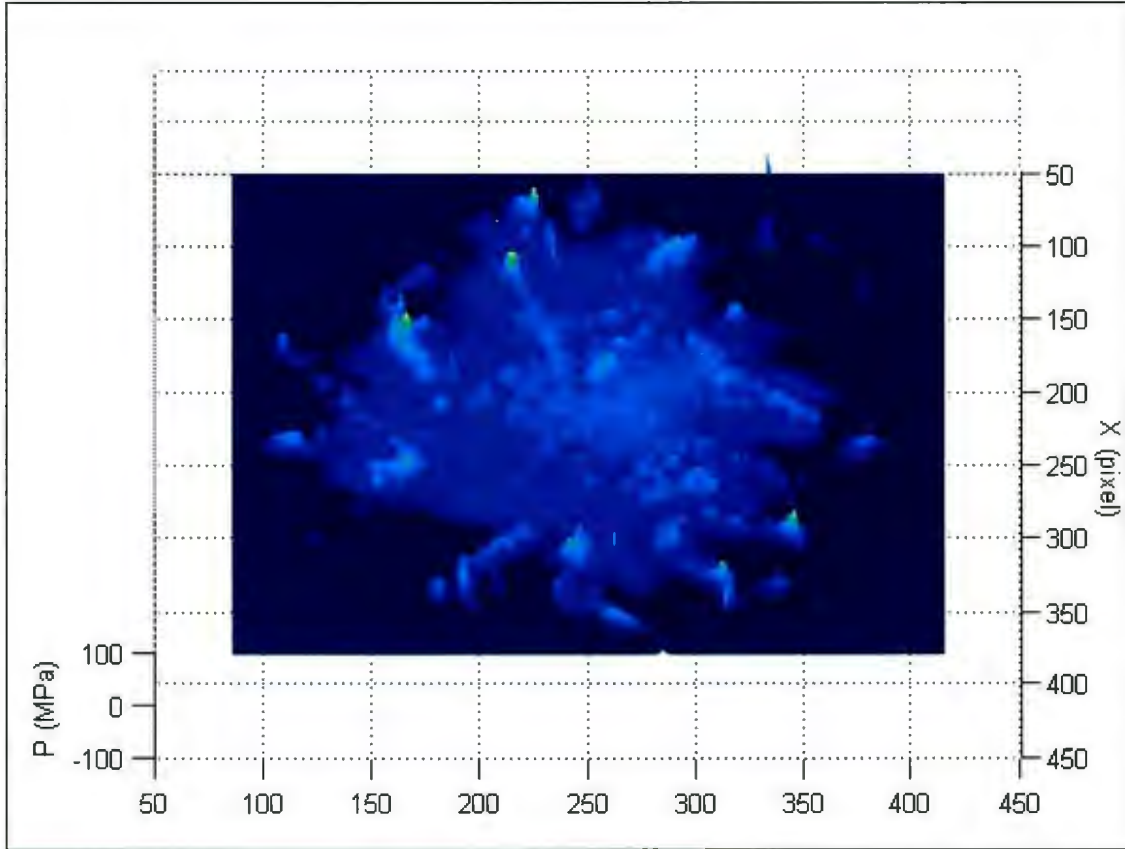


Figure 194 - F13T1c

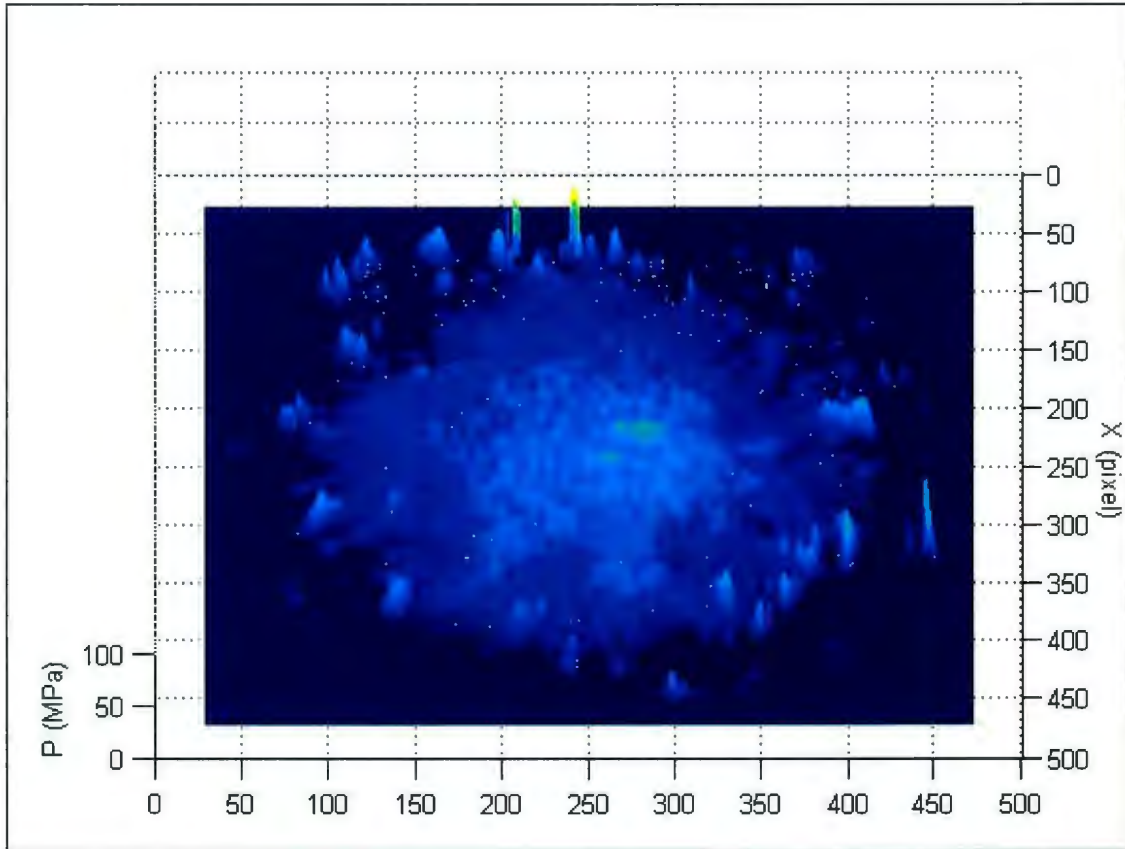


Figure 195 - F13T1d

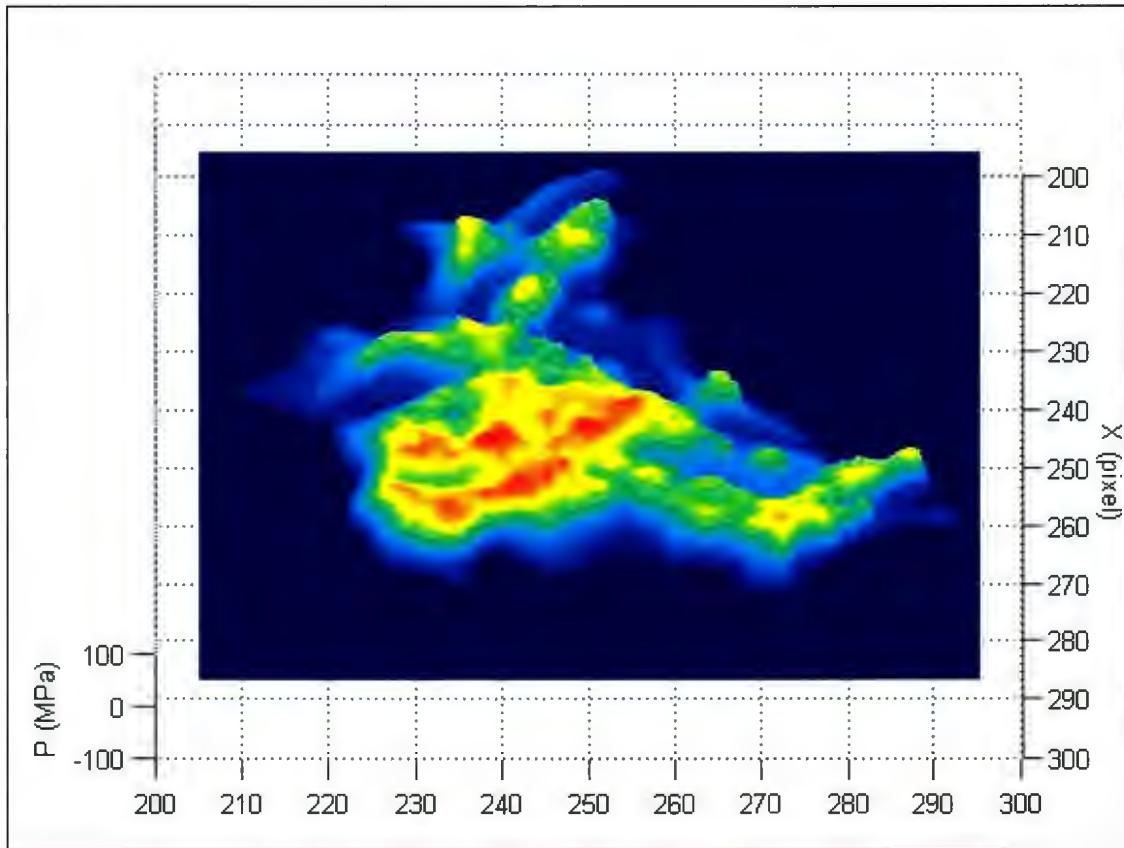


Figure 196 - F13T2a

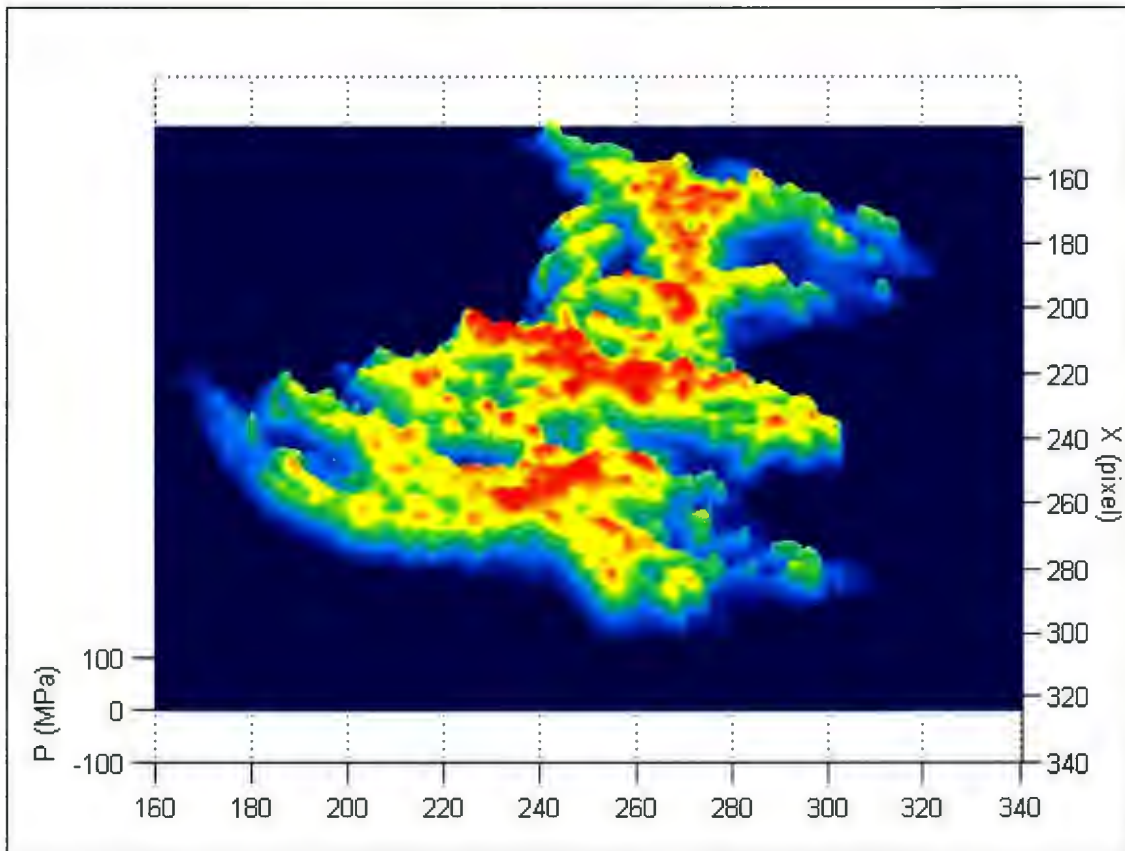


Figure 197 - F13T2b

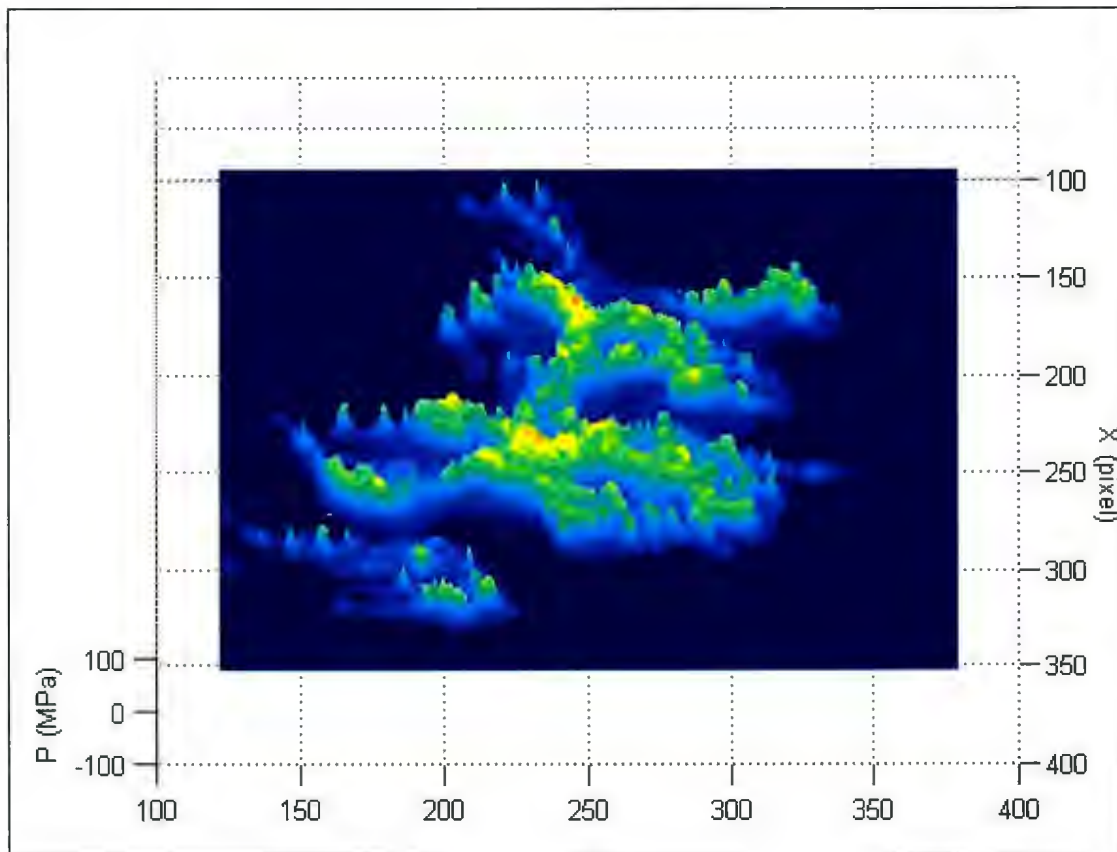


Figure 198 - F13T2c

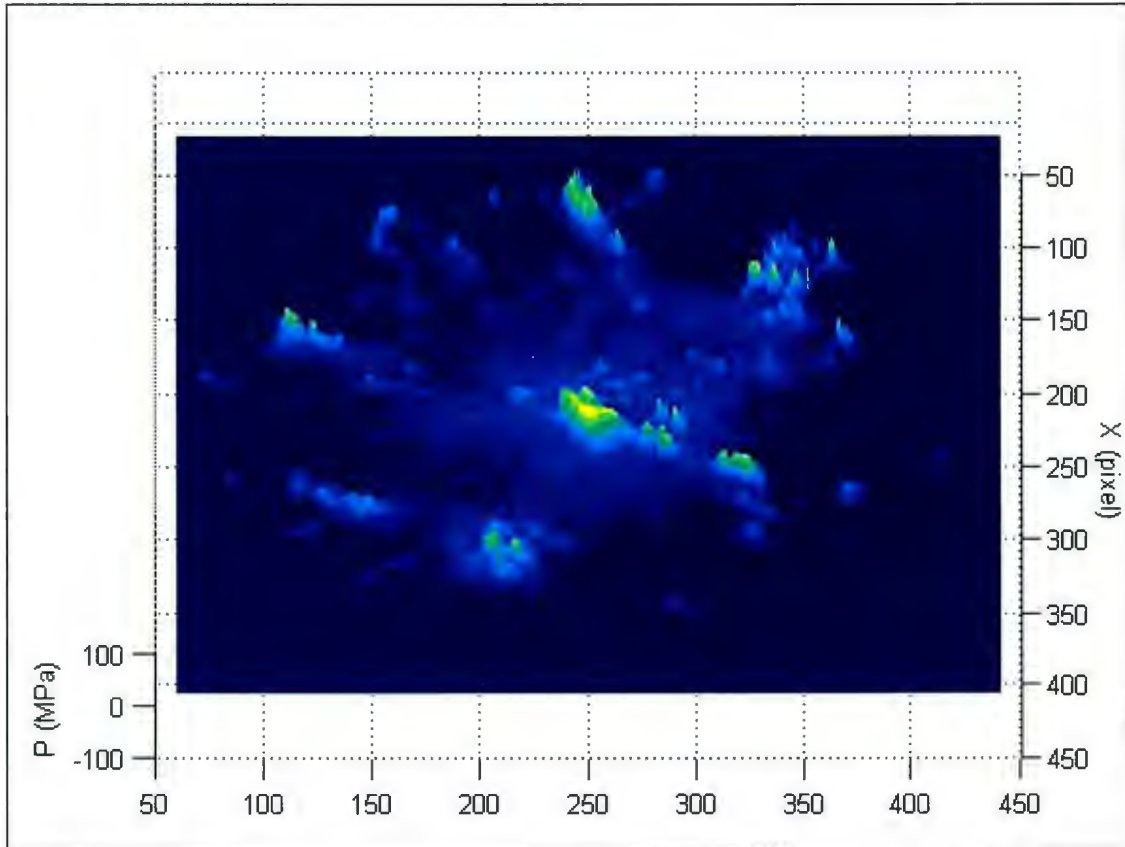


Figure 199 - F13T2d

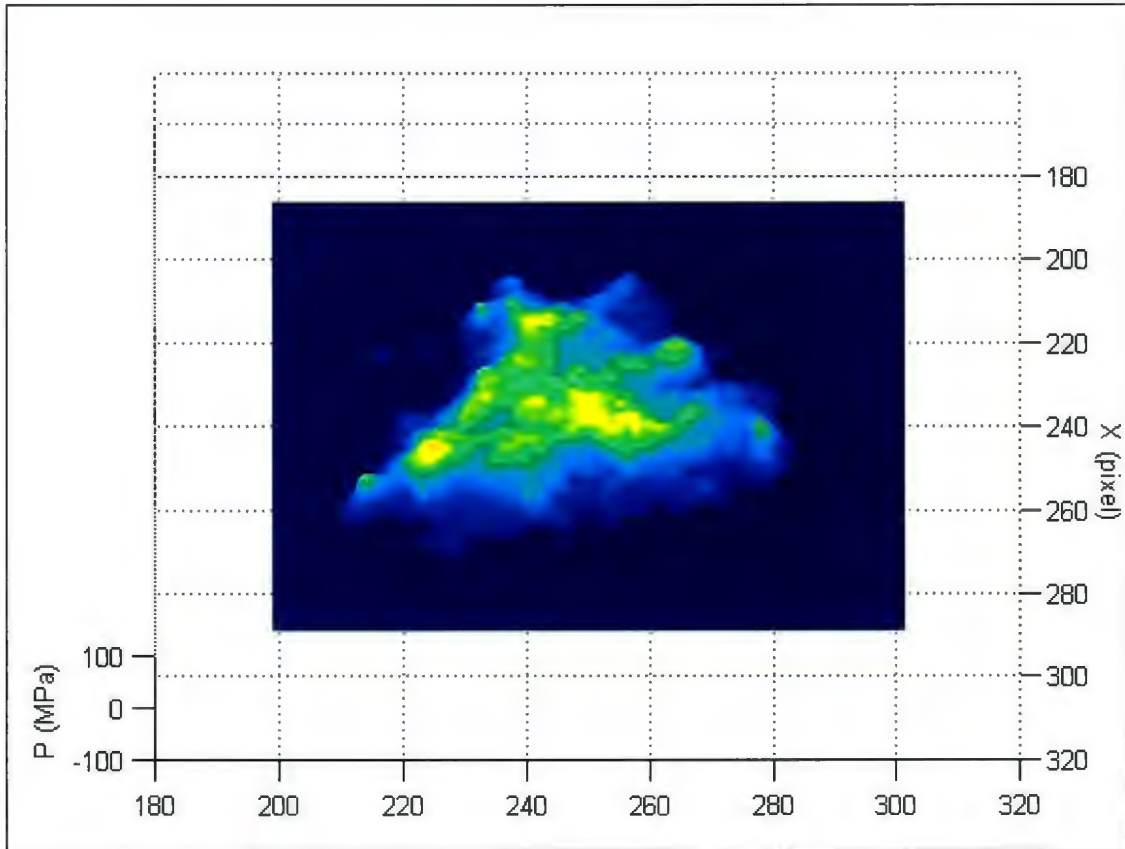


Figure 200 - F13T3a

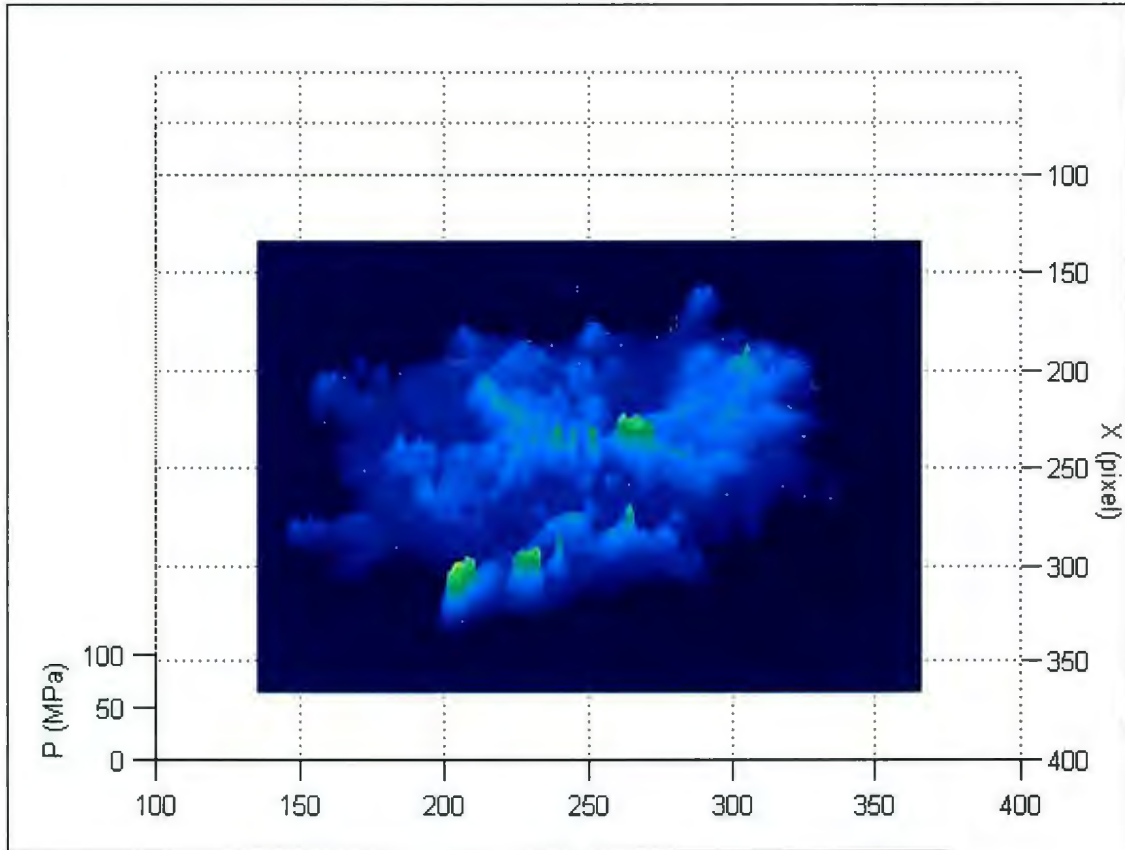


Figure 201 - F13T3b

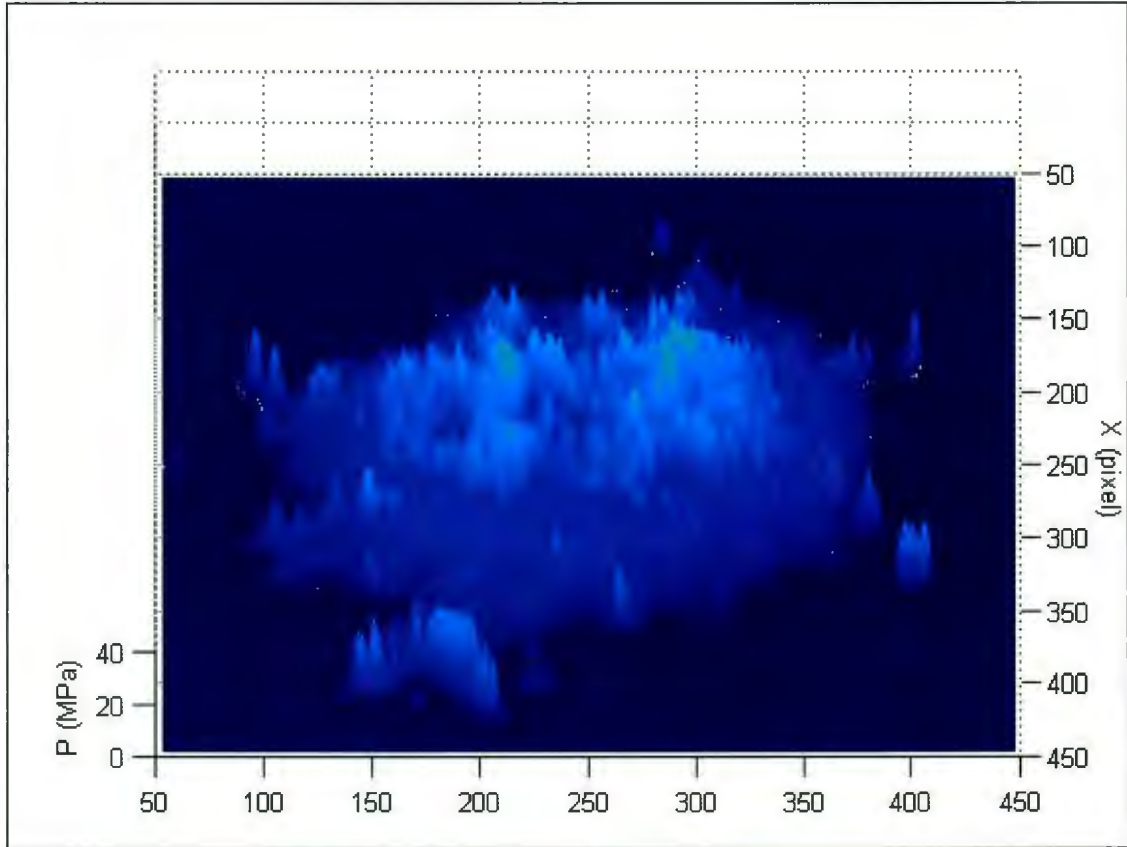


Figure 202 - F13T3c

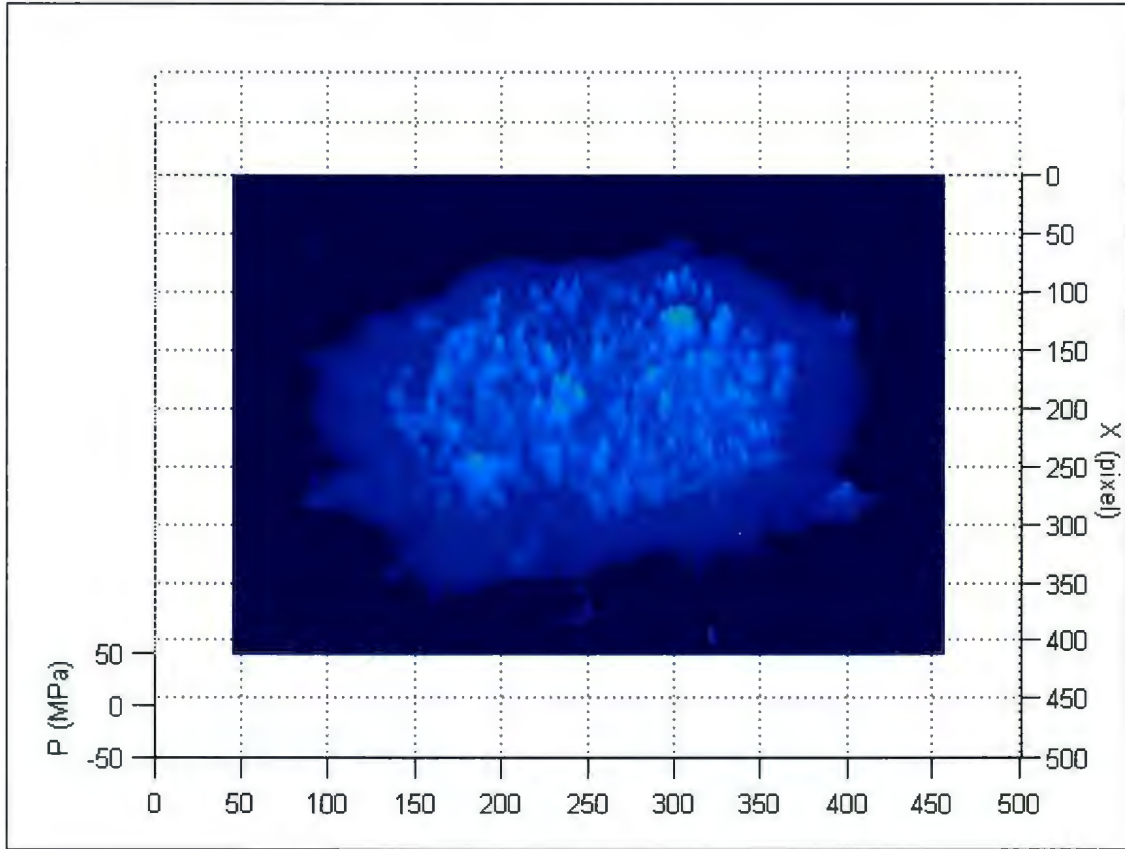


Figure 203 - F13T3d

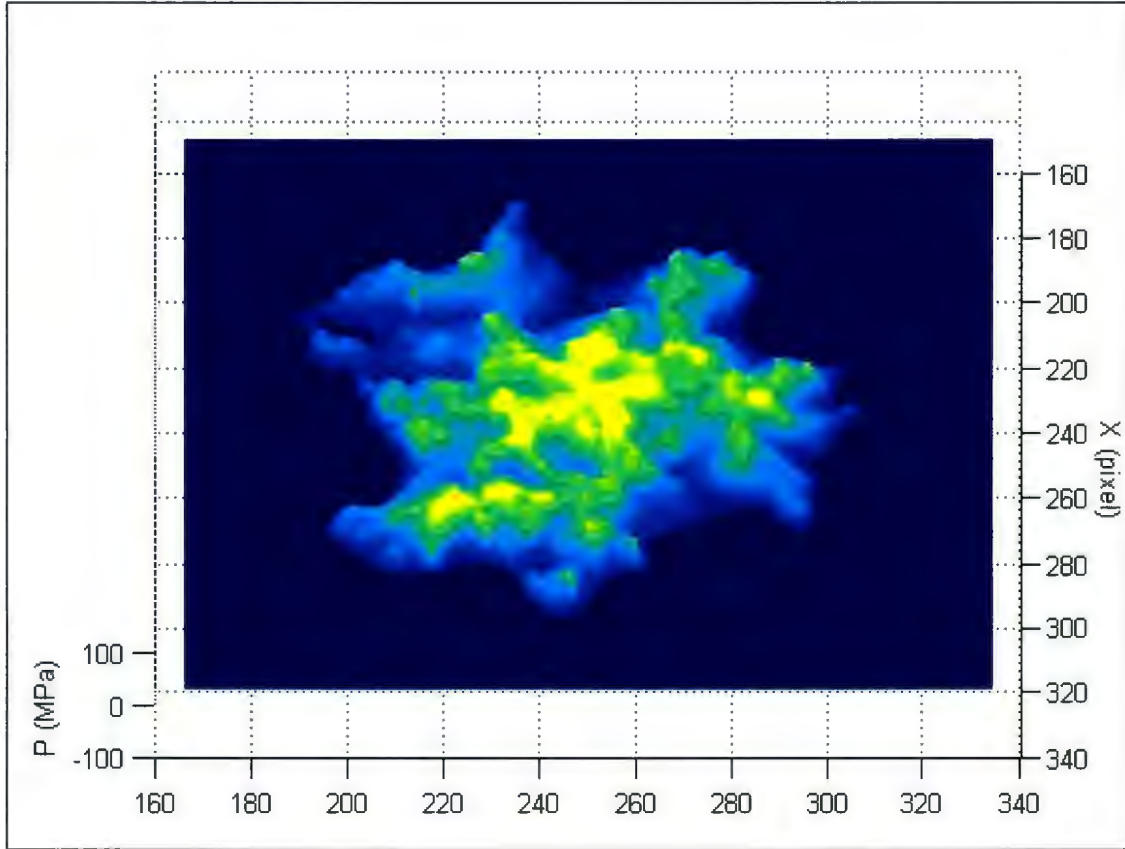


Figure 204 - F16T1a

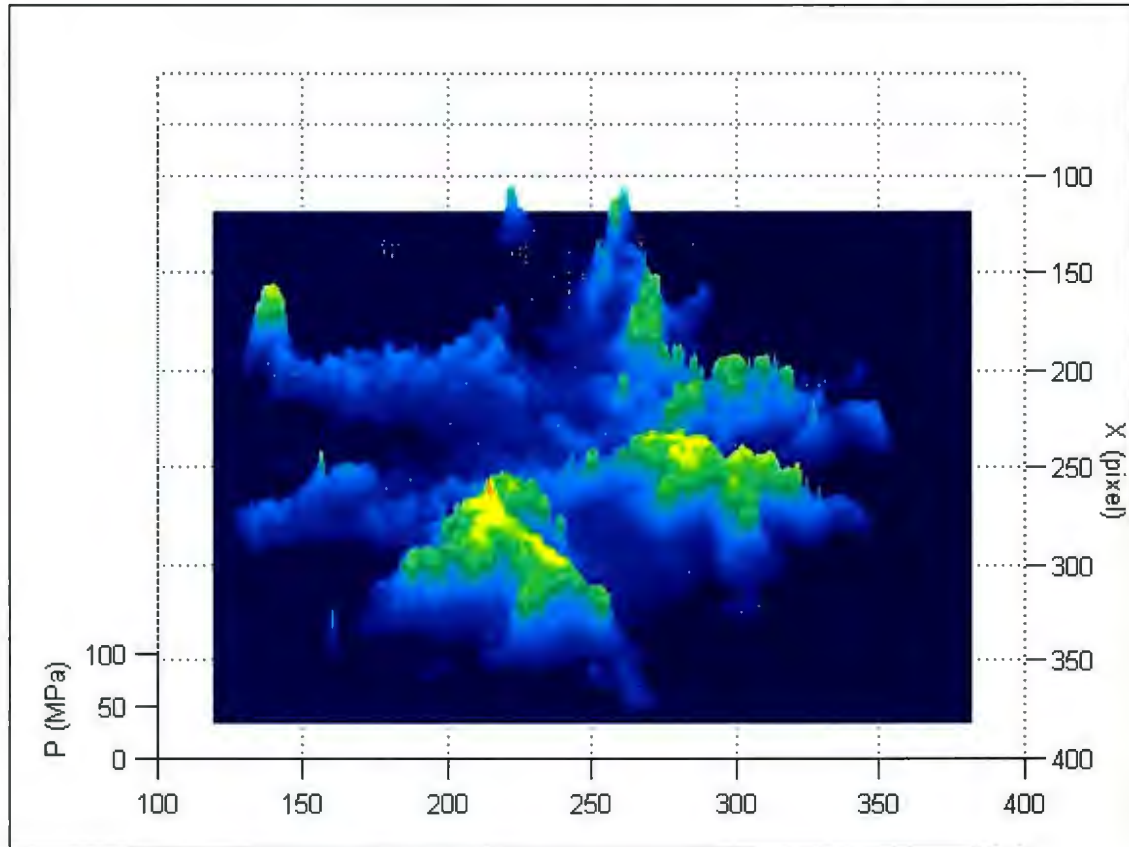


Figure 205 - F16T1b

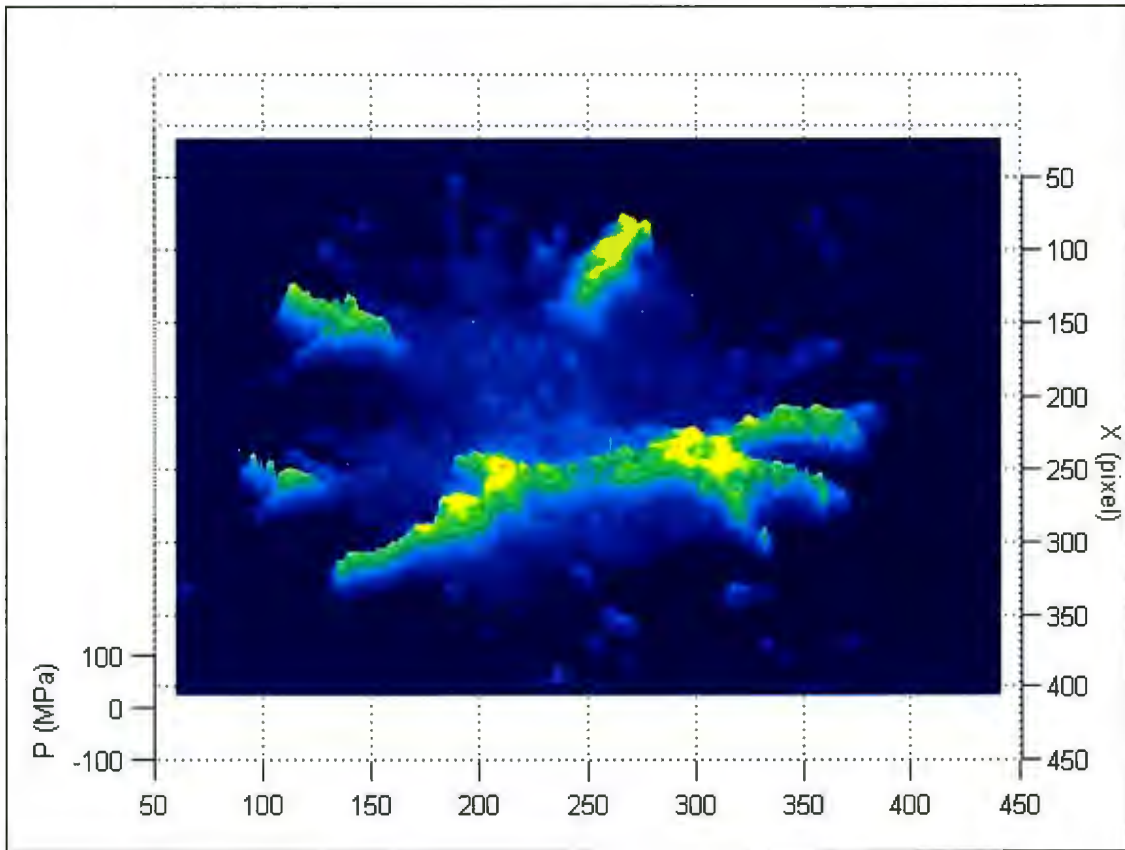


Figure 206 - F16T1c

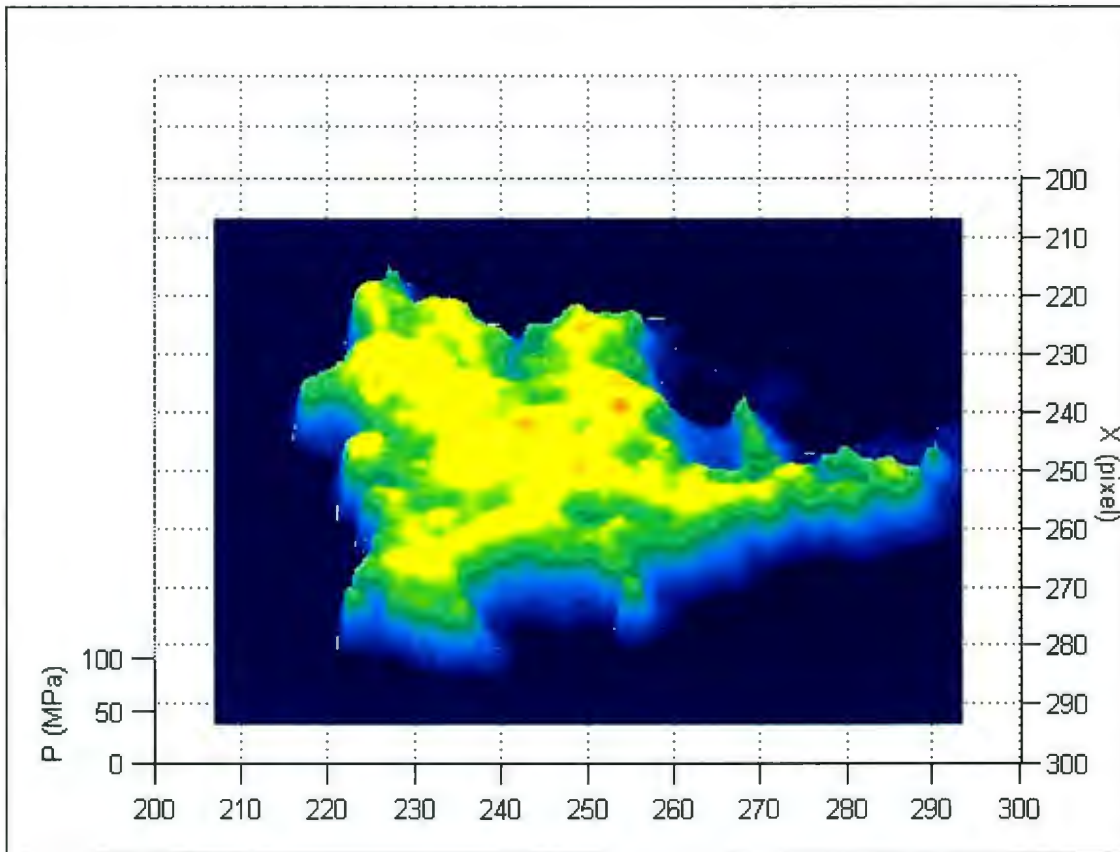


Figure 207 - F20T1a

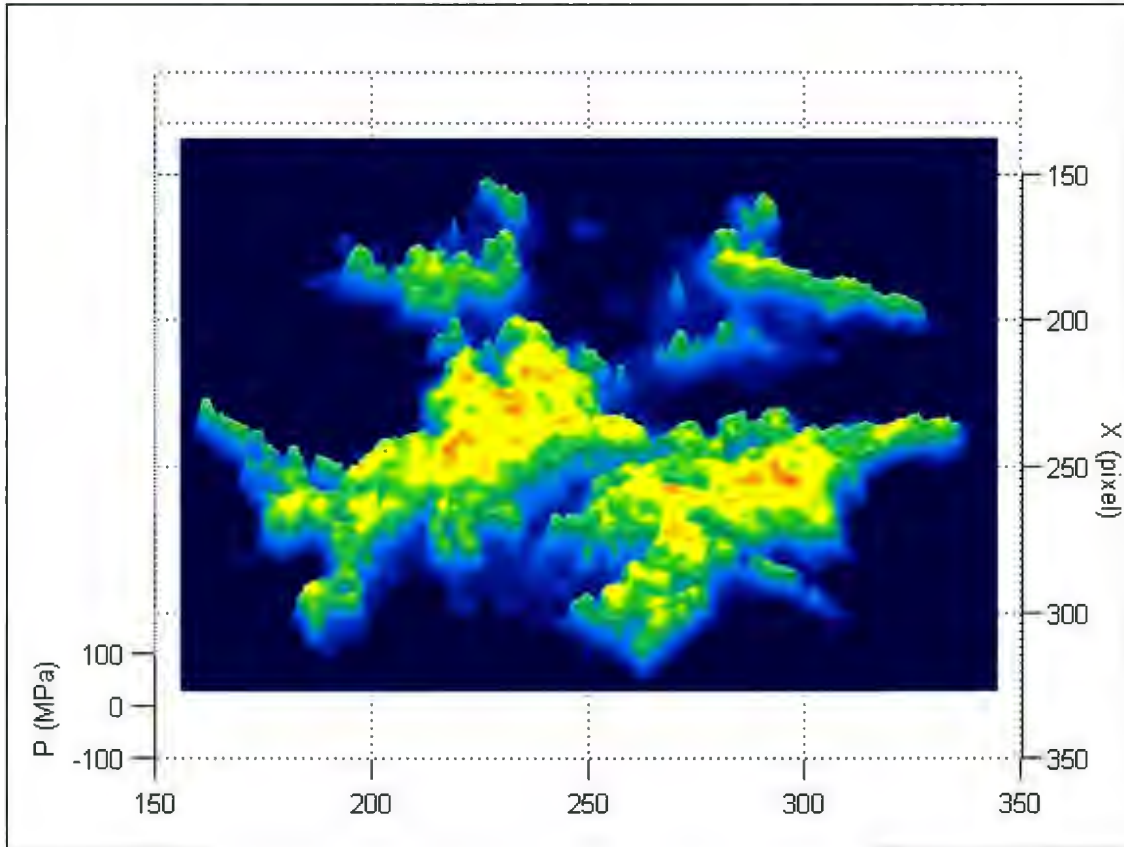


Figure 208 - F20T1b

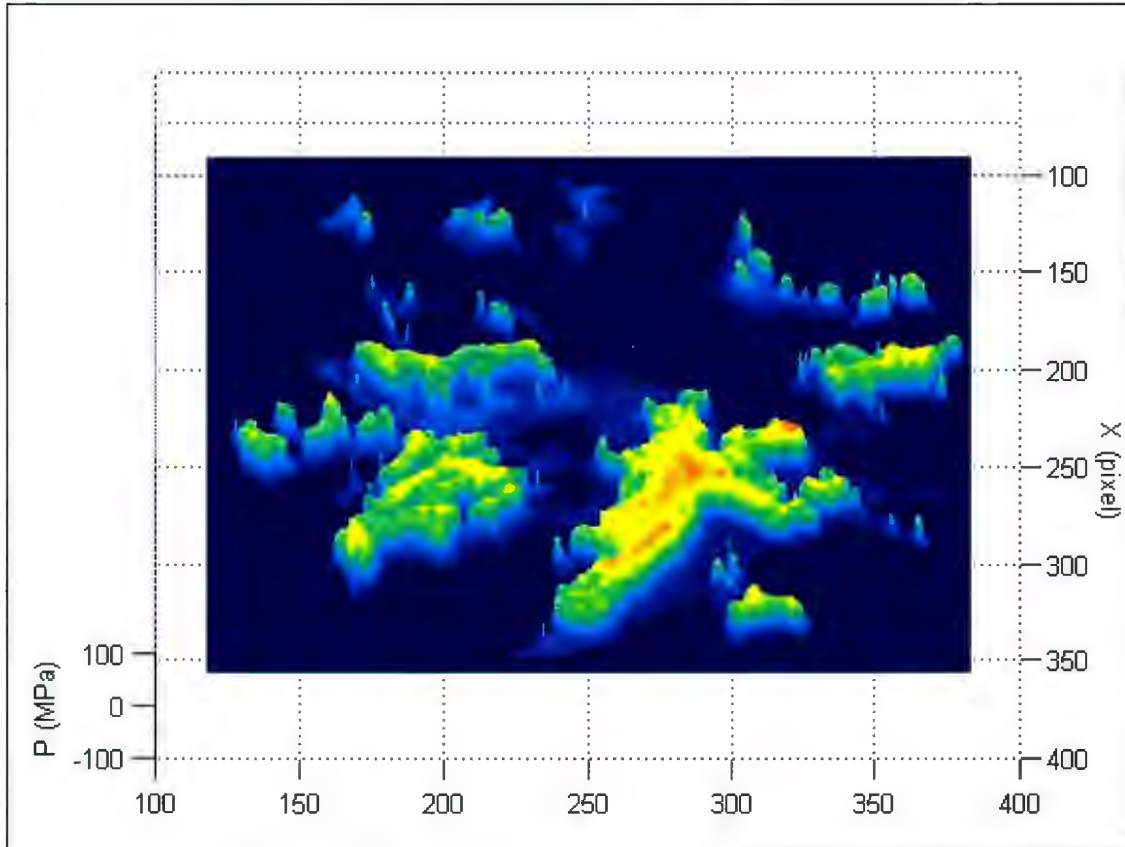


Figure 209 - F20T1c

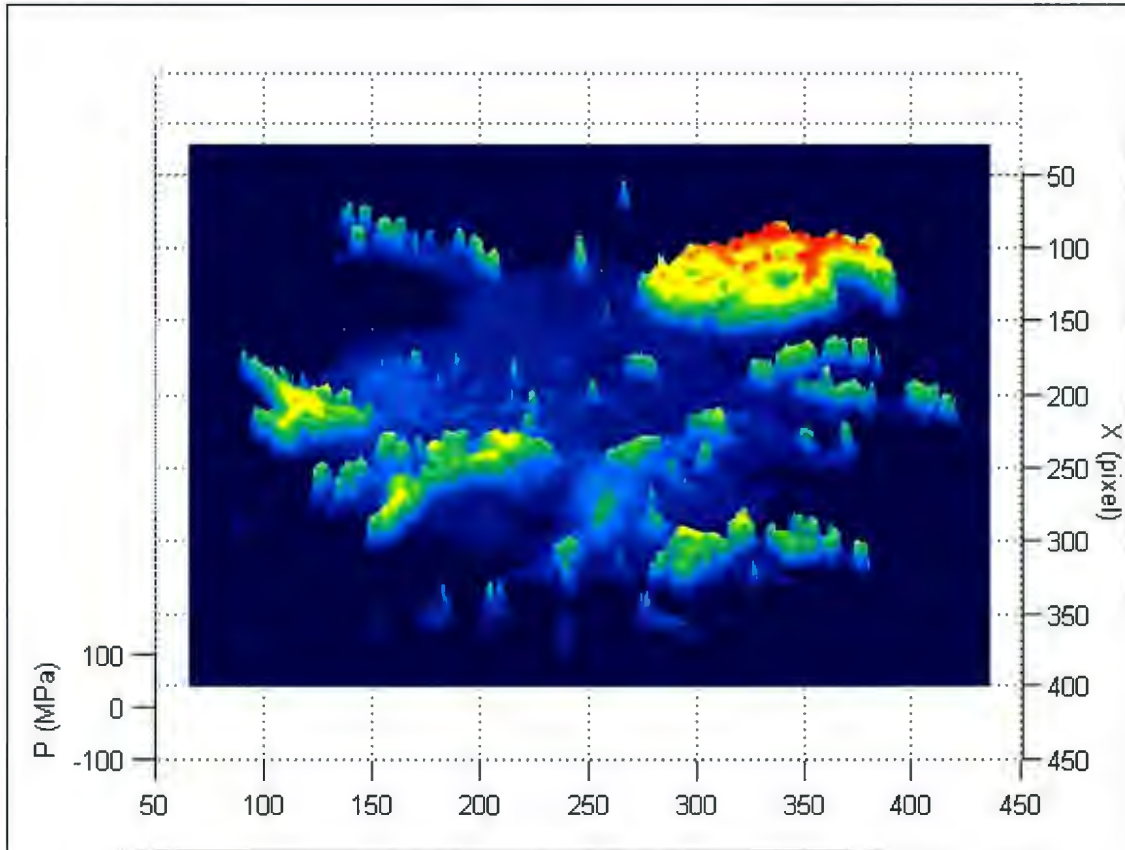


Figure 210 - F20T1d

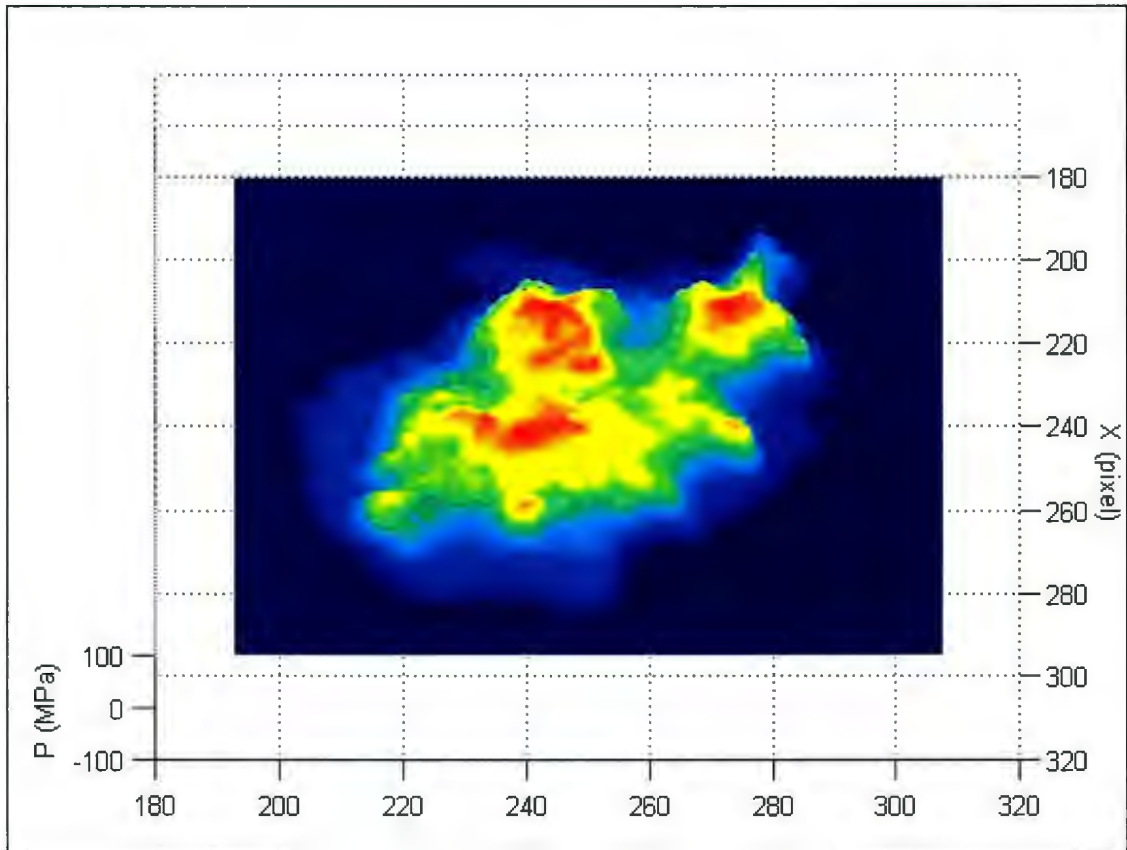


Figure 211 - F20T2a

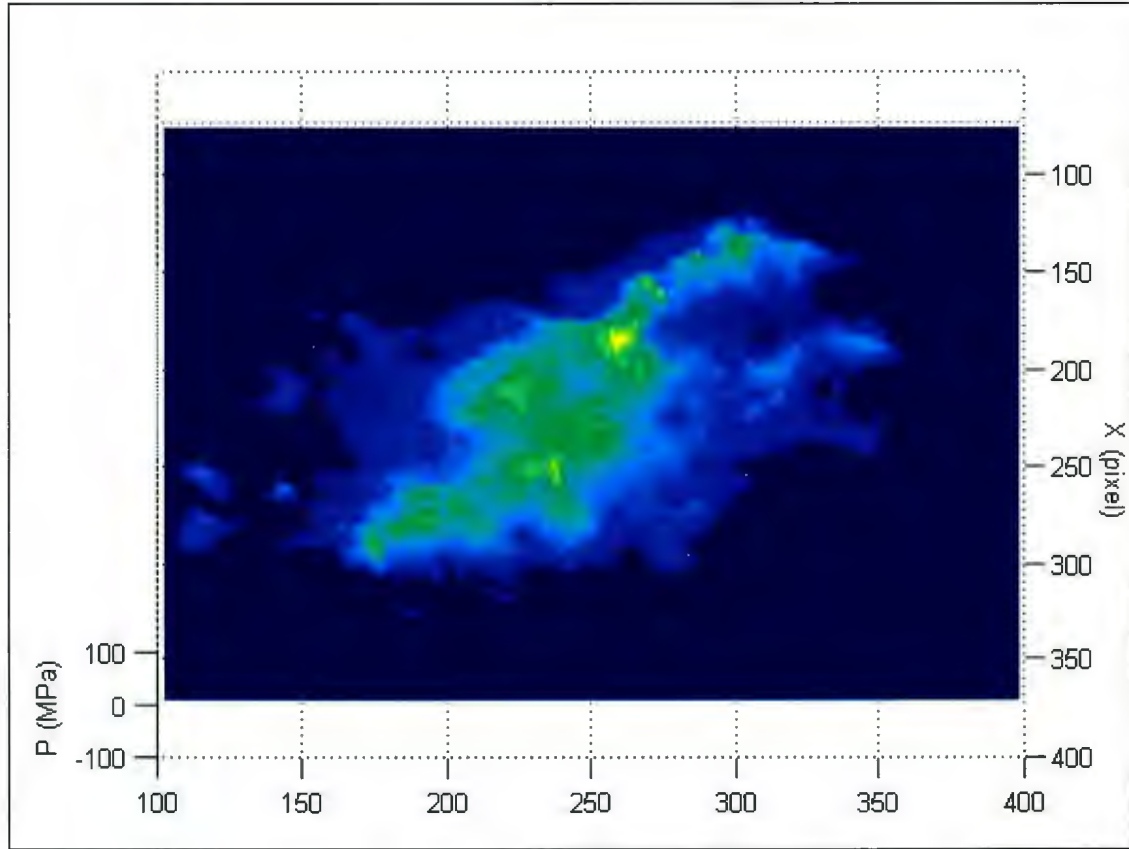


Figure 212 - F20T2b

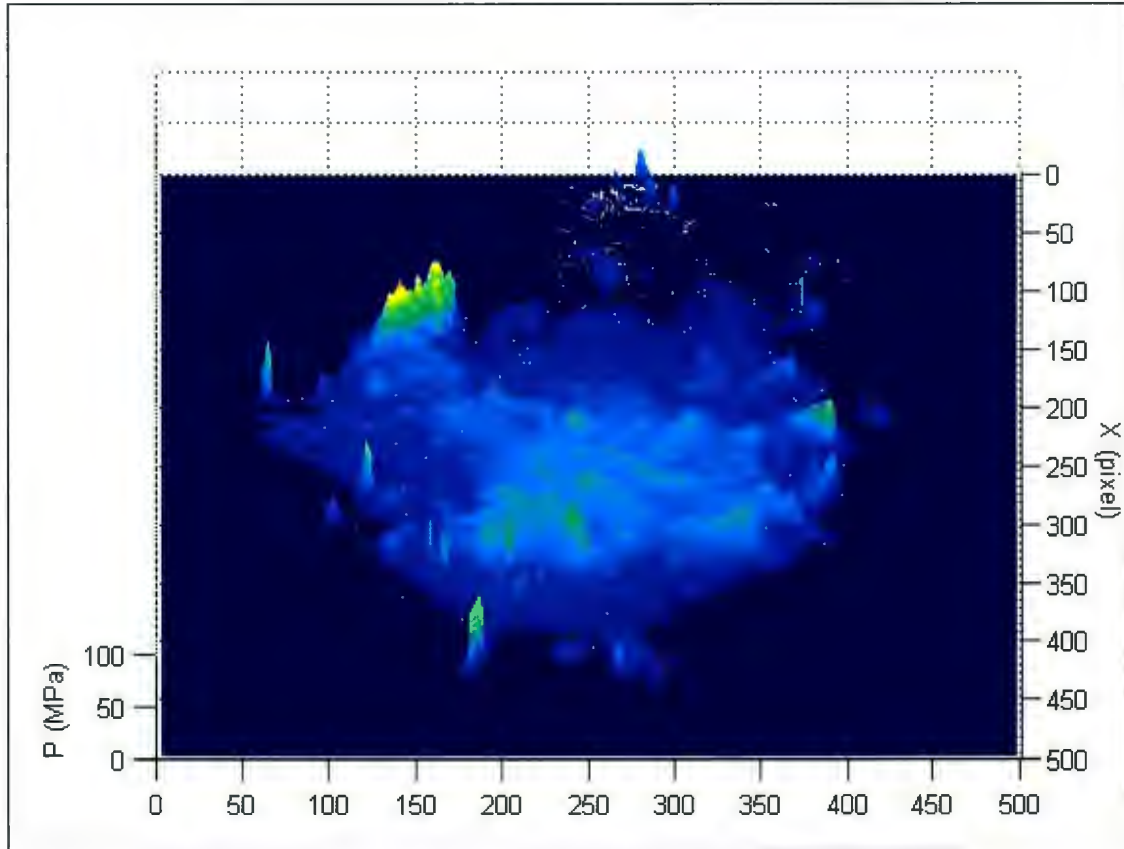


Figure 213 - F20T2c

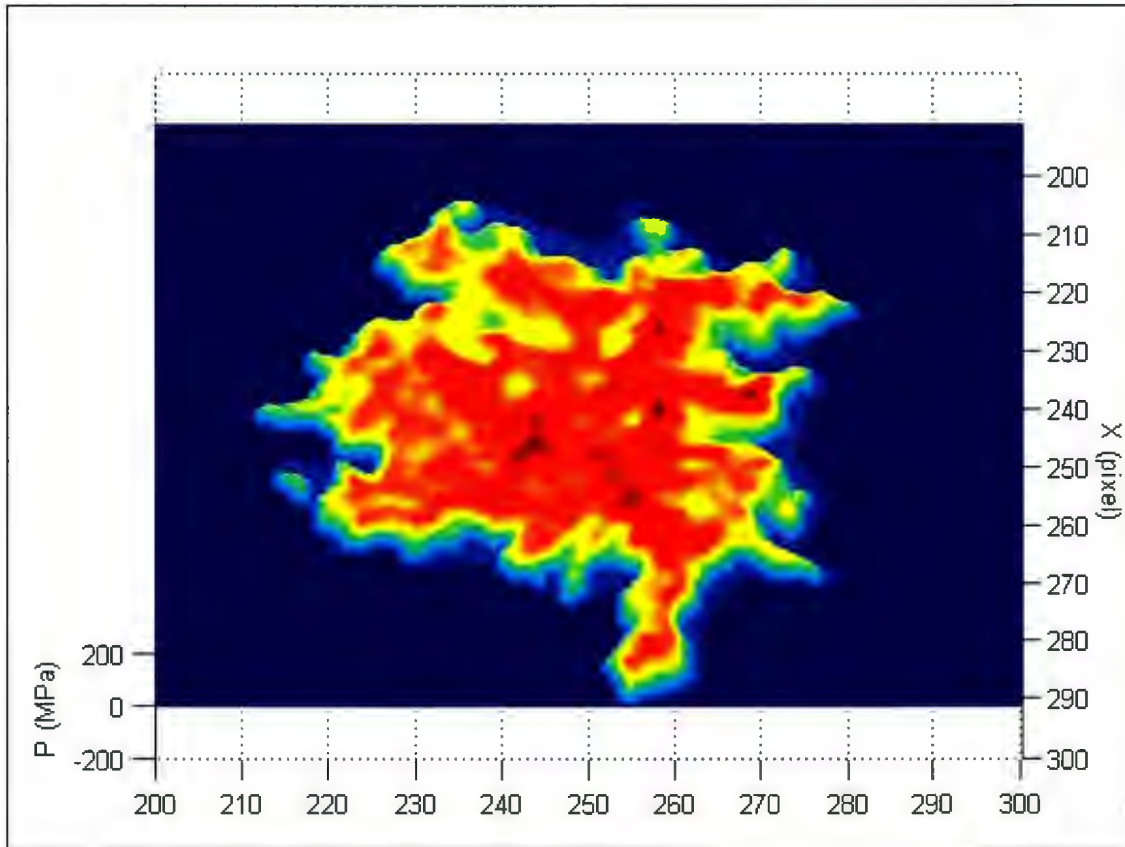


Figure 214 - F28T1a

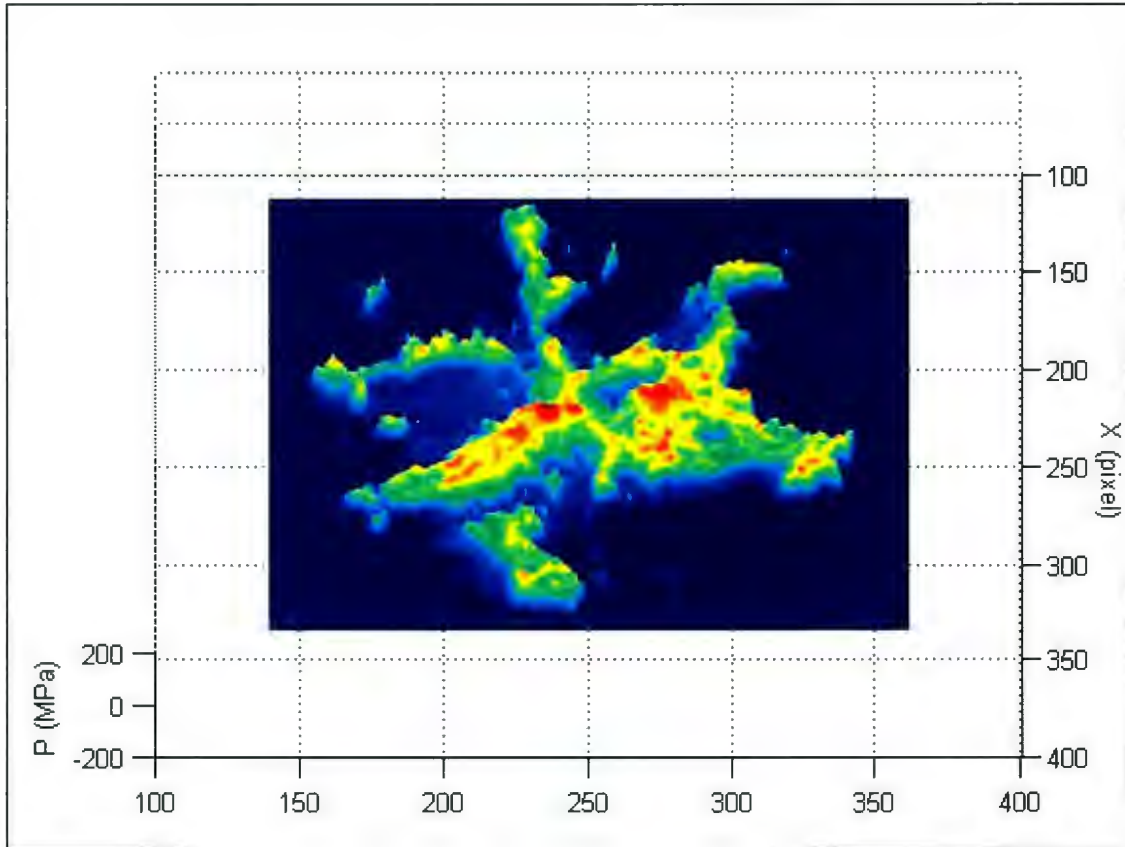


Figure 215 - F28T1b

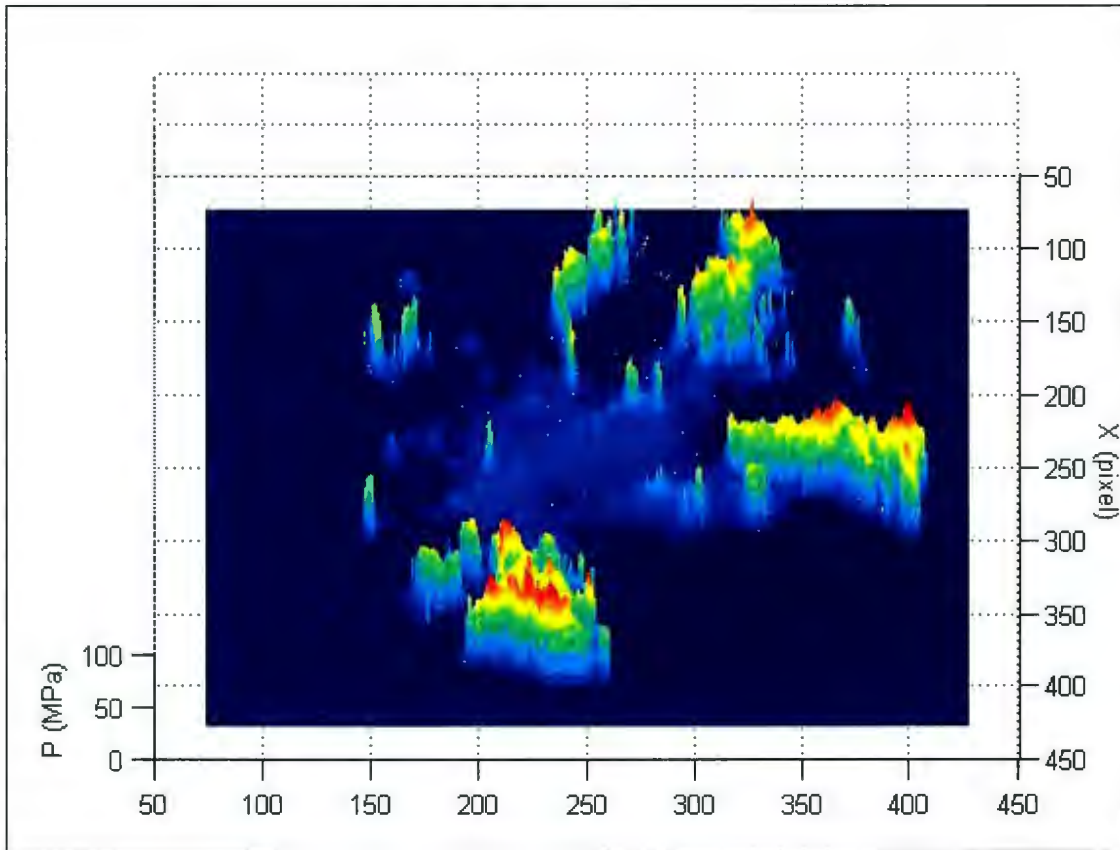


Figure 216 - F28T1c

